Phase Space Linearization and External Injection of Electron Bunches into Laser-Driven Plasma Wakefields at REGAE

Dissertation

zur Erlangung des Doktorgrades
an der Fakultät für Mathematik, Informatik und Naturwissenschaften
Fachbereich Physik
der Universität Hamburg

vorgelegt von

Benno Michael Georg Zeitler

aus München

Hamburg
2016

Gutachter der Dissertation	Prof. Dr. Florian Grüner Dr. Klaus Flöttmann Prof. Dr. Vasili Tsakanov
Gutachter der Disputation	Prof. Dr. Günter Sigl Prof. Dr. Florian Grüner Dr. Klaus Flöttmann Prof. Dr. Franz X. Kärtner Prof. Dr. Hans Peter Oepen
Datum der Disputation	13. Dezember 2016
Vorsitzender des Prüfungsausschusses	Prof. Dr. Günter Sigl
Vorsitzender des Promotionsausschusses	Prof. Dr. Wolfgang Hansen
Dekan der Fakultät für Mathematik, Informatik und Naturwissenschaften	Prof. Dr. Heinrich Graener

Dedicated to my family. In memory of my father.

Abstract

Laser **W**ake**f**ield **A**cceleration (LWFA) has the potential to become the next-generation acceleration technique for electrons. In particular, the large field gradients provided by these plasma-based accelerators are an appealing property, promising a significant reduction of size for future machines and user facilities. Despite the unique advantages of these sources, however, as of today, the produced electron bunches cannot yet compete in all beam quality criteria compared to conventional acceleration methods. Especially the stability in terms of beam pointing and energy gain, as well as a comparatively large energy spread of LWFA electron bunches require further advancement for their applicability.

The accelerated particles are typically trapped from within the plasma which is used to create the large field gradients in the wake of a high-power laser. From this results a lack of control and access to observing the actual electron injection – and, consequently, a lack of experimental verification. To tackle this problem, the injection of *external* electrons into a plasma wakefield seems promising. In this case, the initial beam parameters are known, so that a back-calculation and reconstruction of the wakefield structure are feasible. Such an experiment is planned at the **R**elativistic **E**lectron **G**un for **A**tomic **E**xploration (REGAE). REGAE, which is located at DESY in Hamburg, is a small linear accelerator offering unique beam parameters compatible with the requirements of the planned experiment. The observations and results gained from such an external injection are expected to improve the beam quality and stability of internal injection variants, due to the broadened understanding of the underlying plasma dynamics. Furthermore, an external injection will always be required for so-called staging of multiple LWFA-driven cavities. Also, the demonstration of a suchlike merging of conventional and plasma accelerators gives rise to novel hybrid accelerators, where the matured beam control achievable in conventional electron sources is combined with the huge gradients of a plasma booster stage. In this thesis, the concept of the external injection experiment at REGAE is presented. The physical foundations are illustrated and combined into an extensive start-to-end design study. Using the key constraints from this results, the required beam line design is developed.

An injection into a plasma wave with the aim of diagnosing the accelerating field inevitably requires electron bunches which are much shorter then the period of the plasma wavelength. This reference length is typically on the order of a few ten microns. The conventionally accelerated particle distribution must therefore be compressed. At REGAE the so-called ballistic bunching scheme is applied, leading to bunches with a longitudinal extent of about $3\,\mu\text{m}$. Even better results can be obtained if nonlinearities arising in the compression are compensated. A novel method to achieve this, based on the controlled beam expansion, is the *stretcher mode*. It is developed and described in detail in the second part of this thesis. Simulations that verify the analytic model presented in the thesis suggest a possible decrease in bunch length by a factor of ten and more compared to the design parameters of REGAE. Electron bunch lengths below $300\,\text{nm}$, i.e., below one femtosecond ($1\,\text{fs} = 10^{-15}\,\text{s}$) duration, can be produced. In addition, an energy spread compensation leading to quasi mono-energetic beams can be achieved by this method. Importantly, the approach is not restricted to REGAE or similar machines, but can be generalized to a variety of accelerators.

Zusammenfassung

Laser-Wakefield-Beschleunigung hat das Potential, die nächste Generation der Beschleunigertechnologie zu werden. Insbesondere die hohen Feldgradienten plasmabasierender Beschleuniger sind eine attraktive Eigenschaft, die mit der Möglichkeit einer signifikanten Reduktion der Größe zukünftiger Beschleunigeranlagen verbunden ist. Trotz der herausragenden Vorteile derartiger Quellen, gibt es allerdings derzeit noch Unterschiede bei der Strahlqualität im Vergleich zu konventionellen Techniken. Insbesondere sind Fluktuationen im Bezug auf Emissionsrichtung und Energiestabilität, wie auch die Energiebreite vergleichsweise groß und begrenzen die Anwendbarkeit von derartig erzeugten Elektronenpaketen.

Die beschleunigten Teilchen werden typischerweise aus dem Plasma selbst eingefangen, das auch als Grundlage für die enorm hohen Feldgradienten im sogenannten *wake* hinter dem Treiberlaser ist. Aus diesem Grund ist die Teilcheninjektion nicht vollständig kontrollierbar, nicht komplett nachvollziehbar – und somit auch nicht direkt experimentell bestätigt. Um dieses Problem anzugehen ist die Injektion *externer* Teilchen in ein *wakefield* ein sinnvoller Ansatz. Denn in diesem Fall sind die Anfangsbedingungen bekannt, so dass eine Rückrechnung und Rekonstruktion des beschleunigenden Feldes möglich sind. Ein derartiges Experiment ist an der ***R**elativistic **E**lectron **G**un for **A**tomic **E**xploration* (REGAE) geplant und Gegenstand dieser Arbeit. REGAE ist ein kleiner Linearbeschleuniger bei DESY in Hamburg, und besitzt einzigartige Strahlparameter, die für das beschriebene Experiment geeignet sind. Die aus einer derartigen externen Injektion gewonnenen Erkenntnisse sollen durch das vertiefte Verständnis der zugrunde liegenden Plasmadynamiken zur Verbesserung der Strahlqualität von internen Injektionsmethoden dienen. Außerdem ist eine externe Injektion immer von Nöten, sobald sogenanntes *staging* benutzt wird, d. h. die Aneinanderreihung von mehreren plasmabasierenden Beschleunigerstrukturen. Weiterhin liefert der Nachweis einer derartigen Kopplung von konventioneller und plasmagetriebener Beschleunigertechnik die Grundlage für neuartige Hybridkonzepte, bei denen die ausgereifte Strahlkontrolle konventioneller Elektronenquellen mit den außergewöhnlich hohen Feldgradienten eines Plasma-*Boosters* kombiniert werden. In der vorliegenden Arbeit wird das Konzept eines solchen Externe-Injektionsexperiments dargelegt. Die physikalischen Grundlagen werden erläutert und münden in eine umfassende Simulation des gesamten Versuchs. Mit den daraus gewonnen Erkenntnissen wird der geplante Aufbau des Experiments dargelegt.

Die Injektion in eine Plasmawelle mit dem Ziel das beschleunigende Feld zu vermessen setzt voraus, dass die verwendeten Elektronenpakete deutlich kürzer sind als die zugehörige Plasmawellenlänge. Diese beträgt typischerweise wenige zehn Mikrometer. Die konventionell erzeugten Elektronenpakete müssen deshalb komprimiert werden. Bei REGAE wird dazu der sogenannte *ballistic bunching* Mechanismus benutzt, so dass Elektronenpakete mit einer longitudinalen Ausdehnung von etwa $3\,\mu\mathrm{m}$ entstehen. Noch bessere Ergebnisse können allerdings erzielt werden, wenn Nichtlinearitäten im Zusammenhang mit der Kompression kompensiert werden. Im zweiten Teil dieser Arbeit wird eine neuartige Methode beschrieben dies zu erreichen. Sie basiert auf der kontrollierten Expansion der Pakete und wird daher als *stretcher mode* bezeichnet. Simulationen, die den Ansatz des analytischen Modells bestätigen, lassen darauf schließen, dass Kompressionen im Vergleich zu den Referenzparametern bei REGAE um einen Faktor zehn gesteigert werden kann. Elektronenpakete mit Längen unter $300\,\mathrm{nm}$ sind möglich, also mit einer Zeitdauer von weniger als einer Femtosekunde ($1\,\mathrm{fs} = 10^{-15}\,\mathrm{s}$). Zudem ermöglicht die Methode auch eine Kompensation der Energiebreite des erzeugten Elektronenpakets, so dass ein quasi monoenergetischer Strahl entsteht. Darüber hinaus muss betont werden, dass die Methode nicht auf REGAE und ähnliche Maschinen beschränkt ist, sondern auf eine Vielzahl von Beschleunigern erweitert werden kann.

Contents

1 Introduction

The field of **L**aser **P**lasma **A**cceleration (LPA) has undergone a steep rise during the last decade. The foundation was laid more than 35 years ago, though: In 1979, T. Tajima and J. M. Dawson [1] already described the capability of laser-driven plasma oscillations to create and maintain large electric field gradients which could be employed for electron acceleration. The strength of such fields can exceed 100 GV/m, which is about three orders of magnitude beyond the values manageable with current state-of-the-art **r**adio-**f**requency (rf) resonators used in conventional particle accelerators.

With the invention and development of the **C**hirped **P**ulse **A**mplification (CPA) technique [2], the intensity of laser pulses could be increased to the level required for the first LPA schemes. In various experiments using diverse concepts for the plasma wave generation, the large gradients could be demonstrated and verified. However, the beams produced in the 1990s were of poor quality, typically providing broad, exponential energy spectra [3]. A major breakthrough was achieved in 2004, when three independent groups managed to produce electron bunches of a much better quality, reducing the energy spread to only a few percent [4–6], followed by the acceleration of electrons to the energy of 1 GeV within a 30 mm plasma capillary in 2006 [7]. By now, that benchmark has been shifted to more than 4 GeV [8, 9].

The basic mechanism behind **L**aser **W**ake**f**ield **A**cceleration (LWFA) is the following: A highly intensive ultra-short laser pulse is sent towards a gas target. Due to the high field strength in the focus, the atoms are instantaneously ionized, that is, a plasma is created. Attributed to the intensity variation – described by the temporal and spatial laser profile – the so-called ponderomotive force deflects the electrons on the passage of the plasma, while the ions remain mostly unaffected. The associated density modulation leads to a restoring force, and eventually to an oscillation of the electrons around their rest position. As this perturbation rushes through the plasma, following the driving pulse, a wakefield is created behind the laser.

In order to make use of these fields, particles have to be injected into and trapped inside the plasma wave, i.e., – in mathematical terms – electrons have to be placed on a stable phase space trajectory inside the separatrix, resulting from the solution of the differential equations of the problem. A plasma naturally consists of a plethora of electrons, and there are several injection mechanisms to capture and accelerate some of these *internal* particles. For example, in the self-injection regime, the wake is driven so strongly that wave breaking occurs. This means that particles in the density peak exceed the phase velocity of the wake and are scattered into the wakefield, trapped, and accelerated [3]. A certain degree of control over the injection can be obtained by using the so-called density-downramp injection, which leads to a localized electron trapping [10]. Other mechanisms, for example the colliding pulse method, drive a wake in a milder, quasi-linear regime and use an extra switch – an additional laser pulse – which creates a beat wave with the driver, kicking particles onto stable phase space trajectories [11, 12].

The electron bunches resulting from *internal* injection typically have a very good normalized transverse emittance ($\sim 0.2\,\mathrm{mm\,mrad}$ [13, 14]) and are naturally much shorter than the plasma wavelength ($\lambda_\mathrm{p} \approx 30\,\mu\mathrm{m}$ at a plasma density of $n_\mathrm{e} = 10^{18}\,\mathrm{cm}^{-3}$); measurements demonstrated length of a few femtoseconds ($1\,\mathrm{fs} = 10^{-15}\,\mathrm{s}$) [15, 16]. In this respect, LWFA with internal injection differs fundamentally from rf-based accelerators, which initially create long bunches that have to be compressed during the acceleration process. In combination with the moderate amount of charge, this leads therefore to remarkable peak currents. Based on this, LPAs give rise to laser-plasma-driven light sources [17–20], especially concepts for compact free-electron x-ray lasers [21–23].

However, the percent-level energy spread and rather large energy fluctuations presently delivered by LWFA-driven sources is contrary to most possible applications. This is not surprising, though. Due to the short wavelength and high gradient, an extraordinarily well localized injection with respect to the phase of the wakefield is required in order to achieve results comparable with conventional photo-injectors. The latter are driven by rf pulses with a wavelength on the order of 10 cm. A phase stability of 1 deg, for example, requires a timing stability of less than 1 fs for LPAs, while these tolerances are relaxed by a factor of 1000 for conventional machines. Tolerances which are to be fulfilled on top of complex, possibly nonlinear plasma dynamics, which leads to further instabilities. Also, laser technology in the terawatt-class ($1\,\mathrm{TW} = 10^{12}\,\mathrm{W}$) – the klystron of a laser-driven plasma cavity – brings additional energy and pointing fluctuations, which are passed on to the accelerated particle distribution. At the same time, the repetition rate is on the order of 1 Hz (compared to possible MHz operation in conventional accelerators). It is limited by the high energy amplifiers of the multistage titanium-sapphire lasers and the gas load of the plasma targets, which are typically operated in pulsed mode thus giving rise to further instabilities.

Hence, there is a very high level of complexity in such a system, and therefore a variety of improvements and optimized concepts are possible. Some of them are being tackled in the LAOLA collaboration consisting of several DESY[1] groups and the accelerator physics group of the University of Hamburg [24]. The 200 TW laser system ANGUS which is used as driver for the plasma wakefields at the LUX beam line [25], as well as for the REGAE experiment described here, is optimized for stability and availability – including the beam transport. Also, the development and use of continuous flow targets is identified as a key feature to optimize stability [26] – coupled with sophisticated beam line designs for differential pumping in order to fulfill and maintain the accelerator vacuum conditions [26, 27]. First, this effort is vital due to the coupling of LWFA and a conventional accelerator (REGAE), and second, it reduces plasma instabilities while at the same time enabling the use of the full laser repetition rate.

The external injection project described in this thesis, is part of these improvement efforts [28]. The experiment is designed to provide a diagnostics tool for a laser-driven plasma wakefield in a pump-probe-type manner: Using the high-power laser ANGUS, a plasma wakefield is driven, which is probed with a well-known bunch from the conventional accelerator REGAE. The electrons

---

[1] **D**eutsches **E**lektronen-**Sy**nchrotron, the leading German center for accelerator and FEL research.

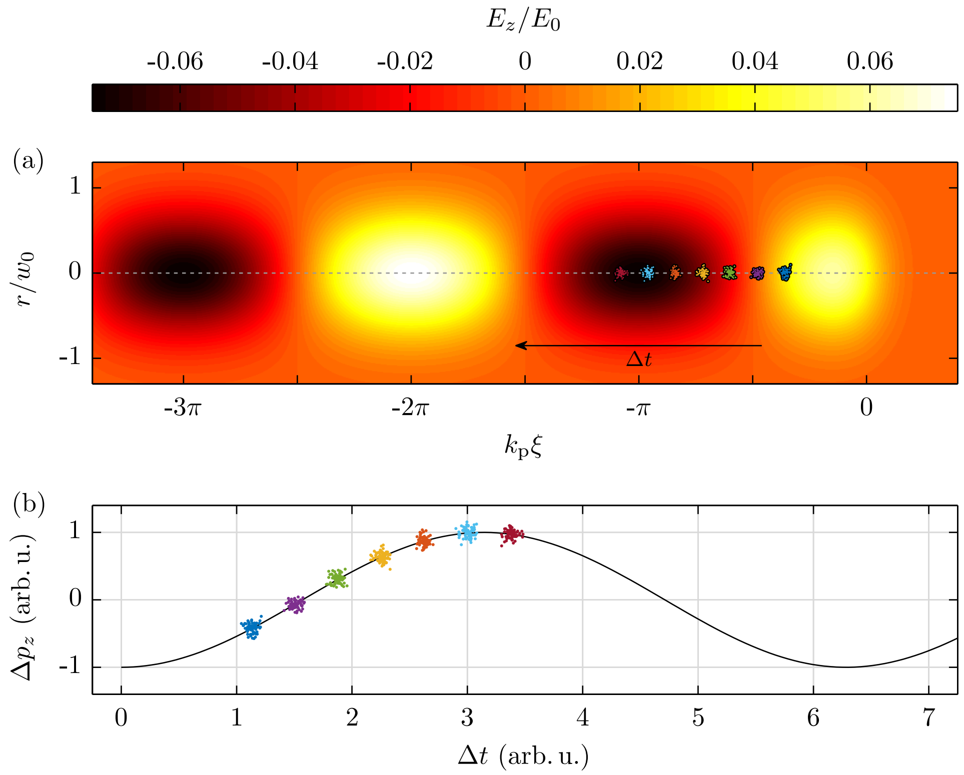

Figure 1.1 – Basic concept of the external injection experiment planned at REGAE: By injecting well-characterized bunches (depicted by the small colored distributions) of known energy at different time delays, Δt, into a laser-driven plasma wakefield [figure (a)], the resulting longitudinal momentum change, Δp_z, is recorded in the energy spectra (b). It should reproduce the shape of the accelerating field, depending on the phase, $k_\mathrm{p}\xi$, where ξ is the distance to the laser and k_p the wave number of the plasma wave. Hence, a measurement of the accelerating field is obtained, enabling a direct reconstruction of the associated plasma wakefield.

are injected at varying time delays Δt between driver pulse and electrons, while the energy gain cause by the plasma is determined; an illustration of the concept is shown in figure 1.1.

The goal is to directly measure and map out the wakefield by analyzing the resulting electron spectra, and to verify and improve the understanding of the plasma properties [28]. Furthermore, the demonstration of an emittance and charge conserving beam transport through the accelerating plasma fields is planned [29]. So far, there is no way to measure the fields inside the plasma directly. Since the initial conditions of the electron bunch as well as the wakefield itself are not known a priori in an experiment with internal injection, it is impossible to make any calculations regarding the field structure based on the energy gain. With a well-known, externally injected bunch from a conventional photo gun, however, one of these unknown variables is removed, and the reconstruction of the wakefield is feasible.

The decoupling of electron source and plasma wakefield allows for an (almost) arbitrary placement of the electrons in the wake structure, enabling a mapping out of the accelerating fields in a wide range – in longitudinal as well as in transverse direction. Moreover, as mentioned, the transverse normalized emittance of electron sources based on LWFA is very good. However, due to the combination of a large energy spread with a significant divergence at the end of the plasma target that beam quality cannot be conserved [30]. Hence, strategies to reduce this effect are necessary and have been and are still being developed [31, 32]. With a well characterized, externally injected bunch, these concepts can be validated, and possibly unknown sources for emittance growth can be identified.

The smallness of the plasma features is reflected in the demands and tolerances of the experiment. A very short bunch, much shorter than the plasma wavelength, is required[2], and likewise a fs-scale on-target synchronization of the accelerator and the driver laser [33]. In addition, the transverse offset of the laser with respect to the electrons should be well below the laser spot size, i.e., in the range of few µm or less. Therefore, the plan is to start with a low plasma density of $n_\mathrm{e} = 10^{16}\,\mathrm{cm}^{-3}$, corresponding to a plasma wavelength of about 330 µm or a period length of one picosecond ($1\,\mathrm{ps} = 10^{-12}\,\mathrm{s}$).

Moreover, to avoid complications with nonlinearities and possible pollution of the results by dark current of particles injected from the plasma itself, a (quasi) linear wake will be driven. This is, however, not a drawback or devaluation of the results to be obtained: The laser strength required to reach nonlinear plasma waves (and even the highly nonlinear bubble regime [34]) is getting weaker when the density is lowered. This is heuristically explained by the fact that there are simply less electrons to be pushed aside, and consequently smaller restoring forces to be overcome by the laser. At the same time, the opposite rule applies to the threshold for self-injection: much more power is required to achieve self-injection at low densities [3]. Hence, in principle, even the nonlinear regime is accessible and can be analyzed at the density of $10^{16}\,\mathrm{cm}^{-3}$ after gaining experience in the linear regime. Moreover, external injection is required whenever a second plasma stage is introduced – independent of the primary particle source. This means

---

[2] At this point it should be mentioned that around 1990 injection experiments into plasma waves were successfully performed. However, the waves were created using the plasma beat wave acceleration mechanism, and the injected bunches were much longer than the plasma wavelength [3].

that the results – how to transport a beam through a plasma – especially in terms of emittance conservation, are vital for any staged, plasma-based accelerator, like proposed high energy linear colliders [35]. All stages behind the source in such booster schemes will be operated in the linear or quasi-linear regime, to offer more control and avoid dark current, exactly like in the experiment described here. A first demonstration of a two-stage plasma accelerator has been shown recently [36]. However, there are large charge losses inside the second plasma stage, which could be reduced with the results from the REGAE experiment.

In particular, the outcome of this experiment should complement and improve the quality of electron bunch production at the second LWFA beamline operated at DESY. The LUX experiments performed in the other side arm of the high-power laser are dedicated to the *application* of plasma accelerated electrons [25]. Especially, the generation of highly brilliant extreme-ultraviolet and (soft)-x-ray radiation by means of undulators [17–20]. The ultimate goal of these experiments is the demonstration of a LWFA based **F**ree-**E**lectron **L**aser (FEL) [21–23].

Finally, the experiment opens the door to hybrid accelerators consisting of a standard photo injector and one (or several) plasma booster stages. Hybrid concepts are already planned and being set up in several accelerator laboratories [37]. One such experiment is going to take place at DESY in the SINBAD facility [38].

One key feature of such hybrid concepts is for sure the control obtainable in terms of electron bunch production – and the possibility to verify these bunch parameters. The quality of a beam in a linear accelerator is set at the source, and can only be spoiled from that point on. Also, the amount of charge can be controlled in a wide range from a few femto-Coulombs ($1\,\mathrm{fC} = 10^{-15}\,\mathrm{C}$) up to several nano-Coulombs ($1\,\mathrm{nC} = 10^{-9}\,\mathrm{C}$). If the bunch can be sufficiently compressed, it can in principle be injected into the plasma wake. The bunch will start to drive a wakefield on its own, though, if the charge is too high. Consequently, this so-called beam-loading yields an upper limit to the amount of charge, which is well below 1 nC [3, 39].

Conventional photo-injectors also offer a lot of possibilities for beam shaping. As mentioned, in rf-based accelerators the bunches have to be compressed in order to achieve short electron distributions and high peak currents. This is also true for REGAE, not only for the case of the external injection experiment, using a plasma wavelength on the order of $100\,\mu\mathrm{m}$, but also for another experiment performed at REGAE: ultra-fast electron diffraction [40–42].

A limit for the minimal bunch length achievable is, of course, given by space charge repulsion. However, there is also another factor which hinders the longitudinal compression, namely nonlinear phase space correlations. At modern FEL facilities, like FLASH [43] or the European XFEL [44] – both located at DESY – the longitudinal phase space is linearized using a dedicated cavity, which is operated at a higher harmonic frequency of the main rf system [45–47].

In the course of this Ph.D. work, a novel technique has been developed to optimize the compression [48]. It is based on a controlled beam expansion after the electron gun, which has similar effects to a higher harmonic structure: By the lengthening of the bunch, the curvature in the particle distribution in the longitudinal phase space is reduced, so that the field applied in the subsequent cavity – operated at the fundamental rf frequency – acts similar to a shorter rf wavelength. The method is denoted as *stretcher mode*. Although the concept is catered to REGAE, it can be generalized and extended to a variety of accelerators.

The thesis is structured as follows. In the next chapter, the physical basics of transverse beam optics are covered, as far as required for the following discourses. Likewise, the mechanism of LWFA is explained, with a focus on the linear regime. In chapter 3, these foundations are applied, leading to a conceptional design of the external injection experiment: By determining the key parameters, an extensive start-to-end simulation has been performed which is evaluated, proving the feasibility of the experiment. In particular, a broad range of the plasma wavelength can be analyzed. A reconstruction of the accelerating field seems promising, as well.

With the constraints from the simulation, the design of the beam line is explained in chapter 4; working out the upgrade of the machine was a major task of this Ph.D. work. Two projects are highlighted in that section: On the one hand, a complex and elaborated interaction chamber has been designed, which houses the three main experiments at REGAE. On the other hand, a differential pumping section has been developed, which allows an operation at the full repetition rate of the high-power laser system ANGUS, using a continuous flow gas target, and more importantly: operating this leaking device within an accelerator grade vacuum system.

Finally, the last chapter deals with the afore-mentioned linearization method. It is described in detail, deriving a complete mathematical formalism. That analytic description is used to determine seed parameters, which are subsequently applied to simulations, in order to verify the technique. The concept not only indicates the possibility to achieve bunches shorter than 1 fs – improving the REGAE design value by one order of magnitude – but also enables other phase space manipulations. In particular, an energy spread compensation is successfully shown in a simulation – which is another kind of a linear phase space distribution. Further (exemplary) capabilities, beyond the REGAE geometry are explored, as well.

The thesis is concluded with a discussion of the results.

1.1 REGAE

The accelerator to be used for the external injection experiment is called REGAE [49, 50]. The **R**elativistic **E**lectron **G**un for **A**tomic **E**xploration is located on the DESY campus in Hamburg. It is a conventional machine, consisting of a state-of-the-art rf photo gun and an additional buncher cavity. The accelerator is designed to provide unique beam parameters, first and foremost to perform time-resolved **U**ltra-fast **E**lectron **D**iffraction (UED) experiments, executed by the group of R.J.D. Miller [42]. The machine and its upgrade for the external injection experiment is described in great detail in chapter 4. Nevertheless, a short overview is given at this point, as far as it is required for the next chapters. The basic layout of the machine is depicted in figure 1.2.

The electron bunches at REGAE are produced in the gun cavity by a laser pulse shining on the cathode, and are subsequently accelerated to up to 5.6 MeV in that rf resonator. After about

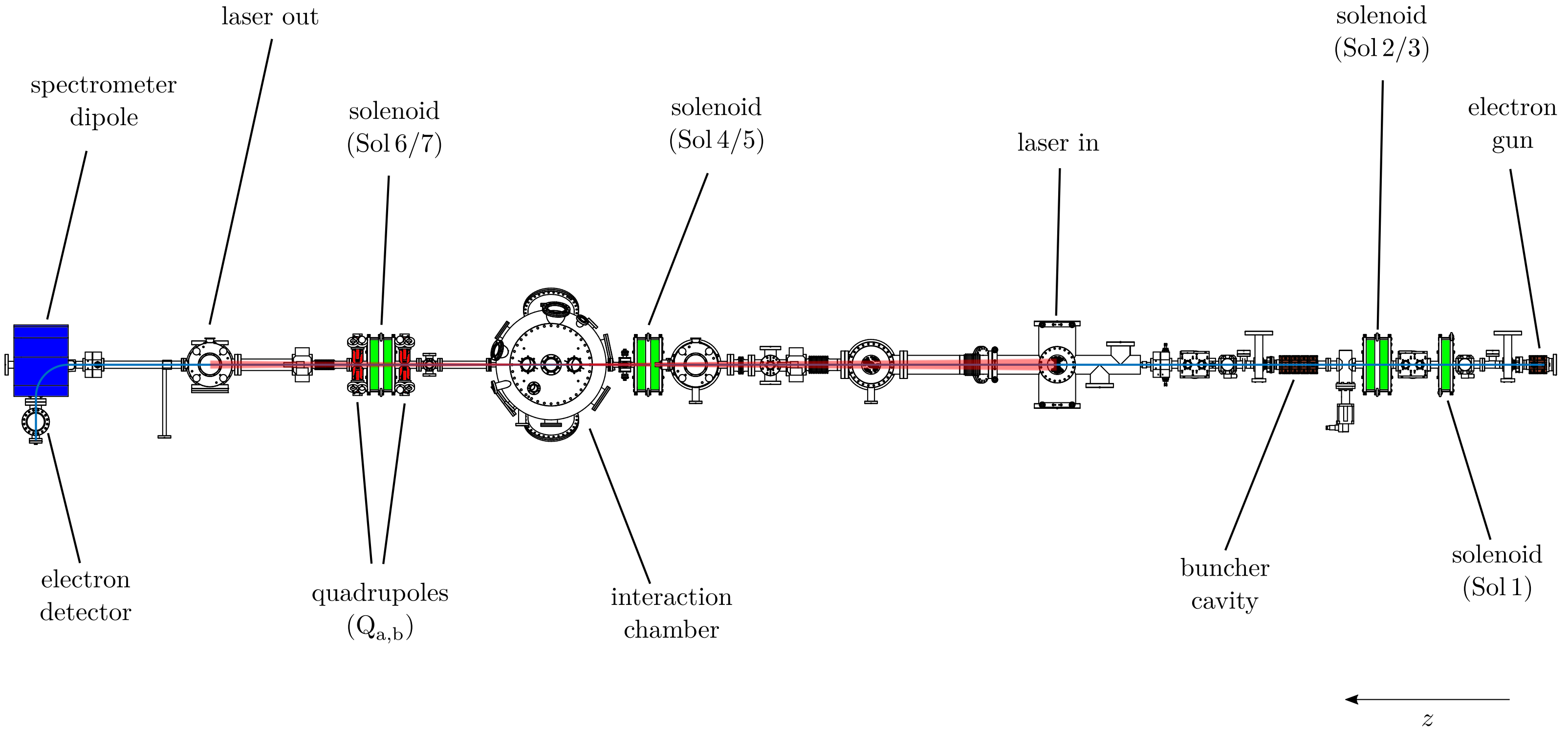

Figure 1.2 – Overview of the REGAE accelerator. The image shows a top view of the layout of the upgraded machine adapted to the external injection experiment.

1.5 m, the electrons pass the buncher cavity. In this accelerating structure no mean energy gain is acquired. Instead, a correlated energy spread is imprinted on the particle distribution, so that the particles in the tail of the bunch are faster than those in the front. The mean velocity at an energy of about 5 MeV is still small enough, and the velocity difference introduced by this method is large enough for the tailing particles to outrun the heading electrons in the adjacent drift. In other words, the bunch is compressed by this so-called ballistic bunching mechanism [51, 52]. The achievable bunch length – without the mentioned linearization – is less than 10 fs.

Due to the typically used charge being low ($Q \leq 100\,\mathrm{fC}$), the spot size of the laser pulse in the cathode can be comparatively small, because space charge effects are likewise reduced. The resulting beam therefore has a very low transverse emittance, i.e., a high quality (see chapter 2). Based on this, there is a large transverse coherence [42, 50], resulting in highly resolved single shot diffraction patterns. Combining this single shot quality with the short bunch length, it is apparent that the machine is suitable to perform UED experiments.

A key feature of the electron approach in these experiments is the interaction cross section. It is several orders of magnitude larger compared to that of x-ray photons. Therefore, the low bunch charges are sufficient to produce a diffraction pattern, and on top of that, non-destructive experimental conditions are given. The targets are rather destroyed by the pump laser pulse creating the dynamics to be probed. The penetration depth of particles in that energy range is also several millimeters, hence, also thicker samples can be used.

The topic of this thesis, however, is the usage of REGAE as photo-injector for a laser-driven plasma wakefield. The short bunches are very well suited for this purpose. However, a transverse focusing is also required. REGAE is equipped with three solenoids in front of the interaction point. The first of these magnetic coils, which act as lenses, is located behind the gun cavity. It is denoted by solenoid 1 (Sol 1). At about one meter behind the gun, solenoid 2/3 (Sol 2/3) is located. The affix 2/3 indicates, that this device is actually a double solenoid consisting of two coils which are oppositely wired. This removes the Larmor angle introduced by a single coil [53]. The same is true for solenoid 4/5 (Sol 4/5), which is about half a meter in front of the target spot. An overview of this basic REGAE layout is given in figure 1.2.

1.2 ANGUS

For the external injection experiment another device is required, namely a TW-class high-power laser. The laser system, ANGUS, is located in a neighboring building to the REGAE facility. It provides 5 J photon pulses on target, which are compressed to a **f**ull-**w**idth-at-**h**alf-**m**aximum (FWHM) length of about $\tau_{\mathrm{FWHM}} = 25\,\mathrm{fs}$. With other words, pulses with up to 200 TW can be unleashed by ANGUS. The repetition rate is 5 Hz, limited by the pump laser in the last amplifier stage. However, due to technical reasons, the pulses will not be maximally compressed for the external injection experiment. Instead, 50 TW will be directed into the gas target, located at the interaction point: The pulse length is quadrupled, $\tau_{\mathrm{FWHM}} = 100\,\mathrm{fs}$.

Angus is a titanium-sapphire based laser system with a central wavelength of 815 nm. It is optimized for stability in terms of low energy fluctuations and in particular minimization of variations in beam pointing. Regae and Angus will be synchronized with one another on a few 10 fs level. To achieve this, a drift stabilized mechanism, based on a Mach-Zehnder electro-optical modulator at 800 nm, will be used [33]. The concept is adapted from Flash, the extreme-ultraviolet and soft-x-ray free-electron laser operated at Desy [54].

1.3 Simulation Tool: ASTRA

For the various particle simulations required in the course of this thesis, the numerical code astra – **A** **S**pace Charge **Tr**acking **A**lgorithm – is used. The program is developed and maintained at Desy [55]. A big advantage of this is that adaptions specialized for issues arising from the external injection experiment could be developed and implemented into the tool.

astra is a particle tracking code. It propagates charged (macro-)particles, taking into account external electromagnetic fields defined by the user [56]. In addition, space charge effects from the Coulomb interaction of the particles in a bunch can be considered in the simulations. If the space charge routine is included, there are two possibilities to evaluate the forces: Either, a cylindrically symmetric algorithm is applied, or a full 3D calculation is started.

In the course of this work, only the cylindrical algorithm has been used. It has the advantage that the electron emission process at the cathode takes mirror charges into account. Furthermore, less (macro)-particles are required. For the calculation of space charge forces, a (cylindrical) grid is set up along the bunch, meaning the bunch is divided into longitudinal slices, which in turn consist of concentric rings in radial direction. The grid is Lorentz transformed into the rest frame, where the space charge fields are evaluated by an integration of the grid cells. The resulting field components are transformed into the laboratory frames and treated like the other external forces acting on the particles. The time propagation is ensured by means of a Runge-Kutta-based integration. In order to save computation time, the space charge routine is not called at every iteration step. Instead, the forces are scaled according to the variation of the evolving bunch dimensions [56].

Laser Module

In order to analyze effects of the interaction of an electron bunch with the pulse of the high-power laser, an additional module has been added to astra [57]. It describes the field propagation of a laser pulse in vacuum for a transverse Gaussian beam, using the paraxial approximation [58]. The model implemented is based on a derivation by [59]; circular and linear laser polarization can be considered. (Higher order effects in diffraction angle are not contained.)

Since the pulse must fulfill Maxwell's equations, the longitudinal profile is described by a hyperbolic secant; a Gaussian temporal profile does not fulfill the free space wave equation [59]. Furthermore, from $\nabla \cdot \mathbf{E} = 0$ it follows that there must be longitudinal field components present as well, because the derivative of the electric field $\mathbf{E}$ in the polarization direction is non-zero. The resulting equations for the fields of a linearly polarized laser pulse are given as [59]:

$$\begin{aligned}
E_x(r,\hat{z}) &= E_0 \frac{w_0}{w} \exp\left(-\frac{r^2}{w^2}\right) \operatorname{sech}\left(\frac{\xi}{\xi_0}\right) \cos\Psi, \\
E_y(r,\hat{z}) &= 0, \\
E_z(r,\hat{z}) &= -\frac{x}{z_R}\frac{w_0^2}{w^2} E_0 \frac{w_0}{w} \exp\left(-\frac{r^2}{w^2}\right) \operatorname{sech}\left(\frac{\xi}{\xi_0}\right) \left(\sin\Psi + \hat{z}\cos\Psi\right), \\
B_x(r,\hat{z}) &= 0, \\
B_y(r,\hat{z}) &= E_x, \\
B_z(r,\hat{z}) &= -\frac{y}{z_R}\frac{w_0^2}{w^2} E_0 \frac{w_0}{w} \exp\left(-\frac{r^2}{w^2}\right) \operatorname{sech}\left(\frac{\xi}{\xi_0}\right) \left(\sin\Psi + \hat{z}\cos\Psi\right),
\end{aligned}$$

with the phase $\Psi = \xi + \phi_{\mathrm{ce}} - \hat{z}r^2/w^2 + \arctan(\hat{z})$ and $\xi_0 = \omega\tau/\mathrm{acosh}\left[\exp(1)\right]$. Here, ϕ_{ce} is the carrier envelope phase, τ is the $1/e$ pulse length, and $\xi = \omega t - kz$ is the phase. $w = w_0\sqrt{1+\hat{z}^2}$ gives the laser beam size evolution. The quantity $\hat{z} = z/z_{\mathrm{R}}$ is the longitudinal position normalized to the Rayleigh length $z_{\mathrm{R}} = \pi w_0^2/\lambda$.

The laser module determines z_{R} using the laser wavelength λ and $1/e$ focus spot diameter w_0, specified in the input deck. A diffraction limited Gaussian beam propagation is assumed, that is the so-called beam quality factor $M^2 = 1$ [60]. A model taking into account different laser profiles is being worked on [57, 61, 62]. This is important, since the ANGUS beam propagation deviates from a Gaussian beam.

Plasma Wakefield Module

The plasma can be described in ASTRA as well [57]. The module for accelerating cavities has been extended to that case. The respective accelerating fields are implemented according to the equations of the linear LWFA regime, which are outlined in chapter 2.2. The validity of the module in the linear regime has been successfully cross-checked in the context of another Ph.D. project using particle-in-cell codes [63].

To calculate the strength and evolution of the plasma wakefield in ASTRA, the plasma profile and maximum plasma density has to be specified. Furthermore, the driving laser pulse is required in terms of pulse length and intensity, since these quantities directly enter the wakefield equations. The transverse laser evolution either follows a Gaussian envelope determined by the Rayleigh length, z_{R}, and the spot size in focus. Or alternatively, the laser envelope can be described by a separate field table. Thus, a constant laser beam diameter over a certain length can be assumed as well, like for example in the case of a guided laser. Furthermore, beams of a beam quality factor $M^2 > 1$ can be included by this method. Finally, the injection phase is specified by the distance between the laser and the electron bunch at the time the bunch enters the plasma region.

With these modules, ASTRA offers all required elements to perform a start-to-end simulation for the external injection experiment described in this thesis.

2 Fundamentals

In this chapter, the fundamental physics required for the external injection experiment is covered. In the first part of the chapter, the basic formalism of the so-called (transverse) linear beam optics is treated. Though, naturally, only aspects that are essential for the course of this work will be looked at. The same holds true for the second part of the chapter, which is dedicated to the essentials of laser wakefield acceleration, especially in the linear regime.

The coordinate system used in this chapter and throughout the whole thesis is defined as follows: z denotes the global coordinate of the beam propagation – be it a laser pulse or an electron bunch. The co-moving coordinate with the laser is ξ, while ζ is employed for the co-propagating systems of electrons. x and y mark the horizontal and vertical transverse axes respectively.

2.1 Linear Beam Optics and Matrix Formalism

In an accelerator, a bunch of particles typically travels along the design trajectory. In the case of a linear accelerator – often abbreviated as *linac* – that reference path is basically[1] a straight line which coincides with the z coordinate. Laser plasma accelerators also belong in this category. Linear *beam optics*, though, does not refer solely to linacs, but is a concept where only linear manipulations to the particle beam are taken into account.

If, in addition, there is no coupling of the dynamics between the coordinate planes, the movement of a particle reduces to the description of three independent, one-dimensional problems. In each plane a particle is then characterized by the distance to the reference coordinate and the rate of change of this, i.e., the velocity or momentum in the respective subspace. For example, in the horizontal plane, it is characterized by x and x' or p_x. Here, the divergence x' is the derivative with respect to the (global) longitudinal coordinate, z. It is connected to the derivative in time by $\partial_t = \beta c \partial_z$, where $\beta = v_z/c$ is the velocity normalized to the speed of light, c. For particles moving with a speed close to c, β approaches $\beta \approx \beta_z \approx 1$, that is, $\partial_t = c\partial_z$ in that case.

A particle in a free drift now changes its position according to $x = x_0 + x_0's$, where s is the longitudinal distance covered in that drift, x_0 is the initial position, and x_0' the initial divergence. This is obviously a linear equation. x' does not change in a free drift. In contrast, a thin lens element would change x', but does not influence x – since a thin lens acts, by definition, instantaneously. It is thus natural, to combine (x, x') into a vector, and include the changes to the particle – i.e., to this vector – in a so-called transfer matrix, M; here, in this simple picture,

---

[1] Of course, there are deviations from that path in transverse deflecting elements like dipole magnets in chicanes.

M is a 2×2 matrix. Of course, focusing elements of finite length can also be included in this formalism.

In short, the transfer matrices for a drift of length s or a thin lens with focal length f are given by [64, 65]

$$M_s = \begin{pmatrix} 1 & s \\ 0 & 1 \end{pmatrix} \quad \text{and} \quad M_f = \begin{pmatrix} 1 & 0 \\ -1/f & 1 \end{pmatrix}. \tag{2.1}$$

A focusing element of finite length can be described by

$$M_K = \begin{pmatrix} \cos(\sqrt{K}s) & \frac{1}{\sqrt{K}}\sin(\sqrt{K}s) \\ -\sqrt{K}\sin(\sqrt{K}s) & \cos(\sqrt{K}s) \end{pmatrix}. \tag{2.2}$$

Here s is again the length of the acting element, while K is the (constant) focusing strength. K can also be negative, which leads to a hyperbolic solution describing a defocusing element. Please note that a free drift is actually included in expression (2.2), which yields M_s for $K = 0$. The focusing strength is typically resulting from a multipole expansion of the acting field, and can be different for the transverse planes. For example, a dipole magnet only acts in one plane (having a simple drift in the second plane), or if a quadrupole magnet has a positive (focusing) $K_x > 0$ in x, then $K_y < 0$ (but $|K_x| = |K_y|$).

For the description of a particle's behavior along an accelerator beam line, the segments of constant K are put together by a matrix multiplication, so that the initial particle state (x_0, x'_0) is mapped to the outgoing coordinates (x, x') by this *linear transformation.* The product of the individual transfer matrices results in the transfer matrix for the respective segment of elements. An element of variable K can thus be approximated by splitting the element description into smaller slices with piecewise constant K, which are then combined into the respective transfer matrix by a multiplication of the corresponding slice matrices. It should be noted that the matrix approach yields a separation of machine parameters described by the matrices and beam parameters, which are included in the particle coordinate vectors.

The generalization of the formalism to a particle bunch is achieved by describing the beam in terms of average and **r**oot **m**ean **s**quare (RMS) quantities. The average or mean (denoted with $\langle\,\cdot\,\rangle$) is given by the so-called first moment for a function $f(x)$ and a normalized density $\rho(x)$:

$$\langle f(x) \rangle = \int \rho(x) f(x)\,\mathrm{d}x, \tag{2.3}$$

while the RMS value, $x_{\text{RMS}} = \sigma_x = \sqrt{\langle x^2 \rangle}$, is connected to the variance or second central moment $\langle\,\cdot^2\rangle$, which is defined as:

$$\left\langle [f(x)]^2 \right\rangle = \int \rho(x)\,[f(x)]^2\,\mathrm{d}x - \left(\int \rho(x) f(x)\,\mathrm{d}x \right)^2. \tag{2.4}$$

2.1.1 Beam Emittance and Courant-Snyder Parameters

The combination of particle position and velocity/momentum into a vector naturally calls for a phase space treatment of the problem. Plotting the individual particle coordinates into the phase space x-p_x yields a cloud of particles covering a certain area. Now, by Liouville's theorem, the phase space density covered by this particle cloud is constant in a conservative Hamiltonian system like the one treated here [64–66]. As a consequence, the phase space volume covered is constant as well, since the number of particles is conserved. This is, strictly speaking, only true for the six-dimensional phase space of the 3D problem, but if there are no couplings between the planes, it is also valid for the projection to the subspaces.

The emittance, ε, is a measure for this phase space volume, and thus a constant of motion. To tackle this mathematically, one basically takes the product of the RMS quantities described above minus possible linear correlations, which change in the phase space evolution (of linear beam optics). This is necessary in order to ensure the conservation of this quantity. Put into a formula, the normalized RMS emittance, $\varepsilon_{\mathrm{RMS}}$, is defined as [30]

$$\varepsilon_{x,\mathrm{RMS}} = \frac{1}{m_{\mathrm{e}}c}\sqrt{\langle x^2\rangle \langle p_x^2\rangle - \langle xp_x\rangle^2}, \tag{2.5}$$

where the second term in the brackets removes the linear correlations, and m_{e} is the electron (rest) mass. The second term is also called the covariance of x and p_x, or generally for functions $f(x)$ and $g(x)$:

$$\langle f(x)g(x)\rangle = \int \rho(x)f(x)g(x)\,\mathrm{d}x - \int \rho(x)f(x)\,\mathrm{d}x \int \rho(x)g(x)\,\mathrm{d}x. \tag{2.6}$$

In that sense, $\varepsilon_{\mathrm{RMS}}$ can also be seen as the square root of the determinant of the covariance matrix, C, which has the variance as diagonal elements and the covariance on the off-diagonal positions [67]:

$$C = \begin{pmatrix} \langle f^2\rangle & \langle fg\rangle \\ \langle gf\rangle & \langle g^2\rangle \end{pmatrix}. \tag{2.7}$$

For a discrete distribution, like (macro-)particles in a simulation, the integrals are replaced by the corresponding sums over all particle coordinates (x_i, x_i').

If there are couplings between the planes, for example x-p_z, or if there are nonlinear correlations which evolve along the beam propagation, the emittance described by this approach is no longer conserved, as will be seen in chapters 3.2 and 5. This, however, does not mean that Liouville's theorem is not fulfilled: The 6D particle cloud still has a constant volume, independent of its shape. The same holds true for the phase space in the projected 2D subspaces, if there are no couplings between the planes. Since correlations are attributed to the shape of the phase space distribution, they are not covered by Liouville's theorem. Hence, the RMS emittance does not describe the phase space volume evolution according to this theorem in this case. It is rather the sum consisting of a Liouville emittance plus nonlinear correlated contributions (which can change and evolve along the beam propagation.) If not stated otherwise, the normalized RMS emittance is used in the following, i.e., $\varepsilon := \varepsilon_{\mathrm{RMS}}$.

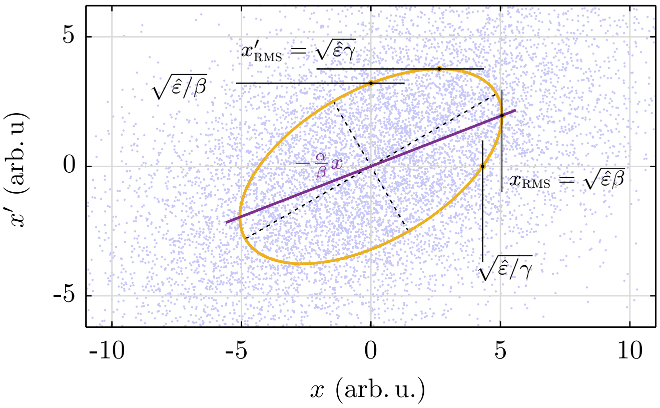

Figure 2.1 – Important points of the phase space ellipse describing the emittance and the according relations to the Courant-Snyder parameters (α, β, γ). (Figure adapted from [30].)

The normalized emittance, ε, has to be distinguished from the geometric emittance – in this work marked by $\hat{\varepsilon}$ – which is defined as [30, 68]:

$$\hat{\varepsilon} = \frac{1}{\langle p_z \rangle} \sqrt{\langle x^2 \rangle \langle p_x^2 \rangle - \langle x p_x \rangle^2} = \frac{1}{\langle \beta\gamma \rangle} \varepsilon. \tag{2.8}$$

Here β is the normalized velocity as above and $\gamma = 1/\sqrt{1-\beta^2}$ is the Lorentz factor. The conversion to the normalized emittance in the last step is obtained using $p_z = \beta\gamma m_{\mathrm{e}} c$. The geometric emittance is hence getting smaller during acceleration, which is called adiabatic damping of the emittance.

As mentioned earlier, the matrix formalism provides a natural separation of beam and machine parameters. By introducing the so-called Courant-Snyder parameters[2], (β, α, γ), [64, 65, 69], the emittance can be parameterized as $\varepsilon = \gamma x^2 + \alpha x x' + \beta x'^2$, which is also known as Courant-Snyder invariant [69].

This equation describes an ellipse in the 2D phase space; see figure 2.1. This ellipse has an area[3], but also further geometric properties, namely the orientation in phase space. Seen from another perspective, one could say the Courant-Snyder parameters make use of this by defining a normalized ellipse which carries along the geometric properties: $\sqrt{\beta}$ is the extent in x, while $\sqrt{\gamma}$ is the width in x'. α defines the correlation, and thus the tilting of the ellipse in that coordinate system. More precisely, $-\alpha/\beta$ describes the slope of the correlation axis going through the outermost points of the ellipse, which lie on $\pm\sqrt{\beta}$; if $\alpha > 0$, the beam is convergent, $\alpha < 0$ describes a divergent beam and $\alpha = 0$ describes a local minimum (focus) or maximum of the beam envelope.

The evolution of the Courant-Snyder parameters can be similarly transported via the matrix formalism. Instead of a vector, though, a matrix is required. It is given by (see for example

---

[2] These parameters are not to be confused with the Lorentz β and γ.

[3] The area contains a factor of π. It is usually included into the units, $[\varepsilon] = \pi\,\mathrm{m\,rad}$, but omitted in the notation.

[64]):

$$\Sigma = \begin{pmatrix} \beta & -\alpha \\ -\alpha & \gamma \end{pmatrix}. \tag{2.9}$$

And for the transport from position 1 to 2, the transport matrix $M_{1,2}$ [e.g. equations (2.2) and (2.1)] and additionally its transpose are needed [64, 65]:

$$\Sigma_2 = M_{1,2}\Sigma_1 M_{1,2}^{\mathrm{T}}. \tag{2.10}$$

Basically, equation (2.9) is once again the covariance matrix for the normalized ellipse. And, hence, it follows: $\beta\gamma - \alpha^2 = \sqrt{1}$, which means that the ellipse is defined as soon as two of these parameters are known. Also, in the extrema of the beam envelope, where $\alpha = 0$, the remaining parameters are obviously coupled by $\gamma = 1/\beta$.

Finally, the beam size and divergence can be calculated to [30, 64, 65]:

$$x_{\mathrm{RMS}} = \sqrt{\hat{\varepsilon}\beta} \quad \text{and} \quad x'_{\mathrm{RMS}} = \sqrt{\hat{\varepsilon}\gamma}. \tag{2.11}$$

See figure 2.1 for an illustration. Please note that the geometric emittance $\hat{\varepsilon}$ is used here. The correlations are also illustrated in figure 2.1. In particular, the RMS emittance (and not Liouville) is a quality criterion for an electron beam. It determines, for example, how well a beam can be focused.

2.2 Laser Wakefield Acceleration

In the second part of this chapter, a short introduction to the mechanisms of laser wakefield acceleration is given, focusing on the so-called linear regime. It is mainly based on the extensive review paper by E. Esarey, C. B. Schroeder, and W. P. Leemans [3].

2.2.1 Ponderomotive Force

A laser pulse can be characterized by its vector potential $\boldsymbol{A}(x, y, z, t)$, where the associated electric and magnetic fields are determined by $\boldsymbol{E} = -\partial_t \boldsymbol{A}/c$ and $\boldsymbol{B} = \nabla \times \boldsymbol{A}$. Especially for high-power lasers, it is convenient to use the normalized vector potential, $\boldsymbol{a} := e\boldsymbol{A}/(m_{\mathrm{e}}c)$: For $a \geq 1$ one speaks of a laser with a *relativistic* intensity, since an electron with charge e acquires a kinetic energy equivalent to its rest mass m_{e} within one half cycle of the pulse, i.e., the Lorentz factor of an electron at rest ($\gamma = 1$) doubles.

The coupling of an electron to the laser fields is given by the Lorentz force, which in terms of $\boldsymbol{A}$ reads [3]:

$$\frac{\mathrm{d}\boldsymbol{p}}{\mathrm{d}t} = \frac{e}{c}\left(\frac{\partial \boldsymbol{A}}{\partial t} - \boldsymbol{v} \times \nabla \times \boldsymbol{A}\right) = \frac{e}{c}\left\{\frac{\mathrm{d}\boldsymbol{A}}{\mathrm{d}t} - \Big[(\boldsymbol{v}\cdot\nabla)\,\boldsymbol{A} + \boldsymbol{v} \times \nabla \times \boldsymbol{A}\Big]\right\}. \tag{2.12}$$

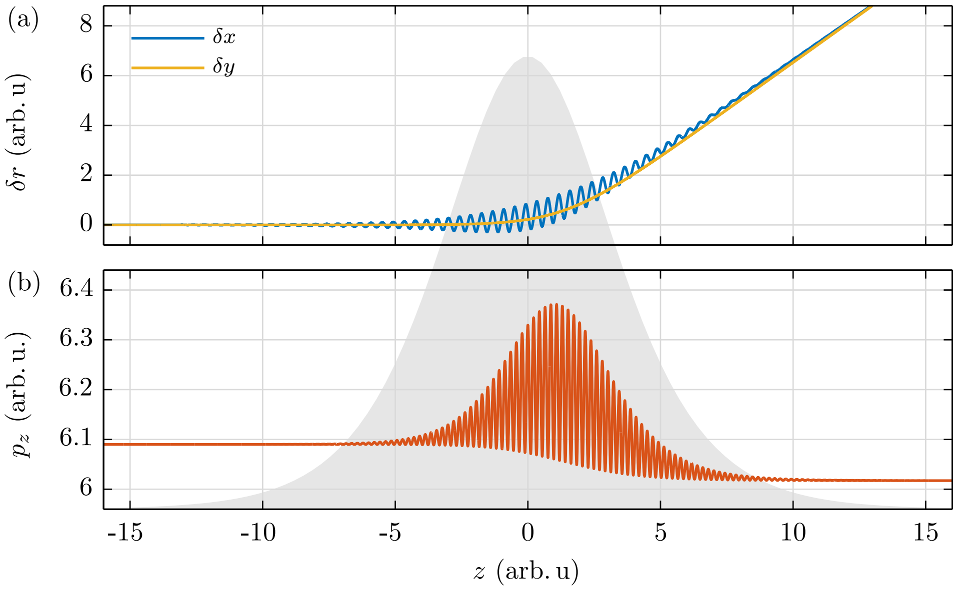

Figure 2.2 – (a) Ponderomotive force acting on two co-moving particles starting at the same distance from the beam axis. The blue colored plot has an offset in the polarization direction of the laser (x), leading to a clearly visible wiggling and a net deflection due to the varying field strength along the oscillating trajectory. The yellow line marks the trajectory of a particle at an offset of the same magnitude, but in y-direction, that is, perpendicular to the polarization. The wiggling is much weaker, since it is coupled to the magnetic field; it is therefore not resolved. The net effect, however, is identical, i.e., the ponderomotive force is (to leading order) radially symmetric, despite the polarized laser. Figure (b) depicts the longitudinal momentum of a particle *co-moving* with the laser. The associated longitudinal ponderomotive force results in a reduction of the momentum p_z after the interaction, because the laser intensity is increasing during the overtaking, so that the ponderomotive force on the descending flank of the laser pulse exceeds the effect caused by the rising flank. The frequency doubling in the oscillation compared to the transverse case is due to the coupling of the magnetic field and the transverse velocity caused by the electric field. The gray area illustrates the intensity profile of the laser for both cases.

To leading order, the electron will follow the rapidly changing electric field described by the first term of the right hand side. The velocity acquired by this so-called quiver motion is $v_{\mathrm{qm}} = eA/(m_{\mathrm{e}}c) = a$, for the case that $a \ll 1$, also called the linear limit. v_{qm} enters the term in square brackets leading to second order effects. The quiver term vanishes in the time-averaged result, while the second order term can be simplified by a vector identity of the double cross product, leading to the ponderomotive force,

$$\boldsymbol{F}_{\mathrm{p}} = -\frac{m_{\mathrm{e}}c^2}{2}\nabla a^2. \tag{2.13}$$

Particles are pushed out of the high intensity region of the laser pulse by this radiation pressure. An intuitive explanation for this effect in the oscillation plane comes from the field-inhomogeneity of the profile: An electron is accelerated in the laser's field and displaced, so that the magnitude of the repelling force upon sign change in the oscillation cycle is weaker – and the particle does no longer reach its starting position. Hence, the electrons accumulate a time-averaged net change in momenta during the interaction with the laser field. The other planes require the coupling via the magnetic field. In that sense, the ponderomotive force relies on a kind of symmetry breaking inhomogeneity and a large enough a in order to achieve a significant displacement within a half laser cycle [70]. An illustration of the ponderomotive force is shown in figure 2.2.

The longitudinal ponderomotive force is also shown in figure 2.2. As can be seen, the oscillation frequency in this case is double the frequency ω of the transverse oscillations. This is due to the coupling of the electric field component $E_x \propto \sin(\omega t - kz)$ and the magnetic field component $B_y \propto \sin(\omega t - kz)$ associated with the longitudinal oscillations in a laser field polarized in x-direction: The corresponding transverse quiver velocity is resulting from

$$v_x \propto \int E_x \,\mathrm{d}t \propto -\cos(\omega t - kz), \tag{2.14}$$

and thus the change in momentum is given by

$$\Delta p_z \propto -\int \sin(\omega t - kz)\cos(\omega t - kz)\,\mathrm{d}t = \frac{1}{4}\cos\left[2\left(\omega t - kz\right)\right] + C, \tag{2.15}$$

which explains the frequency doubling. Here, C is a constant of integration.

The overall loss of longitudinal momentum p_z for the case shown in figure 2.2(b) is due to the electron co-moving with the laser. During the overtaking, the laser intensity increases, since the depicted process happens before the focus. Hence, the effect of the ponderomotive force in the rising flank of the laser is less than the effect in the descending shoulder of the pulse. Thus a net momentum loss is obtained in this case.

2.2.2 Plasma Wakefields

If a laser pulse of significant power is focused on a sufficiently small spot size, the peak normalized vector potential in focus (the so-called laser strength parameter), a_0, can be on the order of $a_0 \sim 1$, and higher. The respective intensity for a 800 nm laser achieves values of $I = 10^{18}\,\mathrm{W\,cm^{-2}}$ in this case. If such a pulse is directed into hydrogen, the gas is instantaneously ionized, since the threshold for barrier suppression ionization of hydrogen is $1.4 \times 10^{14}\,\mathrm{W\,cm^{-2}}$ [70]. Thus, a plasma is created.

The ponderomotive force associated with the pulse displaces the electrons inside the plasma, while the protons are not affected considerably due to their comparatively large mass. The resulting density modulation leads to an oscillation of the electrons with the plasma frequency

$$\omega_\mathrm{p} = \sqrt{\frac{n_\mathrm{e} e^2}{\epsilon_0 m_\mathrm{e}}}\,, \tag{2.16}$$

where n_e is the electron or plasma density and ϵ_0 the vacuum permittivity. The perturbation rushes through the (cold) plasma with the phase velocity, v_p, which is approximately the group velocity, v_g, of the laser in this medium – so-called Langmuir waves are excited by this process [70]; their wavelength is given by the plasma wavelength $\lambda_\mathrm{p} = 2\pi c/\omega_\mathrm{p}$, in practical units $\lambda_\mathrm{p}(\mu\mathrm{m}) \approx 3.3 \times 10^{10}/\sqrt{n_\mathrm{e}(\mathrm{cm}^{-3})}$. Due to the density gradient an (electric) wakefield builds up in the trail of the laser. The magnitude of the wakefield can exceed the so-called cold non-relativistic wave-breaking field [3],

$$E_0 = \frac{c m_\mathrm{e}}{e}\omega_\mathrm{p}. \tag{2.17}$$

This field strength can be expressed in practical units by $E_0(V/m) \approx 96\sqrt{n_\mathrm{e}(\mathrm{cm}^{-3})}$. Thus, for a plasma with $n_\mathrm{e} = 10^{18}\,\mathrm{cm}^{-3}$, an accelerating field of $E_z = 100\,\mathrm{GV/m}$ and more is possible. This value exceeds the gradient of conventional accelerating cavities ($E_z \sim 100\,\mathrm{MV/m}$) by three orders of magnitude, marking *the* key feature of the LWFA technique and plasma acceleration in general.

The response of the plasma to the exciting ponderomotive force depends on the strength of this pump. For $a_0 \ll 1$, a linear perturbation is created, leading to sinusoidal Langmuir waves. The resulting wakefield has a sinusoidal shape, too. The theoretical formulations of this problem can be analytically solved in three dimensions using a quasi-static approach [63]. In the following, a linearly polarized, Gaussian shaped laser pulse – transverse and longitudinal[4] – is assumed. If the polarization is in x-direction, the normalized vector potential can be written as

$$\boldsymbol{a}(r,\xi) = \frac{1}{\sqrt{2}} a(z) \exp\left(-\frac{r^2}{w^2(z)}\right) \exp\left(-\frac{\xi^2}{4\xi_\mathrm{RMS}^2}\right) \cos\left(k_\mathrm{l}\xi\right)\, \hat{\boldsymbol{e}}_x. \tag{2.18}$$

Here, $r = \sqrt{x^2+y^2}$ is the magnitude of the radial vector $\boldsymbol{r}$ while $w(z)$ is the $1/e$ diameter of the beam and $a(z)$ is the amplitude of the vector potential, both evaluated at position z. $\xi = z - v_\mathrm{g} t$ is the transformation to the frame co-moving with the laser pulse, which is possible due to the quasi-static approximation. ξ_RMS denotes the RMS length of the laser pulse. The laser group velocity can be approximated by [3]

$$v_\mathrm{g} \approx \sqrt{1 - \frac{\omega_\mathrm{p}^2}{\omega_\mathrm{l}^2}}\, c = \sqrt{1 - \frac{\lambda_\mathrm{l}^2}{\lambda_\mathrm{p}^2}}\, c, \tag{2.19}$$

---

[4] As mentioned in chapter 1, this is strictly speaking not in accordance with the free space wave equation. However, it is a reasonable approximation used in literature, like for example in [3].

where ω_l and λ_l are the carrier wave frequency and wavelength of the laser. Accordingly, k_l in equation (2.18) is the wave number. The factor $1/\sqrt{2}$ in $\boldsymbol{a}\left(r,\xi\right)$ accounts for the intensity expressed by the laser strength parameter, $a_0^2 = a^2(0)$, which is defined for a circularly polarized laser beam, and has to be corrected for linear polarization [3, 63].

The wakefield in this regime can now be calculated to [3, 32, 63]:

$$\begin{aligned} E_z\left(r,\xi\right) &= \frac{m_\mathrm{e}c^2k_\mathrm{p}^2\xi_\mathrm{RMS}}{2e}\sqrt{\frac{\pi}{2}}\,a^2(z)\exp\left(-\frac{k_\mathrm{p}^2\xi_\mathrm{RMS}^2}{2}-\frac{2r^2}{w^2(z)}\right)\cos\left(k_\mathrm{p}\xi\right), \\ E_r\left(r,\xi\right) &= -r\frac{2m_\mathrm{e}c^2k_\mathrm{p}\xi_\mathrm{RMS}}{e}\sqrt{\frac{\pi}{2}}\frac{a^2(z)}{w^2(z)}\exp\left(-\frac{k_\mathrm{p}^2\xi_\mathrm{RMS}^2}{2}-\frac{2r^2}{w^2(z)}\right)\sin\left(k_\mathrm{p}\xi\right). \end{aligned} \tag{2.20}$$

Hence, there is an accelerating, longitudinal field component, E_z, and a (de-)focusing transverse part, E_r. E_r is shifted with respect to E_z by $-\pi/2$. In the linear regime, only longitudinal oscillations of the electrons are assumed, that is, the beam size w is taken to be much larger than the pulse length ξ_RMS, so that electron displacements in z-direction are entirely dominating.

Using the linear term of a multipole expansion at $r = 0$ of the focusing field yields the focusing strength $K(\xi)$, like for any beam optical element, as mentioned in section 2.1. It is given by [32]:

$$K(\xi) = \frac{e}{\gamma m_\mathrm{e}c^2}\frac{\partial E_r}{\partial r}\bigg|_{r=0} = -\frac{2k_\mathrm{p}\xi_\mathrm{RMS}}{\gamma}\sqrt{\frac{\pi}{2}}\frac{a^2(z)}{w^2(z)}\exp\left(-\frac{k_\mathrm{p}^2\xi_\mathrm{RMS}^2}{2}\right)\sin\left(k_\mathrm{p}\xi\right). \tag{2.21}$$

Please note that due to the phase shift between transverse and longitudinal fields, there is only a quarter of a wavelength where the wakefield is accelerating and at the same time focusing. The fields are illustrated in figure 2.3.

In accordance with equations (2.20), the magnitude of the wakefield generated depends on $a(z)$ in this case, i.e., the *local* driver strength. This is an approximation, taking the evolution of the laser's caustic into account. In other words, at each longitudinal plasma position, a slightly different oscillation is generated. However, as stated earlier, there are only longitudinal oscillations present in the linear regime, meaning that the electrons shift into the regions of different amplitudes. If the Rayleigh length of the laser is much longer compared to the plasma wavelength, the deviation is small, so that the assumption is justified. Also, the plasma density must not vary on too short scales.

The laser intensity can be kept constant in the case of a guided beam. This can be achieved by relativistic self-focusing, which is based on the increasing Lorentz factor γ of the electrons accelerated in the laser's field. For an electron in a laser pulse with vector potential $a(r)^2 \ll 1$ this can be approximated to $\gamma \approx 1 + a(r)^2/2$ [3, 70]. The refractive index of the plasma is given by [70]

$$\eta = \sqrt{1-\frac{\omega_\mathrm{p,rel}^2}{\omega_\mathrm{l}^2}}\,, \tag{2.22}$$

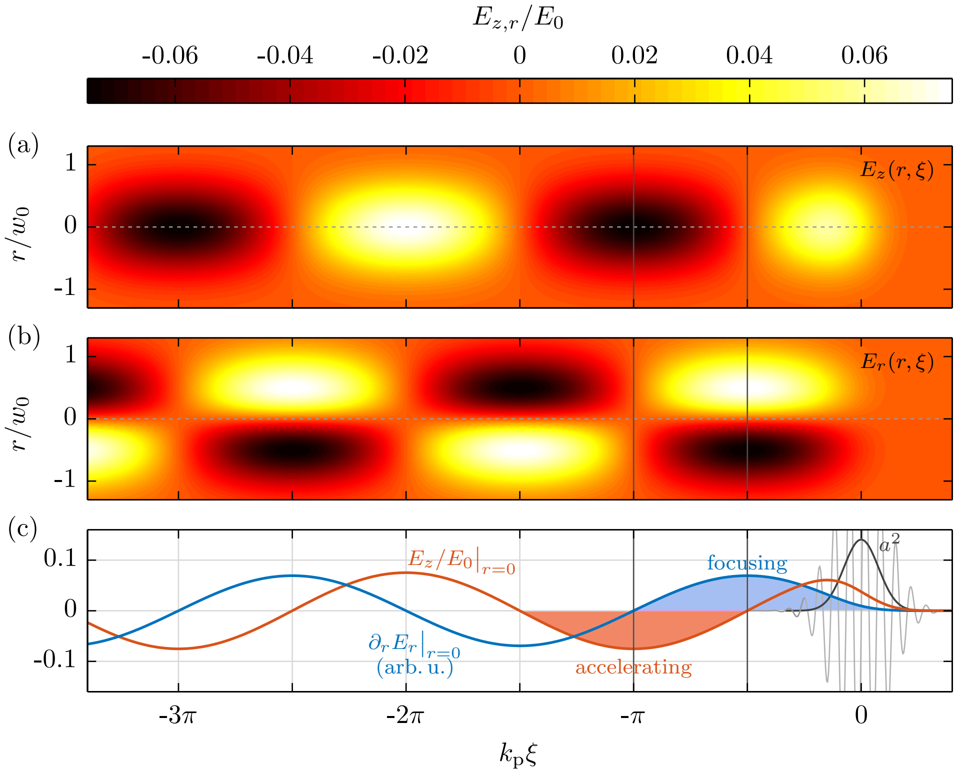

Figure 2.3 – Illustration of the longitudinal and transverse field components in the linear LWFA regime. The fields are solved at the laser focus with $a_0 = 0.75$ and $w_0 = 42.5\,\mu\text{m}$; $n_e = 10^{16}\,\text{cm}^{-3}$. Figure (a) shows the longitudinal field depending on the phase and distance r to the laser beam axis, while in (b) the focusing/defocusing component is plotted. The field pattern is created solely by longitudinal electron displacements: Density extrema are at the zero crossing of the accelerating field, E_z; a maximum is for example found at $k_p\xi = -3/2\pi$, while minima are at $k_p\xi = -1/2\pi$ and $k_p\xi = -5/2\pi$ – compare with figure 2.4. In (c), the accelerating field at the laser axis ($r = 0$) and the on-axis focusing strength $K \propto \partial_r E_r\big|_{r=0}$ are evaluated. Please note the region of simultaneously focusing and accelerating fields, marked by the vertical lines. Figure (c) adapted from [63].

where the plasma frequency has been corrected for relativistic effects; compare with equation (2.19). That means,

$$\omega_{\mathrm{p,rel}} = \sqrt{\frac{n_{\mathrm{e}} e^2}{\epsilon_0 \gamma m_{\mathrm{e}}}} = \frac{\omega_{\mathrm{p}}}{\sqrt{\gamma(r)}}, \tag{2.23}$$

with the non-relativistic plasma frequency ω_{p} [equation (2.16)]. Hence, the refractive index has a radial component depending on the lasers intensity profile, leading to a focusing effect. The threshold for this relativistic self-focusing is given by the critical power [70],

$$P_{\mathrm{c}} = 16\pi\epsilon_0 \frac{m_{\mathrm{e}}^2 c^5}{2e^2} \left(\frac{\omega_{\mathrm{p}}}{\omega_{\mathrm{l}}}\right)^2, \tag{2.24}$$

which can be expressed in practical units as $P_{\mathrm{c}}(\mathrm{GW}) \approx 17.5\,(\omega_{\mathrm{p}}/\omega_{\mathrm{l}})^2$ [3, 70]. Alternatively (and complementary), a shaping of the transverse density profile can also lead to such a focusing effect. For a guided beam, these parameters are matched in such a way, that the natural diffraction of the laser is exactly compensated by this focusing effect, keeping a constant beam radius and thus a constant laser intensity [3, 70].

The wakefield description according to equations (2.20) has been implemented into ASTRA, and benchmarked against a so-called **P**article-**In**-**C**ell (PIC) simulation of high computational effort in order to cross-check and evaluate the approximation. (For details see [32, 63]). Since the results are comparable, the above-described method (and the respective ASTRA module) is used in the following. Please note, PIC codes are lastly numerical models of the processes involved, and thus provide no exact solutions of the problem. Also, there can and will be deviations from the experimental results in this case. Therefore, it is one of the key points of the external injection experiment described in this thesis to offer another, experimentally accessible benchmark for the analytic and numerical descriptions of the wakefield formation.

The validity of the fields described above also diminishes with increasing laser intensity. For relativistic laser intensities, that is when approaching (and exceeding) $a_0^2 \gtrsim 1$, the plasma response gets more and more nonlinear [70]. The increasing Lorentz factor, γ, included in the ponderomotive force, starts to influence the plasma dynamics equations. Also, there is only a finite amount of electrons to be displaced, meaning that at some point a deviation from the sinusoidal fields is inevitable. The result is a spiked electron density profile with almost emptied regions in between. Similar to a homogeneously charged sphere, a linear increasing electric field builds up in these segments of low electron density due to the ion background – resulting in an overall saw-tooth like electric field. Furthermore, the plasma wavelength gets elongated, due to the scaling of the plasma frequency with $\omega_{\mathrm{p,rel}} \propto 1/\sqrt{\gamma}$.

An analytic description of this nonlinear regime is only possible in one dimension, and for certain laser pulse shapes [3]. Figure 2.4 shows an example of the numerical solution for one of these cases, leading to the afore-mentioned density spikes and saw-tooth-shaped wakefield structure. In order to investigate transverse fields, self-injection mechanisms and many other effects, PIC simulations are typically required. A treatment of the nonlinear regime is, however, beyond the scope of this thesis and the experiment. The laser strength parameter in this case is about $a_0 = 0.75$.

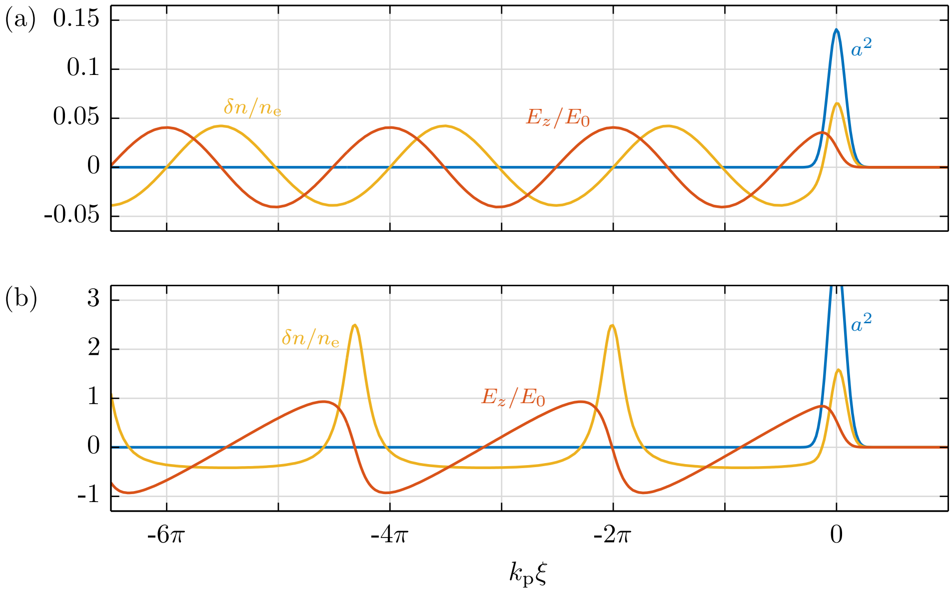

Figure 2.4 – Comparison of the linear LWFA regime (a) to the nonlinear regime (b) for a plasma density of $n_\mathrm{e} = 10^{16}\,\mathrm{cm}^{-3}$. In case (a), the linearly polarized Gaussian driver has a laser strength parameter of $a_0 = 0.75$, in contrast to (b) with $a_0 = 4$. Hence, in (a) a sinusoidal density perturbation $\delta n/n_\mathrm{e}$ is excited, leading to a likewise longitudinal field, E_z. For (b), on the other hand, a lengthening of the plasma wavelength can be seen, accompanied by a spiked density profile and a sawtooth-shaped E_z, which is characteristic for the nonlinear LWFA regime. The curves are calculated by a numeric integration of the Poisson equation for the one-dimensional, nonlinear regime given in [3].

3 Conceptual Design of the External Injection Experiment

Having introduced the basic features of LWFA in the linear regime in the previous chapter, this chapter is dedicated to develop an explicit concept of a first laser-pump electron-probe experiment on such plasma wakefields. The purpose of this experiment is to provide a diagnostics to directly infer the shape of the accelerating field: By determining the energy gain of *well-known* electron bunches injected into the plasma at different wakefield phases, a back-calculation to the respective accelerating field is possible. In other words, the method allows for a mapping of the plasma wakefield structure.

The chapter is structured as follows. First, the key parameters of the conceptualized experiment will be discussed, followed by considerations on the beam transport through the plasma. As will be shown, the bunch is overtaken by the faster laser pulse close to the focus. This technically could spoil the experiment if the effects of the ponderomotive force associated with the laser-electron interaction were too severe. Hence, an investigation of this *overtaking problem* is included. Finally, putting all these considerations together, a start-to-end simulation of the experiment, using ASTRA, is executed and analyzed. It is complemented by investigations of output deviations resulting from fluctuations in the input parameters.

3.1 Key Parameters and Constraints

The first step in conceptualizing the external injection experiment is the definition of key parameters, resulting from technical and physical constraints and limitations. These fall into three categories, namely plasma quantities, laser parameters, and electron bunch properties.

The plasma density is set to $n_\mathrm{e} = 10^{16}\,\mathrm{cm}^{-3}$, corresponding to a plasma wavelength of $\lambda_\mathrm{p} = 334\,\mu\mathrm{m} \mathrel{\widehat{=}} 1\,\mathrm{ps}$. The advantages of such a comparatively low plasma density are derived from several considerations: First, REGAE is capable of producing electron bunches with an RMS length of about $\zeta_\mathrm{RMS} \approx 3\,\mu\mathrm{m} \mathrel{\widehat{=}} 10\,\mathrm{fs}$, i.e., the probe pulse is about $1\,\%$ of the structure to be resolved in this case. This allows for a reasonable resolution for the mapping of the wakefield. For higher densities, the ratio gets worse. It is also important to keep in mind that the field variation of the sinusoidal wave happens within half the wavelength, and on the other hand, ζ_RMS is the RMS value, which means, the whole bunch covers a larger phase interval.

Second, as discussed in chapter 2.2, only about a quarter of λ_p is accessible in the pump-probe experiment, since in the remainder the bunch is spoiled by either defocusing or decelerating

Plasma		**Laser**		**Electrons**	
density	$n_\mathrm{e} = 10^{16}\,\mathrm{cm}^{-3}$	strength	$a_0 = 0.75$	energy	$\langle T \rangle = 5.6\,\mathrm{MeV}$
wavelength	$\lambda_\mathrm{p} = 334\,\mathrm{\mu m}$	beam waist	$w_0 = 42.5\,\mathrm{\mu m}$	Lorentz factor	$\langle \gamma \rangle = 11.95$
peak field	$E_z = 789\,\mathrm{MV/m}$	Rayleigh length	$z_\mathrm{R} = 3.1\,\mathrm{mm}$	beam size	$r_\mathrm{RMS} \approx 5\,\mathrm{\mu m}$
plateau	$L_\mathrm{pt} = 25\,\mathrm{mm}$	pulse length	$\tau_\mathrm{FWHM} = 100\,\mathrm{fs}$	bunch length	$\zeta_\mathrm{RMS} \leq 3\,\mathrm{\mu m}$
ramps	$L_\mathrm{udr} = 5\,\mathrm{mm}$	wavelength	$\lambda = 815\,\mathrm{nm}$	emittance	$\varepsilon_{xy} \approx 50\,\mathrm{nm\,rad}$

Table 3.1 – Overview of the key parameters relevant for the conceptual design of the external injection experiment at REGAE. The peak gradient of the plasma wakefield is calculated from the maximal accelerating phase, $k_\mathrm{p}\xi = -\pi$ at the laser focus position using equation (2.20).

forces. At the low density, the useful region is extended into the decelerating (and focusing) phase, because the expected field gradient is on the order of 1 GV/m, leading to an energy gain/loss of only few a MeV for a centimeter scale target. Thus, the REGAE electrons with about 5 MeV can pass the plasma even within a significant region of the decelerating phase interval. The level and stability of the synchronization between ANGUS and REGAE is closely connected to this accessible field region. The implementation of a concept which suggests a locking of the machines on a few 10 fs level is subject of another Ph.D. project [71, 33]. This jitter interval should be significantly shorter than the structure to be resolved. Furthermore, the probe pulse should possibly stay within the focusing interval. Hence, a plasma density of $n_\mathrm{e} = 10^{16}\,\mathrm{cm}^{-3}$ offers a good compromise.

The plasma profile is chosen to be as simple as possible: A constant plateau of 25 mm length, complemented by a 5 mm long up- and downramp at the beginning and end of the target. It is planned to create the plasma profile using a channel fed by two inlets which define the plateau region; the ramps result from the short segments between beginning and end of the channel and the respective inlet (please refer to chapter 4.2.2). Apart from keeping things simple at the start, the measurement and *verification* of a plasma at such a low density is a challenge on its own; see for example [26, 72–76]. Thus, more complicated profiles (transverse or longitudinal) can probably not be resolved and validated. Moreover, a changing plasma density leads to a variation of the plasma wavelength, adding considerable phase slippage. That circumstance increases the complexity of a back-calculation. In the case of the present upramp, one already has to be careful [63]: The overall acting accelerating and (de-)focusing fields depend on the bucket into which the bunch is injected. The separation distance of the buckets is defined by the periodicity in the plateau region, where the plasma density and hence the wavelength is constant. Since the plasma density in the ramps is less than in the plateau region, the plasma wavelength decreases accordingly. That is, a shift of 2π in the plateau region does not shift the phase by one period in the ramps. Consequently, for each additional shift by one period in the region of constant plasma density, the respective fields in the ramp are different for each of these shifts, while the magnitude of the fields in the plateau is unchanged by the shifts.

However, due to the laser evolution, the effect is very weak in the case treated in the following: The laser will not be guided within the plasma, since this requires much more laser strength than ANGUS can provide at the plasma density aimed for – and/or additional transverse plasma profile

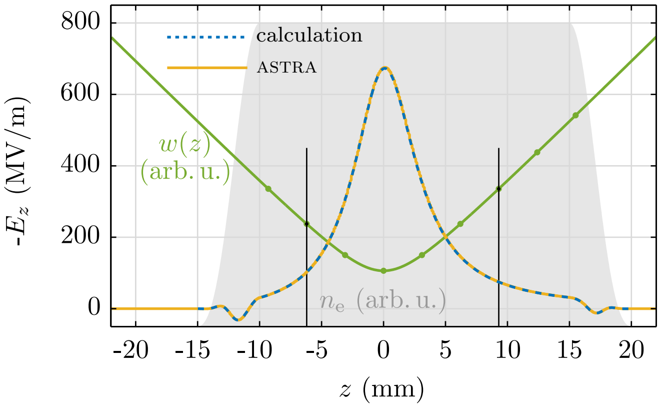

Figure 3.1 – The local on-axis field $E_z(z)$ evaluated for one injection phase ($\xi_0 = -424\,\mu m$). A step-wise solution of equation (2.20) is compared to the output of an ASTRA simulation. Phase slippage of the electrons with respect to the field propagation is taken into account. The gray shaded area marks the region of the plasma. The dots in the laser envelope line, $w(z)$, are multiples ($[-3, \dots, +5]$) of the Rayleigh length, z_R around the focus. The region of strong accelerating (and also transverse) forces is limited by the driver strength, and not by the length of the plasma channel. The main acceleration happens within $-2z_R \le z \le +3z_R$, indicated by the black upright lines. The asymmetry is attributed to the rate of phase slippage, which reduces due to the energy gain. The dips in the ramps are based on density induced phase slippage.

shaping. The critical power for relativistic self-focusing (see chapter 2.2) in a plasma of a density of $n_e = 10^{16}\,\mathrm{cm}^{-3}$ is $P_c = 3\,\mathrm{PW} = 3000\,\mathrm{TW}$. In contrast, ANGUS can provide a peak power up to 200 TW, so that relativistic self-focusing is impossible to achieve at this plasma density.

Instead, the laser is focused 10 mm behind the beginning of the plateau. This value roughly corresponds to three Rayleigh length, z_R. Considerable acceleration is expected within $-2z_R \le z \le 3z_R$ (see figure 3.1), hence, the effect of the up- and downramp is reduced to an acceptable amount. Finally, the group velocity of the laser inside the medium at this density is $v_g/c = 0.999997$ according to equation (2.19), so that a (density profile dependent) correction for the wave propagation is negligible.

ANGUS is focused within $f = 4.2\,\mathrm{m}$ to a spot size diameter of $W = 50\,\mu m$ FWHM, which translates to a $1/e^2$-radius of $w_0 = 42.5\,\mu m$ for a Gaussian beam. However, the beam profile of ANGUS is not Gaussian, but of so-called super-Gaussian shape, (please see chapter 4.1), and the focus profile is close to a sinc^2 distribution. The Rayleigh length in this configuration is $z_R = 3.1\,\mathrm{mm}$, according to the ray tracing code ZEMAX [77, 78]. The laser pulse duration is set to $\tau = 100\,\mathrm{fs}$ FWHM, instead of possible 25 fs. This is a technical limitation determined by the damage threshold of the last mirror before the focus. In this case, the normalized vector potential in the focus amounts to $a_0 = 0.75$. With these parameters, a comparatively long Rayleigh length is achieved, while the laser intensity around the focus is high enough to excite a quasi-linear plasma wave. It is noteworthy that an efficient plasma wake generation at a higher density of $n_e = 10^{17}\,\mathrm{cm}^{-3}$ is also possible with these settings.

The electrons emitted from the REGAE gun have a maximum energy of 5.6 MeV when the gun cavity is operated on-crest at a gradient of 120 MV/m. Since the buncher cavity is operated at the zero crossing phase, this mean energy is not changed, meaning the probe particles are injected with a Lorentz factor $\gamma \approx 12$, and a normalized velocity $\beta = v/c = 0.9965$. As the wakefield trails the laser pulse with the group velocity of the laser, there will be considerable slippage of the electron bunch with respect to the wakefield phase, the Lorentz factor of which is $\gamma_\mathrm{g} \approx 400$. This has to be included in the calculation of the local wakefield the bunch encounters, for example by step-wise solution for the local field $E_z(z)$, where ξ is updated each step according to the local velocity difference of laser and electrons determined by the energy gain in this accelerating field. A comparison of that method with an ASTRA simulation for the same parameter set is in very good agreement, as can be seen in figure 3.1. The maximum gradient reached for the specific phase settings in the example is about 700 MV/m, and thus close to the maximum possible accelerating field. The peak gradient is determined by $E_z(z = 0, k_\mathrm{p}\xi = -\pi) = 789\,\mathrm{MV/m}$, resulting from the amplitude of equation (2.20) evaluated at the position of the highest laser intensity $a(z) = a(0) = a_0$. (It is identical to equation (3.13) later in this chapter.)

3.2 Matching Strategy

In order to couple the electron beam from REGAE into the plasma target, it is essential to match the beam envelope to the beta function of the accelerating structure. As discussed in section 2.2, apart from the longitudinal field gradient, there are focusing and defocusing forces present in the wakefield dependent on the phase. Since an external electron bunch will have a considerable length, compared to the plasma wavelength, it will cover a certain phase interval of the accelerating wave – acquiring some energy spread. The same is true for the transverse fields: Electrons located at different longitudinal positions inside the bunch will be subject to different transverse fields, resulting in a different focusing strength, $K(\xi)$, given in equation (2.21). Hence, in the phase space picture, the ellipse of a longitudinal slice in the front of the bunch will rotate at a different speed than that of a slice in the back of the bunch: The slice emittance ellipses will fan out, and the overall phase space volume occupied by the bunch will grow, i.e., the emittance will increase.

For a constant focusing channel (achieved by guiding of the laser), this effect has been analyzed [79]: The emittance growth can by avoided if the beta function is matched to the focusing channel. That is, the emittance drives a transverse expansion of the tightly focused beam, which is exactly compensated by the focusing fields of the plasma. The slice emittance ellipses maintain an upright shape in the phase space. The rotation of the ellipses is suppressed by this mechanism and, hence, no emittance growth by the betatron phase mixing described above can occur. The single particles circulate on these phase space ellipses; this motion is characterized by the so-called phase advance [64, 65]. The conditions to achieve this setting are [79]:

$$\beta_{\mathrm{m},0} = \frac{1}{\sqrt{K(\xi)}} \quad \text{and} \quad \alpha_{\mathrm{m},0} = 0, \tag{3.1}$$

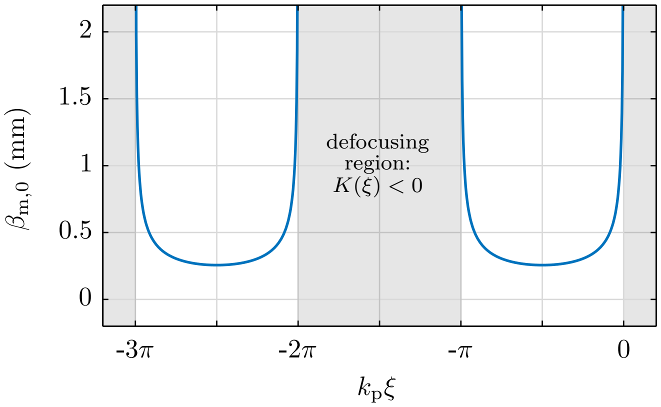

Figure 3.2 – The matched beta function, β_m, depending on the injection phase, $k_\mathrm{p}\xi$, according to equation (3.1) for a plasma density of $n_\mathrm{e} = 10^{16}\,\mathrm{cm}^{-3}$. In the gray shaded regions the wakefield becomes defocusing, and consequently there is no real solution. Please note, K scales with $K \propto 1/\gamma$ according to equation (2.21).

i.e., the electron beam must be focused to a certain spot size, given by $x_\mathrm{RMS} = \sqrt{\hat{\varepsilon}\beta_0}$ [equation (2.11)].

As can be seen in figure 3.2, the matched beta function in focus for a plasma with a density of $n_\mathrm{e} = 10^{16}\,\mathrm{cm}^{-3}$ is $\beta_{\mathrm{m},0} < 0.5\,\mathrm{mm}$ for almost the entire focusing phase intervals. Assuming an energy of 5.6 MeV and a normalized transverse emittance of $\varepsilon = 100\,\mathrm{nm\,rad}$, this translates to a spot size of $r_\mathrm{RMS} < 2\,\mu\mathrm{m}$ – which is very challenging, if not impossible, to achieve.

However, there is no constant focusing channel in the case treated here. Instead, the transverse fields increase when approaching the laser focus, and decrease behind that spot. The matching conditions [equations (3.1)] have been complemented by an analysis of the transition zones into and out of the plasma [31]: It can be shown that for an adiabatically changing focusing strength the beta function evolves according to

$$\beta_\mathrm{m}(z) \approx \beta_{\mathrm{m},0}\sqrt{\frac{K_0}{K(z;\xi)}}. \tag{3.2}$$

Adiabatic in that context means that the Courant-Snyder parameters evolve slowly compared to the phase advance, so that α and β are quasi constant per revolution of a particle on its phase space ellipse. In this case, it is sufficient if the beta function is matched at an arbitrary point along the plasma: the evolution of this matched beta function will be guided by the focusing fields, while being automatically matched at the same time [31, 57].

These two results can be combined to solve the issue for the case treated here. Instead of a focusing channel, conditions (3.1) are only fulfilled in the laser focus, i.e., at the point of maximal fields. Due to the laser evolution with a long Rayleigh length, the adiabatic change of K is ensured, so that a matching should be possible according to equation (3.2). Using the generally valid relation $\alpha = -\beta'/2$ yields the Courant-Snyder parameters at the plasma entrance.

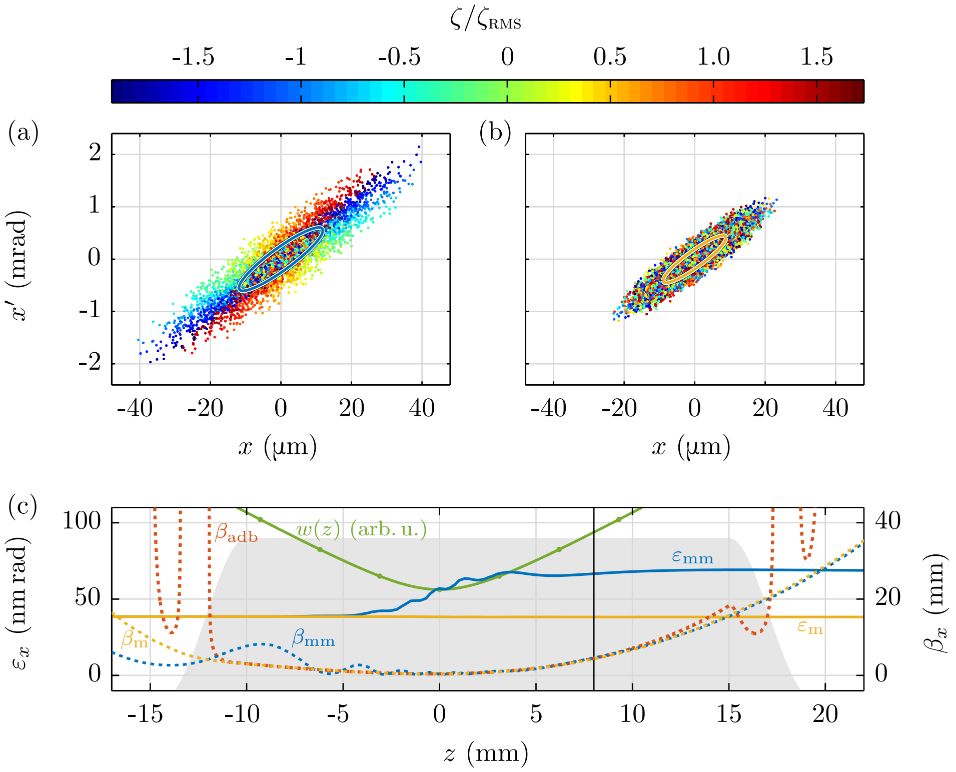

Figure 3.3 – Emittance growth for a mismatched beam compared to a matched bunch. The beam in (a) enters the plasma, and the phase space ellipses of different longitudinal positions start to rotate at different speeds. This is due to the varying focus strength $K(\xi)$ depending on the position behind the laser. Consequently, K also varies with longitudinal particle positions along the bunch, characterized by ζ. In contrast, figure (b) shows a matched case for the identical plasma parameters and a bunch with the same initial emittance, but with parameters that were adjusted to the matching conditions. As can be seen, the area of the ellipse in (b) is smaller, and, in contrast to (a), a distinction of the slices is not possible. The beam is already in the expanding section behind the focus; the black line at about $z = 8\,\mathrm{mm}$ in (c) marks the position of the phase spaces depicted in (a) and (b). Figure (c) shows the development of the emittance growth along the propagation z inside the plasma. The dashed lines mark the evolution of the respective beta functions. As can be seen, there are large betatron oscillations for the mismatched case β_{mm}, resulting from the rotating ellipses; the frequency of these oscillations increases with the rising focusing strength K. In contrast, the matched envelope β_{m} does not show that effect. Instead, the beta function evolves smoothly and does not vary significantly. The unmatched case converges to the matched curve due to the betatron phase mixing, albeit at the cost of an increased emittance: The smear out effect seen in figure (a) eventually yields an ellipse with the same shape, but of larger extent. The emittance growth saturates. The red dashed curve marks the beta function β_{adb} calculated according to the adiabatic assumption, equation (3.2). β_{adb} agrees very well with the matched beta function in the plateau region, i.e., the adiabatic matching condition is fulfilled. In the up- and downramp the electrons slip through a defocusing section. The beam is not considerably influenced by this, however, $\beta_{\mathrm{adb}} \propto 1/\sqrt{K}$ diverges at the zero crossing of the focusing strength K, and is not defined for $K < 0$.

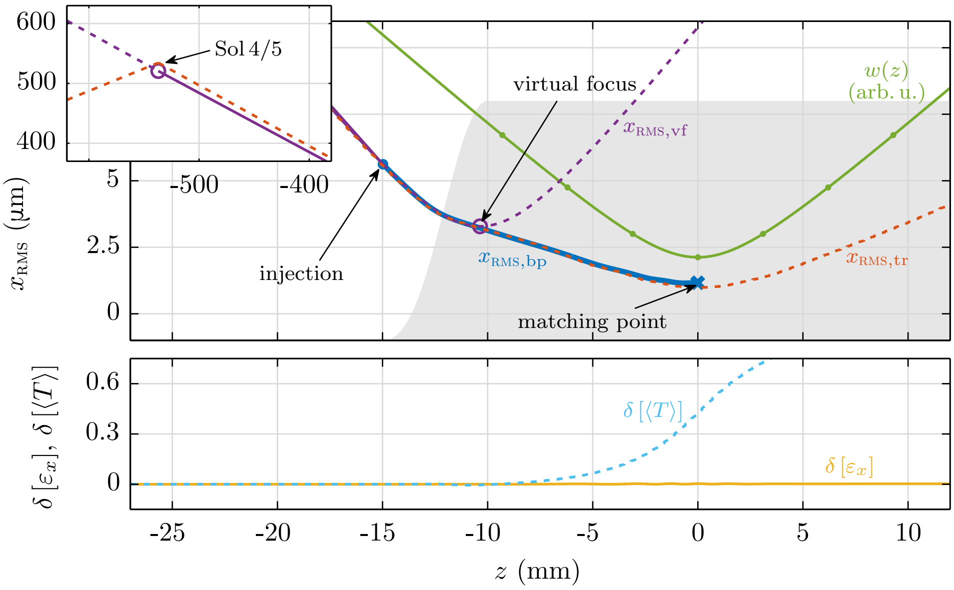

Figure 3.4 – Matching procedure for the injection process (top). First, the reversed beam path from the matching point is calculated ($x_{\mathrm{RMS,bp}}$), which yields the required Courant-Snyder parameters at the entrance of the plasma. A forward propagation ($x_{\mathrm{RMS,vf}}$) with these values yields the position of a virtual focus, while the result of a backward propagation is the required beta function (and thus the beam size) at the location of the focusing element creating this focus; at REGAE this will be Sol 4/5 (see chapters 1.1 and 4). $x_{\mathrm{RMS,tr}}$ is the beam size evolution of a tracked bunch using ASTRA. It is injected with the calculated parameters and almost exactly follows the calculated route. The figure at the bottom depicts the energy gain and emittance change. The symbol $\delta[\,\cdot\,]$ marks the relative difference to the reference value, in this case the initial parameters for kinetic energy $\langle T\rangle$ and transverse emittance ε_x.

Figure 3.3 shows the phase space for a mismatched case, compared to an accordingly matched coupling into the plasma. As can be seen, the emittance of the mismatched case increases, in contrast to the matched beta. Also, the mismatched beta function performs so-called betatron oscillations, that is, the beam size increases and decreases upon the rotation of the phase space ellipse. In the matched case this effect is not present.

It can be concluded then that in accordance with equations (3.1) and (3.2), a matched transport of the beam through the plasma is possible. Moreover, the adiabatically increasing focusing strength will guide the beam into the focus. That is, the constraints for the required focusing optics are relaxed. The local focusing strength along the plasma target, $K(z,\xi)$, can be evaluated by the same approach used to calculate the accelerating field in figure 3.1. Instead of the adiabatic approximation (3.2), the beta function at the plasma entrance is determined differently in the following, though. Using the matrix formalism with piecewise constant K and the initial parameters given by equations (3.1), the Courant-Snyder parameters at the plasma entrance are obtained. Importantly, K also depends on the energy described by the Lorentz factor γ; see equation (2.21). Alternatively, one could also solve the beam envelope equation [32, 65],

$$x''_{\mathrm{RMS}} + K(z)x_{\mathrm{RMS}} - \hat{\varepsilon}^2/x^3_{\mathrm{RMS}} = 0, \tag{3.3}$$

using numerical methods.

The matrix approach, which is chosen here, directly yields the Courant-Snyder parameters α, β, γ at the entrance of the plasma. Since an arbitrary set of Courant-Snyder parameters is rather complicated to adjust and determine, the following strategy is used: The knowledge of α, β, and γ at the plasma entrance allows for a forward calculation – without plasma. By this approach, suggested in [32], a virtual focus is found. This focus is a much more accessible machine setting. Using the matrix formalism once more – again for a simple free drift but backwards from the plasma entrance – the beta function in the last solenoid before the plasma can be determined. These two parameters – position of the virtual transverse focus and beta function (i.e., beam size) in the last focusing element – suffice to adjust the beam for a matched coupling into the plasma: Using the second last focusing element, the beam size in the last solenoid before the plasma is set. Then, this last element is adjusted for the position of the focus, while the plasma target is not in the beam path. The combination yields the correct setting of α, β, γ at the entrance of the plasma. An illustration of this matching strategy is depicted in figure 3.4.

Another source for beam quality degradation can be found at the plasma exit. However, in this case it is not a mismatched beam which drives the emittance growth. The source is rather the inevitable energy spread accumulated by the plasma passage, due to the finite (and comparatively large) phase interval covered by the bunch. This, in combination with a typically large divergence at this point, increases the emittance in the subsequent drift [30]. As a consequence, it is either important to refocus the beam as soon as possible, or to use the plasma once more to expand the beam in a controlled way – for example by slowly adjusting the plasma profile in order to adiabatically reduce the focusing strength. Since the emittance is conserved during the expansion in this approach, the divergence must consequently shrink, so that the beam can be safely transported [31, 32].

As a side note, it should be mentioned that the same effect of emittance growth can occur if the focusing required to achieve the virtual focus is too steep, since the REGAE bunch prior to the injection already has a considerable energy spread, due to the ballistic bunching mechanism. Thus, the plasma matching is highly beneficial as it relaxes the constraints for the focus size.

3.3 The Overtaking Problem

The external injection experiment is a pump-probe type scanning of the injection phase of the REGAE electron bunch with respect to the distance of the pump pulse delivered by ANGUS. In order to achieve this configuration, electrons and laser have to travel collinearly – at least close to the plasma target – with the photons being located ahead of the bunch. (For technical reasons, this co-propagation region already starts about 3 m in front of the target in the experiment.) However, there is a velocity difference between electrons and photons: While the laser pulse is traveling with the speed of light, c, the electrons, though relativistic, move slightly slower at $\beta = v/c = 0.9965$ and can never catch up with the photons.

As a consequence, it is inevitable that the electron bunch enters the co-propagation section with a head start to the laser. During the co-propagation the bunch is overtaken by the laser pulse, in order to realize the desired phase offset on the order of the plasma wavelength, i.e., $|\xi| \sim 100\,\mu\mathrm{m}$ at the target. The distance to the plasma target at which this overtaking takes place can be calculated by the velocity difference (see also [80, 81]),

$$\Delta z_{\mathrm{ot}} = \frac{\beta\xi}{1-\beta} \approx 2\gamma^2\xi. \tag{3.4}$$

Hence, for typical REGAE parameters with $\gamma \approx 12$, it is obvious, that the described process happens at a distance of a few centimeters in front of the target. Since this is very close to the laser focus, it is questionable whether the electron beam withstands the interaction with a laser pulse of such intensity. Also, this proximity of the overtaking point to the plasma target explains why an injection scheme based on a chicane (or similar magnetic arrangement) is hard, if not impossible, to realize. In addition, such a concept would increase the beam emittance. A mirror or foil close to the target would not survive the laser intensity, as well, and also spoil the emittance of the REGAE beam. An analysis of this *overtaking problem* was also subject of a bachelor's thesis [80], which covered the collinear case as well as offset scans summarized below.

The length of the interaction is given by the sum of the duration of the electric field of the laser ($\tau_{\mathrm{EM}} = \sqrt{2}\,100\,\mathrm{fs} \approxeq 50\,\mu\mathrm{m}$ FWHM) and the electron bunch length ($\zeta_{\mathrm{RMS}} = 3\,\mu\mathrm{m}$). Both quantities are likewise scaled with $2\gamma^2$, since the same mathematics applies. Assuming six standard deviations as a measure to cover the whole interaction range from the tail of the bunch experiencing the first photons to the complete pulse having passed the electrons, the overtaking takes place within a length $\delta z \approx 4\,\mathrm{cm} \approxeq 140\,\mathrm{ps}$; $z = z_{\mathrm{ot}}$ lies in the center of this interval.

The effect of the laser pulse on the electrons is described by the ponderomotive force. It is dependent on the magnitude and shape of the laser profile. Since the following analysis is done on the assumption of a Gaussian transverse laser profile, it is important to bear in mind that the results are not necessarily valid for the ANGUS beam. The radial intensity profile of ANGUS is close to a so-called super-Gaussian distribution of eighth order with a $1/e^2$ beam diameter of $W = 76\,\mathrm{mm}$, i.e.,

$$I(r) \propto \exp\left[-\left(\frac{r^2}{2\sigma_r^2}\right)^8\right] = \exp\left[-2\left(\frac{2r}{W}\right)^{16}\right], \tag{3.5}$$

where r is the radial coordinate and σ_r is the RMS value of the underlying Gaussian distribution[1].

However, for the description of an evolving pulse of initially super-Gaussian profile on its way to the focus[2], a (Maxwell-conform) analytic treatment is impossible and an implementation of such

---

[1] Please note that there is also another definition of the super-Gaussian order which absorbs the square of the Gaussian curve.

[2] A sinc^2-like profile is to be expected in the focus, given by the Fourier transform of the almost top-hat shaped super-Gaussian profile.

a scenario into ASTRA has not been completed up to now [57]; it will be part of another Ph.D. thesis [61]. The Gaussian case, in contrast, is implemented in the particle tracking tool (see chapter 1), and the results were verified by analytic calculations using the (Lorentz transformed) ponderomotive force [81]. The idea behind this that the ponderomotive force given in chapter 2.2 does not contain relativistic effects, so that a description of the overtaking in the rest frame of the electrons with a subsequent Lorentz transformation of the resulting momenta was used to account for that.

To analyze the overtaking process, extensive ASTRA delay scans have been performed. Since the interaction point lies within the caustic of the laser beam, the Rayleigh length z_R needs to be adapted to optimally mimic the super-Gaussian intensity increase towards the focus: As stated above, a (diffraction limited) Gaussian beam is used in this model, which has a different transverse beam evolution for the same focal length, or – stated more formal – another beam parameter product [82].

The $1/e^2$-radius of the unfocused ANGUS beam is $w_\mathrm{sg8} = W/2 = 38.0\,\mathrm{mm}$, which can be converted to RMS for a super-Gauss function of eighth order by

$$\sigma_{r,\mathrm{sg8}} = \frac{1}{2^{\frac{1}{16}}}\sqrt{\frac{\Gamma\left(\frac{3}{16}\right)}{\Gamma\left(\frac{1}{16}\right)}}\, w_\mathrm{sg8} \approx 0.54\, w_\mathrm{sg8}, \tag{3.6}$$

employing the gamma function, $\Gamma(t) = \int_0^\infty x^{t-1}e^{-x}\,\mathrm{d}x$, as extension of the factorial [83]. The result is obtained by a straightforward calculation of the RMS value according to the definition, equation (2.9). Hence, $\sigma_{r,\mathrm{sg8}} = 21.5\,\mathrm{mm}$. The substituting Gaussian beam profile should consequently start with that RMS value, $\sigma_r = \sigma_{r,\mathrm{sg8}}$, and be focused with the same focal length in order to ensure a comparable slope of the caustic evolution during the overtaking process. This, of course, results in a wrong focus spot size (and thus a wrong intensity *in* the focus), but the focus is irrelevant for the laser-electron interaction.

The resulting Gaussian beam has an $1/e^2$-radius of $w = 2\sigma_r = 41.0\,\mathrm{mm}$. Solving the beam envelope equation,

$$w(z) = w_0\sqrt{1+\frac{z^2}{z_\mathrm{R}^2}}\,, \tag{3.7}$$

in combination with the Gaussian focus spot size, $w_0 = \sqrt{\lambda z_\mathrm{R}/\pi}$, yields a Rayleigh length of $z_\mathrm{R} = 2.72\,\mathrm{mm}$ for the ANGUS wavelength of $\lambda = 815\,\mathrm{nm}$ and focal length, $z_\mathrm{f} = 4.2\,\mathrm{m}$. Figure 3.5 shows a comparison of the transverse beam profiles and beam sizes along the propagation towards the focus. The RMS beam sizes of both profiles agree very well at all positions.

The other laser pulse parameters in the ASTRA simulations are a FWHM length $\tau = 100\,\mathrm{fs}$, an energy of $E = 5\,\mathrm{J}$ and a focal spot size $w_0 = 26.6\,\mu\mathrm{m}$, which reflects the focal length of $z_\mathrm{f} = 4.2\,\mathrm{m}$, and is – as mentioned above – smaller than the real ANGUS focus. The laser is polarized in the x-direction. The parameters are summarized in table 3.2.

Having found a way to deal with the laser evolution, the next step is the determination of a criterion for the electron beam quality. Since the goal of the experiment is the injection of a

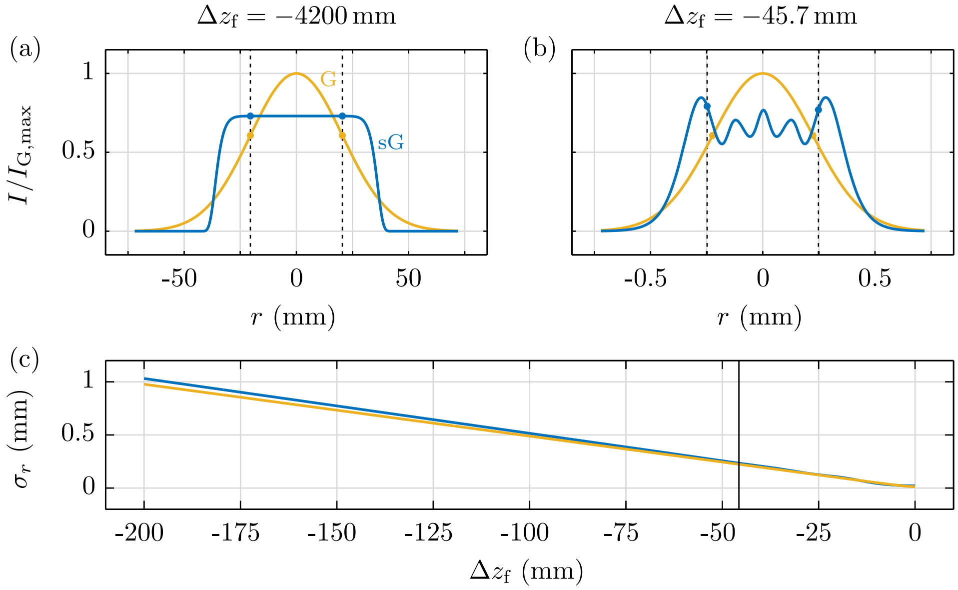

Figure 3.5 – Comparison of the super-Gaussian profile and the mimicking Gaussian beam at the final focusing parabola, (a), and in the region of the overtaking process, (b), that is at a distance $\Delta z_\mathrm{f} = 45.7\,\mathrm{mm}$ in front of the focus. The RMS beam envelopes, (c), agree very well. The position marked by the black line corresponds to the one in figure (b). Data for the propagated super-Gaussian beam simulated with ZEMAX by [61] and [84].

Laser Parameters	
wavelength	$\lambda = 815\,\mathrm{nm}$
Rayleigh length	$z_\mathrm{R} = 2.72\,\mathrm{mm}$
pulse energy	$E = 5\,\mathrm{J}$
pulse length	$\tau_{\mathrm{FWHM}} = 100\,\mathrm{fs}$
(spot size)	$w_0 = 26.6\,\mu\mathrm{m}$
polarization	x-direction
Electron Parameters	
kinetic energy	$\langle T \rangle = 5.6\,\mathrm{MeV}$
emittance	$\varepsilon_{xy} = 40\,\mathrm{nm\,rad}$
spot size	$r_{\mathrm{RMS}} = 3.5\,\mu\mathrm{m}$
bunch length	$\zeta_{\mathrm{RMS}} = 2.1\,\mu\mathrm{m}$

Table 3.2 – Overview of the simulation parameters used to analyze the effect of the overtaking process with ASTRA. The electron parameters are similar to those achieved in the start-to-end simulation presented in section 3.4.

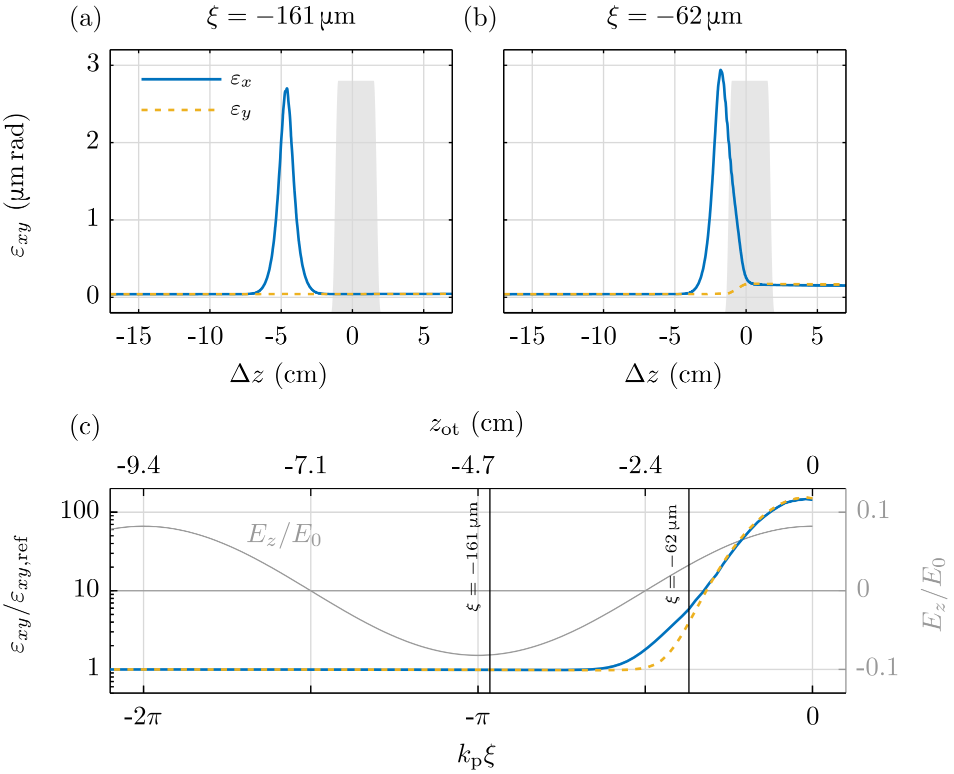

Figure 3.6 – Emittance change due to the ponderomotive force during the overtaking process. If the laser hits the electrons too close to the focus, (b), the emittance is not conserved, while the reduced laser intensity due to an overtaking further away, (a), does not influence the emittance after the laser passage; the large amplitudes are originating from the transverse momenta during the overtaking process. The gray areas mark the position of the gas target. Figure (c) shows the emittance increase compared to a reference case without laser. A significant deviation only occurs up to the start of the accelerating section of the first bucket. Hence, an injection should be possible behind this point. (Please note the logarithmic scale for $\varepsilon/\varepsilon_{\mathrm{ref}}$.)

well-known bunch into the plasma wakefield, there are several important quantities to be looked at. The most important parameter of the electron beam is the (transverse) beam emittance, ε_{xy}, which should be conserved as well as possible. The effect of the laser pulse on this beam quality criterion can be seen in figure 3.6, where the emittance behavior after the overtaking is compared to a reference case without laser. The respective normalized emittance values, ε and ε_{ref}, are evaluated at the injection point, i.e., after the passage of the laser. If the overtaking point, z_{ot}, is too close to the focus, the laser increases the emittance by a factor of more than 100. However, this unsatisfactory zone extends only slightly into the accelerating part of the first bucket, so that almost the entire wakefield should be accessible in the pump-probe experiment for a density of $n_e = 10^{16}\,\text{cm}^{-3}$. The emittance increase during the overtaking originates from the rapid transverse oscillations of the particles within the laser pulse and the accordingly large transverse momenta, which enter the calculation of the emittance – but have no net effect to first order, as discussed in section 2.2.

Results obtained previously with another particle tracking tool [85], utilizing a similar laser pulse with $\tau = 25\,\text{fs}$, are discussed in [28]. The results are comparable, indicating that for a distance of $|\zeta| \gtrsim 100\,\mu\text{m}$ the transverse emittance is not influenced by the laser, and the first bucket should hence be accessible. The same holds true for the results obtained in [80], where ASTRA was used. The collinear overtaking scenario shown here and the analysis have been redone in the context of the start-to-end simulation presented in the next section of this chapter, so that this data, shown in figures 3.6 and 3.7, is used in the following.

The beam size at the injection point is the second parameter which should be looked at, i.e., x_{RMS} and y_{RMS}. If the laser has too strong a defocusing effect, the bunch will no longer be matched to the plasma, leading to an emittance growth inside the plasma. The same holds true for the divergence of the beam (x'_{RMS}, y'_{RMS}) – which is, of course, coupled with the beam size. Figure 3.7 shows the results of this analysis, depicting the deviations from a reference case without laser – normalized to that reference case. The symbol $\delta\left[\,\cdot\,\right]$, which is used frequently throughout this chapter is defined as

$$\delta\left[X\right] := \frac{X - X_{\text{ref}}}{X_{\text{ref}}}. \tag{3.8}$$

Similar to the transverse emittance, the influence of the laser vanishes close to the accelerating section of the first bucket (and greater delays). Close to the laser focus, however, the beam size rapidly increases sixfold, and the divergence is increased by a factor of about 25. These result are, of course, not entirely astonishing. The ponderomotive force of the laser deflects the particles, leading to an increased divergence, which consequently translates into an increased spot size in a drift. Since the emittance is calculated from the product of these two parameters, they are also the origin for the increase in ε. In this context, it is also interesting to look at the position of the transverse focus, z_{f}. The closer the overtaking comes to the laser focus, the further downstream the transverse minimum of the electron beam envelope is displaced – until a sudden change in the position occurs, with the electron focus shifted upstream of the original position. This behavior is explained as follows: At the changing point the defocusing of the laser is so strong that the bunch is directly expanding after the laser interaction, i.e., the focus now lies around the overtaking

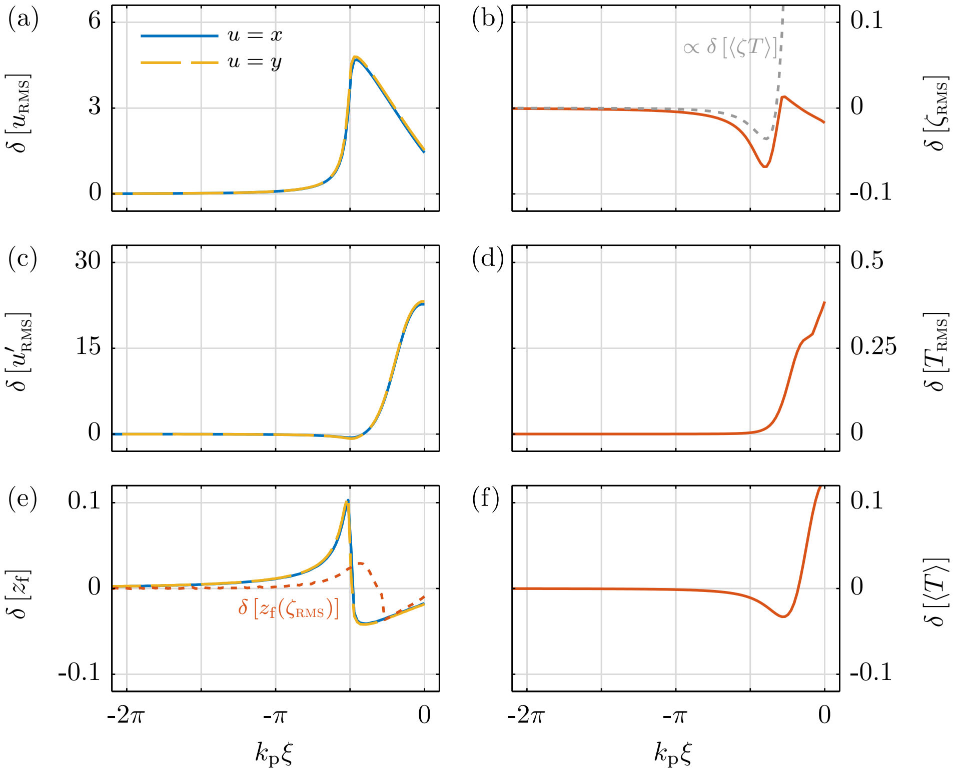

Figure 3.7 – Analysis of variations of important beam parameters due to the overtaking process. The size (a) and divergence (c) of the beam are almost unaltered beyond a phase offset $k_{\mathrm{p}}\xi \gtrsim \pi$. However, the focus position (e) is slightly shifted downstream, except for an overtaking close to the focus; the red line marks the longitudinal focus position in figure (e). In the region of milder laser intensity, the laser has also very little influence on the energy as depicted in figure (f) and the energy spread (d). The laser reduces the bunch length (b), which can be explained by the change in the correlated energy spread, $\langle\zeta T\rangle$.

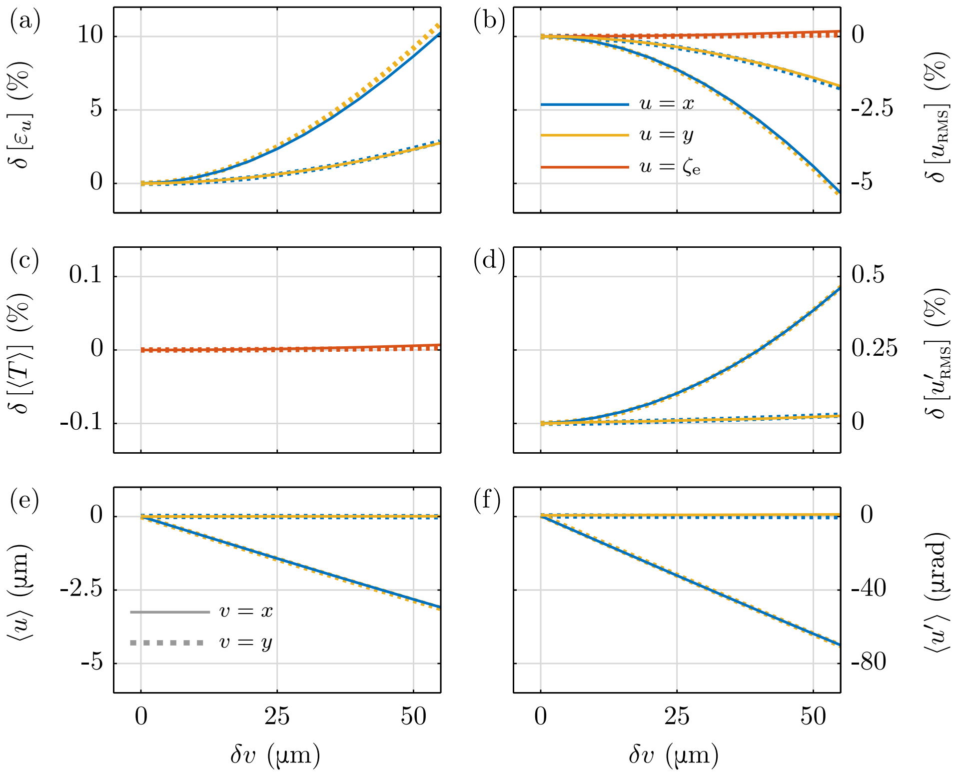

Figure 3.8 – Parameter variations of the electron beam for the overtaking process with a transverse offset of the laser denoted by δv (with $v \in \{x, y\}$). Changes to the emittance (a), beam size (b) and divergence (d) are small. Longitudinal parameters, energy (c) and bunch length (b, red line) are almost unaffected. There is a net angle (f) and an additional offset (e) resulting from this angle. Dashed lines mark the offset in y. The plots also demonstrate the symmetry of the ponderomotive force, despite the polarized laser. Data from [80].

point. For a weaker laser intensity, on the other hand, the beam is only less convergent, shifting the minimum further downstream.

To further investigate the beam quality, it is also important to look at longitudinal parameters. Interestingly, the laser has a positive effect on the bunch compression: Since the overtaking is happening in the focusing region of the laser, the intensity increases while a particle slips through the laser, so that a net deceleration of the particle occurs. In other words, the descending shoulder of the pulse profile is effectively steeper, leading to a net deceleration by the ponderomotive force. Particles in the front of the beam are surpassed later, that is, closer to the focus and, thus, experience a greater deceleration. The bunching energy correlation, $\langle\zeta T\rangle$, of the beam is enhanced, leading to a shorter bunch length, ζ_{RMS}. However, the influence on the overall bunch energy, $\langle T\rangle$, is negligible in the region beyond a phase offset of π – which is of uttermost importance, since the energy change of the plasma is the main quantity analyzed in the context of the external injection experiment. The bunch energy should, therefore, not be altered by non-plasma effects.

To map the experimental situation as best as possible and to include various eventualities, additional analyses of two scenarios have been performed: Firstly, the effect of a laser offset with respect to the electron axis has been looked at [80]. Secondly, possible angular deviations of laser propagation and bunch trajectory have been simulated [86]. In the following, a brief summary of the results of these two scenarios will be given.

Figure 3.8 shows the changes to the electron bunch caused by the overtaking process, if the laser has a transverse offset with respect to the electron propagation axes. The offset was scanned in x- and y-direction, up to $100\,\mu\mathrm{m}$ at an overtaking position of $\Delta z_{\mathrm{ot}} \approx 5\,\mathrm{cm}$, which coincides again with the accelerating and focusing region of the first bucket of the plasma wake. The reference case in this analysis is the respective beam parameter determined for the same distance Δz_{ot}, but without offset. From the figure it can be seen, that there is a mild effect on the emittance, ε, exceeding a $5\,\%$ growth at about $\delta x = 30\,\mu\mathrm{m}$. The influence on the beam spot size, r_{RMS}, is likewise negligible. The same is true for the beam divergence, u'_{RMS} with $u \in x, y$. There is a slight asymmetry of the effects for these three quantities, explicable by the divergence behavior: As can be seen, u'_{RMS} is only affected in the offset plane – which is completely compatible with the ponderomotive force: All particles on the respective side of the laser are deflected further away, spreading the beam. Hence, the beam size grows in that dimension, and so, consequently does the transverse emittance. However, as already mentioned, the effect is very weak.

There is also a net deflection of the whole beam, characterized by $\langle u' \rangle$, because all particles sit on one side of the laser pulse in the offset plane and, thus, experience a ponderomotive force in the same direction. Furthermore, the beam gains an additional offset $\langle u \rangle$ resulting from this. This deviation, however, is much smaller than the initial offset. Longitudinal effects can hardly be detected, even for large offsets. As a side note, it is worth mentioning the plots again demonstrate the symmetry of the ponderomotive force, despite the x-polarization of the laser.

The results for a scan with a crossing angle $\psi_{x,y}$ between laser and electron trajectories are shown in figure 3.9. ψ_x is defined as the angle between the trajectories in the x-z-plane, and ψ_y is defined analogously. For both cases, ψ has been varied within $\psi = \pm 1\,\mathrm{mrad}$. The type and magnitude of the effect on the bunch is almost identical to the offset analysis. There are also no changes on the longitudinal parameters. The transverse parameters are influenced more in the plane of rotation. This similarity can be explained by the crossing angle resulting in an offset of the beam to first order.

As a conclusion, it can be stated that an injection into the first bucket of a plasma wakefield with $n_{\mathrm{e}} = 10^{16}\,\mathrm{cm}^{-3}$ ($\lambda_{\mathrm{p}} = 334\,\mu\mathrm{m}$) should be possible, despite the fact that the bunch has to be overtaken by the intense laser pulse. Only the decelerating region directly behind the laser ($|\xi| < 100\,\mu\mathrm{m}$) is inaccessible according to the simulations. For higher plasma densities only an injection into later buckets will be feasible as long as the electron energy is not considerably increased. The overtaking is relatively insensitive to transverse deviations of the propagation paths: Offset and angular deviations only have small additional effects compared to the initial deviations, i.e., a transverse offset during the overtaking will in any case lead to an off-axis injection into the plasma wakefield, since the wakefield is defined by the laser axis. A slight

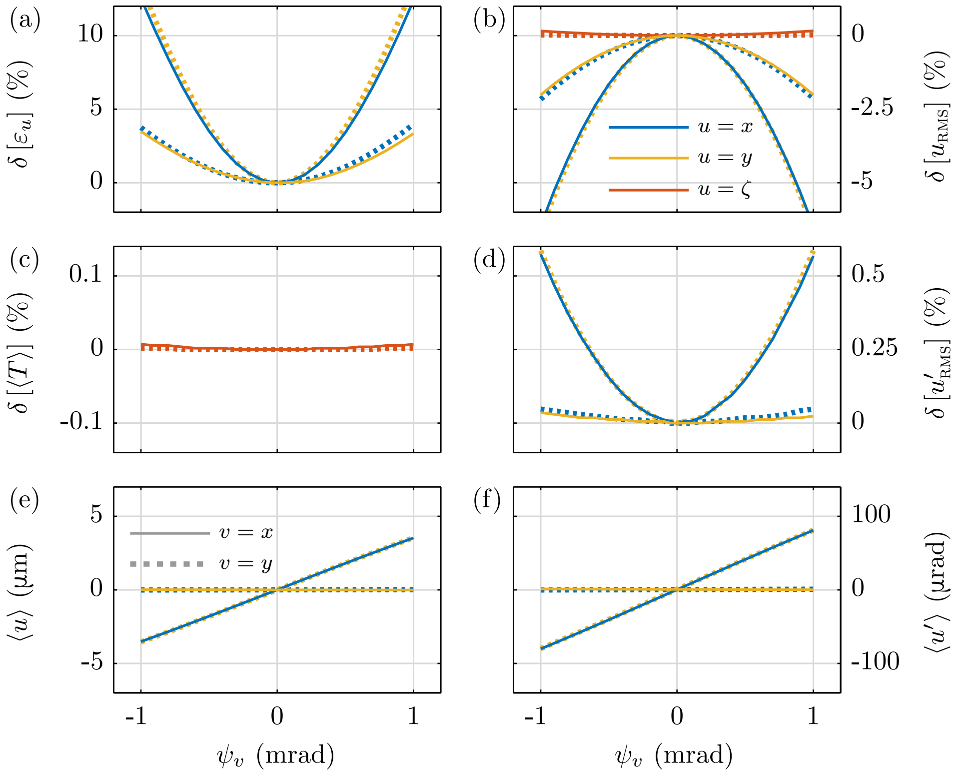

Figure 3.9 – Change of electron beam parameters due to overtaking by laser and electrons propagating with an angular deviation in the range of $\delta\psi = \pm 1\,\mathrm{mrad}$. The effect is similar to an off-axis overtaking. Longitudinal effects like the bunch length (b, red line) and energy (c) are very weak. Changes to the transverse emittance (a) are within few percent. The transverse momenta (d) change by less than 1 %. In this case, a transverse offset (e) of a few microns and an additional angle between the propagation directions (f) are introduced as well. Data from [86].

additional shift due to the laser overtaking will only have a minor impact compared to the already mismatched beam.

Due to the different laser profile in the experiment, additional investigations are required. Although the mean intensity during the overtaking should be comparable for both cases, the profile is not. And since the ponderomotive force is given by the gradient of the laser profile, there will be deviations. A model to propagate such a more realistic beam is already implemented into ASTRA, employing field maps generated with ZEMAX. However, it is still being worked on [57, 61]; it is planned to be presented in [62].

Finally, it should be stressed that such a model is just this: a model. Hence, it is of utmost importance to measure the effects of the overtaking as best as possible, as soon as the ANGUS laser system is connected to the accelerator. Lastly, resulting influences on the REGAE bunches by the overtaking process must be quantified in order to ensure a well-characterized electron bunch.

3.3.1 Bunch Length Diagnostic: Collinear Ponderomotive Scattering

The deviations from the beam path caused by an off-axis overtaking can also be used to perform an electron bunch length diagnostics. Since the bunch is co-propagating with the laser pulse, different sections of the bunch are surpassed with different laser intensities. Thus, a particle in the front will gain a larger transverse momentum than one in the back of the bunch. Hence, measuring the width of the distribution on a screen after the overtaking should in principle be correlated to the duration of the overtaking process. And since the laser pulse length is known – and constant – this duration depends only on the longitudinal bunch extent. The concept is depicted in figure 3.10.

It is vital to know at which z-position the electron bunch has been hit by the laser. However, this is also encoded into the image if the transverse offset is known – which can be measured directly using simple screens: The mean deviation of the distribution on the screen behind the overtaking depends on the mean ponderomotive force acting, that is, on the longitudinal position of the electron bunch within the laser's caustic.

Hence, this collinear ponderomotive scattering in principle provides a timing and bunch length diagnostics, where the timing (i.e., the longitudinal offset) is determined by the mean (or first moment) of the deflected beam, while the bunch length is encoded into the width of the distribution – that is, the second moment. The determination of timing and bunch length, which is very delicate at such a low charge as it is used at REGAE, is transferred to a geometrical problem (in combination with very precise knowledge of the laser envelope and beam profile). Figure 3.11 shows exemplary screens for the distributions of bunches with different lengths. In a separate master's thesis, the potential resolution was determined to be in the region of a few femtoseconds [81].

The feasibility strongly depends on stable experiment conditions, though. The electrons must have a constant mean energy, and the transverse position of electrons with respect to the laser

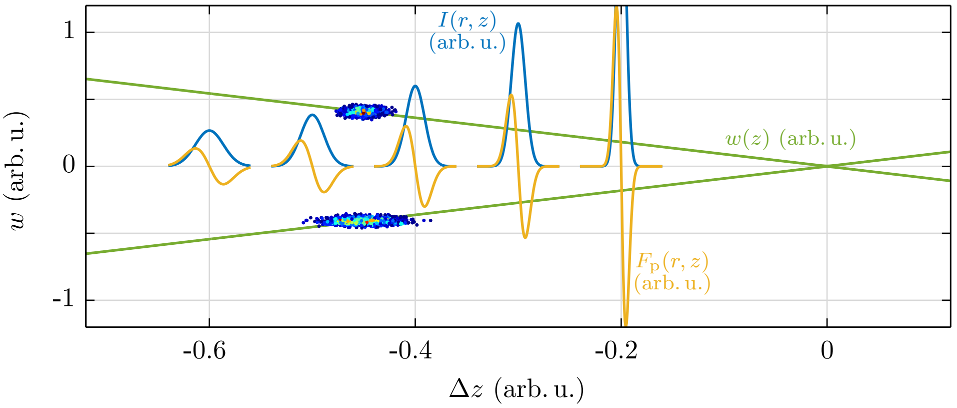

Figure 3.10 – Concept of the *collinear ponderomotive scattering* diagnostic. If an electron bunch is overtaken off-axis, it gains a net deflection due to the ponderomotive force $F(r,z)$. Since the laser intensity, $I(r,z)$, is increasing during the overtaking process, an electron in the front of the bunch gains a higher transverse momentum than a trailing particle. Consequently, for a longer bunch (drawn schematically below zero), which is overtaken at the same mean position, the transverse momentum spread must be larger.

beam caustic must be known and fixed as well. Thus, the pointing jitter of the laser should be minimized. Moreover, a characterization of the laser profile evolution over the whole distance of the overtaking is important – which, in addition, should not fluctuate from shot to shot.

Lastly, the technique is a translation of the temporal properties to spatial parameters, requiring very precise settings. However, some of these requirements can be measured independently after the interaction. Especially, the laser's pointing and longitudinal profile will be constantly monitored. This possibly yields a correction for that deviations, so that the constraints are reduced. If experimentally viable, the method provides a single shot arrival time and bunch length diagnostics. Moreover, all required instrumentation will be available at beam line, anyways, since these components are also needed for the external injection experiment.

3.4 Start-to-End Simulation

Equipped with the various parameters and results from the previous analysis, especially the matching strategy, it is now possible to implement all of this information into a start-to-end simulation using ASTRA. For this, the standard REGAE lattice is used – slightly modified to reflect changes discussed in the next chapter – complemented by a laser model for the overtaking process and a module for plasma acceleration. In the post-plasma region, the new beam transport as well as the shifted (and upgraded) electron spectrometer are added. The simulation itself is divided into several steps, which mimic a possible real scenario. First, the longitudinal focus is adjusted to the position of the plasma target, followed by a characterization of the plasma fields, which enables the calculation of the matched beam size. Applying the matching strategy, the

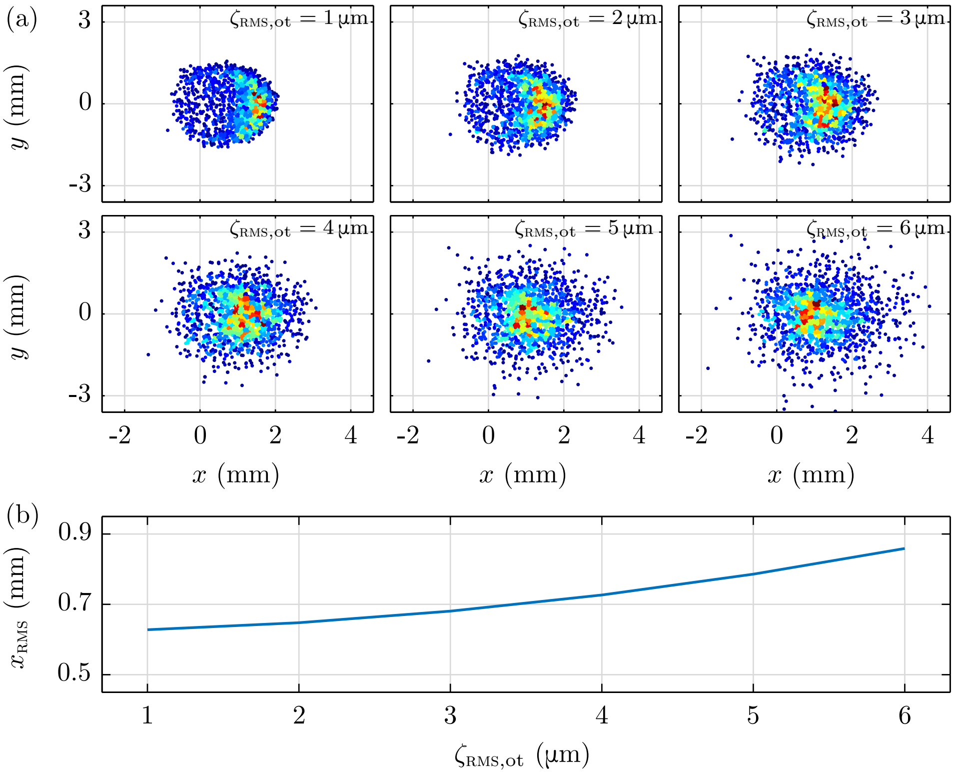

Figure 3.11 – (a) Spatial, transverse distribution of bunches with different lengths $\zeta_{\mathrm{RMS,ot}}$ hit by an identical laser pulse during an off-axis overtaking process. The increasing transverse momentum spread manifests itself in an increasing width x_{RMS} on the beam image and is clearly dependent on the bunch length, as can also be seen in figure (b). For a further analysis please refer to [81].

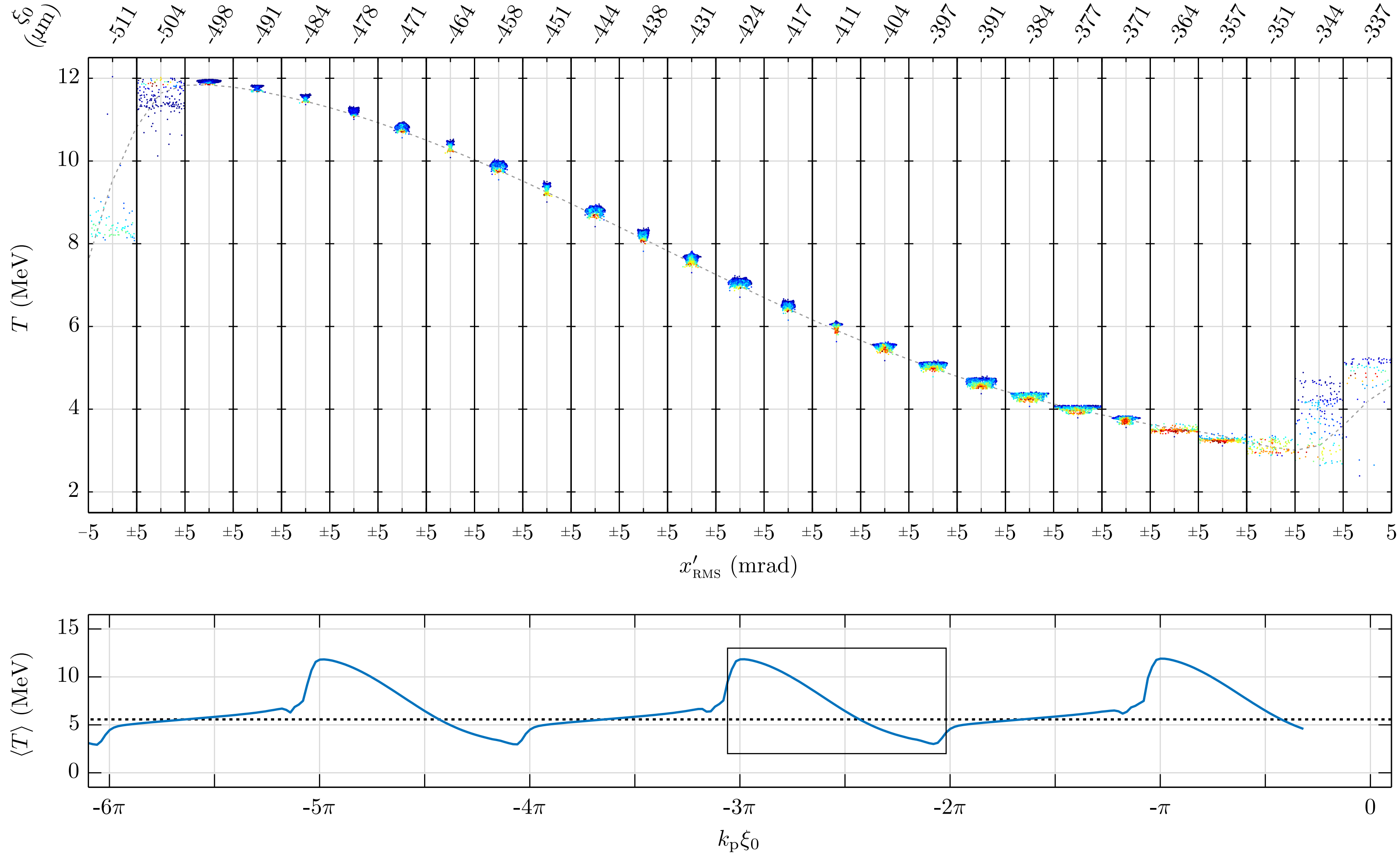

Figure 3.12 – Phase scan of an externally injected electron beam with an initial kinetic energy of $\langle T\rangle = 5.6\,\text{MeV}$. Similar to a spectrometer screen, the plots in the top row show the particles' energy versus the transverse deflection the for several injection phases in the second bucket. Especially the accelerating and focusing region looks very promising, while the beam diverges strongly in the defocusing area.

Cavity	E_z (MV/m)	φ (deg)	z (m)
gun	120.00	0.00	0.000
buncher	31.77	-90.00	1.290

Table 3.3 – Cavity settings used in the start-to-end simulation in order to achieve a bunching configuration. The buncher cavity is operated at the zero crossing of the accelerating field: This does not yield a net energy gain, but applies a negatively correlated energy spread.

bunch charge	$Q = 100\,\text{fC}$
kinetic energy	$\langle T \rangle = 5.570\,\text{MeV}$
energy spread	$T_{\text{RMS}} \approx 25\,\text{keV}$
emittance	$\varepsilon_{xy} \approx 50\,\text{nm rad}$
beam size	$r_{\text{RMS}} \approx 8\,\mu\text{m}$
bunch length	$\zeta_{\text{RMS}} \approx 2.5\,\mu\text{m}$

Table 3.4 – Parameters of the electron bunches at the plasma entrance. The approximate values vary slightly due to the adjustments required by the matching. The kinetic energy is fixed.

beam size in solenoid 4/5 (Sol 4/5) is set via the upstream lens (Sol 2/3) – see figure 1.2 on page 7. Focusing effects from the buncher cavity are also taken into account. In a next step, the focus position is adjusted to the location of the virtual focus. At this point, the plasma is added (based on the linear model described in chapter 2.2) and the laser is switched on – the latter meaning that the overtaking process is explicitly taken into account[3]. The cavity settings resulting from this strategy are given in table 3.3. The parameters of the electron bunch prior to the injection are summarized in table 3.4.

Using this method a phase scan varying the injection phase at the plasma entrance, ξ_0, over about 1.2 mm has been performed for a target with properties as described above: It consists of a 25 mm long plateau of constant density, confined by an additional up- and downramp of 5 mm; the profile in the ramp follows a sinc^2-shoulder, which is an adequate description of this pressure decrease [87]. The density in the plateau range is $n_{\text{e}} = 10^{16}\,\text{cm}^{-3}$; the laser is focused 10 mm behind the start of this constant density region. In the machine coordinate system, this point lies 5.5 m downstream of the origin: the gun cathode. However, for the analysis in the following, the laser focus is used as origin of the coordinate system. The matching point hence lies at $z = z_{\text{m}} = 0\,\text{mm}$ as well.

Figure 3.12 shows the final energy of the bunch after the plasma target, as well as a sequence of spectra for a second bucket injection. There is a clear periodicity visible in the phase scan, but also a large deviation from a mere cosine function. Such a deviation is not surprising, though, since this behavior happens especially in the defocusing region of the plasma. As can be seen

---

[3] Please note that a matching with the laser switched on is experimentally not feasible, since the required screens would be destroyed by the highly intensive pulse. Therefore, a characterization of the laser's influence must be performed prior to the experiments, ideally excluding regions where the bunch is disturbed.

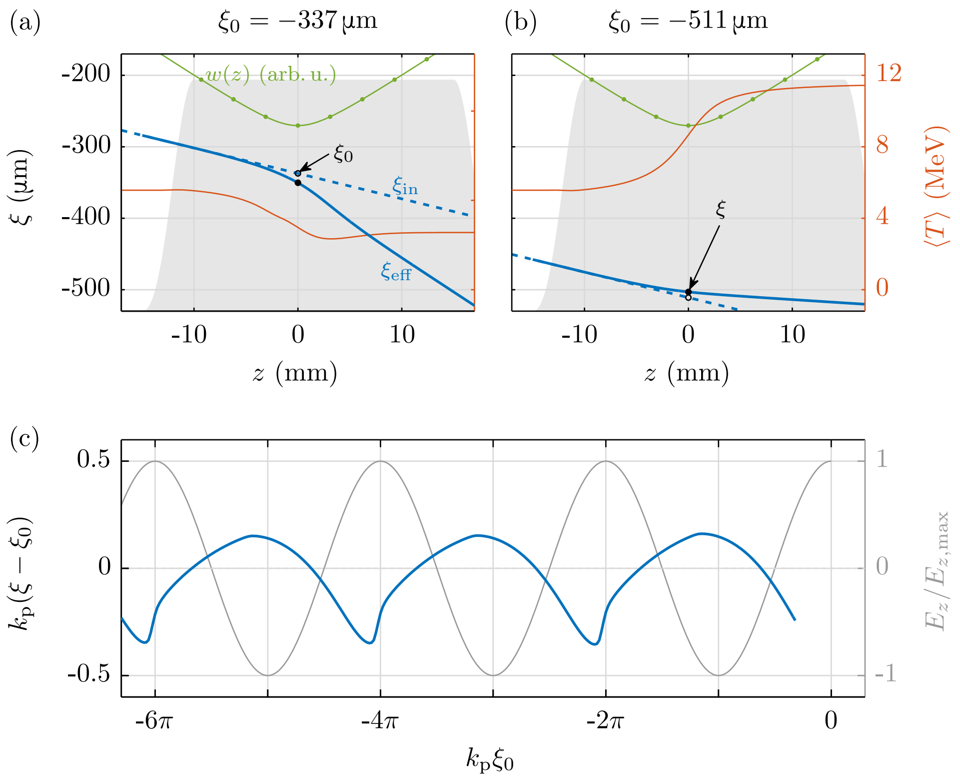

Figure 3.13 – Phase correction taking into account velocity changes within the plasma up to the laser focus position at $z = 0$. Plots (a) and (b) show the deviation of the initial phase offset ξ_{in} with respect to ξ_{eff} due to the velocity change within the plasma for an accelerating (a) as well as a decelerating case (b). The corrected phase at the position of the laser focus is defined as ξ. The deviation of ξ from ξ_0 over about three periods is shown in figure (c).

from the scatter plots in that domain, the bunch is strongly defocused and expelled by the plasma fields, the result being that it hardly gains any energy. (In the real experiment, these electrons would not reach the electron spectrometer.) Also, the magnitude of the divergence shows an oscillating pattern in the focusing and accelerating section, but for all cases of this region, the values are well below 5 mrad. The decelerated, yet focused beams are more spread out – but can still pass the plasma, extending the measurable region to almost the whole focusing range, as mentioned above.

In order to do a more thorough analysis, one has to apply a phase correction: Due to the beam energy changes along the plasma, the phase slippage is not constant. However, the injection phase ξ_0 is calculated from the distance between the pump pulse and an electron beam of the injection energy, where the reference $\xi_0 = 0$ is defined as the overlap of particle bunch and laser at the position of the laser focus, i.e., at $z = z_{\text{f}} = 0$ in the plasma coordinate system. Taking into account the velocity changes during acceleration up to that reference point – by a stepwise integration as in 3.1 – a slightly modified phase occurs, which is defined as ξ in the following. The change is illustrated in figure 3.13. Please note, that the largest deviation happens, of course, in

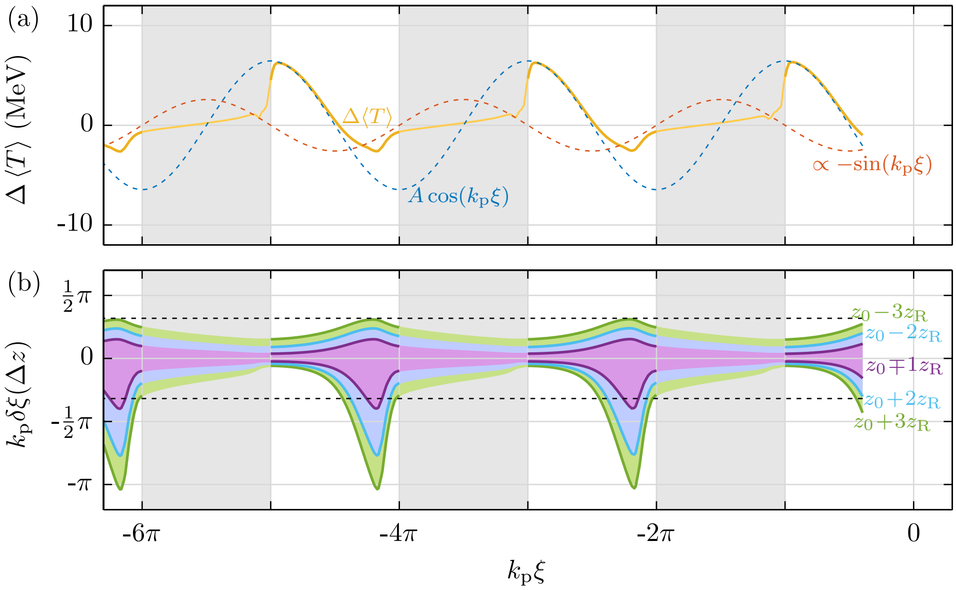

Figure 3.14 – (a) Energy gain curve from the simulation in comparison to an analytic estimation, given by $A \cos(k_\mathrm{p}\xi)$; the amplitude can be calculated to $A = -6.45\,\mathrm{MeV}$. The periodicity of the curves is identical. There is also an excellent agreement of the curves in the accelerating and focusing range. The deviations are explained by increasing phase slippage and the lack of energy gain of the particles being ejected out of the wake in the defocusing fields, which are proportional to $-\sin(k_\mathrm{p}\xi)$. Figure (b) illustrates the phase slippage: $\delta\xi$ is calculated as the difference of the phase at symmetric positions $z = \pm q z_\mathrm{R}$, $q \in \{1, 2, 3\}$, with respect to the phase $k_\mathrm{p}\xi$ at $z = 0$, where the laser is focused at. In the decelerating and focusing section, the phase slippage increases drastically, especially in the second half of the plasma channel, due to the constant deceleration of the particles. An asymmetric shape evolves in that region. The dashed lines in figure (b) depict $k_\mathrm{p}\delta\xi = 1$. The gray-shaded areas mark the defocusing sections; they will be used throughout this chapter.

the decelerating region, as the velocity difference is getting larger in this case.

Using this correction, the energy gain ΔT can be compared to an analytic estimation, which to first order reproduces a cosine shape:

$$\begin{aligned} \Delta T &= \int_{z_\mathrm{in}}^{z_\mathrm{out}} E_z(z)\,\mathrm{d}z = \int_{z_\mathrm{in}}^{z_\mathrm{out}} \hat{E}_z(z) \cos\Big\{k_\mathrm{p}\left[\xi - \delta\xi(z)\right]\Big\}\,\mathrm{d}z \\ &= \hat{E}_z(0) \int_{z_\mathrm{in}}^{z_\mathrm{out}} \frac{1}{1 + (z/z_\mathrm{R})^2} \cos\Big\{k_\mathrm{p}\left[\xi - \delta\xi(z)\right]\Big\}\,\mathrm{d}z, \end{aligned} \tag{3.9}$$

where the argument in the cosine given by the phase slippage interval around the injection phase, ξ. $E_z(z)$ is the longitudinal accelerating field according to equation (2.20), centered around the laser focus at $z = 0$. The amplitude $\hat{E}_z(0)$ is the maximal on-axis field in the focus, i.e.,

$$\hat{E}_z(0) = \frac{m_\mathrm{e} c^2 k_\mathrm{p}^2 \xi_\mathrm{RMS}}{2e} \sqrt{\frac{\pi}{2}}\, a_0^2 \exp\left(-\frac{k_\mathrm{p}^2 \xi_\mathrm{RMS}^2}{2}\right). \tag{3.10}$$

For the parameters used in the simulation (see table 3.1 on page 26), this amounts to $\hat{E}_z(0) = 789\,\mathrm{MV/m}$.

To estimate the integral, it is useful to approximate the cosine by a Taylor expansion at ξ:

$$\cos\Big\{k_\mathrm{p}\left[\xi + \delta\xi(z)\right]\Big\} \approx \cos\left(k_\mathrm{p}\xi\right) - k_\mathrm{p}\sin\left(k_\mathrm{p}\xi\right)\delta\xi(z) + \cdots. \tag{3.11}$$

Since the first term of this approximation is independent of z, the integral to leading order is

$$\int_{z_\mathrm{in}}^{z_\mathrm{out}} \frac{1}{1 + (z/z_\mathrm{R})^2}\,\mathrm{d}z = z_\mathrm{R}\arctan\left(\frac{z}{z_\mathrm{R}}\right)\Big|_{z_\mathrm{in}}^{z_\mathrm{out}}, \tag{3.12}$$

where the integration has to be performed over the plasma length, $\delta z = z_\mathrm{out} - z_\mathrm{in}$. Looking at a typical energy gain curve – see for example the red curve in figure 3.13(b) – can serve as a plausibility check: The function seems to be described well by an arctan-like shape.

Combining these results, the energy gain can be expressed as $\Delta T = A\cos\left(k_\mathrm{p}\xi\right)$, with the amplitude,

$$A = z_\mathrm{R}\arctan\left(\frac{z}{z_\mathrm{R}}\right)\Big|_{z_\mathrm{in}}^{z_\mathrm{out}}\hat{E}_z(0) = -6.45\,\mathrm{MeV}, \tag{3.13}$$

if the integration limits are $z_\mathrm{in} = -10\,\mathrm{mm}$ and $z_\mathrm{out} = 15\,\mathrm{mm}$, which covers the region of constant plasma density. The up- and downramp are neglected.

In figure 3.14, this approximation with the numerical value for A from equation (3.13) is compared to the energy gain determined by the simulation. The approximation works exceptionally well in the accelerating and focusing region.

To understand this agreement as well as the deviations in the decelerating range, it is helpful to look at plot (b) of the figure: In this graph, the phase difference $\delta\xi$ with respect to ξ is plotted at symmetric positions around z_0, namely at $z = z_0 \pm q z_\mathrm{R}$ with $q \in \{1, 2, 3\}$. As can be seen, there is a considerable slippage in all of these intervals – at any phase. However, in the focusing and accelerating section, the slippage is still much smaller than one, and more importantly, it is almost symmetric, as can be deduced from the shaded areas. This means that the function $\delta\xi(z)$ must be close to an odd function in these symmetric parts, since the sign changes and $\delta\xi(z = z_0) \equiv 0$ by definition, i.e., $\delta(-z) \approx -\delta(z)$. So, the higher order integral vanishes (for symmetric integral bounds). Also, close to the maximum accelerating field, the sine in this second term of the Taylor expansion vanishes as well, so that the higher order influence is negligible around that point, even though the symmetry is not perfect.

Actually, at the phases around the maximal energy gain, a slight asymmetry to the positive side is given – which is easily explained: Since the particles gain momentum in the field, the velocity difference between the wave and the electrons reduces, with the result that the slippage is less in the second half. Towards the decelerating field, this trend turns, so that a strong asymmetry builds up in the opposite direction, since the particles are delayed. In the worst case, there is a phase difference $k_\mathrm{p}\delta\xi > \pi$, i.e., the particles are pushed back into the accelerating region, and even regain some of the lost energy. This explains the bend at the minimum of the energy gain curve which is close to this point of maximal slippage.

On the other end of the energy scale, one finds that the maximum possible gain is not achieved. This is again explained by slippage: Particles which would end up at the maximum energy will eventually slip into the defocusing region and are, thus, swiftly scattered out of the wake, stopping any further energy gain. The same is true for particles entering the plasma in the defocusing sections, which explains the flat energy gain curve in these regions.

The next step is to look at the matching quality. Figure 3.15(a) compares the change in the emittance at the entrance with the one at the exit of the plasma. Once more, the symbol $\delta[\,\cdot\,]$, as defined in equation (3.8), is used. For an artificial bunch with ideal parameters calculated with the strategy described in section 3.2, the matching in the focusing and accelerating region is almost perfect, with an emittance growth close to zero; in the decelerating region the emittance suffers, starting at the position of the turning point known from the energy gain curve. Particles beyond this region are probably injected into the defocusing region and shifted back into a focusing part by the decelerating fields before the transverse fields can push them completely out of the plasma. However, the emittance is spoiled during this injection process; this range is denoted as *extended defocusing* region in the following. In contrast, the REGAE bunches, which are tracked along the whole machine and matched to the plasma using the beam optics elements to achieve the virtual focus, pass the plasma in the *good-field* region with an emittance growth of about $\delta[\varepsilon_{xy}] \approx 25\,\%$; at injection, the absolute normalized transverse emittance lies around $\varepsilon_{xy,\mathrm{in}} \approx 50\,\mathrm{nm\,rad}$.

Figures 3.15(b,c) depict the beta function β_{vf}, and the accompanying transverse beam size x_{RMS} in the virtual focus. As can be seen, these quantities are smaller for the ideally matched, artificial bunch compared to the REGAE case. Therefore, the matching condition is not fulfilled for the latter case, leading to an increased emittance. This can also be seen from in 3.16, which illustrates an exemplary matching for a certain phase setting. The ideal trajectory, $x_{\mathrm{RMS,id}}$, passes the plasma without visible betatron oscillations, in contrast to the REGAE beam, $x_{\mathrm{RMS,RG}}$. Thus, the respective emittance grows because of betatron phase mixing as explained above.

Two factors can be identified as the cause of the deviating beam size: First, the ideal bunch is tracked without space charge, which leads to an increased beam size and a different beta function close to the waist. Second, the solenoids are no thin lenses. Hence, a beam size *at* the focusing element is not well defined; also, the divergence change happens over a certain distance and not instantaneously, as would be the case in the thin lens approximation. Thus, the decoupling of parameters by first setting a calculated beam size at the final solenoid and then adjusting the focus position with this last lens has its limitations. These issues explain the slightly deviating beam profile and the resulting emittance growth – which is, nevertheless, not very dramatic. One should also keep in mind that, depending on the steepness of the focusing and divergence at the plasma exit, there can be additional emittance growth within the free drifts [30].

Finally, $\beta_{\mathrm{m},0}$ in graph (b) of figure 3.15 depicts the much smaller beta function that has to be achieved at the matching point – and thus illustrates the charm of the plasma guidance by means of an adiabatically increasing focusing fields. A sharp transition without a density ramp and the laser focused directly at the entrance of the plasma channel would require a much smaller beam spot to be reached only with the REGAE beam optics, which is almost impossible to achieve due to space charge repulsion.

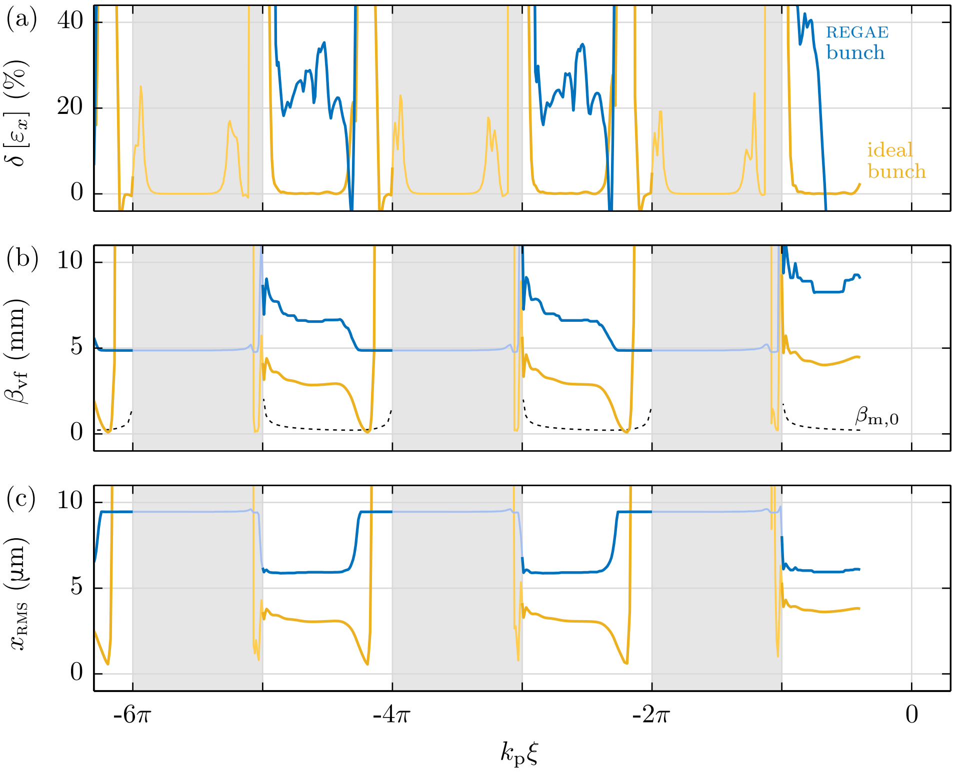

Figure 3.15 – Analysis of the matching quality. Figure (a) displays the emittance growth between plasma entrance and exit versus the injection phase. An ideal beam, according to the matching strategy, has almost no emittance growth, while a start-to-end beam shows a mild increase of about 25 % in the focusing and accelerating section. The relative emittance value in the defocusing region for the ideal bunch is a numerical artifact, resulting from an extremely large reference emittance. In figure (b), the respective beta function at the virtual focus is shown, explaining this discrepancy: the REGAE bunch does not achieve the injection parameters perfectly due to space charge repulsion and deviations from the thin lens approximation. In comparison, the black, dotted line shows the required beta function at the matching point – which would be very challenging to achieve without the final focusing from the plasma fields due to space charge repulsion; the matched beta function is not defined in the defocusing region. Figure (c) shows the corresponding beam size in the virtual focus, which is about twice as large as required in the case of the REGAE beam – driven by space charge and deviations from the thin lens approximation. In the *extended defocusing* region, a matched injection is impossible.

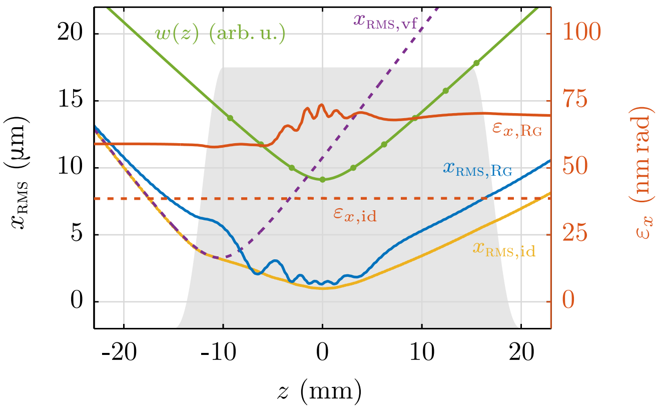

Figure 3.16 – Exemplary beam evolution within the plasma for a distance of $\xi = -472\,\mu\mathrm{m}$, which is close to the maximum accelerating phase of the second bucket. The ideal beam evolution, $x_{\mathrm{RMS,id}}$ differs slightly from the actual beam parameters in the start-to-end REGAE simulation: Space charge effects and deviations from the thin lens approximation lead to a different focus. Hence, the emittance increases from about $\varepsilon_{\mathrm{RG}} = 50\,\mathrm{nm}$ to $\varepsilon_{\mathrm{RG}} = 60\,\mathrm{nm}$, while there is almost no emittance growth in the ideal case.

In the defocusing range, the matched beta function is not defined. In this region, which is extended by phase slippage, an emittance conservation is impossible despite the result displayed for the ideal bunch in figure 3.15(a). The apparent emittance conservation in that regions is due to a numerical artifact caused by an extremely large reference value. These segments are mostly neglected in the subsequent discussion and marked by the gray shaded area in the following plots. Likewise, the first bucket is excluded owing to the deviating results, which presumably result from the overtaking process.

Figure 3.17 shows the settings necessary for the beam optics to achieve the relevant beam sizes. For the accelerating region, it is interesting to note that the farther away the position of the virtual focus shifts from the matching point, the closer the injection phase moves towards the maximum gradient (figure 3.17(b)). The explanation for this is as follows: The focusing forces are maximal around the zero crossing of the accelerating field. However, the focusing strength also depends on the particle energy: $K \propto 1/\gamma$ [equation (2.21) in chapter 2.2]. That is, in the decelerating region, the overall focusing strength is larger. Hence, the matched beam size is reached faster, i.e., within a shorter distance. Thus, the virtual focus is closer to the matching point. For the high accelerating gradients, the focusing forces are weaker, requiring a longer action of the guiding fields. An important consequence of this discussion is, that the injection optics has to be (slightly) tuned for each injection phase.

Figure 3.18 depicts the most relevant parameters for the beam transport and imaging onto the spectrometer screen. As can be seen, an energy spread on the order of about 100 keV is accumulated, which is well below 5 % with regard to the mean energy. It is especially low around the maximal accelerating field. As in the case of a standard accelerating cavity (see 5), this is due to the flatness of the cosine curve at the maximum and the consequently vanishing slope,

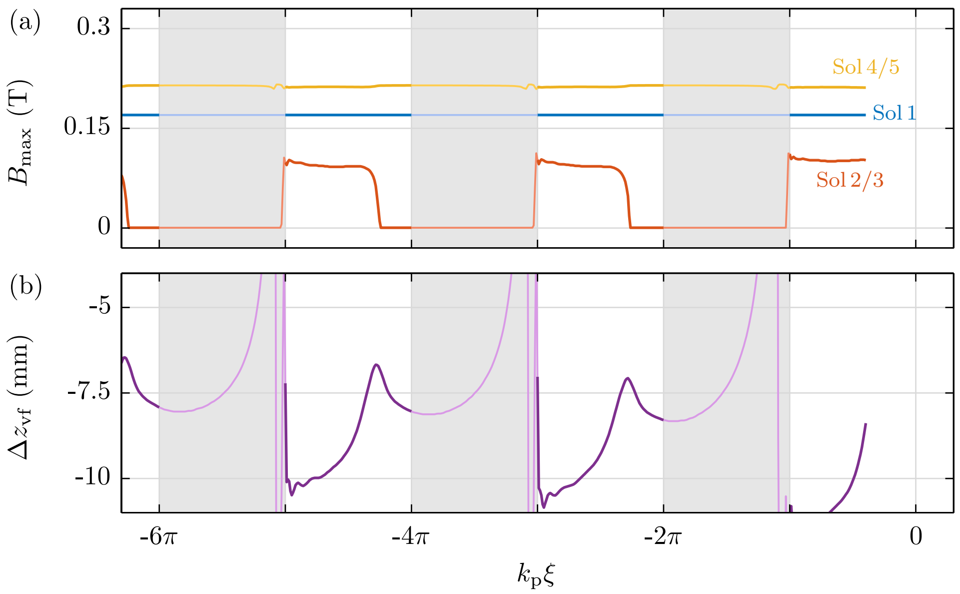

Figure 3.17 – (a) Solenoid settings according to the start-to-end simulation to achieve the matched beta function at the plasma entrance. For the defocusing phases there is of course no meaningful solution, because the matching condition is not valid. The matching algorithm calculates an unrealistic small beta function, which requires a very large beam size in solenoid 4/5, so that the preceding lens is switched off. Figure (b) shows the position of the virtual focus. Due to the increased focusing forces towards the decelerating section, the bunch reaches the matched focus faster, resulting in the position of the virtual focus being closer to the matching point.

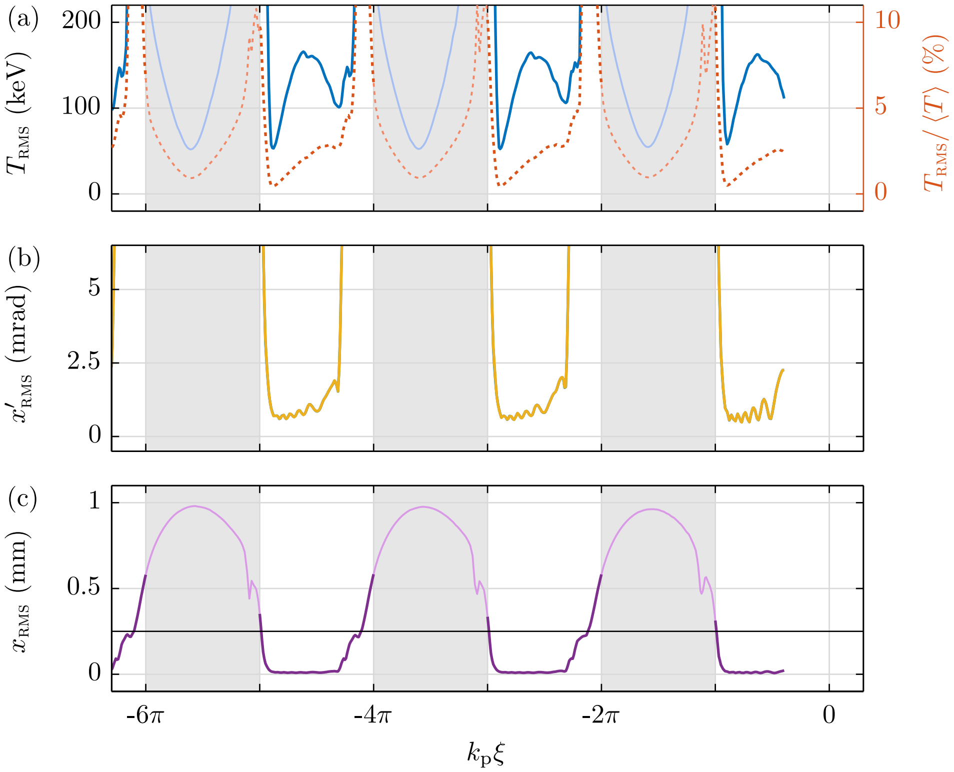

Figure 3.18 – Investigation of the resulting RMS energy spread (a), beam divergence (b), and beam size (c) after the plasma passage. The energy spread is less than $T_{\text{RMS}} < 200\,\text{keV}$, so that the relative energy spread $T_{\text{RMS}}/\langle T\rangle$ is well below 5 % in the good-field region. The transverse divergence, x'_{RMS} is on the order of 1 mrad, while the beam size is about $x'_{\text{RMS}} \approx 10\,\mu\text{m}$ in this region. The purpose of the last plot (c), however, is to demonstrate the particle loss in the extended defocusing range: Most of the particles will be deflected into the boundaries of the plasma target, which are depicted by the black line.

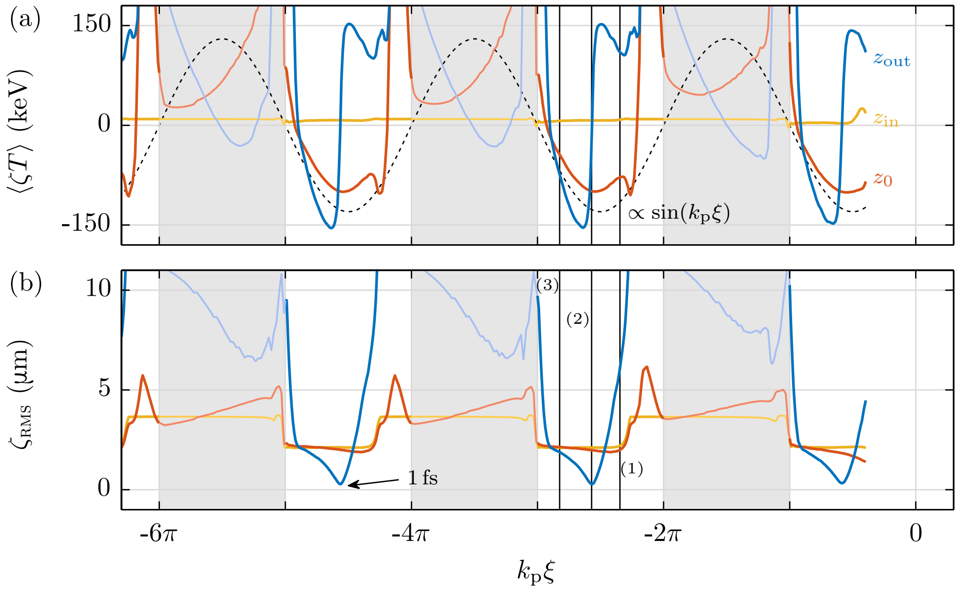

Figure 3.19 – Correlated energy spread (a) and bunch length (b) at three locations along the plasma: Yellow marks the beginning of the plasma (z_{in}), red the position of maximal field (z_0), and blue the exit of the plasma channel (z_{out}). In the accelerating region, the wakefield always imprints a negatively correlated energy spread: The beam is further compressed (below 1 fs) and even partly over-compressed. The black lines mark cases (1) to (3) shown in figure 3.20. The correlated energy spread results from the slope of the accelerating fields, which is proportional to $\sin(k_\mathrm{p}\xi)$. As can be seen, the red curve in the good-field region mainly resembles that shape.

so that only the quadratic order contributes. Of course, the (correlated) energy spread acquired depends on the bunch length achieved at the injection point. The divergence at the exit of the plasma, figure (b), is about $x'_{\mathrm{RMS}} \approx 1\,\mathrm{mrad}$ in the good-field region – a promising value. In the complementing phase intervals this parameter strongly increases, due to the defocusing plasma fields. The lower graph shows the beam size at the exit of the plasma target with the black line depicting the radius of the channel. Thus, the defocused electrons are already scattered into the target material, so that a transport to and detection in the electron spectrometer is not possible: The beams injected in these phases are lost.

The development of the correlated energy spread, $\langle\zeta T\rangle$, provides much information about the bunch length behavior inside the plasma; both parameters are shown in figure 3.19. Since the usable part of the wakefield is completely contained within the bunching slope of the accelerating field, and the beam enters the plasma with almost zero correlated energy spread, the strong fields further compress the electron bunch inside the plasma. Space charge forces are easily surpassed by the plasma fields. Particles around the zero crossing are even compressed below a bunch length of $t_{\mathrm{RMS}} < 1\,\mathrm{fs}$ at the end of the plasma.

In the decelerating region, the beam reaches the minimum bunch length within the plasma.

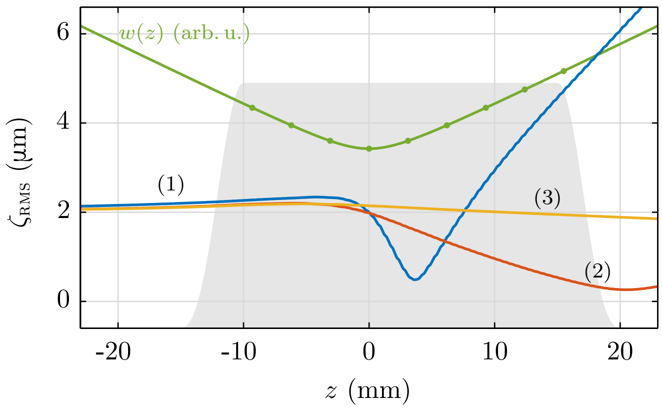

Figure 3.20 – Bunch length evolution for three different injection phases. Case (1), with $\xi_{(1)} = -392\,\mu\mathrm{m}$, is in the decelerating region. The bunch is strongly compressed and reaches its longitudinal focus within the plasma. (2) is around the zero crossing of the field, $\xi_{(2)} = -430\,\mu\mathrm{m}$. Here, the bunch length minimum is – by chance – around the plasma exit. Finally, (3) is injected close to the peak field, at $\xi_{(3)} = -472\,\mu\mathrm{m}$. Due to the energy gain, the bunching mechanism is strongly suppressed, shifting the longitudinal focus downstream of the plasma.

Therefore, the energy-position correlation is positive in that phase interval at the end of the plasma channel, as can be seen from the figure. On the other hand, the length of high energy bunches is kept almost constant. Both behaviors can be explained by the scaling of bunch compression using ballistic bunching. As will be seen in chapter 5, the effect of this method scales with $1/\gamma^3$ (where γ is the Lorentz factor). Hence, if the particles lose energy (while maintaining or increasing the correlated energy spread), the compression is enhanced. If the energy is increased, ballistic bunching is strongly suppressed and the bunch length is frozen – or at least, the minimum is shifted downstream. Figure 3.20 complements figure 3.19, explicitly showing the bunch length evolution for three exemplary bunches.

3.5 Beam Transport

Knowing the key characteristics of the resulting bunches from the previous section, the next step is to address the beam transport of the particles from the plasma target to the detector in order to measure the properties described above. The electron spectrometer (eSpec), which is used for this purpose, is located about 2.5 m downstream of the plasma cell.

Thus, a proper beam optics is required to transport the bunches towards the spectrometer. Ideally, the magnets used minimize the beta function of the design energy in the (horizontal) dispersion plane for a high resolution. At the same time, it is desirable to reduce the divergence in the vertical plane, while avoiding a focus. With such a configuration, spectra like in figure 3.12 would be produced. Solenoids, which are typically used at REGAE, are no longer a viable option. The focusing strength of solenoids K_{s} scales with $1/\gamma^2$ [53], which already requires quite big

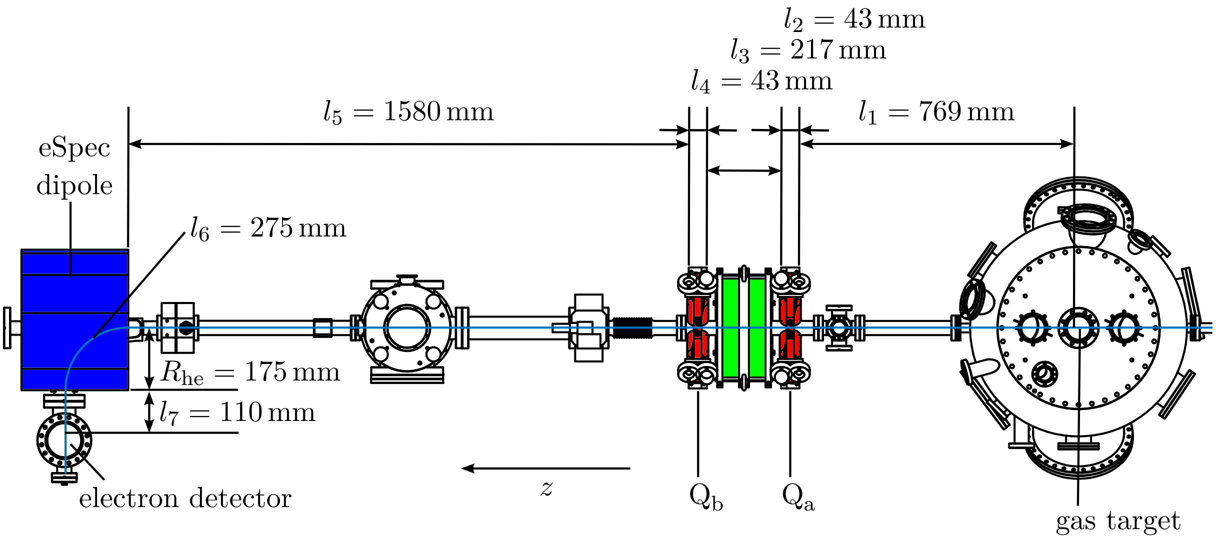

Figure 3.21 – Drift lengths for the calculation of the transfer matrix according to equations (3.15), describing the beam transport from the end of the plasma target to the electron detector in the eSpec.

and elaborate solenoids for the higher energies achieved in the experiment. Therefore, two small quadrupole magnets will be used instead. They have a better energy scaling ($1/\gamma$) and also enable an astigmatic focusing and, thus, yield the desired asymmetric imaging in this experiment.

The dipole magnet of the electron spectrometer is a focusing device as well – at least in the dispersion plane. This becomes obvious when looking at the transfer matrix of a dipole in the dispersion plane [64, 65]:

$$M_\mathrm{dp} = \begin{pmatrix} \cos(s/R) & R\sin(s/R) \\ -\frac{1}{R}\sin(s/R) & \cos(s/R) \end{pmatrix}. \tag{3.14}$$

Thus, M_dp is simply a version of M_K defined in equation (2.2), where the focusing strength is given by the radius of curvature, i.e., $R = 1/\sqrt{K}$. And, since $R > 0$, the dipole has focusing properties.

Once again the matrix formalism can be used to find a solution for this problem and obtain the desired focusing. Basically, one has to multiply the transfer matrices of the two quadrupoles, the dipole and the drifts in between:

$$\begin{aligned} M_{\mathrm{bt},x} &= M_s(l_7)\cdot M_\mathrm{dp}(R,l_6)\cdot M_s(l_5)\cdot M_K(K_b,l_4)\cdot M_s(l_3)\cdot M_K(K_a,l_2)\cdot M_s(l_1), \\ M_{\mathrm{bt},y} &= M_s(l_7)\cdot M_s(l_6)\cdot M_s(l_5)\cdot M_K(-K_b,l_4)\cdot M_s(l_3)\cdot M_K(-K_a,l_2)\cdot M_s(l_1). \end{aligned} \tag{3.15}$$

Here, $K_a < 0$ and $K_b > 0$ are the strength of the individual quadrupole magnets. The first magnet is thus chosen to be defocusing, while the second one is focusing in the dispersion plane, and vice versa in the vertical plane. In this second plane, the dipole matrix describes a simple drift of length l_6; this length is also linked to the radius of curvature, R, since the eSpec is designed for a 90 deg bend. This means $l_6 = \pi R/2$. l_1 is the distance between plasma and first magnet, while l_7 is the final drift after the dipole towards the scintillator screen of the detector. The drift lengths l_1 to l_7 are fixed by the geometry of the (upgraded) REGAE accelerator. R is the radius of curvature for the design energy, and hence fixed as well. Thus, there are two free parameters, K_a and K_b, which suffice to find a solution. The drift lengths are depicted in figure 3.21.

As only a focus in the dispersion plane is required, the problem is actually over-determined. A whole class of solutions can be calculated which yields $\alpha = 0$, i.e., a focused beam at the detector. The result with the smallest beta function at the eSpec scintillator is chosen – provided it does not violate the second demand: to map the transverse momentum distribution in the y-plane, reducing the divergence, but avoiding a focus at the same time. The calculation with the focusing strength has the advantage that it is energy independent. So, the solutions of K_a, K_b (like R) are constant over the whole energy range, but the magnetic fields have to be adjusted for the respective energies. However, this poses no significant problem: All magnets have to be adjusted for the same particle energy – which is given by the longitudinal momentum the dipole is set for. In other words, the magnet currents have to be tuned depending on the injection phase. But the current in the dipole also automatically determines the required magnetic strength of the quadrupoles, because the dipole determines which energy is monitored anyway. (In that sense, one could also treat the focusing optics and the dipole as one single instrument that has to be adjusted to a certain energy.)

One thing is missing to calculate K_a and K_b, though: The initial Courant-Snyder parameters are required. And in principle, this can spoil the universal solution for the focusing strengths K, since the beta function is not necessarily constant at the end of the plasma for different phases. Put differently, the lattice should be matched to the preceding accelerator segment, i.e., the Courant-Snyder parameters at the end of the plasma. An analysis of the emerging beta function is therefore necessary. As can be seen in figure 3.22, the beta function at the end of the plasma is on the order of $\beta_{\mathrm{pe}} \approx 0.025\,\mathrm{m}$, varying at most by a factor of two. The other Courant-Snyder parameters fluctuate in a similar range around $\alpha_{\mathrm{pe}} \approx -2$ and $\gamma_{\mathrm{pe}} \approx 200\,\mathrm{m}^{-1}$.

The beam transport according to equation (2.10) is described by

$$\Sigma_{\mathrm{det}} = \begin{pmatrix} \beta_{\mathrm{det}} & -\alpha_{\mathrm{det}} \\ -\alpha_{\mathrm{det}} & \gamma_{\mathrm{det}} \end{pmatrix} = M_{\mathrm{bt}} \begin{pmatrix} \beta_{\mathrm{pe}} & -\alpha_{\mathrm{pe}} \\ -\alpha_{\mathrm{pe}} & \gamma_{\mathrm{pe}} \end{pmatrix} M_{\mathrm{bt}}^{\mathrm{T}}, \tag{3.16}$$

which has to be evaluated for the x and y plane with the respective transport matrix given in equation (3.15). Using the mean Courant-Snyder parameters in combination with the positions and lengths of the beam transport elements specified in figure 3.21, the combinations for K_a and K_b can thus be calculated by solving for $\alpha_{x,\mathrm{det}} \equiv 0$; the results are shown in figure 3.23. The minimal beta function in x is found for $K_a = -61.5\,\mathrm{m}^{-2}$ and $K_b = 63.6\,\mathrm{m}^{-2}$. The resulting evolution of β is depicted in figure 3.24. As it turns out, the focusing strength of the dipole is so strong that it requires the source to be located close to the magnet entrance due to associated short focal distance; this effect was also found in [88]. Hence, the quadrupole system focuses the beam in front of the dipole, creating an additional beam waist. This situation is not ideal since Coulomb repulsion in this transverse focus could spoil the measurement. However, the bunch is

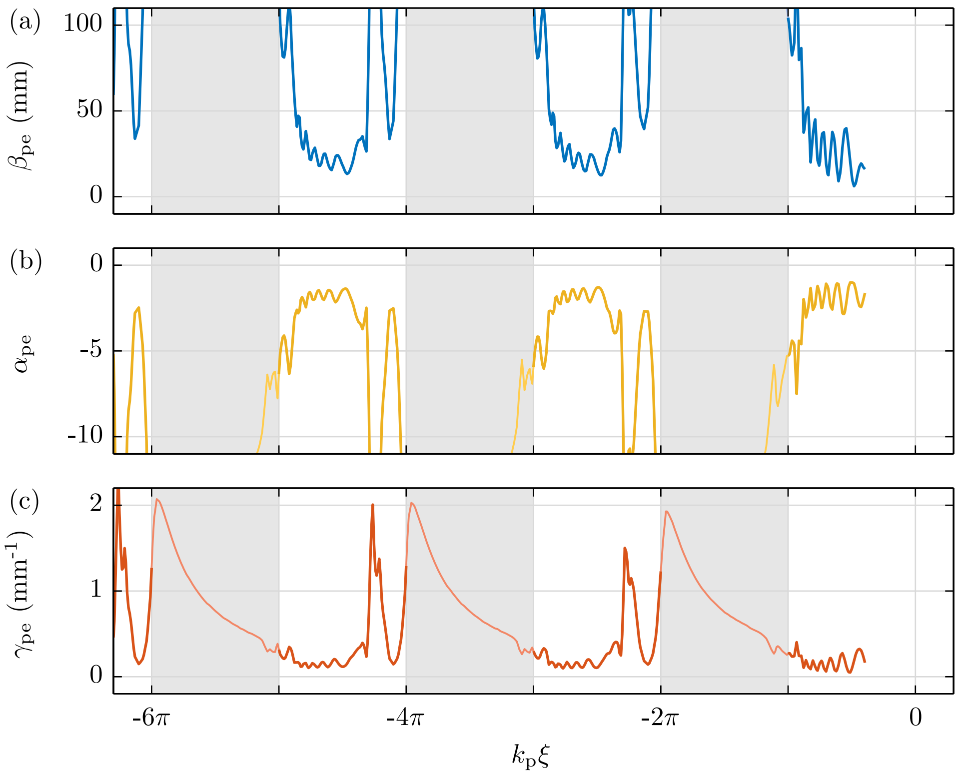

Figure 3.22 – Courant-Snyder parameters at the end of the plasma channel. The beta function in the good-field region varies slightly around $\beta_{\text{pe}} \approx 25\,\text{mm}$. The correlation parameter α shows a similar behavior.

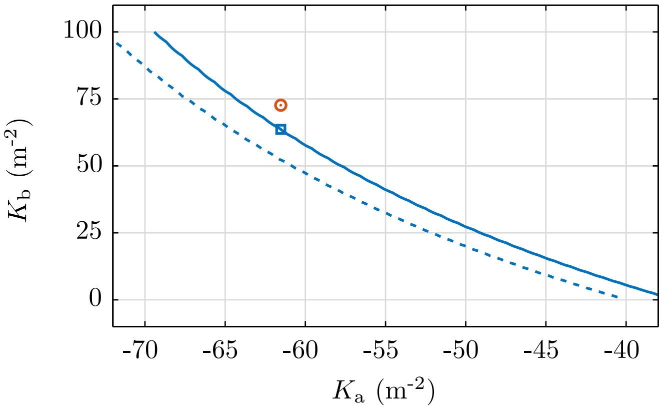

Figure 3.23 – Possible solutions for a focused beam at the eSpec detector using the matrix formalism. The square marks the chosen parameter combination, which is corrected for an optimized focus in the spectrometer using ASTRA in a next step. This slightly deviating value is marked by the red circle. The dashed lined marks the second solution resulting from the quadratic dependence on M in equation (3.16).

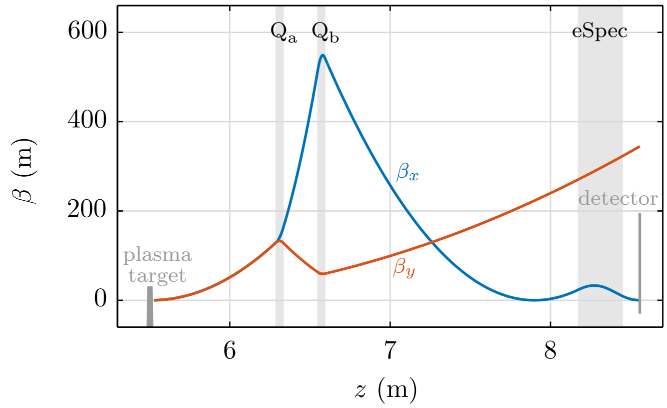

Figure 3.24 – Beta functions for the transverse planes in the post-plasma section. The first quadrupole, Q_a, is defocusing in the dispersion plane, while the second one, Q_b, creates an additional beam waist in β_x in front of the eSpec. Since the dipole magnet has a comparatively strong focusing effect in the dispersion plane, this artificial source is required for a proper imaging at the detector. In the vertical plane, y, the beam divergence is reduced behind the second quadrupole.

already significantly expanded in the longitudinal dimension at this point, which is why space charge effects are only a minor issue.

The focusing strength of the dipole with a (hard edge) radius of curvature of $R_{\mathrm{he}} = 175\,\mathrm{mm}$, see chapter 4.2.2, is about $K_{\mathrm{dp}} = 1/R_{\mathrm{he}}^2 \approx 30\,\mathrm{m}^{-2}$ which is roughly half of the values obtained for the quadrupoles. But at the same time, the drift length inside the dipole is more than six times larger, explaining the comparatively short focal length.

In a next step, the result is verified and refined with ASTRA by scanning the second quadrupole strength. This shifts the focus position in front of the eSpec, optimizing the final focus at the detector. The resulting parameter is $K_b = 72.6\,\mathrm{m}^{-2}$, due to the shift $\Delta K_{\mathrm{b}} = 9\,\mathrm{m}^{-2}$; see figure 3.25. The energy resolution will be dominated by the beam size, as can be deduced from an analysis of the spectrometer [88]: As can be seen in figure 3.25, the beam spot for a mono-energetic bunch amounts to $x'_{\mathrm{RMS}} \approx 250\,\mu\mathrm{m}$ and is thus much larger than the detectors pixel size, which is about $6\,\mu\mathrm{m}$. The resolution can be estimated to about $\delta p_z/p_z = 0.1\,\%$. For a detailed description of the eSpec see chapter 4.2.2 and [88].

The analytic method is used to check the tolerance of the focusing system with respect to fluctuating beta functions at the end of the plasma channel. By varying the Courant-Snyder parameters at that position within a range of about $10\,\mathrm{mm} < \beta_{x,\mathrm{pe}} < 50\,\mathrm{mm}$ and $-4 < \alpha_{x,\mathrm{pe}} < -1$, it can be seen that the beta function at the detector is not influenced to a large degree: The solutions for $\beta_{x,\mathrm{det}}$ in the parameter space are depicted in figure 3.26. The Courant-Snyder parameters at the plasma exit, obtained from the ASTRA simulations in the previous section, are marked by the yellow dots. For the majority of cases, the beta function in x is about $\beta_{x,\mathrm{det}} \approx 250\,\mathrm{mm}$, varying below a factor of two. Only for parameter combinations which seem to be very unlikely, the increase can be larger – but still less than one order of magnitude. Therefore, a constant

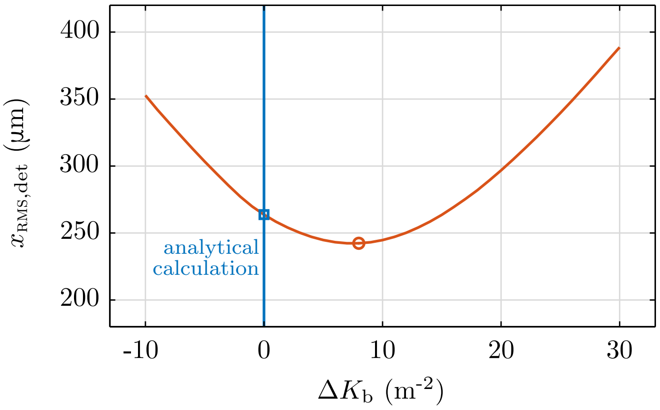

Figure 3.25 – Beam size at the detector, $x_{\mathrm{RMS,det}}$, depending on the focusing strength of the second quadrupole, $\mathrm{K_b}$. The blue square denotes the calculated value, while the red curve results from an ASTRA simulation. The circle marks the refined focusing strength chosen, also depicted in figure 3.23.

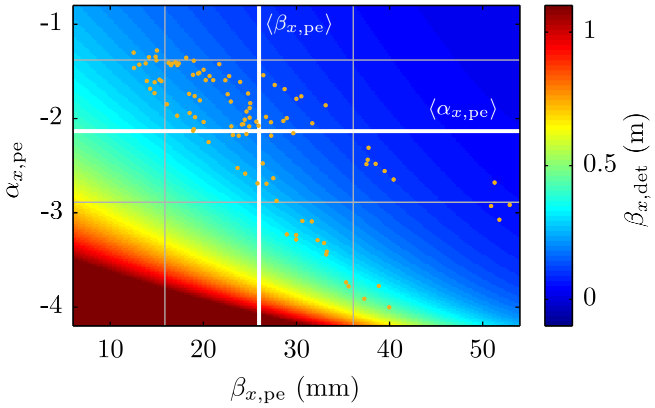

Figure 3.26 – The resulting beta function, $\beta_{x,\mathrm{det}}$, at the detector, analytically solved for a parameter space $(\beta_{x,\mathrm{pe}}, \alpha_{x,\mathrm{pe}})$ at the exit of the plasma. The yellow dots mark the Courant-Snyder parameters at the plasma exit in the accelerating regions, gained from the simulations discussed in chapter 3.4. The white lines depict the mean value for this distribution, complemented by the standard deviations (thin lines). The beta function at the detector is not very sensitive to the input variation. For this reason, it should be possible to use the constant focusing strengths, K_{a} and K_{b}.

K-setting is used in the following, regardless of the phase in the plasma: $K_{\mathrm{a},x} = -61.5\,\mathrm{m}^{-2}$ and $K_{\mathrm{b},x} = 72.6\,\mathrm{m}^{-2}$.

Finally, a comparison of the spectra obtained in the analysis of the previous section and the resulting images on the spectrometer screen is possible. The images in the previous section have been obtained from the phase space shortly behind the plasma exit. Using ASTRA, the bunches are now transported to the eSpec detector, employing measured field maps for the magnets. Figure 3.27 shows the three exemplary cases once again: $\xi_{(1)} = -392\,\mu\mathrm{m}$, $\xi_{(2)} = -430\,\mu\mathrm{m}$, $\xi_{(3)} = -472\,\mu\mathrm{m}$.

The determined energy and energy spread from the spatial position on the detector screen is very close to the actual values, which is also attributed to the simulation environment. However, the plots demonstrate that the structure of the spectra determined directly behind the plasma can in principle be transported to the detector and can be resolved.

In connection with this, the divergence at the plasma exit can, furthermore, be estimated from the eSpec image, using the matrix formalism once more. The beam size at the detector is $y_{\mathrm{RMS,det}} = \sqrt{\hat{\varepsilon}\beta_{y,\mathrm{det}}}$, with the geometric emittance $\hat{\varepsilon}$. Using equation (3.16), the relationship with the beta function at the plasma exit is explicitly given by [64, 65]:

$$\beta_{\mathrm{det}} = M_{1,1}^2\beta_{\mathrm{pe}} + M_{1,2}^2\gamma_{\mathrm{pe}} - 2M_{1,1}M_{1,2}\alpha_{\mathrm{pe}}. \tag{3.17}$$

The Courant-Snyder parameters at the exit of the plasma are not known, which prevents a solution of this equation. However, some assumptions can be made. Using $\beta\gamma - \alpha^2 = 1$, equation (3.17) can be written as

$$\beta_{\mathrm{det}} = M_{1,1}^2\beta_{\mathrm{pe}} + M_{1,2}^2(1+\alpha_{\mathrm{pe}}^2)/\beta_{\mathrm{pe}} - 2M_{1,1}M_{1,2}\alpha_{\mathrm{pe}}, \tag{3.18}$$

where $M_{i,j}$ are the respective matrix elements of $M_{\mathrm{bt},y}$.

The elements of the transport matrix M are machine parameters and can be calculated from the settings of the beam optics lattice. The values for $K_{\mathrm{a},y} = 61.5\,\mathrm{m}^{-2}$ and $K_{\mathrm{b},y} = -72.6\,\mathrm{m}^{-2}$ yield $M_{1,1} = -2.8$ and $M_{1,2} = +1.7\,\mathrm{m}$, which means that the products of the matrix elements appearing in equation (3.17) are of similar magnitude. Furthermore, the beam is diverging at the plasma exit, i.e., $\alpha_{\mathrm{pe}} < 0$, so the last term is negative, while the other two are positive. The beam size at the plasma exit, $x_{\mathrm{RMS,pe}}$ is small, and consequently $\beta_{\mathrm{pe}} \ll 1\,\mathrm{m}$. Hence, the first term in equation (3.17) can be neglected compared the second one, so that

$$\beta_{\mathrm{det}} \approx M_{1,2}^2(1+\alpha_{\mathrm{pe}}^2)/\beta_{\mathrm{pe}} - 2M_{1,1}M_{1,2}\alpha_{\mathrm{pe}} \approx \Big[3(1+\alpha_{\mathrm{p}}^2)/\beta_{\mathrm{pe}}(\mathrm{m}) - 10\alpha_{\mathrm{pe}}\Big]\,\mathrm{m}. \tag{3.19}$$

Here, $\beta(\mathrm{m})$ means that the beta function has to be given in meters. The explicit values for $M_{i,j}$ from above are included.

The ratio $10\alpha_{\mathrm{pe}}/[3(1+\alpha_{\mathrm{pe}}^2)]$ is bounded by $|10\alpha_{\mathrm{pe}}/[3(1+\alpha_{\mathrm{pe}}^2)]| \lesssim 2$, so that the first term in equation (3.19) is dominating due to the smallness of β_{pe}. Hence, the beta function at the detector β_{det} is almost completely determined by $\gamma_{\mathrm{pe}} = (1+\alpha_{\mathrm{pe}}^2)/\beta_{\mathrm{pe}}$.

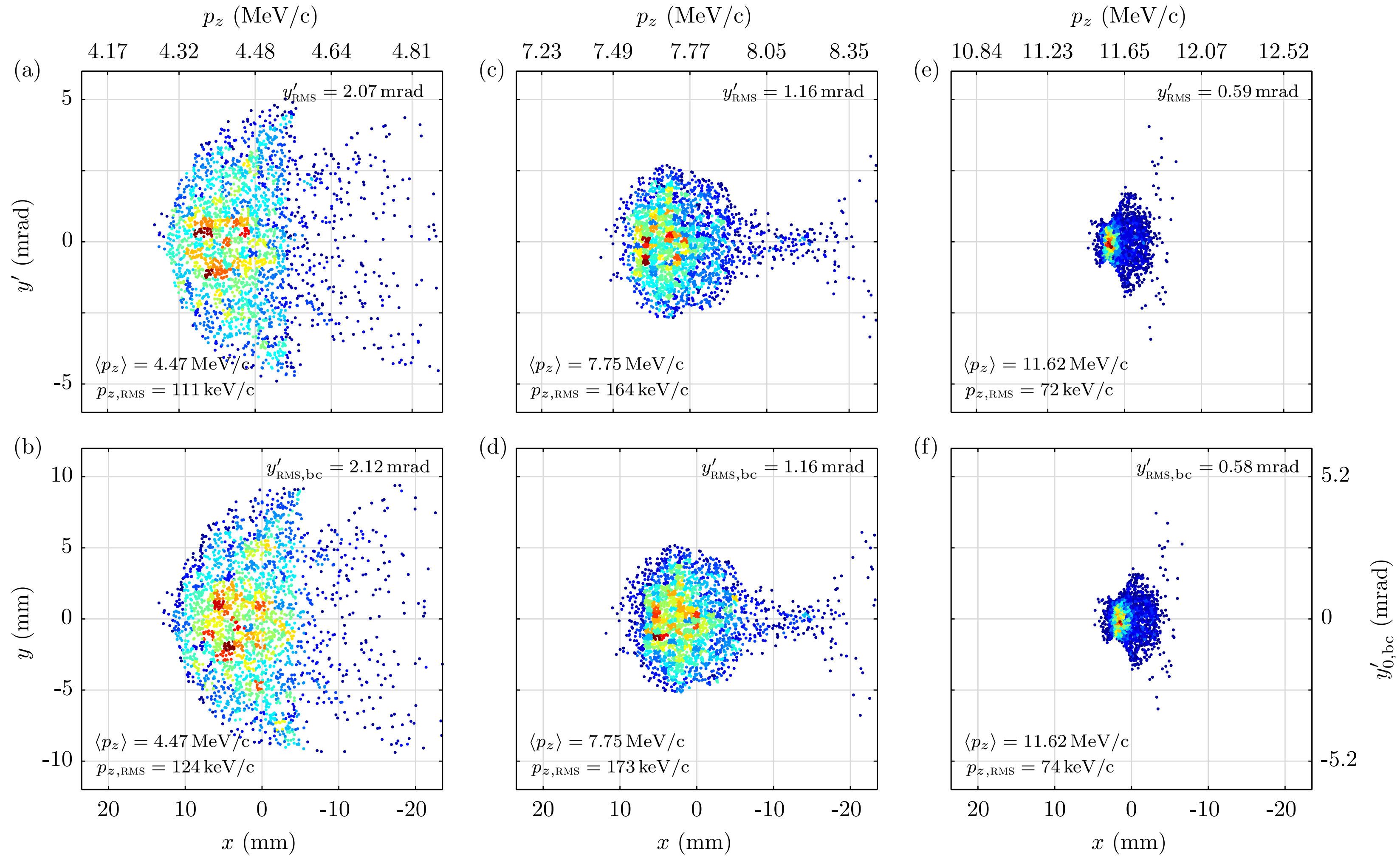

Figure 3.27 – Comparison of exemplary energy spectra for $\xi_{(1)} = -392\,\mu\mathrm{m}$ (a,b), $\xi_{(2)} = -430\,\mu\mathrm{m}$ (c,d), and $\xi_{(3)} = -472\,\mu\mathrm{m}$ (e,f). The top row shows the parameters 8 cm behind the plasma exit, while the bottom row displays the particles transported to the electron spectrometer. x and y are the spatial coordinates of the scintillator screen; the limits of the x-axis are in accordance to the size of that screen ($\Delta x = 47\,\mathrm{mm}$). The structure is very well reproduced. Also, the longitudinal momentum $\langle p_z \rangle$ and the momentum spread $p_{z,\mathrm{RMS}}$ agree very well, as does the back-calculated divergence, $y'_{\mathrm{RMS,bc}}$. The energy calibration of the eSpec is presented in chapter 4.2.2; the estimation of $y'_{\mathrm{RMS,bc}}$ is done by the method described in the text.

Assuming that the emittance is not changing in the drift from the plasma to the detector, the divergence $y'_{\mathrm{RMS,pe}} = \sqrt{\hat{\varepsilon}\gamma_{\mathrm{pe}}}$ can thus be estimated from the beam size at the detector:

$$y'_{\mathrm{RMS,pe}} \approx \frac{y_{\mathrm{RMS,det}}}{|M_{1,2}|}. \tag{3.20}$$

Please note, that this approximate expression is similar to the beam transport of a single particle. For the three exemplary cases, this method determines the divergence with a remarkable accuracy. The deviation is about 3 % in the worst case. The calculated values are given in figure 3.27. The respective phase spaces (and thus the back-calculated divergence values) are taken 8 cm behind the plasma exit, so that $M_{1,2} = 1.9$ is slightly different from the value given above, due to the reduced drift length l_1.

With these results, the idealized start-to-end scenario illustrated in the last sections is completed. Of course, it is important to keep the limitations in mind: First of all, there is a perfect environment assumed in a simulation, which is in this case applied to one specific plasma target configuration. In addition, ASTRA uses the linear plasma model without the plasma wake decaying or damping with increasing distance to the laser. However, experiments have shown the formation of about ten and more buckets with similar structures in plasma wakefields [89]. Also, the laser evolution – and thus the local field strength – is only an approximation. This is exactly one of the purposes of the experiment: proving the viability of the model or gaining information that can lead to its improvement.

In summary, the simulations show that matched injection of electrons from REGAE into a laser-driven plasma wakefield is in principle feasible over almost the entire focusing region of the plasma fields. The overtaking of the electron bunch by the laser seems to be manageable. An analysis making use of the super-Gaussian laser profile is necessary, though. As long as the damping of the plasma wakefield is not an issue, injection into a higher bucket is always an option in case the bunch should be spoiled too much by the driver laser.

In addition, a transport of the accelerated bunch towards the detector can be achieved through relatively simple standard methods, making it possible to determine the energy and the energy spread to a high degree. Furthermore, a reconstruction of the transverse momenta at the plasma exit can be achieved. The structure of the p_z-p_y closely behind the target is clearly mapped to the detector screen. A detailed analysis of the visible structure is beyond the scope of this thesis.

The a priori required knowledge of the beta function at the end of the plasma channel is of course somewhat unsatisfactory. In the real experiment, one will probably need to scan and tune the beam optics lattice for the highest resolution on the spectrometer screen. (Which is of course challenging, since the beam has a considerable energy spread.) The calculated values should still provide a good starting point for such scans. Clearly, this requires a high stability of the injection mechanism, especially in terms of timing. However, the eSpec is always set for a certain energy, and the resulting beam will jitter around this position. In that sense, the spectrometer also serves as a filter, allowing for the identification of shots which yield central hits and, thus, enable a sorting of the results. Since the bunches leading to central hits should have the right energy, they can be used for the optics adjustment.

If the resolution is not sufficient for detailed analyses, the spectrometer can be extended by a second detector, which is further away from the dipole (see chapter 4.2.2). Another option would be to use a more elaborate spectrometer design, like a concept suggested in [90–92], which is optimized for imaging over a certain energy range. However, such a device should sit close enough to the plasma target to image the source directly, which is impossible at this point in time due to space constraints.

3.6 Parameter Tolerances

In the start-to-end scenario of the previous section, the conditions are taken to be almost ideal – apart from measured magnet field maps. In the experiment, there will be deviations from such ideal conditions, though. There will be jitter sources, like the temporal synchronization of laser and electron gun, or the beam pointing stability of the laser system and its beam transport. Also, systematic errors can occur, such as for example a mismatched beam due to space charge effects in the case discussed above – or deviations in the plasma profile.

Therefore, parameter scans have been performed in order to gain estimates of the impact of *single* parameter deviations at the beginning of the plasma on the resulting beam at the exit. Each input parameter is varied in a separate analysis, so that the resulting deviations at the plasma exit are directly related to this input variation. The goal of these considerations is twofold. On the one hand, it serves the identification of misconceptions which could spoil the experiment realization. On the other hand, it allows for beam line adaptions, so that beams injected under less-than-ideal conditions can still be detected.

ASTRA is used again for the investigations. The scans are done within the usable phase interval of the second bucket, i.e., from $\xi = -381\,\mu\text{m}$ to $\xi = -490\,\mu\text{m}$ which covers about one third of the plasma wave length. The phase interval is sampled in about $3\,\mu\text{m}$ steps, resulting in 41 different phase settings; the three exemplary points used in the previous section lie within this region. The respective input parameter is scanned for each of the injection phases around the optimal case determined in the previous section; space charge is not taken into account to avoid overlaying effects. The resulting output parameters are then compared to the ideal case, using the same notation as in section 3.3:

$$\delta\left[X\right] = \frac{X - X_{\text{ref}}}{X_{\text{ref}}}. \tag{3.21}$$

Based on the phase sampling, 41 results are obtained for each deviating step from a particular reference parameter. To quantify the impact of a certain parameter offset for all phase settings, it is necessary to find a way which combines the output for all phases into one figure of merit for each parameter step.

The first candidates for such quantities are the arithmetic mean and the standard deviation, i.e., the first and second moment of the distributions. However, the meaningfulness of the variance in particular is limited in this case: The resulting distribution is not the statistical fluctuation around a measuring point. Instead, for each phase, a direct relation to the input parameter is given. Furthermore, the distributions tend to be highly asymmetric. Especially the phases close

Interval	Lower Percentile	Upper Percentile
50 %	25 %	75 %
80 %	10 %	90 %
90 %	5 %	95 %
100 %	0 %	100 %

Table 3.5 – Definition of the percentile-intervals in figures 3.28 to 3.34.

to the interval boundaries can have large deviations from the majority of data points, meaning that the mean and variance can get extremely large by only a few outlying points. Of course, this is also caused by the small number of sampling points, based on the steps of about three degrees in the preceding start-to-end simulation.

Therefore, another measure is additionally used, which is less sensitive to the influence of these outlying points, and in addition provides a method to determine the symmetry of the distribution: The median, combined with so-called percentiles [93, 94]. The median of a distribution simply separates the higher half of numbers from the lower half. This means the same amount of sample points is located on the left side of the median as on the right. In a similar manner, the first quartile is the intersections where 25 % of the distribution have a lower value and 75 % are larger. The third quartile marks the exact opposite: 75 % of the values are below that boundary, and the rest above [95]. The median in that sense is the second quartile. The percentile is a generalization of that definition to arbitrary percent ratios. These measures directly include possible asymmetries in the distribution, since for example the first and third quartile are specified to be lower/higher than the median – in contrast to the standard deviation, which does per se not tell anything about the distortion of the distribution and the direction of deviations. (This would be contained in the third moment, also called the skewness.) Also, the percentiles provide an estimate how many bad points lead to the deviation.

In the graphs of this section, the following percentiles are used and combined: The median gives the trend, while the first and third quartile mark the upper and lower boundary of the region into which half of the deviations fall. The 80 % region is likewise defined by the 10 %-to-90 % span, to the median. The other intervals are similarly defined by such symmetric borders; please see table 3.5. The processing of the data by this method thus combines the 41 results into a trend line, which is less sensitive to possible large deviations of single outliers compared to the mean value. Also, the number of outliers and the shape of the distribution of the results is included. The graphical illustration can be treated similar to level curves, giving the number of cases within the respective interval.

The following analysis is divided into two parts. The first one concerns errors which lead to transverse symmetric deviations while the second one deals with errors that result in different deviations in the horizontal and vertical plane. The reference values are taken from the *ideally* matched case in section 3.4. The value is determined at the entrance of the plasma channel. The resulting beam parameters are obtained at the end of the channel.

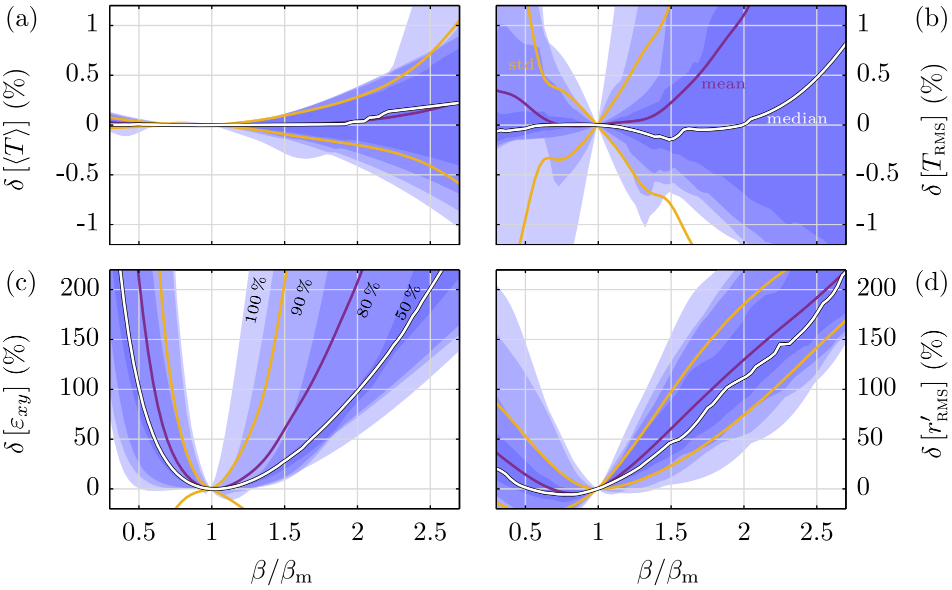

Figure 3.28 – Variation of the beta function at the beginning of the plasma with respect to the matched parameter, β_{m}. Only symmetric quantities are influenced. The main deviations occur in the emittance (c) due to a mismatched beam, and tied to this an increased divergence (d). The relative changes in the mean energy (a) and the RMS energy spread (b) are on a percent level or less. The shaded areas marking the percentile sections will be kept throughout all tolerance plots in the following; the percentage values apply to these areas. The mean, as well as the standard deviation are plotted for reference. 41 equally spaced phase settings in the range of $\xi = -381\,\mu\mathrm{m}$ to $\xi = -490\,\mu\mathrm{m}$ have been analyzed and are depicted in the distributions illustrated by the percentiles.

Beta Function and Correlation Parameter

The first parameter to be varied is the beta function at the start of the plasma. Consequently, this leads to a mismatch of the beam, compared to the reference. Since the focusing elements before the plasma are only solenoids, the deviations should by symmetric, i.e., the radial beam shape is scaled, but not deformed. The radius is varied within a range, starting with a factor of 0.5 and ending with 2.5 times the initial value. The output should be symmetric as well, since the plasma fields obey the same symmetry. Thus, only four quantities are analyzed: Mean kinetic energy $\langle T\rangle$, energy spread T_{RMS}, transverse emittance ε_{xy}, and divergence x'_{RMS}. As can be seen in figure 3.28, the first two (longitudinal) quantities are not influenced, as for e.g. $\langle T\rangle$ varies by less than 1 %. The median of the energy spread is also in that range. However, there are fluctuations of a few percent. The emittance, however, is drastically increased by the mismatch. This applies to both cases, if the beam size is either too small or too large. An increase of β by a factor of two also doubles ε_{xy}. Likewise, the divergence is increased by a factor up to two. Since the RMS emittance is given by $\varepsilon_x^2 = \langle x^2\rangle \langle x'^2\rangle - \langle xx'\rangle^2$ [compare (2.5)], but scales similar to the divergence this means that there are no additional correlations added by the mismatched plasma passage.

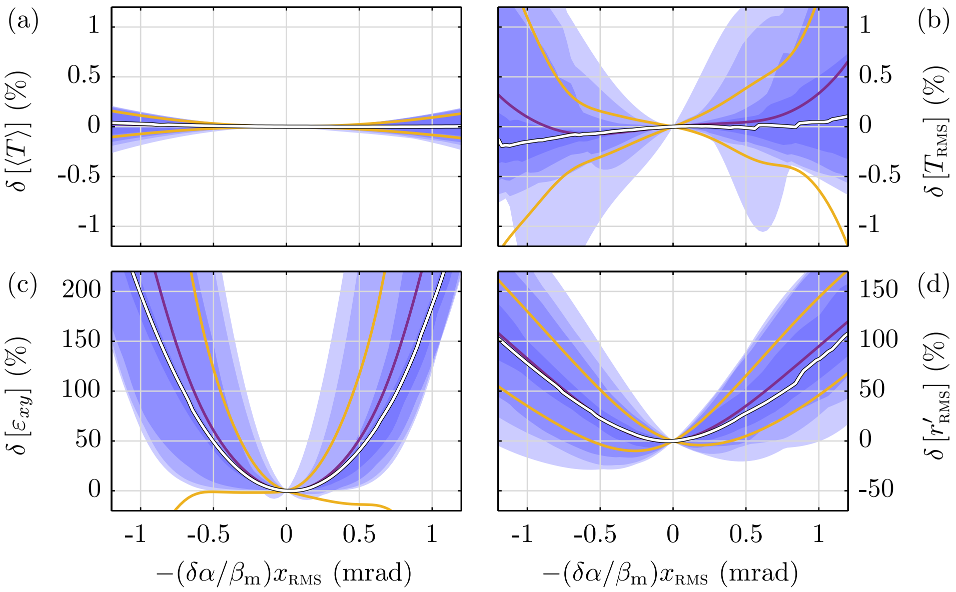

Figure 3.29 – Dependencies of the symmetric beam quantities on the correlation coefficient, α. The longitudinal parameters, i.e., mean energy (a) and RMS energy spread (b) show no considerable influence, the emittance (c) and divergence (d) are increasing. (Basically, a change in α also amounts to a mismatched beam.)

As a side note it should be mentioned that the emittance behavior is an example for the shift of the mean by outlying parameters with respect to the median, showing the highly asymmetric distributions and large influence of those outliers.

The behavior of all four quantities is as expected. The beam size at injection should not alter the energy parameters greatly because the phase is unchanged. The emittance must, of course, grow, since the beam is no longer matched, as discussed in section 3.2. In the matching analysis of the previous chapter, a similar emittance growth for the real beam could be observed. It was, however, weaker than figure 3.28(c) would suggest. A direct comparison of the two graphs is not valid, though. In the previous chapter, the beta function of the virtual focus was analyzed, while in this discussion, the beta function is taken at the beginning of the plasma, instead.

The increased emittance is attributed to a similarly increased divergence, which enters the calculation of ε_{xy}. For the experimental situation, these increases are, however, not as bad as one could assume: An increase of the incoming emittance by a factor of two is still on the 100 nm rad level. Finally, the divergence increases to a few mrad, and should so be transportable towards the detector without considerably beam loss.

A change of the correlation parameter, α, shows a very similar behavior; see figure 3.29. It is depicted in figure 3.29. In the end, it also changes the beta function at the matching point, which means that the results are comparable. In this case, the linear phase space correlation, $-(\alpha/\beta)\,x_{\mathrm{RMS}}$, has been varied within ±1 mrad. Since the reference value is not zero, the behavior

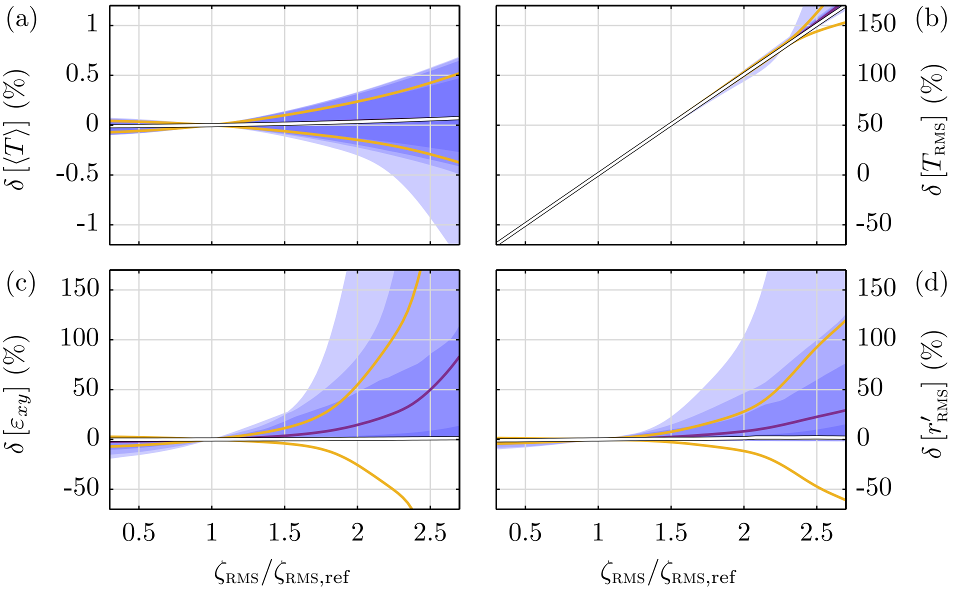

Figure 3.30 – Variation of the electron bunch length. The RMS energy spread (b) is influenced most, while the mean energy (a), as well as the transverse emittance (c) and the divergence (d) stay constant for the main part of the analyzed phase interval. Certain outliers can be explained by parts of longer bunches reaching into the defocusing regions.

is slightly asymmetric. Again, this has almost no influence on the energy parameters and only causes an increase of the transverse quantities by a factor up to two. Hence, although the beam is not perfectly matched, it should still be measurable within these boundaries.

Bunch Length and Arrival Time

The bunch length is the next parameter to be screened. Again, the assumption is that no asymmetric effects will occur. The results are shown in figure 3.30. There is no deviation in the energy, since the phase is unchanged. The energy spread, thought, shows a clear dependence: Since a longer bunch covers a larger phase interval, it, thus, accumulates a larger correlated energy spread – and vice versa for a shorter bunch. Rearranging the definition of the symbol $\delta[\,\cdot\,]$, one obtains

$$\frac{T_{\mathrm{RMS}}}{T_{\mathrm{RMS,ref}}} = \delta\left[T_{\mathrm{RMS}}\right] + 1, \tag{3.22}$$

which yields that the relative change in $\zeta_{\mathrm{RMS}}/\zeta_{\mathrm{RMS,ref}}$ directly translates into the relative change of the RMS energy spread. For example, at $\zeta_{\mathrm{RMS}}/\zeta_{\mathrm{RMS,ref}} = 2$, the analysis results in $\delta[T_{\mathrm{RMS}}] = 1$ according to figure 3.30(b), and thus $T_{\mathrm{RMS}}/T_{\mathrm{RMS,ref}} = 2$. The change in the energy spread is hence purely due to the correlated contribution added by the wakefield.

In the majority of steps in the analyzed phase interval, emittance and divergence remain unchanged. The median is a constant line, which also covers the 50 % region almost entirely. (It

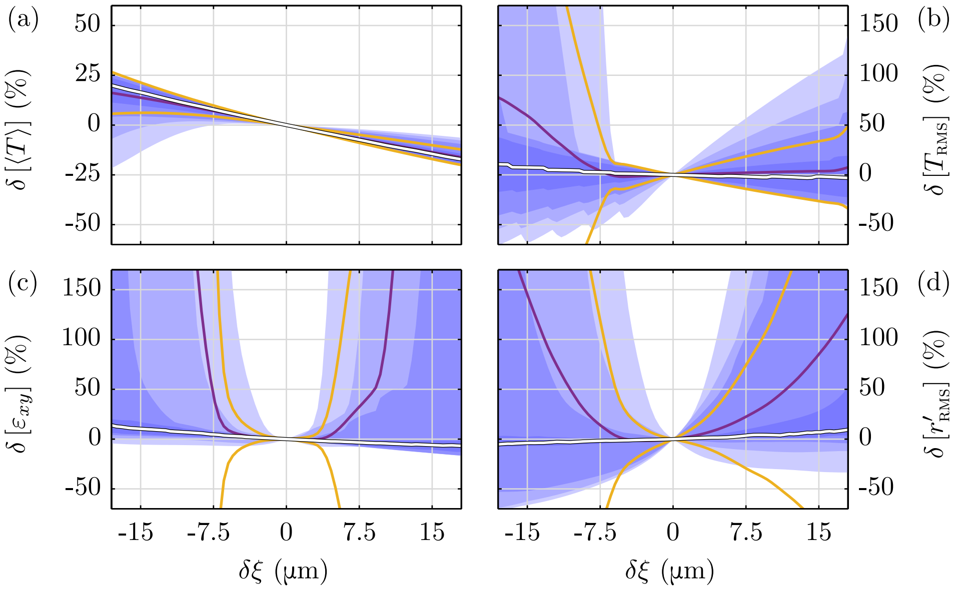

Figure 3.31 – Dependency of the output parameters on the arrival time. As to be expected, the resulting mean energy (a) correlates with the deviating injection phase. The other quantities, i.e., RMS energy spread (b), emittance (c), and divergence (d), are less affected according to the median, but show a larger variation, especially for large deviations in ξ: Here, more and more bunches from the good-field interval enter the defocusing section.

is thus a very peaked distribution.) For larger bunch lengths there are certain outliers, probably caused by parts of longer bunches reaching into the defocusing fields. Also, the increased energy spread will lead to an emittance growth in the subsequent drift. Nevertheless, a variation of the bunch length in the analyzed range does not pose a risk to the experiment.

A major issue in conducting the experiment is the synchronization of the laser with respect to the electron gun. Scanning the plasma wakefield requires a much more stable locking between the systems than the plasma period. According to [33], a few 10 fs should be achievable. Thus, ξ is scanned in the limits of $\delta\xi = \xi - \xi_{\mathrm{ref}} = \pm 15\,\mu\mathrm{m} \mathrel{\widehat{=}} \pm 50\,\mathrm{fs}$. Of course, this will alter the final energy, because it means that the acceleration subsequently happens on a different phase. The deviation is up to 25 % and, thus, larger than the range covered by the eSpec detector. An analytic estimate yields a comparable value: A shift of $\delta\xi = 15\,\mu\mathrm{m}$ corresponds to a phase offset of $\delta\phi = 2\pi\delta\xi/\lambda_{\mathrm{p}} \approx 0.28\,\mathrm{rad}$. The slope of the cosine is maximal around the zero crossing. Approximating the deviation in energy at this point by a Taylor expansion simply amounts to

$$\Delta T \approx A\cos(k_{\mathrm{p}}\xi) - A\sin(k_{\mathrm{p}}\xi)k_{\mathrm{p}}\delta\xi. \tag{3.23}$$

The cosine vanishes, since it is at the zero crossing, while the sine is equal to one. A is the maximum energy gain of the accelerating field, which was determined above to $A = -6.45\,\mathrm{MeV}$ (equation (3.13)). Moreover, the reference energy is $T_{\mathrm{ref}} = T_{\mathrm{in}} = 5.6\,\mathrm{MeV}$, because no mean energy gain is acquired at the zero crossing. From that it follows that

$$\delta\left[T\right] = \frac{T - T_{\mathrm{ref}}}{T_{\mathrm{ref}}} = \frac{\Delta T}{T_{\mathrm{ref}}} \approx 1.2\,\delta\phi \approx 0.3. \tag{3.24}$$

The eSpec screen only covers an energy range of about $\Delta p_z / \langle p_z \rangle \approx \pm 10\,\%$. Thus, the timing is required to be within $\delta t < \pm 25\,\mathrm{fs}$ to resolve every shot. The other way round, the plasma provides a measurement for the level of the synchronization achieved – assuming the wakefield behaves as expected. If the timing is not as good as required, not every shot will hit the detector, which would be unsatisfactory, but does not spoil the experiment.

For the majority of cases, the other three parameters – mean energy, emittance, and divergence – are again almost not influenced and show a slightly linear correlation. All of this is simply based on the phase offset, which leads to a slightly different slope of the field, which in turn explains the altered energy spread. It also accounts for the change in emittance, since the matching condition is calculated for a different phase. The divergence is increased in a similar manner. The latter is, however, only very mildly affected. The emittance change shows that, in principle, the matching has to be adjusted for each phase. Moreover, there are several outliers, which are again caused by bunches being shifted into the defocusing region. (These bunches will not reach the detector in any case.) Here, the advantage of using the median as measure can also be seen: Especially in figure 3.31(c), where the emittance is depicted the mean is artificially boosted to extreme values by only 5 % of the cases, while the majority yields almost identical results.

Spatial Offset and Beam Pointing

Apart from the rotational symmetric input parameter variations, there are two asymmetric deviations which should be analyzed: an off-axis injection into the plasma and the injection with an angular variation. Both scenarios are likely to happen due to pointing instabilities of the laser, which defines the symmetry axis of the wakefield.

Thus, an offset scan has been performed, increasing the distance to the plasma axis from $\langle x_{\mathrm{in}} \rangle = 0\,\mu\mathrm{m}$ to $\langle x_{\mathrm{in}} \rangle = 25\,\mu\mathrm{m}$, which corresponds to about half a laser spot diameter in the focus; the laser (and laser transport) is assumed to provide a stability on that level. The number of quantities to be analyzed increases due to the symmetry breaking. Emittance and divergence have to be treated in both planes, while in addition an offset as well as an angular deviance of the exiting bunch could occur. The results are shown in figure 3.32.

As in the previous cases of an unchanged injection phase, the energy is almost unaffected with changes on the order of 1 % or less. The energy spread is also only mildly affected; the phase interval covered is unchanged, after all.

In contrast, the emittance in the offset plane is rising up to six times the reference value. But it is still below $\varepsilon = 1\,\mu\mathrm{m\,rad}$, taken a reference value of about $100\,\mathrm{nm\,rad}$. Of course, an influence of the emittance was to be expected.

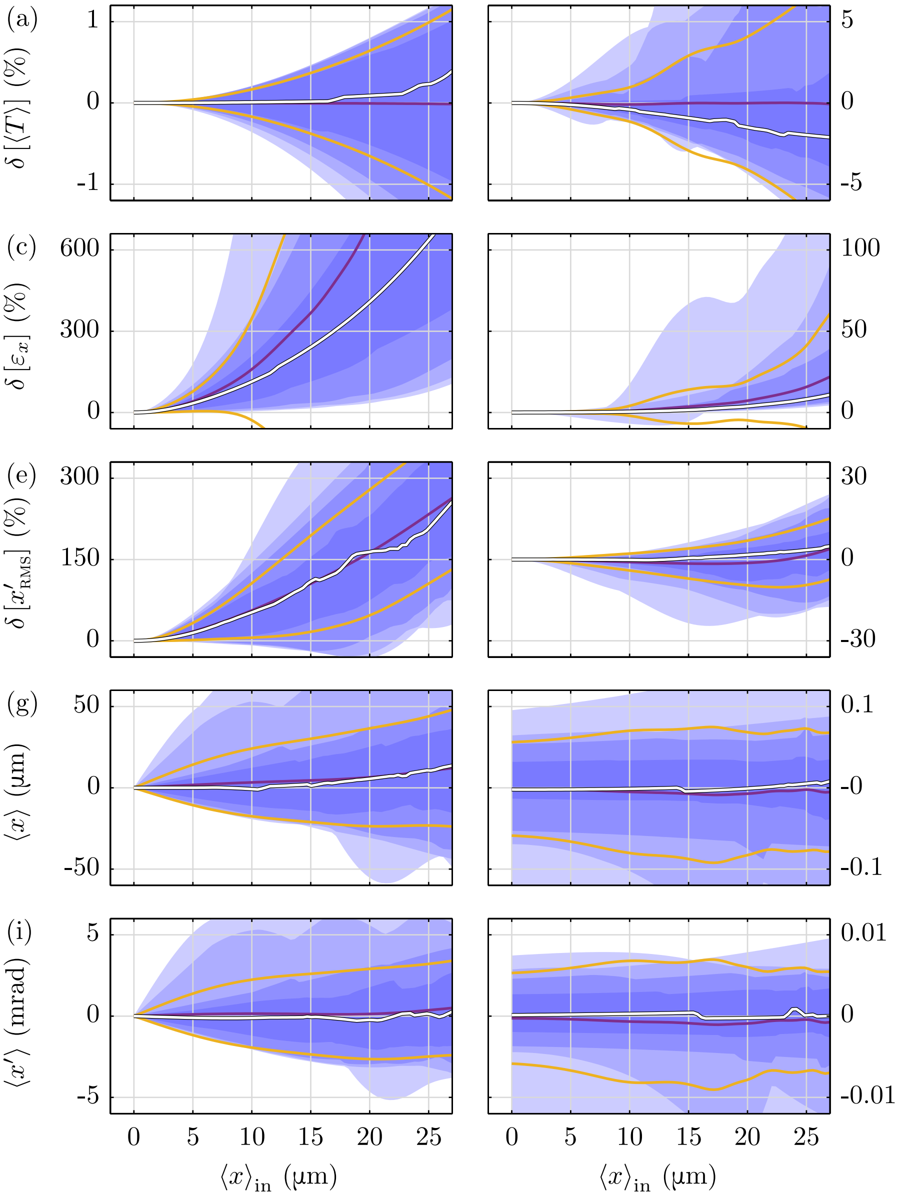

Figure 3.32 – Deviations caused by an off-axis injection in x-direction. Emittance (c) and divergence (e) in the off-axis plane show a great dependence, while the influence of the respective quantities (d,f) in the other plane is much less. The same holds true for the resulting off-set (g,h) and beam pointing (i,j); these quantities are almost unaffected in the y-plane. The changes to the mean energy (a) and the RMS energy spread (b) are on the level of a few percent only.

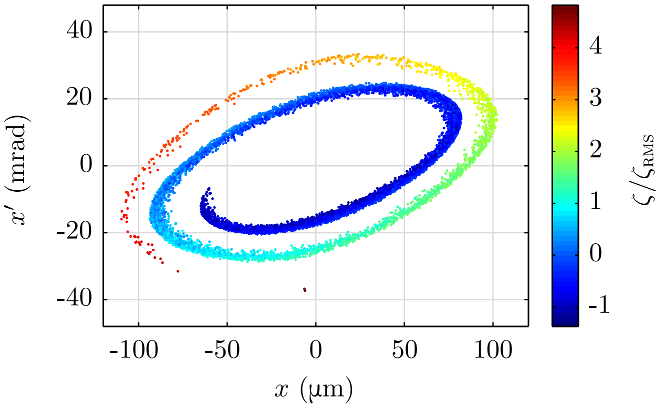

Figure 3.33 – Phase space distribution for an off-axis injected particle bunch into a plasma wakefield. The beam is injected at a decelerating phase. Due to the additional dipole component, the beam wiggles around the symmetry axis given by the plasma. Since the dipole strength varies along the bunch, the beam is pulled apart. The change in energy changes the influence of the plasma fields and thus the amplitude of the oscillations. The combination of these effects results in a spiralized phase space distribution.

An off-axis injection means that the bunch as a whole sees a deflecting force towards the symmetry axis defined by the laser. The deflection can be described by an additional dipole component present on top of the focusing term, analogous for example to an off-axis passage in a quadrupole magnet. The bunch acquires transverse momentum and starts to wiggle around the symmetry axis of the wakefield. In the phase space picture this means that the whole bunch now rotates on an ellipse, the center of which is defined by the laser axis. Like in the case of the focusing forces, the dipole component varies along the bunch, and hence the associated rotation speed in phase space is different for the separate bunch slices. As a result, the phase space distribution is pulled apart – an analogous effect to the fan out of the slice emittance ellipses discussed in section 3.2; [39, 57]. The effect can be seen in figure 3.33. If a bunch is injected on purpose in such an off-axis configuration, the correlation of the transverse fields strength with the longitudinal position can be exploited to build a plasma-based diagnostic similar to a transverse deflecting structure [63, 96]. The plasma interaction must be limited to dimensions much shorter than an oscillation period for this application.

The additional spiralization in the phase space of figure 3.33 is attributed to the change in energy of the bunch. The action of the deflecting forces depends on the inverse of the Lorentz factor γ, and thus, the acceleration of the beam changes the dipole strength for each slice. Therefore, the amplitude of the oscillation is no longer constant. In the case of figure 3.33, the bunch is decelerated, so that the dipole component is increasing, and hence the amplitude gets smaller. That is, the beam spirals around the plasma axis defined by the laser. The RMS emittance of such a structured phase space distribution is consequently increased compared to the initial shape.

In the vertical plane, the emittance increases only very slightly for the majority of cases. Just some outliers reach values of several 10 % and more. In this plane, the focusing is still symmetric with respect to the bunch position. But, due to the transverse oscillation of the bunch as a whole in the horizontal plane, that focusing force gains an additional breathing, so that the matching is getting spoiled. Yet, the effect is rather small.

Looking at the divergence, there is a similar behavior to the one described for the emittance. In the x-plane, there is a huge increase, up to the double of the reference value, while the y-plane is influenced much less. The explanation for this is the same as for the emittance discussion: The transverse wiggling in the offset plane changes the momentum distribution which *is* the divergence. In the second plane, the mismatch manifests due to the different – but still symmetric – forces.

The offset at the exit is almost symmetric with respect to the plasma axis: In this case, the absolute value is plotted – including the initial offset. However, the mean and median values are below this initial offset. This can be attributed to the oscillation potential, which has its minimum at the symmetry axis of the wakefield. That is, despite the offset injection, the rest position of the oscillations is still the plasma axis. The exit position depends on the oscillation period, which is in turn connected to the forces acting. These, however, vary across the different injection phases. And thus, the exit positions will be distributed around the plasma axis, rather than around the offset axis at injection. Still, a slight trend of the offset is also visible, but is is not even half of the initial offset at injection. Importantly, the resulting offsets are small enough, so that there does not occur a clipping of bunches at the walls of the plasma target. The y-plane is not affected at all, which is to be expected due to the symmetry.

The angular deviation of the bunch at the exit of the plasma due to an offset injection shows a similar behavior to the resulting offset at the plasma exit. In the vertical plane, figure 3.8(j), there is no influence. But, in x, the bunches are expelled, almost symmetrically distributed with respect to the beam axis, with a standard deviation of up to $\langle x' \rangle_{\mathrm{RMS}} \approx 3\,\mathrm{mrad}$. The behavior is likewise explained by the betatron oscillations, the whole bunch experiences. The magnitude of the angular deviance seems to be manageable, except when the offsets are too large: In combination with the associated beam divergence, the beam transport gets critical, due to possible particle loss at the beam pipe.

As a side note, due to the acceleration also adiabatic damping effects can be expected. In the case of an acceleration, the divergence is decreased since the ratio of transverse and longitudinal momentum is decreased [64, 65]. At the same time, the deflecting and focusing forces decrease due to the scaling with $1/\gamma$, leading to larger oscillation amplitudes – which is coupled to a reduced divergence as well. For the decelerating phases these effects are reversed. Hence, the effects are expected to be less critical for the accelerating part of the wakefield.

Finally, the injection under an angle is analyzed, see figure 3.34. The injection point in this case is on the symmetry axis and the rotation is in the x-plane. The energy is – once again – not influenced. Also the energy spread is only very mildly affected for larger angles. The quantities in the y-plane also do not see great effects, since in this case, the symmetry is unspoiled. The minor variations in the symmetric transverse quantities, i.e., ε_y and y'_{RMS}, can be attributed to the additional deviation in the focusing forces due to the betatron motion in the x-plane: Due to the angle between laser axis and electron trajectory, the whole bunch drifts off-axis, until

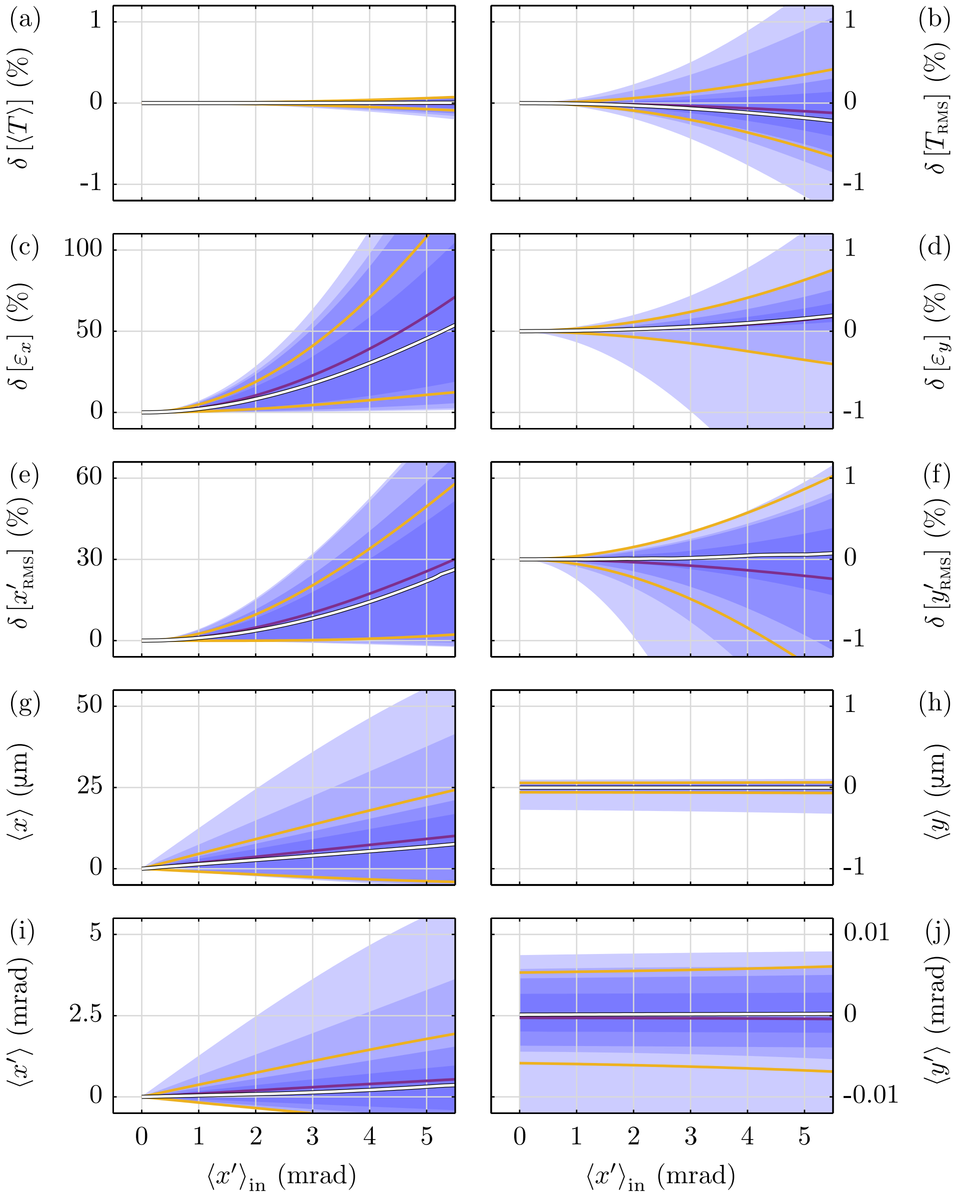

Figure 3.34 – Beam parameter changes for an angular deviation in x-direction. Mainly the values in the x-z plane are influenced, i.e., emittance (c), divergence (e), offset (g), and beam pointing (i). The respective quantities (d,f,h,j) in the y-z plane show very little changes. The mean energy (a) and the RMS energy spread (b) are also almost unaffected.

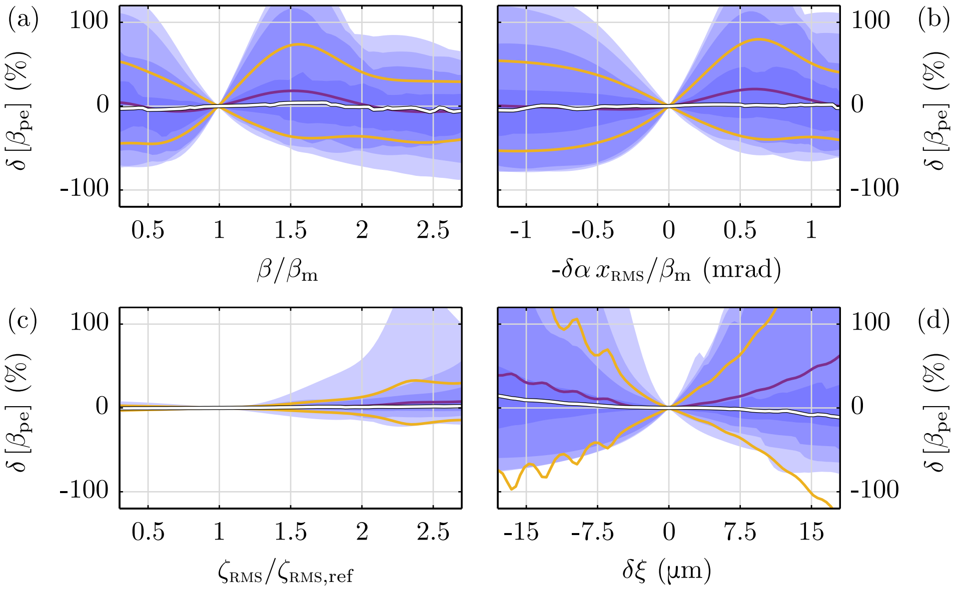

Figure 3.35 – Deviation of the beta function at the end of the plasma channel for the variation of symmetric input parameters, i.e., the beta function at the plasma entrance (a), the correlation parameter (b), the bunch length (c), and the injection phase (d). Mean and median of the distributions are close to zero. For most cases, the deviations are on the order of a few 10 % or less.

the transverse momentum is overcome, leading to a similar situation like in an off-axis injection scenario discussed above. Hence, the same pattern results in the x-quantities: The emittance and divergence increase, but to a manageable degree.

Since there is an overall transverse momentum present in the bunch distribution, there exists an additional asymmetry. This manifests in the asymmetric distributions of final offset and angle, which clearly follow the trend of the input angular deviance. Since the transverse momentum is not zero, the beam has a mean drift away from the axes around which it oscillates. The parameters gained from this trend analysis are not dramatic, and, in addition, the laser pointing jitter is expected to be on the order of 100 µrad; see chapter 4.

Beta Function for Beam Transport

In this context, one should also investigate the development of the beta function at the plasma exit, β_{pe}, since this parameter defines the beam size and resolution at the spectrometer. Figures 3.35 and 3.36 show the results for all parameters varied in this section. In the first figure, the symmetric cases are depicted, while in the second one the asymmetric parameters are plotted. The variation of the beta function in all cases is typically below a factor of two. Thus, according to the analysis in the previous chapter, figure 3.26, the beta function should not degrade the resolution to an unfeasible value. One should, however, keep in mind that also increased emittances will

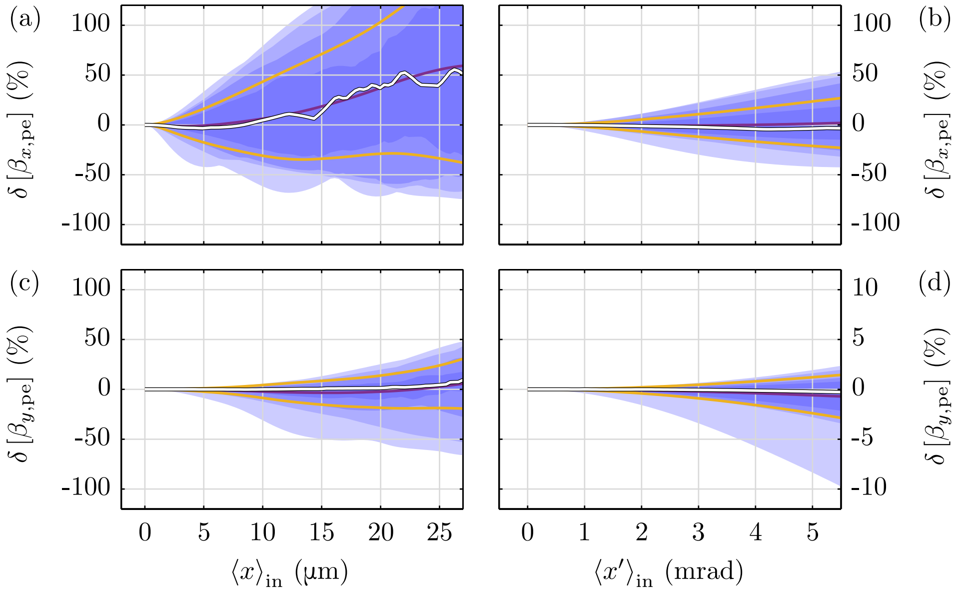

Figure 3.36 – Deviation of the beta function at the end of the plasma channel for an off-axis injection (a,c), and an angular deviation (b,d). For the latter, no considerable increase in the beta function is determined in both planes. For the offset, an increase of median and mean by about 50 % can be observed in the offset plane (a). A few cases show enhancement by more than a factor of two. Still, the image quality at the eSpec should be sufficient.

enlarge the spot size at the eSpec screen. Hence, especially transverse offsets should be minimized as best as possible.

Conclusion

For the analyzed parameters, it follows that especially deviations in arrival time and spatial offsets have a considerable impact on the beam parameters at the exit of the plasma channel. Sources for such deviations are mainly identified to be the timing jitter between ANGUS and REGAE and the pointing instabilities of the laser, respectively. Therefore, a high degree of stability in terms of synchronization – ideally (much) better than 25 fs on target – is mandatory. Likewise, a minimization of laser pointing jitter is essential, so that the transverse focus position fluctuates less than half of the laser focus size. The latter possibly requires a stabilization concept for the laser transport beam line, for example using fast, piezo-based adaption of the mirrors to the signal of a high repetition rate pilot laser beam [97]. Fluctuations in the beam path of the 5 Hz ANGUS pulse could be reduced by this method. However, the laser stability on target has not been measured yet. A final conclusion regarding this instrumentation can thus not be made at this point in time.

In case the stability of this jitter sources cannot be increased to the required level, the experiment can still be executed. However, it is necessary to acquire a large statistics, so that the impact of the fluctuations is reduced by averaging over the results for each nominal injection settings. This also allows for a sorting of the results with respect to the reference given by the average. Furthermore, it provides a measure which makes it possible to identify and exclude strongly deviating shots resulting from large fluctuations. If, in addition, the fluctuations can be measured independently, a correlation with the respective single-shot spectra is possible.

For the timing, in the worst case, not every shot is successfully recorded by the eSpec detector, since it is only this parameter, for which the energy shows a significant variation. An on-target arrival time diagnostics is planned, which enables a sorting of the results and the attribution of lost shots. This, however, depends on the resolution of this so-called beam arrival cavity, which is still under development. Asymmetric injections, in particular transverse offsets resulting from the pointing jitter of the laser, could be more problematic. The large emittance growth due to phase space mixing and spiralization can spoil the measurement, because of the enlarged image at the eSpec detector. However, the spiralization shows a clear dependence on the longitudinal bunch coordinate, meaning that the image at the eSpec will show an oscillating pattern, that might be clipped due to the amplitude of this oscillation, but still can be attributed to this effect. The imaged structure thus reveals the spiralization, and allows for a sorting of these shots and moreover for an analysis of this effect. Also here, it may happen that some shots are lost, but the impact can be overcome by a sufficiently high statistics. Furthermore, the post-plasma laser diagnostics is planned to record the final pointing direction, allowing for a correlation of the results with the pointing jitter.

For the non-jitter deviations, like a mismatched beta function, the influence on the beam quality is weaker. And since these errors are systematic, parameters can be optimized by scans, for example, minimizing the beam spot in the dispersion plane of the eSpec. This approach is of course hampered – but not spoiled – by the possible high statistics required due to fluctuations based on temporal and spatial jitter.

Especially the average energy can by determined in almost any scenario, because this parameter is only notably influenced by the beam arrival time. Apart from that, an image larger than the detector screen hampers the measurement of the energy spread. Thus, the first experimental campaign, which will be dedicated to the final energy depending on the injection phase, should be realizable. The experience gained from that can then be included in further investigations.

4 REGAE Beamline Upgrade

Knowing the key constraints to the external injection experiment from the concept and analysis presented in the previous part of this thesis, the required adaptions of the REGAE beam line to the demands of the experiment can be described in the following chapter. Apart from the REGAE front-end, which contains the accelerating structures, the whole beam line will be rebuilt.

The following description is structured according to the sections of the whole setup. First, the laser which has to be included into the system, as well as the required laser transport beam line will be introduced. This part has been developed by members of the LUX team [25]. The planning and design of the electron beam line, which is presented afterward, was part of this Ph.D. project. In particular, the interaction chamber and the differential pumping scheme developed in the course of this work are thus discussed in detail.

4.1 Laser

The ANGUS laser system is housed close to the REGAE facility. ANGUS is a titanium sapphire (Ti:Sa) based high-power laser system providing pulses up to 200 TW at a repetition rate of 5 Hz. The amplification of the light pulses to energies of about 5 J is accomplished in an amplifier chain based on the chirped pulse amplification technique [2]. After the final compression, the pulse has a duration of 25 fs. The transverse intensity profile at this stage is of a super-Gaussian shape of eighth order with a $1/e^2$ beam diameter of $W_{1/e^2} = 76\,\mathrm{mm}$, as already discussed in chapter 3.3. The main parameters of the laser system are summarized in table 4.1.

The laser is a commercial system with a focus on availability and stability. In order to maintain and improve the already outstanding performance, the laser group has implemented a multitude of diagnostics and automations. Being attached to an accelerator center, the philosophy is to treat the laser like a klystron[1] [98]. In accordance with this underlying idea, all diagnostics, as well as the automatization and feedback systems are implemented in the standard DESY accelerator control system.

The system is mainly used for two purposes. On the one hand, it serves the LUX experiments [25], where the focus lies on self-injection based LWFA, and the application of these accelerators. Especially LWFA-driven x-ray light sources are on the agenda of this experimental campaign, basing on the previously achieved results: the generation of LWFA driven undulator radiation at a wavelength of $\lambda = 17\,\mathrm{nm}$ [17, 18] as well as the stabilization and advancement of this source towards higher photon energies at $\lambda \approx 4\,\mathrm{nm}$, which lies in the so-called water-window [19, 20].

---

[1] A klystron delivers the rf pulses powering conventional accelerating structures.

Parameter	**Value**	**Remark**
peak power	200 TW	
pulse duration	25 fs FWHM	minimal
repetition rate	5 Hz	
pulse energy	5 J	
relative energy stability	1.5 % RMS	over 500 shots
contrast ratio	$10^{10}:1$	at 100 ps
	$10^{8}:1$	at 10 ps
central wavelength	815 nm	
spectral bandwidth	40 nm FWHM	
Strehl ratio	0.9	
beam pointing stability	3 µrad RMS	over 500 shots
beam profile	super-Gaussian	8th order
beam diameter	76 mm	$1/e^2$
REGAE Beam Line Specific		
pulse duration	100 fs FWHM	beam damage limit
effective focal length	4.2 m	
Rayleigh length	3.1 mm	simulation
focus position stability	25 µm RMS	assumptions
focus pointing stability	100 µrad RMS	assumptions

Table 4.1 – Main performance parameters of the ANGUS laser system [78] and pulse properties in the focus at the REGAE beam line. The lengthened laser pulse in the REGAE case is necessary to stay below the damage threshold of the coating of the last mirror before the focus.

The ultimate goal is the demonstration of a laser-driven free-electron laser [19, 21, 22]. Once again, the main objective is to improve the LWFA technique so it becomes a usable and reliable tool.

The other experiment ANGUS is planned to be used for is the external injection campaign described in this work. Since there is naturally a big overlap of the experimental environment and demands, there is, of course, also a big overlap of design concepts and a constant exchange of ideas with the LUX group. Lastly, both systems are LWFA-driven with a focus on reliability and stability and connected to the same laser, which in turn is attached to the same vacuum system of a conventional accelerator. Hence, both experiments have a lot of problems in common, resulting in joint efforts to find solutions for them. The presented results are based on a very fruitful collaboration with the LUX group [25].

4.1.1 Laser Transport Beam Line

The last element in the ANGUS amplification chain is the grating based compressor. At the same time, it is the first segment of the **L**aser **T**ransport **B**eam **L**ine (LTBL). Like the whole LTBL, the compressor is part of the vacuum system, in contrast to the amplifier chain, which is operated in air. Since the accelerating cavities of REGAE are located at the other end of that tube system, it needs to be compatible with DESY vacuum standards [27]. This approach is in line with the intent to build and set up a reliable (laser) system.

The LTBL is depicted in figure 4.1. From the compressor onwards the pulse is transported over a distance of about five meters. There it passes the so-called switch yard, where the beam can either be sent to the experiments in the LUX tunnel or to REGAE. On the second route, which has an approximate length of 30 m, there are seven turning mirrors. The mounting of the mirrors, as well as the chambers and the support were carefully designed in order to minimize the influence of external vibrations [99]. Furthermore, at each mirror, the position and pointing direction of the laser pulse can be determined by the analysis of the leakage signal through the deflector. Additionally, four of the turning mirrors are motorized, so that the laser beam alignment can automatically be adjusted and monitored.

At the end of the LTBL, the chamber for the final focusing parabola is mounted. It is named MBA and based on the design of its big sibling installed at the LUX beam line, especially the sophisticated parabola alignment based on (motorized) universal joints [100]. The 12.5 deg off-axis parabola has an effective focal length of $f = 4.2\,\mathrm{m}$; the focus position can be shifted by about $\pm 20\,\mathrm{mm}$ by an according shift of the parabola. Just like in the turning mirror chambers, position and beam pointing can also be diagnosed at this essential spot.

From the MBA onwards the beam size reduces. However, it still has to pass one mirror, located in the so-called **I**ncoupling **C**hamber (**R**EGAE), ICR, which is the entry point into the REGAE beam line; see figure 4.2. From there on, electrons and photons travel along the same pipe. This has some peculiar implications. First of all, it leads to the *overtaking problem* discussed in chapter 3. The necessity of the 2.8 m long co-propagation towards the focus results from the damage threshold of the ICR mirror coating: The beam has a diameter of about 50 mm at that

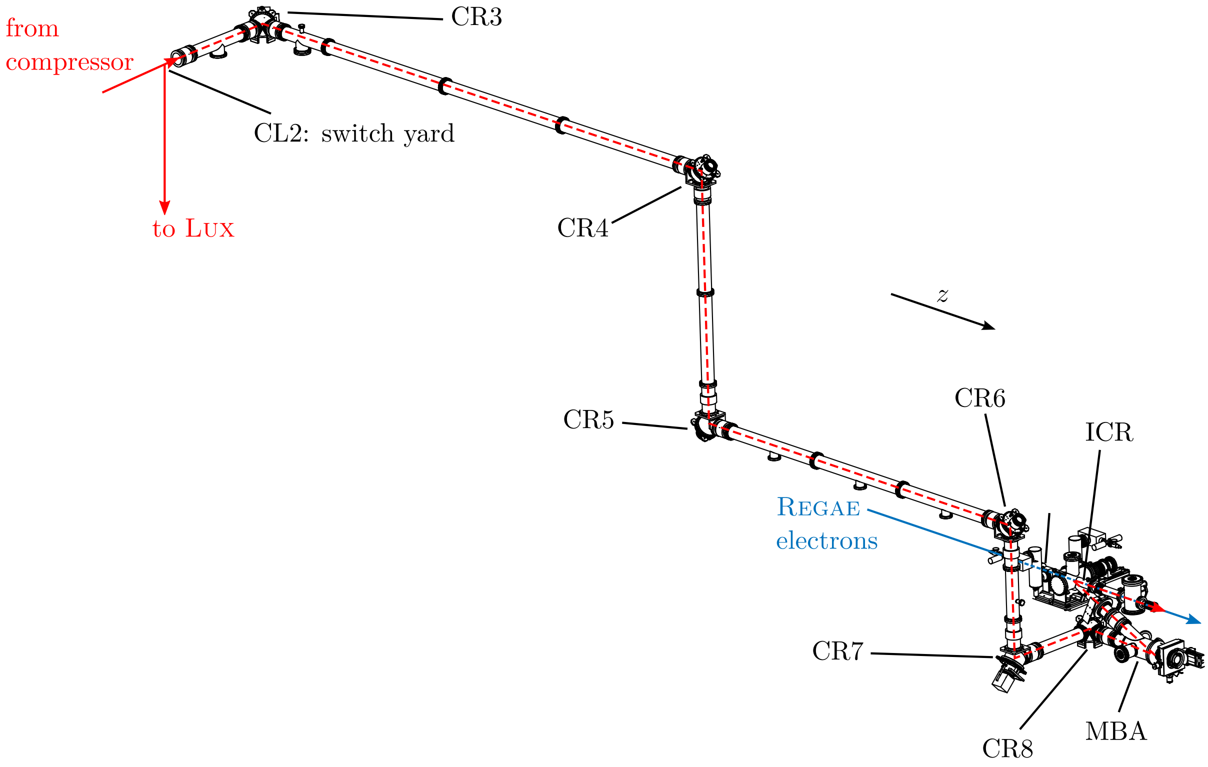

Figure 4.1 – Laser transport beam line from Angus to Regae. The turning mirror chambers are labeled by CR3–CR8. The MBA houses the final focusing parabola while the laser enters the Regae beam line at the ICR. Concept by the Lux team [25] and D. Kocoň (ELI Beamlines. Prague, Czech Republic).

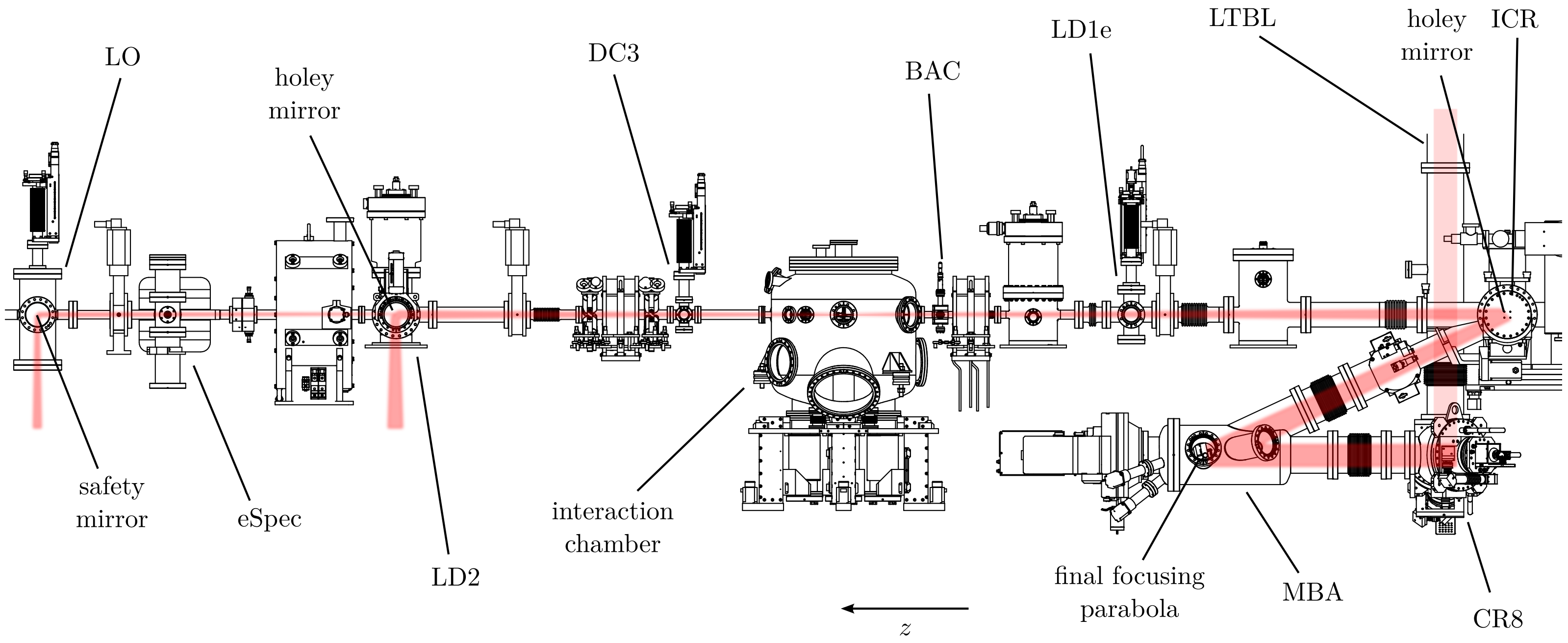

Figure 4.2 – Path of the Angus laser beam in the Regae beam line shown from the side.

BAC: **B**eam **A**rrival **C**avity — CR8: **C**hamber **R**egae **8** — DC3: **D**iagnostic **C**ross **3** — eSpec: **e**lectron **Spec**trometer — ICR: **I**ncoupling **C**hamber **R**egae — LD1e: **L**aser (and **e**lectron) **D**iagnostics **1** — LD2: **L**aser **D**iagnostics **2** — LO: **L**aser **O**ut — LTBL: **L**aser **T**ransport **B**eam **L**ine — MBA: **M**ini **BA**.

point and, thus, about 2.5 times the intensity as compared to the mirrors in the LTBL. This is close to the damage threshold of the already optimized coating, leaving not much room for possible transverse intensity fluctuations and hotspots. However, a coupling into the beam line further upstream towards the cavities is not possible, since there is no space, and even if it were possible, the beam would be clipped by the cavity irises.

This problem of intensity is also the reason for the lengthening of the pulse to 100 fs, since the company providing the mirror does not have specifications for standard ANGUS parameters, and thus cannot guarantee the suitability. However, the scaling of the wakefield strength with pulse length is rather weak: On the one hand, one looses a factor of $\sqrt{4} = 2$ in terms of a_0, but on the other hand, the wake is driven closer to the resonance, which almost compensates for this, so that the amplitude of the wakefield is nearly the same [3, 39]. A reduction of the focal length instead is not an option. In this case, the Rayleigh length would be shortened, so that the accelerating region would be reduced, as discussed in the previous chapter.

The mirror in the ICR has to have a hole of a diameter of 5 mm for the electrons to pass through it; (for this reason, this special deflector goes by the name of *holey mirror*). To avoid charge up effects due to dark current electrons from REGAE being dumped into the mirror material, a thick collimator is located upstream of the mirror substrate, so that the electrons are stopped before they reach the substrate. Charge concentrations inside the mirror would lead to a static field, possibly influencing the accelerator's electron beam, and in the worst case also could lead to the mirror breaking because of uncontrolled discharge.

The effect of the holey mirror on the focus quality has been analyzed by [61]. Since the hole cuts a fraction of the beam, deviations from the sinc^2 distribution are possible. The analysis using ZEMAX [77] shows slightly enhanced wings of this distribution. In order to also measure and verify the difference, it was decided to add a second mirror without a hole, but with identical parameters. This, of course, requires the mirrors to be motorized. However, this was planned all along: The holey mirror reduces the aperture for the electron beam, meaning it needs to be removed if it poses a problem for the other experiments at the REGAE beam line; see chapter 4.2.1. In addition, if the mirror charges up – despite the precautions to avoid this – it is inevitable to remove the item from the beam path.

The next chamber within the joint beam line section that is relevant for the laser is a vacuum cross – LD1e: **L**aser (and **e**lectron) **D**iagnostic **1** – containing a so-called wedge which can be driven into the beam path and deflects a fraction of the laser pulse towards the pre-target laser diagnostics table. With this diagnostics stage, the lasers caustic and intensity profile can be analyzed close to the focus. Without the wedge, the beam travels towards the target chamber, where it enters the hydrogen filled gas cell and creates the desired plasma wakefield. In order to properly align the beam, there are also several sapphire screens close to the target to allow a determination of the beam position and axis; see also section 4.2.2.

Behind the target section, the beam is decoupled from the beam line at the **L**aser **D**iagnostic **2** chamber (LD2). Once again, a holey mirror is used at this point, so that the electrons can pass this deflector, since the electron spectrometer has to be located further downstream. The mirror is about two meters behind the target and, thus, even closer to the laser focus than the

ICR deflector. Hence, it is subject to an even higher fluence. Of course, it would be preferable to first deflect the electrons and then mirror out the complete laser beam, but the beam line diameter is reduced to a size smaller than the laser beam diameter behind the present position of the mirror owing to the requirements of another experiment. The **e**lectron **Spec**trometer (eSpec) also cannot be shifted closer to the target, since there is either not enough space or, where there is space, the eSpec chamber does not have a wide enough aperture for the laser. Thus, the mirror position cannot be shifted, leading to the unfavorable situation described, completed by a second simple (safety) mirror behind the eSpec inside the **L**aser **O**ut cross (LO). The mirror deflects the remaining fraction of the laser pulse, in order to safely dump the photons and protect the diffraction detector located further downstream.

The main diagnostic for the laser is located at LD2. The pulse is weakened by the reflection at several wedges and then sent to the diagnostics table. Here, the laser profile after the interaction is analyzed – as good as possible despite the second hole, which will have an influence, of course. (Also here, a variant without whole is planned, to analyze that effect.) Furthermore, beam parameters like pointing direction, position, spectrum and especially the pulse length will be diagnosed, using the FROG technique [101]. The laser diagnostics is a copy of the version used at LUX, but has not been finalized yet. Thus, it is still subject to changes.

A redundant safety and control concept is required to ensure that all relevant mirrors are in the right positions: It is important, that the laser only can be sent in, if all three mirrors are driven in the REGAE beam line, while electrons only are allowed if no or only holey mirrors are in. Joint operation is only possible with the combination of holey mirrors and safety mirror.

4.2 Electron Beam Line

4.2.1 REGAE

The **R**elativistic **E**lectron **G**un for **A**tomic **E**xploration (REGAE) is a small conventional, yet novel, accelerator designed to deliver low charge, ultra-short high quality electron pulses. The machine consists of two accelerating rf structures: the electron gun and the buncher cavity, both operated in the S-band at 3 GHz. The front-end of the machine is depicted in figure 4.3.

The electron gun is a scaled version of the electron source used at the FLASH[2] accelerator, which is operated at a different rf frequency. It is a so-called photo gun, meaning that the electron bunches are produced by use of the photoelectric effect of a laser pulse shining on the photo cathode. The cathode plane marks the origin of the accelerator coordinate system. The particle cloud, which is released by this process, mimics the shape of the triggering light pulse. By this means, a high level of control over the initial electron distribution is achieved, for example enabling the beam quality that is required for the operation of an FEL like FLASH or the European XFEL. Also, other beam manipulations, as discussed in the next chapter, are enabled by these electron sources. In the case of REGAE, the electrons are released by frequency tripled Ti:Sa laser pulses

---

[2] FLASH is a (conventional) soft-x-ray FEL facility operated at DESY.

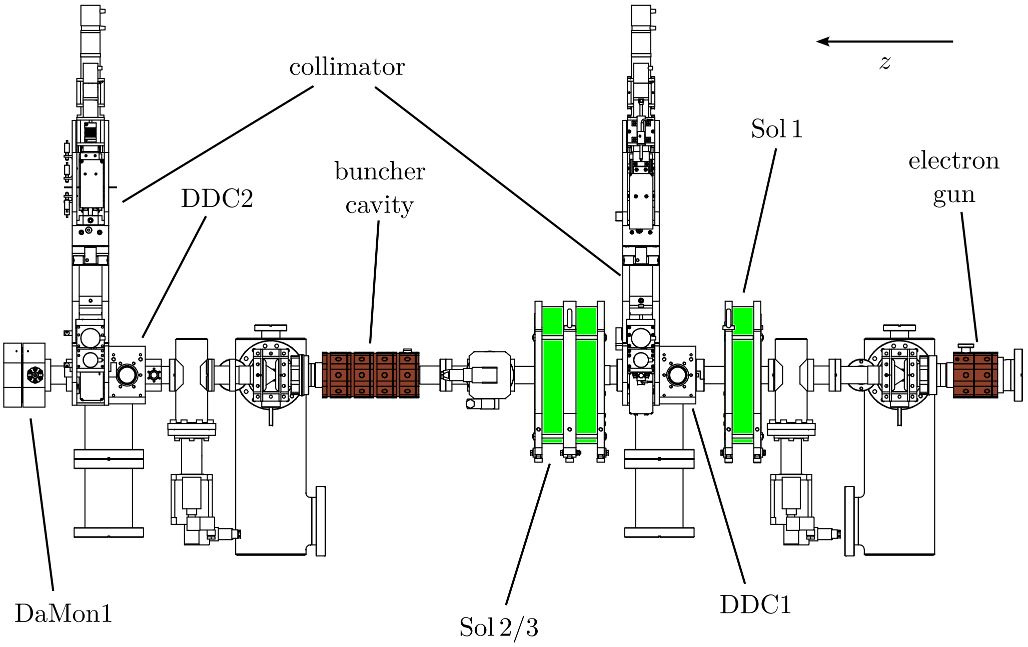

Figure 4.3 – Schematic of the Regae front-end shown from the side. DaMon1 marks the interface to the next segment.

DaMon1: **Da**rk current **Mon**itor 1 — DDC: **D**ouble **D**iagnostic **C**ross — Sol: **Sol**enoid.

with a wavelength of about 270 nm. The pulses typically have an energy of about 150 nJ within $\sim$ 500 fs FWHM [102]. Ideally, the laser is focused to an RMS spot size of a few 10 µm, enabling the low transverse normalized emittance ($\varepsilon \sim 30\,\mathrm{nm\,rad}$) of this machine.

Within the 1.5 gun cells, the electrons are accelerated by a field gradient of up to 120 MV/m, so that bunches with a maximum kinetic energy of $\langle T \rangle = 5.6\,\mathrm{MeV}$ are produced. In the second cavity, the buncher, the particles do not gain additional energy. Instead, this four-cell cavity is operated at the zero crossing of the longitudinal sinusoidal field, such that the electrons in the head of the bunch are decelerated, while the trailing electrons gain energy. As a consequence, the faster particles at the back will outrun those in the front of the bunch, leading to a reduction of the bunch duration up to the longitudinal focus, which is reached at the position of the target chamber. In that sense, the buncher cavity can be seen as a longitudinal lens, since the description in the phase space is equivalent to that of a transverse focusing element. After that point, at $z = 5.5\,\mathrm{m}$, the beam expands again, due to the still present energy spread. For a formal description of this process, which is called ballistic bunching, please refer to the next chapter. After the beam has passed the target area, it drifts up to the diffraction detector and is dumped. At the moment, both cavities are fed by one klystron, the power of which is distributed by means of a splitter and a phase shifter. Since this, however, is not ideal and proves to be insufficient to achieve the tolerances required for the design parameters of REGAE, it is planned to install a second klystron in the near future.

The magnet lattice of the machine consists of solenoid magnets and steerer magnets. There are four magnetic lenses in total: one single solenoid (Sol 1) and three solenoid pairs (Sol 2/3, Sol 4/5, and Sol 6/7). Sol 1 is located close to the gun, while Sol 2/3 is straight in front of the buncher cavity. The other two lenses are positioned symmetrically around the target chamber at $z_{\mathrm{S45}} \approx 5.0\,\mathrm{m}$ and $z_{\mathrm{S67}} \approx 6.0\,\mathrm{m}$. The steering magnets are small dipole magnets arranged in pairs, so that the beam can be deflected horizontally and vertically. The lattice is completed by the dipole of the electron spectrometer, which is presently located close behind the buncher cavity at about $z = 2.6\,\mathrm{m}$. Due to the low energy of the REGAE bunch, the beam optics lattice is complemented by a pair of Helmholtz coils, formed by two coils spanning the whole machine, in order to compensate for the transverse component of the earth magnetic field [103].

The machine is equipped with several diagnostic stations, which typically house one or several scintillator screens. These three so-called (**D**ouble) **D**iagnostic **C**rosses (DC and DDC) are located behind the cavities and at the electron spectrometer [104, 105]. The scintillator material used in theses stations is LYSO [106], because of its short decay time of about 50 ns and high light yield [107]. This combination is complemented by intensified CCD cameras with a comparable gating time, allowing to detect bunches of very low charge: At REGAE, few 10 fC are typically used and resolved by this technique [105]. The charge itself can be measured using so-called Faraday cups, located in the three diagnostic crosses and at the end of the beam line. In addition, the DaMon cavity provides another, very sensitive and non-invasive method to detect bunches with a resolution below 10 fC [105, 108]. In the beam line from gun to DaMon1, two collimators are installed, i.e., movable tantalum blocks with small holes of various sizes. They are used to stop electrons from dark current. In addition it is possible to scrape of outlying fractions of the REGAE beam, shaping the phase space and improving the emittance [29, 109]. The machine up to the

DaMon forms the front-end of Regae, containing all relevant parts for the acceleration, except for the eSpec. It is depicted in figure 4.3.

Downstream of that section, there is – in the *present version* of the beam line – mainly drift space, the target chamber, and the so-called diffraction detector at the end of the beam line; please see figure 4.4. At the target chamber, a movable sample holder is installed, which also contains a LYSO crystal, and various diffraction targets. The scintillator is imaged by an elaborate camera system, allowing for different magnifications and a switchable intensifier [107]. At the target chamber, a laser pulse, split of the injector laser, can also be coupled into the system to pump target materials.

Finally, the diffraction detector is based on another type of scintillator. Here, CsI:Tl is used, grown on a plate of optic fibers. In fact, a multitude of separate scintillator crystals is created by this method, each having a diameter of $6\,\mu\mathrm{m}$ [110]. The advantage of a this configuration is that light created inside the CsI crystal leaves the scintillator in a directed way, resulting in a high spatial resolution and better yield than for a LYSO crystal [111]. These devices are called **F**iber **O**ptic **S**cintillator (FOS) [110]. In combination with an intensified camera, they allow for the detection of single electrons [112].

Furthermore, the combination of these devices allows for a high dynamic range. A detector of that quality is necessary to detect single shot diffraction patterns resulting from the time-resolved UED experiments, the purpose the machine is built for: At the low charge of $80\,\mathrm{fC}$ (about 5×10^5 electrons), a bunch length of less than $\tau_{\mathrm{RMS}} = 10\,\mathrm{fs}$ can be achieved at Regae. At the same time, the low charge mitigates space charge repulsion at the gun cathode, enabling a very low transverse emittance of about $\varepsilon \sim 30\,\mathrm{nm\,rad}$. A bunch like that has a large transverse coherence, enabling high quality diffraction patterns [42, 50]. Thus, Regae is well suited for single shot diffraction experiments.

Moreover, owing to the moderate, but still relativistic kinetic energy of $\langle T \rangle = 5.6\,\mathrm{MeV}$ ($\gamma = 12$, $\beta = 0.9965$), the particles can penetrate comparatively thick samples, in contrast to low energy machines of $100\,\mathrm{keV}$ electrons. On the other hand, the scattering cross-section is several orders of magnitude higher than for photons used for comparable diffraction experiments [42]. Also, the targets are not destroyed by the electron probe.

The machine, thus, offers the possibility to investigate, for example, phase transitions or chemical reactions, which are triggered by a pump pulse split of the injector laser. Each snapshot taken, thus, has a time resolution given by and ultimately limited by the bunch length on target and the laser length, i.e., on the level of a few femtoseconds. This potential is also implied by the accelerator's name: Relativistic Electron Gun for Atomic Exploration. In short, the machine is designed for one specific goal [40]:

> *"Making the molecular movie."* – R. J. D. Miller

Another project campaign planned at Regae is about so-called time-resolved transmission electron microscopy (TEM) experiments [42, 113, 114]. In this case, a real imaging of target objects is aimed for, with the resolution limited by space charge. For this reason, strong solenoid lenses of high quality are required, although they are not yet implemented in the machine.

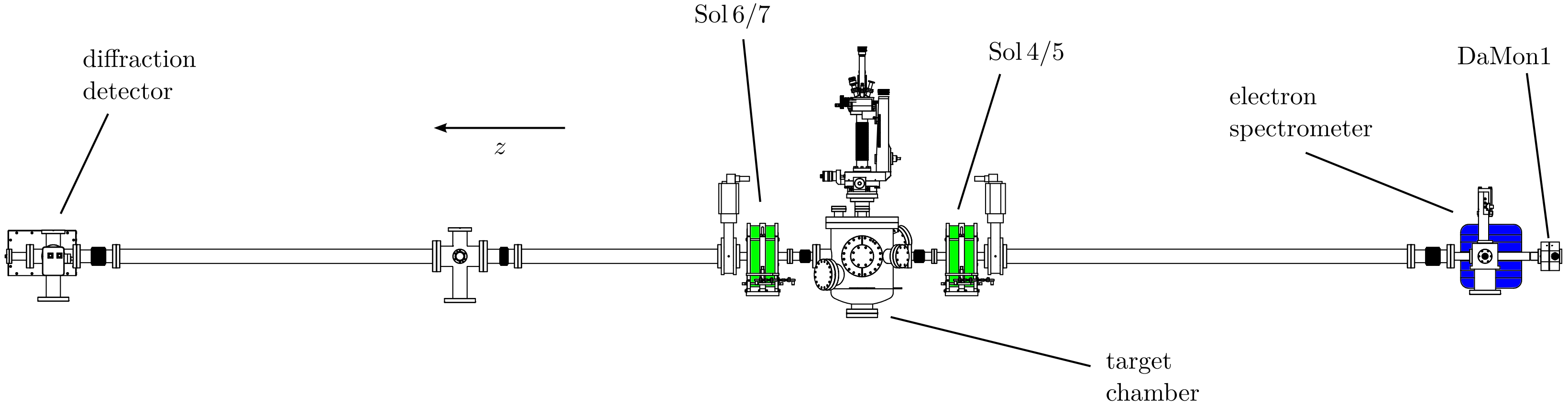

Figure 4.4 – Side view of the *present* Regae beam line. The electron spectrometer will be shifted downstream and the target chamber will be replaced by the new interaction chamber. These changes are topic of chapter 4.2.2.

DaMon: **Da**rk current **Mon**itor — Sol: **Sol**enoid

Finally, the external injection experiment discussed in the previous chapter is also designed with Regae in mind and scheduled for that machine. But for both of these future experiments, a major beam line adaption must first realized, the conception and design of which regarding the external injection experiment is part of this Ph.D. project and, thus, described in the following.

4.2.2 Beam Line Upgrade

The illustration of the beam line *upgrade* is split into three sections, each of which is based on certain segments of the machine. It starts behind the Regae front-end, which is unchanged, with the subsequent drift. In this co-propagation section, the laser is coupled into the main beam line. Then, there is the interaction region, containing the target chamber and required infrastructure. Finally, the area after the interaction chamber, sometimes called post-plasma or diagnostics section, also requires a huge amount of rework. Naturally, the sections overlap with the already described path of the laser.

Co-propagation Section

The co-propagation section starts directly behind the Regae front-end, i.e., after DaMon1. An illustration of this segment is shown in figure 4.5. The electron spectrometer has to be removed and is shifted downstream behind the target chamber, so that also the particles passing the plasma can be measured. Instead, the ICR chamber is placed at this point. It contains the last turning mirror and three pumping ports, as the chamber is a key element for the differential pumping, described in section 4.4. A vacuum shutter between the ICR and the MBA, containing the final focusing parabola, makes it possible to separate the accelerator vacuum system from the laser transport beam line.

Importantly, the overall diameter of that section has to be increased, starting with pipes of a diameter of $D = 100\,\mathrm{mm}$, reducing step by step, following the lasers caustic with a safety margin of about the 1.65-fold[3] of the $1/e^2$-diameter to avoid clipping. Within the drift section, two additional pumping chambers (nEVOC3, NEGcross), separable by a vacuum shutter, are foreseen. This is important insofar as the pump further upstream is a so-called non-evaporable getter pump (see section 4.4) which cannot be switched off. Hence, without the shutter, this pump would be saturated every time the target chamber is vented. Between the two pumps, a diagnostics cross for laser and electrons is housed (LD1e). A screen for the latter is required for the matching, though it is not situated directly at solenoid 4/5, which is located close to the target chamber at the end of the co-propagation section.

The last element before the interaction section is the **B**eam **A**rrival **C**avity (BAC). As the name suggests, it is a device to determine the arrival time of the electron bunch. The reference signal for this measurement will be the Regae master oscillator. At a later stage it would be desirable to directly reference the signal to a fraction of the Angus pulse. Thus, a timing reference close

---

[3] The factor of 1.65 is deduced from the ratio of the laser beam diameter and the effective mirror size in the laser transport beam line.

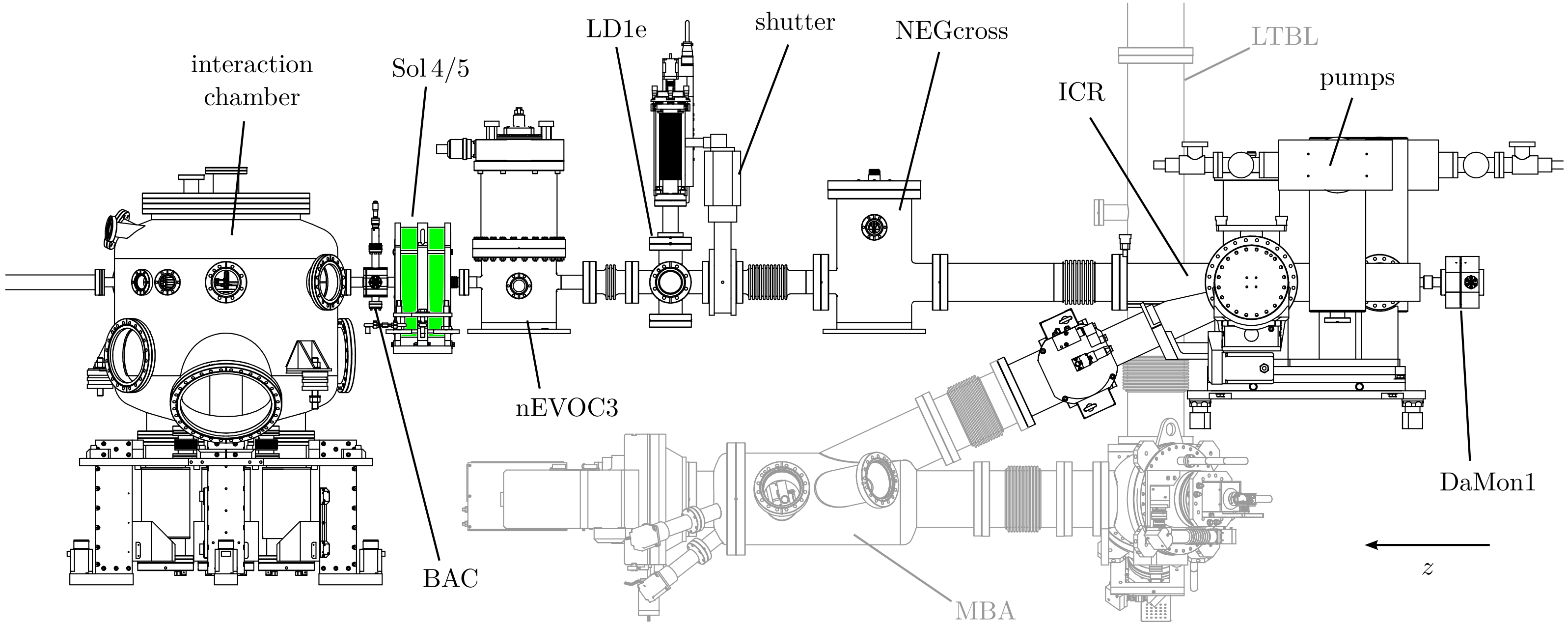

Figure 4.5 – Illustration of the co-propagation section between Regae front-end and interaction chamber shown in a side view. The laser is coupled into the electron beam line at the ICR.

BAC: **B**eam **A**rrival **C**avity — DaMon1: **Da**rk current **Mon**itor **1** — ICR: **I**ncoupling **C**hamber **R**egae — LD1e: **L**aser (and **e**lectron) **D**iagnostic **1** — LTBL: **L**aser **T**ransport **B**eam **L**ine — MBA: **M**ini **BA** — Sol: **Sol**enoid.

to the target is established, in addition to the elaborate synchronization of the laser oscillators to the rf master oscillator, as described below. Basically, the cavity picks up the electric field carried by the charged particles of a REGAE bunch. The decay of that signal can be used in order to determine the arrival time. However, due to the low charge of a typical REGAE bunch, the carried field is very weak, of course. This requires a stable, high quality resonator [115, 116], state of the art electronics and more details beyond the scope of this thesis. Despite the challenges, a concept has been developed in a collaboration together with DESY and the Technical University of Darmstadt, Germany, which could allow for a precision in arrival time measurement on the order of 10 fs at a charge of 1 pC.

Interaction Chamber: “Sancho Panza”

The heart of the experiment is located within the interaction chamber. The center of the vessel is located at $z = 5.5\,\mathrm{m}$ downstream of the gun cathode. At this position, the bunches are longitudinally focused, reaching their minimal duration. Thus, all three experiments (UED, TEM, and LWFA) are clustering at this point. In addition, the bunch length determination and further beam characterization measurements are complex experiments in their own – and also have to be performed in this location.

In order to meet these requirements, a sophisticated **I**nter**a**ction **C**hamber (IAC), also called “Sancho Panza”, had to be developed during the course of this thesis. It is depicted in figure 4.6. The chamber has about 30 flanges for various purposes. It is bigger in diameter (600 mm) than the present target chamber, but offers all the options of its predecessor. The IAC has a large lid, on top of which the four-axis manipulator for the diffraction experiments is mounted, as well as two cameras with lighting for the observation of the various motorized components inside the chamber. In addition, a pressure gauge can be mounted here. The vessel itself has four laser grade view ports for the pump laser of the UED experiments. For the UED and TEM experiments, a so-called **Liq**uid **C**ell (LQC) is installed, allowing for the investigation of liquid samples. The TEM also requires additional collimators, mounted on a separate manipulator. Furthermore, several flanges allow access for assembly, partly also used for monitoring the inner workings. Of course, the reused target camera – which has to be adjusted – also requires an access port, complemented by a second window for lighting. Moreover, due to the expected high gas load, two big turbo molecular pumps are mounted on the vessel (see section 4.4). These have magnetic bearings and vibration amplitudes below 20 nm [117].

A window, which is transparent for infrared signals, is used to determine the bunch length by **C**oherent **T**ransition **R**adiation (CTR, [118–120]): A charged particle carries an electric field, which has to change if the particle passes the boundary of two media of different dielectric constants. The associated energy loss is emitted as radiation in a broad energy range. For the case of multiple particles, like in an electron bunch, this radiation is emitted coherently in the wavelength regions longer then the bunch length. Monitoring the spectrum over a preferably wide span enables a back-calculation of the bunch length and even the charge distribution along the bunch: The so-called form factor can be deduced from the spectrum, so that a Fourier transform yields the aforementioned result. However, since the phase is unknown, the reconstruction is not

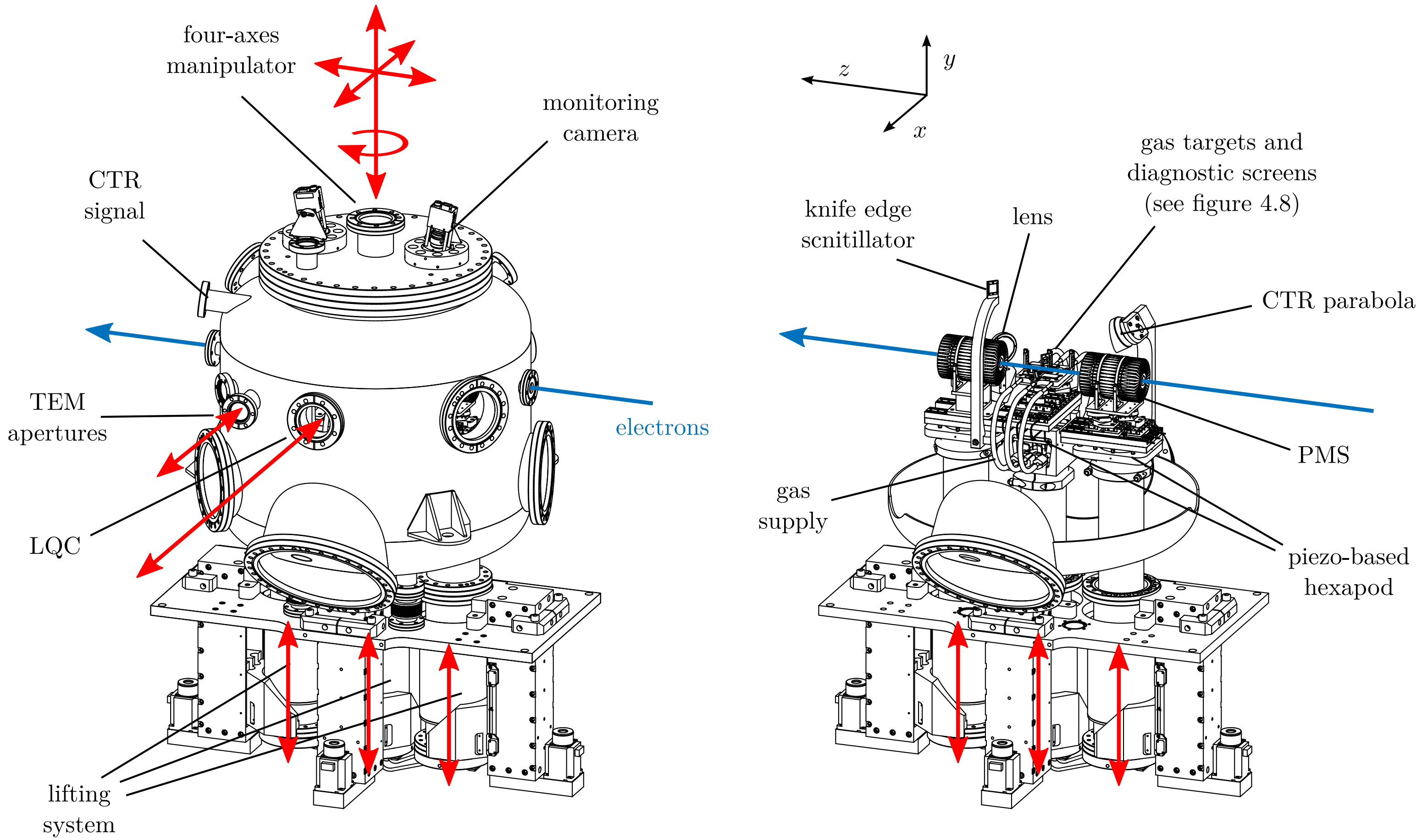

Figure 4.6 – Illustration of the interaction chamber (*Sancho Panza*). The red arrows indicate the respective movement axes. A detailed view of the setup inside the chamber is shown in figure 4.8.

CTR: **C**oherent **T**ransition **R**adiation — LQC: **L**iquid **C**ell — PMS: **P**ermanent **M**agnetic **S**olenoid — TEM: **T**ransmission **E**lectron **M**icroscopy.

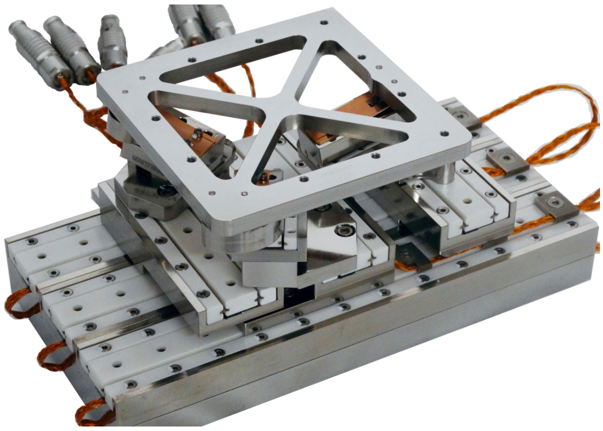

Figure 4.7 – Piezo-based hexapod mechanics. Picture by courtesy of SmarAct GmbH (Oldenburg, Germany).

unique, such that certain assumptions are required. At the low bunch charge used at Regae, however, it is unclear whether the signal will be strong enough for a successful measurement.

The plasma experiments at *Sancho Panza* are served from the bottom by two additional linear translators, complemented by a third, identical manipulator for the TEM experiment (see figure 4.6): Two of these move **P**ermanent **M**agnetic **S**olenoids (PMS) [121] in and out of the beam path, which can be used for the external injection, and are required for the microscope experiments – thus creating synergies between the experiments. This so-called lifting system is complemented by additional flanges which allow for an optional bread board decoupled from the main chamber, thus minimizing vibrations. (This option is not considered at this point in time, though.)

All in all, there are six independent manipulator arms reaching into the chamber, the paths of which can overlap partly, especially at the desired center of the chamber. On top of the lifting system, there are two piezo based hexapod positioning systems and one linear stage based on the same principle. So, overall there are even 22 independent movement axes – requiring a sophisticated and failsafe collision avoidance system.

The hexapod mechanics are specially designed for the demands of the experimental environment: The material used is suited for accelerator grade vacuum and nonmagnetic. The travel ranges are about ±75 mm and ±25 mm in the horizontal plane, and 2 mm in the vertical direction. The latter is sufficient, since the movement in this direction is complemented by the lifting system. Despite this large travel range, the positioning devices offer a precision of 1 nm. The hexapods can carry a weight of more than 1.5 kg. Figure 4.7 shows a photograph of the item. The movement axes are depicted in figure 4.8.

On each of the outer lifting system axes, a solenoid based on permanent magnets (PMS) is mounted. They can be positioned along the electron beam axis with one of the hexapods (upstream, long travel range aligned in z) or the linear stage (downstream). The PMS serve as lenses to achieve very small beam sizes of about 2 µm, which is too small to achieve a matched beam at a plasma density of $10^{16}\,\mathrm{cm}^{-3}$, as discussed in the previous chapter. However, for higher gas

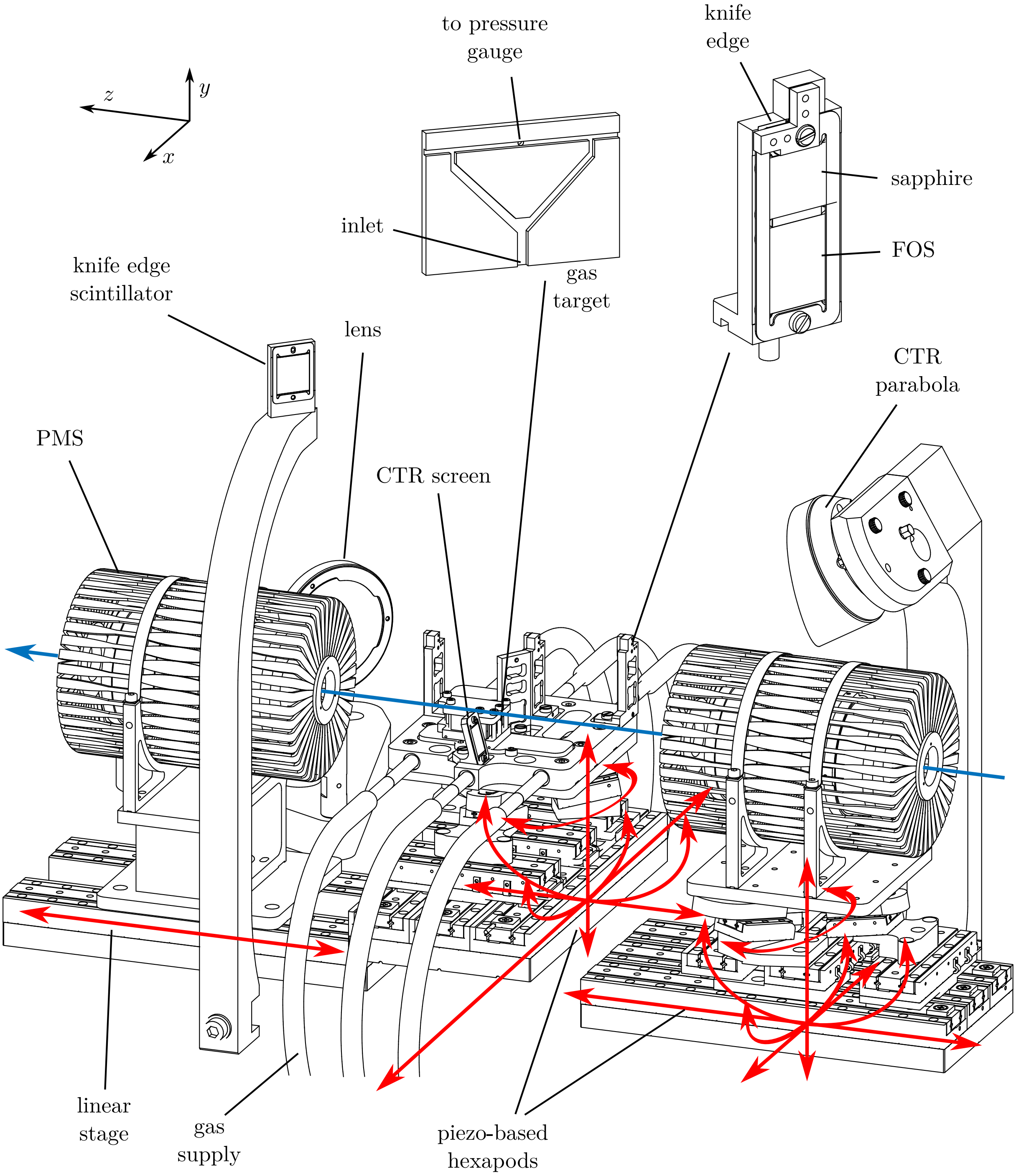

Figure 4.8 – Detailed view of the setup inside the target chamber. The red arrows mark the movement axis of the piezo-based hexapod positioners and the linear stage.

CTR: **C**oherent **T**ransition **R**adiation — FOS: **F**iber **O**ptic **S**cintillator — PMS: **P**ermanent **M**agnetic **S**olenoid.

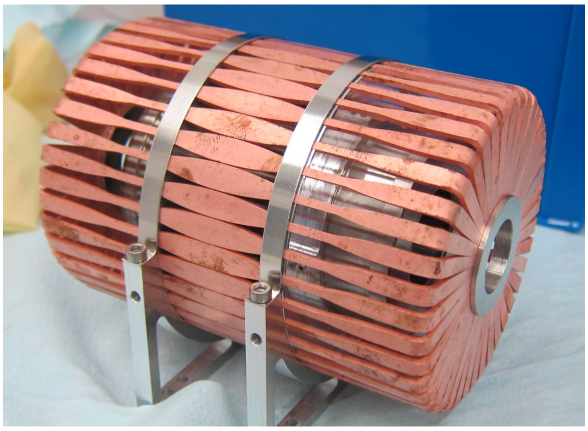

Figure 4.9 – Permanent magnetic solenoid surrounded by the shielding made of pure iron and coated with copper.

densities such small spot sizes could be necessary. In order to shield stray fields of the magnets, which could disturb the Regae beam if the solenoids are moved out of the beam line and also to minimize attractive forces between the two PMS, the magnets are surrounded by a shielding of pure iron, coated with copper. An image of a PMS is shown in figure 4.9. A detailed description of the PMS design and properties can be found in [53, 29, 121].

The central pillar of the lifting system brings the plasma targets into position. The hexapod on top of this linear translator is mounted in such a manner that the long horizontal motion axis is perpendicular to the beam path. With this configuration, a multitude of different diagnostics can also be shifted in and out of the beam path. An overview is shown in figure 4.10. As mentioned, a CTR measurement is planned in order to characterize the bunch length on target. Therefore, an aluminum coated silicon wafer is mounted in an angle of about 13 deg upwards, intersecting the beam path if in position. The backwards emitted radiation is directed onto a gold coated parabolic reflector, mounted on top of the upstream lifting pipe. The light is collimated by the mirror and sent out of the chamber through a zinc selenide window, which is transparent for infrared radiation in a wavelength range between $\lambda_{\mathrm{ir}} = 0.6\,\mu\mathrm{m}$ and $\lambda_{\mathrm{ir}} = 15\,\mu\mathrm{m}$. From here, the light is transported to two wavelength selective detectors measuring the integrated signal in a limited spectral range, since the signal will not suffice for a complete characterization of the spectrum. However, an estimate for the bunch length can still be retrieved [122, 123], and a more precise knowledge of the substructures of the bunch is not required at this point.

As a second diagnostics, several scintillator screens are mounted on the central hexapod at four different locations, see figure 4.10. At each of these positions an FOS based diagnostics is chosen, as in the diffraction or eSpec detector, due to their high light yield. Three of these – one a few centimeters upstream, one on height of the injection point and one a few centimeters downstream – are oriented perpendicular to the beam path. They are monitored via a camera system downstream of the chamber in propagation direction. Hence, distortions caused by the camera perspective and refraction at the scintillator edges are avoided [111]. It is, therefore, possible to achieve a high position accuracy of the electron beam at these locations and, thus,

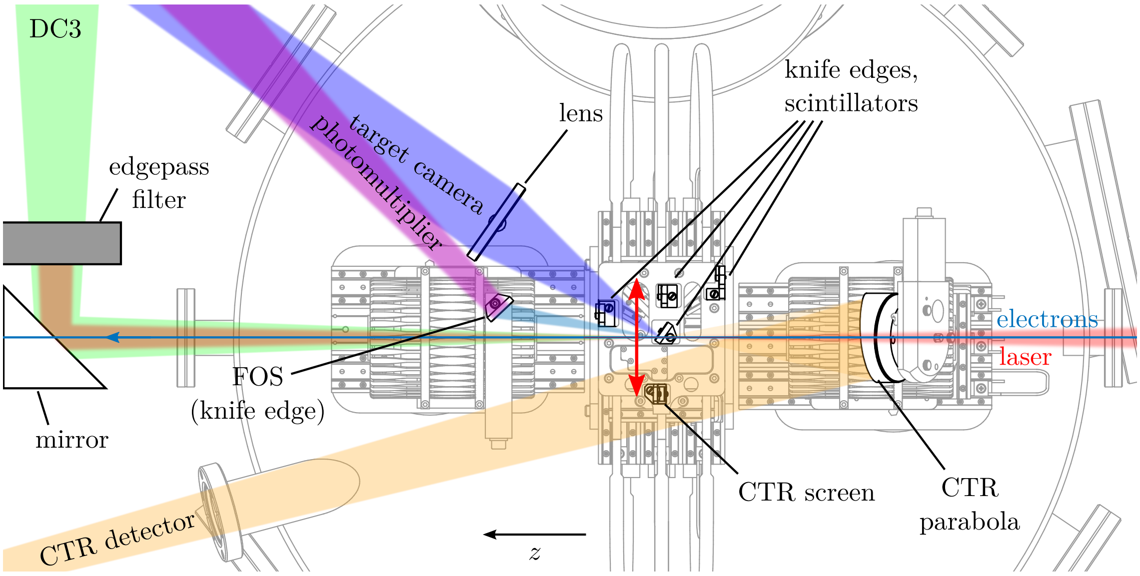

Figure 4.10 – Top view of the diagnostics inside the interaction chamber. The colored patches illustrate the light path of the diagnostics signals.

CTR: **C**oherent **T**ransition **R**adiation — DC3: **D**iagnostic **C**ross **3** — FOS: **F**iber **O**ptic **S**cintillator.

determine the electron beam axis. To relate this position to the laser beam propagation, sapphire plates are mounted in the same three imaging planes, which can be driven into the beam path, instead. It is planned to visualize the laser positions at these locations by white-light generation [78, 124, 125].

The idea behind this is the following: In order to monitor the laser's position at a specific location with a diagnostics in the beam path direction, a separation of the direct laser light from the co-propagating diagnostics photons is required. The laser signal is much stronger, so that the photons from the screens cannot be determined because of that huge background signal. Using a nonlinear process, like white-light generation or alternatively second harmonic generation [124], the laser photons are shifted towards higher energy, so that the main pulse can be blocked by an edge pass filter. Since the FOS signal from the electrons is around 550 nm [126, 111], it is not blocked by the edge pass filter and can likewise be detected using the identical camera setup. In other words, both signals, which are to be referenced to each other, can be monitored with the same imaging system. The signal from the nonlinear process also contains less photons compared to the laser itself. Thus, the demand on the dynamic range of the associated camera system is reduced. The white-light generation is chosen, since the sapphire plate is much cheaper than, for example, a BBO crystal, which can be used for a second harmonic generation. Also, the white light has a broad spectrum, allowing for a better adjustment and damping of the transmitted signal by the choice of the edge pass filter. That is, it is better suited to adjust for the dynamic range of the camera. This also explains the choice of the scintillator type. The radiation produced by the FOS is directed, as mentioned above, thus maximizing possibility the photons eventually being detected by the camera [111].

A fourth scintillator stage is included on the central hexapod on the height of the targets, as can be seen in figure 4.10. It is tilted 35 deg with respect to the beam axis, so that the surface plane of the crystals is parallel to the imaging plane of the re-designed target camera. This monitoring system is attached to a window flange of *Sancho Panza*, rotated by that angle. Here, likewise a sapphire plate is included, as well as an FOS and a LYSO crystal. The imaging system includes an in-vacuum lens which is located as close as possible to the targets, i.e., in a distance of about 100 mm to the center of the chamber, so that the light collection efficiency and especially the resolution is increased, compared to the present setup at REGAE [112]. The increased resolution is important to determine the beam size $< 10\,\mu\text{m}$ of the electron bunches. Using the Abbe criterion, the resolution limit of the imaging system with this configuration is about

$$r = 1.22\,\frac{\lambda f}{D} \approx 1\,\mu\text{m}, \tag{4.1}$$

where r is the radius of the first zero of the Airy disc, $f \approx 100\,\text{mm}$ the focal length, and $D = 50\,\text{mm}$ the diameter of the entrance pupil given by the $2''$ in-vacuum lens; the scintillator wavelength of LYSO is about $\lambda \approx 400\,\text{nm}$ [111]. The camera system is completed by a commercial high quality objective outside of the chamber in a distance of about 250 mm from the lens; it is attached to an intensified CCD camera. (Without the in-vacuum lens, the resolution that might theoretically be reached by the imaging system would worsen to $r = 3.5\,\mu\text{m}$, limited by the aperture of the window flange.)

The resolution of the whole system will be limited by the scintillators. The fiber optics plate of the FOS has a pixelated structure with a fiber diameter of $6\,\mu\text{m}$, which is on the order of the focused electron beam size. Hence, structures below about $10\,\mu\text{m}$ cannot be resolved. The LYSO crystal does not have this intrinsic structuring. However, the image formation inside that crystal type leads to a so-called Lambertian source [107]: The photons are emitted along a line in the $300\,\mu\text{m}$. This must be taken into account because the photon spot will thus be larger and differ from the electron beam size, so that the resolution of the FOS will be better compared to the LYSO crystal. In addition, the image plane for which the camera is set for in the crystal is important. Hence, some image post-processing is required [111]. The same is true for the sapphire screen which is included here as well. For this laser detector, there is an additional refraction effect to be considered: The photons are already deflected when entering the tilted screen. Thus, if the electrons are geometrically matched to the laser position, the spots on the camera system will differ. Consequently, it is necessary to conduct some image analysis and make additional calculations correcting for deviations from Snell's law [111].

The perpendicular screens described above can also be driven into the beam. In this case, no offsets from refraction are to be expected. However, the surfaces of the crystals are no longer parallel to the image plane, which again complicates a proper imaging and reconstruction of the beam positions and size. Since there is no experience, which configuration is better suited, all of these are implemented into the system. Also, a LYSO perpendicular to the beam is included in the diffraction setup, which can, thus, additionally be used. Please refer to [111] for a detailed analysis and description of the scintillator setups and imaging.

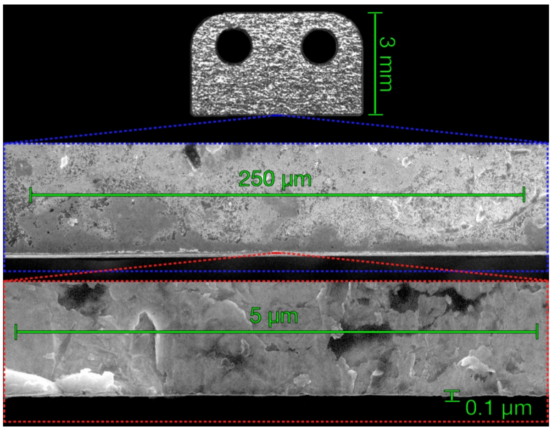

Figure 4.11 – Scanning electron microscope image of a polished knife-edge foil. The unevenness of the edge is reduced to a value below 100 nm. The quality achieved is sufficient for the knife-edge based bunch diagnostics. Image from [111] by courtesy of K. Krausert.

Due to the imaging limit in the scintillator approaches, another method has been developed in order to determine the beam position and, more importantly, the beam size. It is an adaption of the well-known wire scanner technique and also inspired by the knife-edge based beam profiling used in laser physics. Owing to the high precision of the hexapod axes, a scattering foil can be driven into the beam, partly shadowing the bunch. Of course, in this case, the particles are not stopped, like photons of a laser, but scattered. Stopping the REGAE electrons would require a few millimeter thick high-Z material like copper or tantalum, as used in the case of the collimators within the REGAE front-end.

The scattering rate into a certain solid angle, however, depends on the amount of particles hitting the foil. And thus, a stepwise scanning of the electron beam and determination of the scattering signal allows for the reconstruction of the beam size, since the relative quantity of scattered particles in dependence of the position yields the integrated beam profile. Assuming a Gaussian distribution, one would, for example, expect the shape of an error function [83]. (Since the distribution is two-dimensional, the back-calculation is more complicated, of course [111].)

Gold is used as a scattering material because of its good processing properties, vacuum compatibility and high Z value. The thickness and edge of the 25 µm thick foil must be very precise to ensure a constant scattering cross section. Especially the variations of the latter must be much less than the size of the electron beam, which can be focused down to about 2 µm, using the permanent magnetic solenoids. For a matched injection, the beam size is ideally on the order of 5 µm, see chapter 3. Such precision cannot be reached using laser cutting methods, especially, since the edge must also be perpendicular to the surface of the foil. Thus, a grinding method has been used, suggested by [127] from the Technical University of Darmstadt, who provided the foils. It was successfully tested at the DESY sources lab [111], as can be seen in picture 4.11. It shows the image of a polished edge recorded with a scanning electron microscope.

One knife-edge is mounted in the vertical and horizontal direction each, perpendicular to the beam on the central hexapod in the target chamber. More precisely, at each of the three perpendicular scintillator positions discussed above a knife-edge setup is implemented. This makes it possible to determine and cross-correlate the beam size and position at these three locations. (Also the laser can in principle be located with that setup if it is attenuated enough to not destroy the foil.)

The scattering signal is collected by another FOS, which is located downstream of the knife edge setups, located on the third lifting pillar; see figure 4.10. In this case, it is a 400 µm thick CsI:Tl scintillator layer on top of the fiber optics plate, in order to maximize the light yield. Since the relevant quantity is the (relative) number of electrons scattered into the solid angle covered by the detector, the spatial resolution is not important. Therefore, the $15 \times 15\,\mathrm{mm}^2$ wide scintillator is not imaged using the target camera, but the light is directed onto a photo-multiplier, instead. Thus, the scintillator is used similar to a photo diode. In addition to this, the diffraction detector downstream of the target chamber can be used to measure the complementary signal from the undisturbed electrons.

In principle, the method provides an option to determine the beam size and position with a sub-micron precision. However, since it is a multi-shot technique, it is susceptible to shot-to-shot fluctuations. For this reason, it requires a very solid positioning of the lifting system, as well as a stable electron beam. A comprehensive analysis and discussion of all the transverse beam diagnostics systems planned in the target chamber can be found in [111].

The main elements on top of the central hexapod platform are the gas targets. Three targets of different lengths are planned: One with the dimensions calculated in chapter 3, i.e., 25 mm length with additional 5 mm on both sides where the pressure drops rapidly to the pressure inside the chamber. The second target is shorter, with a 10 mm plateau, but similar up- and downramp. Finally, a short target of $\sim 2\,\mathrm{mm}$ length without dedicated ramps is foreseen, which allows to probe the plasma almost without phase slippage effects [39]. The matching condition is harder to fulfill in this case, probably requiring the use of the PMS lens.

The longer targets with a plateau have symmetric inlets confining the range; see figure 4.8 on page 97. The short one has only one inlet, which restricts the quasi-constant region to the dimensions of this feed. The targets are produced either by laser ablation machining [76] or CNC milling. Therefore, they have a square profile with an edge length of 500 µm for the shorter ones and 1 mm for the long version. These dimension are a compromise between the diameter of the driver laser beam at the channel ends and the gas flow required to achieve the desired pressure. The latter should be minimized, since it results in a lower overall pressure in the system. This is important for the differential pumping section described in section 4.4, which needs to be able to handle the gas load put into the setup. The targets are made of sapphire, which has a very high ablation threshold of about $8\,\mathrm{J/cm}^2$ for a 100 fs laser pulse [128]. It can thus withstand the intensity of the Angus beam in the side lobes, associated with the sinc^2 distribution close to the focus [61]. The target structure is machined into a 2 mm thick sapphire plate, which is afterward covered with an untreated second sapphire plate. Thus, no careful alignment of the two halves is required. The two parts are brazed together. A prototype based on the target design is under construction at this point in time.

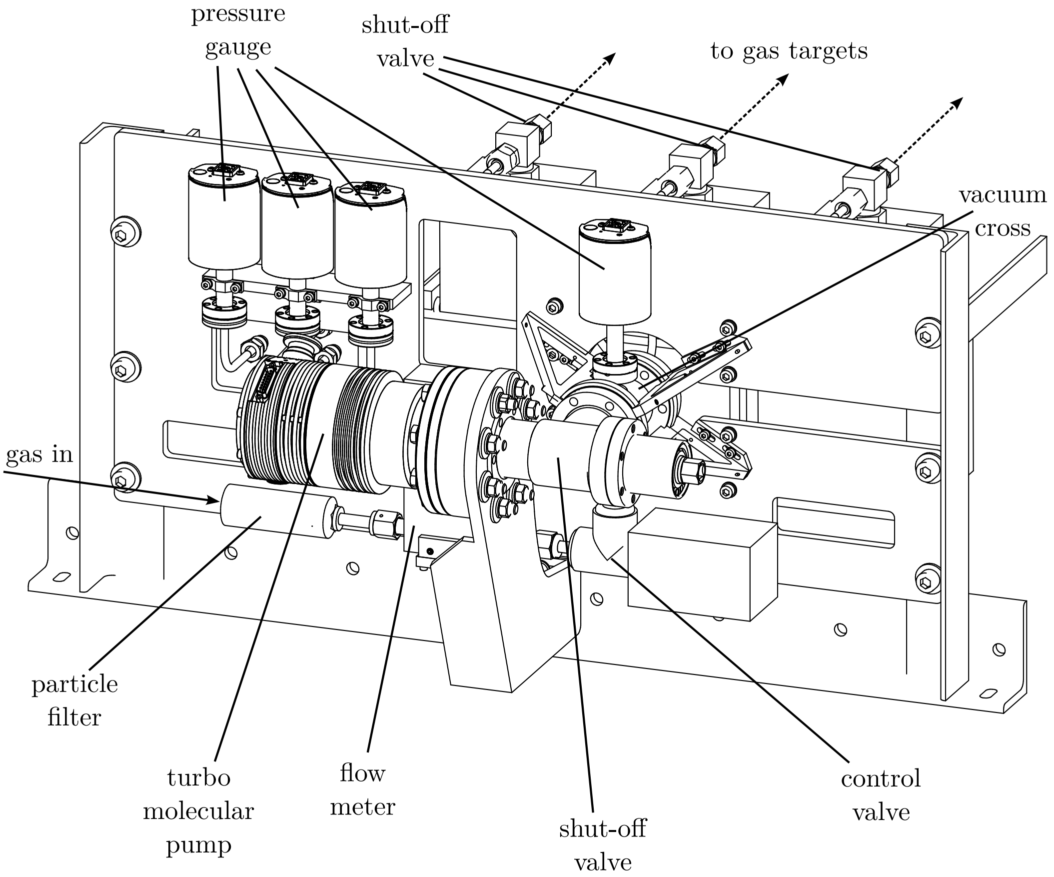

Figure 4.12 – Illustration of the gas distribution system.

An additional hole is located in the middle of the target channels. At this point a capacitive pressure sensor is connected, which allows to determine the gas pressure with an accuracy better than 1 %, similar to the targets used at the Lux beamline [26, 76]. The measurement requires a continuous flow operation of the targets. Only then is a stable equilibrium pressure built up. Simulations with the described target geometry, using the fluid dynamics code OpenFOAM [129], show that these produce the desired density profile [87], including the pressure measurement. Also, first measurements on similar target geometries show promising results – at least for symmetric targets, like those planned for Regae [76].

The gas targets are supplied through conduits in the hexapod plate. The connection to the pressure gauges is achieved that way as well. Flexible hoses are connected to feedthroughs in the lifting pipe, keeping most movable parts out of vacuum. By this approach, the risk for complications like the entanglement of the supply lines inside the vacuum chamber is reduced. Furthermore, it minimizes the outgassing rate into the vacuum system because the overall surface of the inside of the interaction chamber is reduced accordingly. For the same reason, the electric connections for the piezo drives are done through the pipe, as well.

Outside of the chamber, the gas distribution system is located. It is illustrated in figure 4.12.

The first element in the supply line is a particle filter, ensuring that the particle free accelerator environment is not spoiled by the hydrogen source. After that, a flow meter is located measuring the gas flow. Then, a fine regulating valve sets the flow/pressure eventually achieved in the targets. To stabilize the system, a small buffer volume is included. It is contained in a vacuum cross, which has a separate pressure gauge and is connected to a pump, which can evacuate the system. This is important, since a pumping through the supply lines and targets, using the pumps attached to the interaction chamber is very inefficient. Thus, a reduction of the pressure in the targets could hardly be achieved without the separate pump. Also, if no plasma experiments are executed, the gas system would act like a virtual leak if not pumped by its own. A vacuum valve separates the pump from the buffer volume if not required. At the last flange of the cross, the inflow is split into three lines which feed the gas targets. Each conduit can be opened and closed by a full-metal sealed valve. Finally, the pressure gauges for the gas targets are also mounted at the gas distribution board.

The hydrogen gas used is produced in a hydrogen generator via electrolysis. Hydrogen is a highly explosive gas with a lower explosive limit of 4 % and an upper explosive limit of 75 % [130]. Therefore, the amount of hydrogen gas held in stock in the accelerator tunnel is reduced to a minimum by the use of the generator. Also, it allows for an (additional) regulation and stabilization of the flow. For the same safety reasons, a dilution with an inert gas like nitrogen is necessary at the pumps evacuating the system. Both of these gases are however scentless, not visible and suffocating. Hence, a controlled emission into the environment is taken care of, combined with a leakage control of the vacuum and gas system, as well as warning sensors for hydrogen levels and oxygen lack.

Post-plasma Section

Behind the target chamber, a diagnostics section is located. It is illustrated in figure 4.13. It starts with a so-called **T**ransverse **D**eflecting **S**tructure (TDS) [131]. This is another type of rf cavity, however it exerts a (time-dependent) transverse momentum change, instead of a longitudinal acceleration. I.e., the electron bunch gets a transverse kick, which varies along the bunch length, so that the longitudinal phase space is mapped to transverse coordinates which can easily be imaged on a subsequent screen. With such a configuration, the longitudinal structure of the bunch at the location of the TDS, that is, the bunch length and even the current profile, can be determined.

The next element in this beam line section is a diagnostics cross, labeled DC3. Here, the downstream imaging system monitoring the in-line beam diagnostics in *Sancho Panza* is located. Also, an additional FOS and a LYSO scintillator are positioned here, combined with another sapphire plate. That is, at this point an additional reference for the overlap of laser and electrons is located. Moreover, a Faraday cup is added here for charge measurement.

Directly behind DC3 two quadrupole magnets, $Q_{a,b}$, are used to image the plasma electrons. They have a distance of 260 mm to each other. In between another solenoid (Sol 6/7) is located,

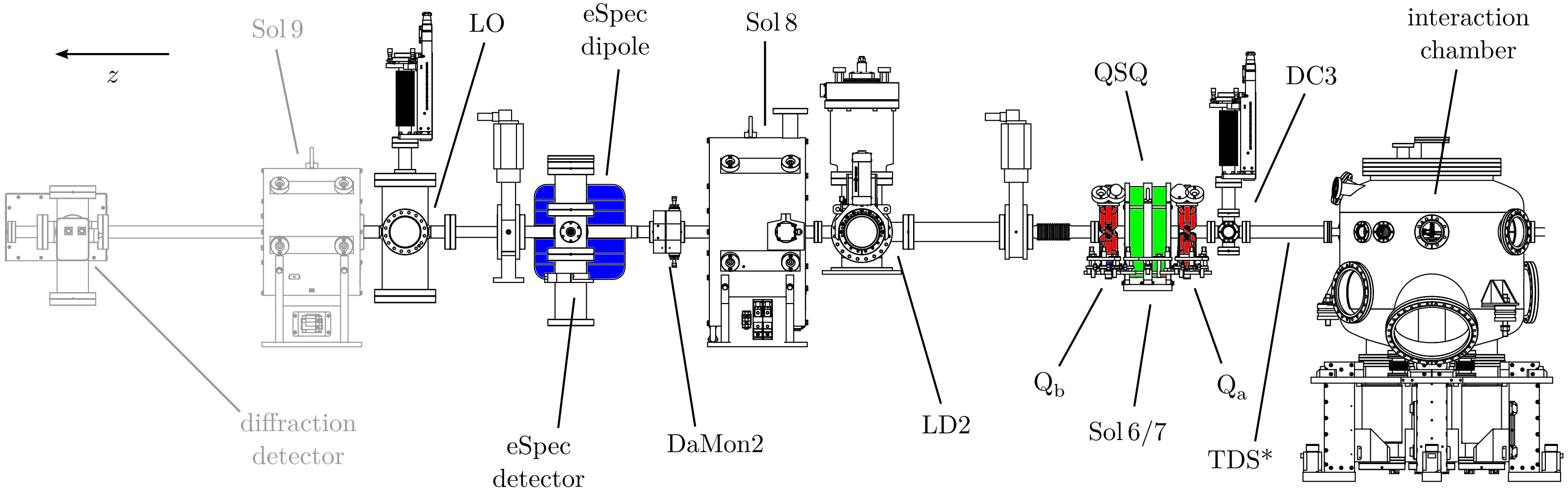

Figure 4.13 – The diagnostics section downstream of the interaction chamber shown in a side view. *: The TDS is not shown in the figure.

DaMon: **Da**rk current **Mon**itor — eSpec: **e**lectron **Spec**trometer — LD2: **L**aser **D**iagnostics **2** — LO: **L**aser **O**ut — Q: **Q**uadrupole QSQ: **Q**uadrupole-**S**olenoid-**Q**uadrupole — Sol: **Sol**enoid — TDS: **T**ransverse **D**eflecting **S**tructure.

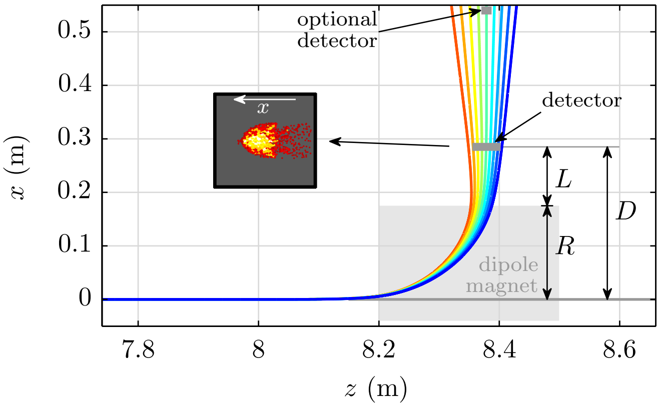

Figure 4.14 – Geometry of the upgraded REGAE spectrometer. The nominal radius of curvature is $R = 175\,\mathrm{mm}$. The detector is located at a distance of $L = 110\,\mathrm{mm}$ measured from the edge of the dipole magnet. A second detector which is further away can be optionally included into the setup. Please note the x-direction on the detector, defined by the co-moving coordinate system of the electrons.

hence this segment is labeled QSQ. Sol 6/7 is of the same type as the previous Sol 2/3 and Sol 4/5 upstream of the target chamber. The solenoid is used for the diffraction experiments.

Behind QSQ another diagnostic cross is located. Here, the (main) laser diagnostic, LD2, is set up. Thus, the chamber contains the holey decoupling mirror mentioned above, as well as a version without a hole. The laser beam is sent towards the laser diagnostics table, as discussed in section 4.1. The beam pipe from *Sancho Panza* is gradually increased up to this point, following the laser beam expansion. LD2 is neighboring the first TEM solenoid, Sol 8. This is a stronger lens than those installed in the upstream beam line of REGAE. Also, this element, which cannot be shifted further downstream due to imaging reasons, determines the position of LD2: The diameter of the beam pipe has to decrease to a size smaller than that of the laser caustic diameter, which means that the photons have to be sent out of the beam line at this position. Behind Sol 8, another **Dark** current **Mon**itor (DaMon2) is located. Thus, the charge of the accelerated plasma electrons can be verified, and more importantly, compared to the charge accelerated by REGAE. That is, the ratio of injected and transmitted particles can be measured using the signals of DaMon1 and DaMon2.

Behind DaMon2, the electrons enter the field of the eSpec dipole magnet. The nominal radius of curvature of the electrons in the B-field is $R = 175\,\mathrm{mm}$, determined by the dimensions of the magnet. The geometry of the spectrometer is shown in figure 4.14. To calculate the dispersion, the beam optics formalism introduced in chapter 2 must be extended by including the linear momentum deviation $\delta = \Delta p_z / \langle p_z \rangle$; the underlying differential equation gets inhomogeneous. The solution can be described by a 3×3 matrix [64, 65], while the particle vector gains an additional entry, δ. The resulting elements x and x' in the linear approximation for an off-momentum particle in a dipole are then given by

$$\begin{aligned} x &= x_0 \cos(s/R) + x_0' R \sin(s/R) + \underbrace{\delta R\left[1-\cos(s/R)\right]}_{\Delta x}, \\ x' &= (x_0/R)\sin(s/R) + x_0' \cos(s/R) + \underbrace{\delta \sin(s/R)}_{\Delta x'}. \end{aligned} \tag{4.2}$$

Thus, one can calculate the deviations within the magnet to

$$\begin{aligned} \Delta x_{\mathrm{dp}} &= \delta R\left[1-\cos(s/R)\right] = \delta R, \\ \Delta x'_{\mathrm{dp}} &= \delta \sin(s/R) = \delta. \end{aligned} \tag{4.3}$$

Here, the sine and cosine terms vanish, since the eSpec is designed for a 90 deg bend, i.e., $s/R = \pi/2$.

The offset between particles of different longitudinal momentum is further increased during the drift towards the detector due to the resulting divergence at the dipole exit. It is thus simply described by $\Delta x_{\mathrm{dr}} = L\Delta x'_{\mathrm{dp}}$, where L is the distance between magnet edge and detector screen. The overall offset is then given by

$$\Delta x_{\mathrm{det}} = \Delta x_{\mathrm{dp}} + \Delta x_{\mathrm{dr}} = \delta(R+L) = \delta(R+D-R) = \delta D = \frac{\Delta p_z}{\langle p_z\rangle} D, \tag{4.4}$$

using $D = L + R$ which characterizes the perpendicular distance of the detector to the original beam axis. This is again only valid for the 90 deg bend case. The distance is $D = 285\,\mathrm{mm}$ for the upgraded REGAE eSpec, as can be seen in figure 4.14.

Using D, it is possible to determine a relative energy calibration and estimate the resolution of the eSpec. Assuming a beam spot with $x_{\mathrm{RMS}} = 250\,\mu\mathrm{m}$ as deduced in section 3.5 of the previous chapter, the ratio yields $x_{\mathrm{RMS}}/D \approx 0.1\,\%$ as a rough estimate for the resolution of the instrument.

Figure 4.15 shows a calibration curve according to equation (4.4). In addition, a quadratic fit to the results of an ASTRA reference case is shown, taking into account deviations from the linear model. This yields a slightly better result. The corresponding fit model is

$$\Delta x_{\mathrm{det}} = a\left(\frac{\Delta p}{\langle p_z\rangle}\right)^2 + b\frac{\Delta p}{\langle p_z\rangle} + c, \tag{4.5}$$

with $a = 144.6\,\mathrm{mm}$, $b = -278.5\,\mathrm{mm}$, and $c = 0.6\,\mathrm{mm}$. The linear factor, b, is almost equal to D.

The deviations are due to two reasons: First, only the linear momentum deviation is included in the analytic model, i.e., there are deviations for larger values of δ. Second, when one looks at figure 4.14, one can see that the electrons are not perfectly bent by 90 deg in the magnet. In fact, the bend starts already prior to the hard edge of the magnet and lasts longer. Fringe fields of the dipole extend the effective field area. A corresponding effective radius of curvature can be estimated to $R_{\mathrm{eff}} \approx 220.0\,\mathrm{mm}$ using the calibration simulations with a measured field map. This,

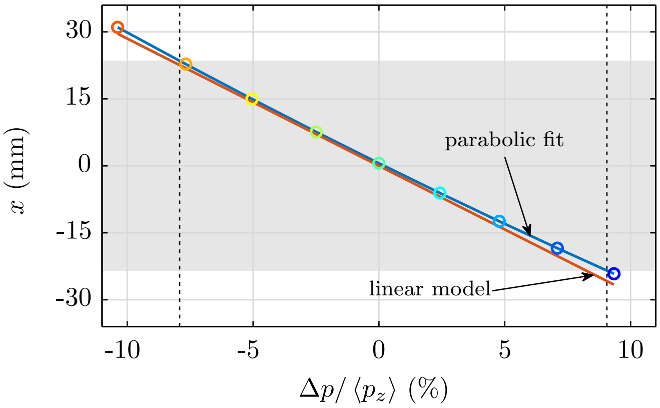

Figure 4.15 – Calibration curves for the eSpec detector located at $L = 175\,\mathrm{mm}$. The linear model is slightly refined by a quadratic fit. The gray shaded area marks the size of the detector. The boundaries of the covered relative momentum interval are $\Delta p / \langle p_z \rangle |_{\mathrm{min}} = -8\,\%$ and $\Delta p / \langle p_z \rangle |_{\mathrm{max}} = +9\,\%$.

for example, shifts the detector position slightly downstream by 4.3 mm to 179.3 mm measured from the dipole edge.

The absolute energy calibration for the magnet can be deduced from the simulation:

$$\frac{B}{\langle p_z \rangle} = \frac{1}{cR_{\mathrm{eff}}} = 15.16\,\frac{\mathrm{mT\,c}}{\mathrm{MeV}}. \tag{4.6}$$

The spectrometer is equipped with a $47 \times 47\,\mathrm{mm}^2$ wide FOS screen, imaged by an intensified CCD camera. The energy interval covered ranges from about $\Delta p / \langle p_z \rangle |_{\mathrm{min}} = -8\,\%$ to $\Delta p / \langle p_z \rangle |_{\mathrm{max}} = +9\,\%$. The mirror behind the scintillator, which deflects the signal by 90 deg, is a aluminum coated silicon wafer. This avoids a back scattering of electrons from the mirror material, which would produce erroneous signals from the FOS [112]. Also, the particles can be caught by a Faraday cup, so that the charge can be determined. Thus, a cross-calibration of the light emission to the bunch charge is possible. If the resolution above is not sufficient, the eSpec is designed in a way that makes it possible to attach an additional detector allowing for a longer drift. (In fact, the detector of the original instrument can be easily attached.) However, this requires a careful balancing in terms of imaging.

An elaborate analysis of the eSpec can be found in [88]. The resolution determined in that work, however assumes more optimistic parameters at the end of the plasma target, so that the influence of the emittance and beta function on the resolution is less dominating. Furthermore, the change in resolution along the detector is investigated in that work, since the electron imaging suffers from chromaticity.

Finally, directly behind the eSpec the last component related to the external injection experiment is located: the **L**aser **O**ut (LO) chamber. It contains a mirror which deflects the laser light passing the hole in the previous LD2 mirror. It is to protect the beam line segments beyond that point from damage caused by the laser pulses. If the mirror is not driven into the beam line, the laser may not be sent into the REGAE beam line. The electrons in turn can now drift towards the two FOS based diffraction detectors, passing additional TEM magnets and being finally dumped into a Faraday cup at the end of the beam line.

To summarize and disentangle this description of the beam line, figure 4.16 shows a schematic illustration of diagnostic elements.

4.3 Synchronization of the RF System and ANGUS

The synchronization between ANGUS and REGAE should be on a few 10 fs level in order to successfully demonstrate the injection and map out the wakefield. To achieve this, the following concept will be implemented, which is presented in detail in [33]:

Timing drifts between the rf reference generated from the rf master oscillator and ANGUS will be minimized by a Mach-Zehnder modulator based laser-to-rf phase detector [71, 132]. The setup has been built recently and tested [33]. It is similar to the concept described in [54]. This provides a drift free and very precise phase determination between rf and laser pulse trains. Also, it is a balanced scheme, meaning that it is virtually insensitive to fluctuations of the input optical power. The REGAE injector laser will be locked by the same mechanism.

In addition, there are instabilities and drifts in the distribution to various points where the reference rf signal is tapped. The source for such timing fluctuations is related to environmental disturbances, like for example temperature and humidity changes. Therefore, the plan is to set up an rf interferometer, based on a concept developed at Fermilab [133]. The basic principle of this instrument is to hold the end of a transmission line at constant phase, terminate the line with a short, and sum the forward and reflected wave at each directional coupler down the line to cancel out the phase drifts. By this synchronization scheme, the oscillators of the two lasers and the rf system should be locked with the required precision. The development of these systems is the topic of another Ph.D work. Please refer to [33] for a detailed description.

There are additional sources for timing fluctuations in the laser chains, as well as time-of-flight jitters of the REGAE electrons. The latter have been measured and analyzed in [134]. According to the results obtained, the fluctuations are about 50 fs, based on the phase and amplitude stability at REGAE. However, two major changes will be made to improve the situation. The first consists in the mentioned change to the phase locking of the gun laser to the rf system and the second in the implementation of a separate klystron, which will power the buncher cavity. The new rf-source allows for a more precise setting of the cavity parameters and eliminates coupling effects between the two resonators which are currently present.

Within the laser chains, environmental changes can and will cause an arrival time jitter at the target. For the gun laser, this translates into a phase instability of the gun, so that the electrons are emitted at slightly different accelerating gradients from shot to shot, contributing to the time-of-flight jitter. The pulses from ANGUS will likewise arrive at different time delays on target. In order to minimize this effect, the above-described BAC will be installed. It does not minimize

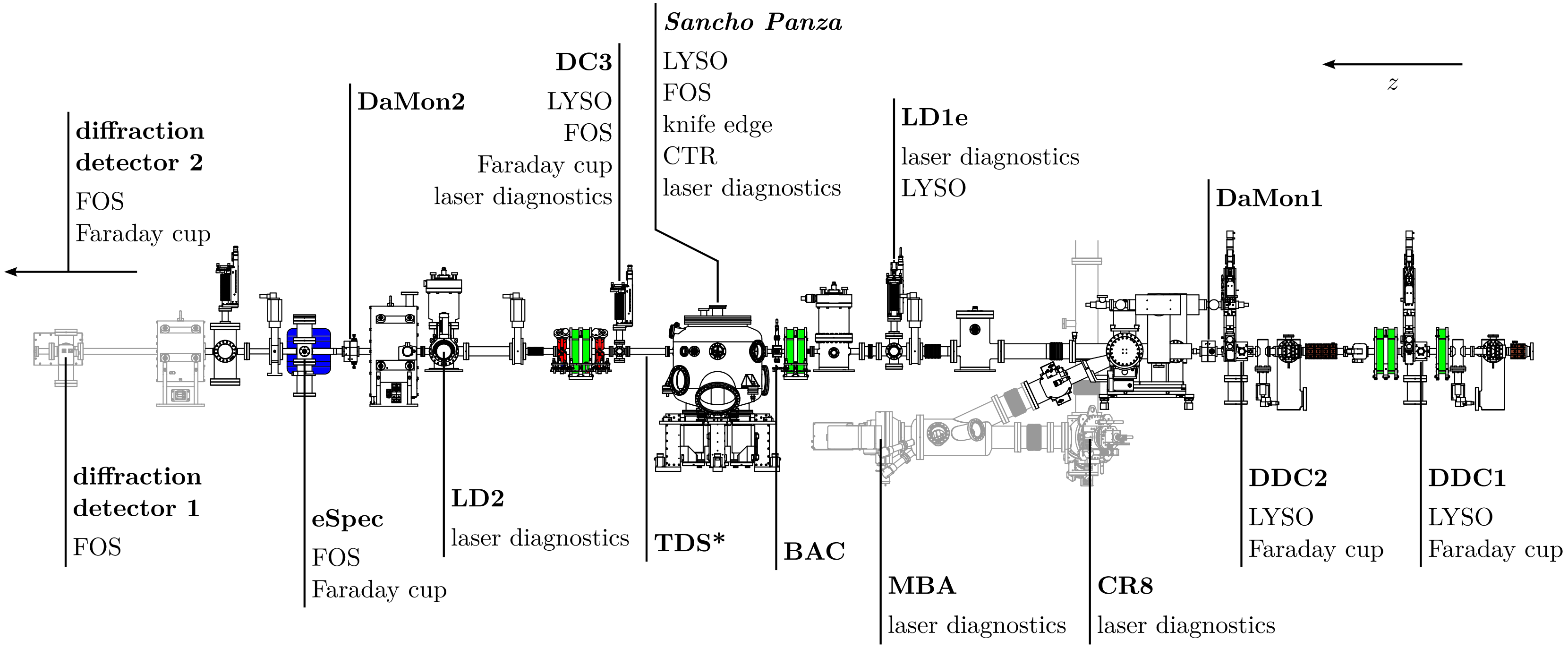

Figure 4.16 – Overview of the diagnostics elements at the upgraded REGAE beam line. The beam line is shown in a side view. *: The TDS is not depicted in the drawing.

the arrival time jitter, but allows for a sorting of the results by detecting the electron arrival time close to the target. The signal of the BAC includes all jitter sources, which can consequently be eliminated to a large degree from the measurements.

In order to change the delay between ANGUS and REGAE on purpose, as required for the phase scans in the external injection experiment, a delay stage will be included into the ANGUS laser chain.

4.4 Differential Pumping Section

The combination of a high-power laser beam line and a conventional accelerator brings additional complications, especially in the case of the planned LWFA experiments: As discussed, the experiment is conceived for a continues flow gas target, which seen from a vacuum system perspective is simply a (big) leakage. This, of course, conflicts with the demands set by a particle accelerator grade vacuum system. Hence, the gas load must be removed from the system as well and efficiently as possible. Ideally, the gas is removed before it enters the cavity sections, which are very sensitive to rising pressures, leading to break down effects and the emission of dark current.

The standard approach to deal with such a situation is to design and implement a differential pumping section, where the pressure is gradually reduced by the iterative combination of pumps and apertures which allow only for a small gas flow towards the direction of low pressure. In an optimal scenario, the apertures are displaced with respect to each other, and not aligned collinearly, in order to back-scatter particles coming from a high pressure zone. However, the beam pipe of a linear accelerator naturally does not offer the possibility for displaced apertures – at least without chicanes. In addition, the co-propagation of light pulses and electron bunches within one beam pipe towards the target chamber requires large diameters on the order of several centimeters to avoid clipping of the laser. This means the conditions somewhat undermine the concept of an efficient differential pumping section allowing for a significant pressure reduction.

Nevertheless, a differential pumping concept has been developed for the REGAE upgrade. It will be described and analyzed in the following.

4.4.1 Analytic Estimations

The rate of particles moving along a vacuum system of varying pressure $p(z)$ is characterized by the flow, $Q = -c(z)\,\mathrm{d}p/\mathrm{d}z$ [135], where $c(z)$ is the specific molecular conductance of the system, describing the probability of a particle passing the associated segment. The unit of this quantity in the following is $[Q] = \mathrm{mbar\,l/s}$.

If c is constant within a length L, for example in a pipe of constant diameter, the conductance is $C = c/L$. The description of the particle flow Q in a vacuum system with segments of two different pressure regions $p_{1/2}$ connected by a pipe can then be treated similar to a electric circuit of resistors: The pressure difference $\Delta p = p_1 - p_2$ corresponds to the potential difference, while the conductance value C of the pipe is treated like the conductance of the resistor. The resulting flow in the pipe corresponds to the current in the circuit analogue [87, 136].

A problem with this simplified description is that, strictly speaking, the pressure in the separate chambers is not known a priori, but instead adjusts dynamically, depending on the incoming and outgoing flow. However, vacuum science deals with orders of magnitudes, meaning that two chambers in a differential pumping section, connected by a pipe, usually have a large pressure difference so that this pressure difference can be approximated by the higher pressure. An iterative description of the differential pumping chain can then be deduced as follows: A flow Q_{in} enters a vacuum chamber which is equipped with a pump of a certain pumping speed S. The ratio of Q_{in} and S determines the resulting pressure p_1 in that chamber – and thus the potential difference $\Delta p \approx p_1$. If the chamber is connected to another vessel by a tube, which has a certain conductance value C, the flow into the next chamber can immediately be estimated to $Q_1 = C\,\Delta p \approx C\,p_1$. Using the pumping speed at that chamber, the next pressure can be determined and the iterative application of these steps allows for a calculation of the whole cascade.

The conductance depends on the mass, temperature, and density of the particles, as well as on the geometry of the connecting element. It describes the probability of a particle entering and passing the connection. For simple geometries it can be estimated with analytic calculations. More complex structures are typically evaluated using Monte Carlo simulations (see also 4.4.5), the results of which are, however, valid only in the molecular flow regime. This regime requires a low enough pressure, so that the mean free path L of the particles is (much) larger than the characteristic length of the vacuum vessels, D_{c}. This means that the probability of a collision with the chamber walls are much more likely than collisions with other particles. This is typically described by the Knudsen number $\mathrm{Kn} = L/D_{\mathrm{c}}$, which consequently should be larger than one for the molecular flow regime [136].

The conductance of a sequence of elements, for example pipes of different diameter or several apertures without pumping section in between, results from a summation of the reciprocals of the individual conductance values. Thinking back to the current circuit analogy helps to understand why this is the case: In a series connection resistance is calculated by the sum of the resistances of the single elements. The conductance is the analogous of the inverse resistance.

For molecular flow, which is assumed for the following analysis, the dependence of the conductance on the gas parameters scales typically with $\sqrt{T/M_{\mathrm{m}}}$, where T is the temperature and M_{m} is the molecular mass. Hence, the efficiency of a differential pumping section is higher for heavy gases at low temperature compared to light gases – like hydrogen – or gases at high temperature. The conductance of a circular aperture, C_{ap}, scales with the area and thus with d^2, where d is the diameter of the element. Inside tubes (C_{ln}) with a length l, the scaling is proportional to d^3/l [136]:

$$C_{\mathrm{ap}} = \frac{\pi d^2}{4}\sqrt{\frac{R_0 T}{2\pi M_m}}, \qquad C_{\mathrm{ln}} = \frac{\pi d^3}{3l}\sqrt{\frac{R_0 T}{2\pi M_m}}, \tag{4.7}$$

$$C_{\mathrm{tb}} = \frac{1}{1/C_{\mathrm{ap}} + 1/C_{\mathrm{ln}}}. \tag{4.8}$$

Here, R_0 is the universal gas constant. The last equation gives the result for a tube, which consists of the circular entrance aperture and the effects inside the tube. As pointed out, they have to be summed up reciprocally.

For hydrogen, the conductance values can be expressed in practical units as [136]

$$C_{\mathrm{ap}}(\mathrm{l/s}) = 0.346 \times d^2(\mathrm{mm}) \qquad \text{and} \qquad C_{\mathrm{ln}}(\mathrm{l/s}) = 0.461 \times \frac{d^3}{l}(\mathrm{mm}). \tag{4.9}$$

The values C_{ln} inside the tube are precise for a ratio of $l/d > 50$. For smaller values, a correction of up to 15 % can occur [136]. However, the formalism is used only to get an estimate on the pump strength required at certain points and to provide a measure to identify reasonable pump locations. Hence, equations (4.9) suffice for such a rough estimate. The final calculations will be crosschecked with results from Monte Carlo simulations.

4.4.2 Numerical Analysis

As described in the previous section, the vacuum pressure in the distinctive chambers will set dynamically in accordance with leakage/outgassing and pumping speed. This can be expressed by a linear differential equation [135],

$$\frac{\mathrm{d}}{\mathrm{d}z}\left[c(z)\frac{\mathrm{d}p(z)}{\mathrm{d}z}\right] - s(z)p(z) = -q(z), \tag{4.10}$$

where $c(z)$ is the specific conductance as defined above, $s(z)$ is the linear pumping speed, and $q(z)$ is the specific outgassing rate. If c, s and q are assumed to be piecewise constant, a solution to the problem can be achieved analogously to the transfer matrix approach of beam optics (see chapter 2). This is the basis for numerical tools like VAKTRAK [135], which has been used for the calculation of various accelerator vacuum systems.

The advantage of this tool is its computation speed. Furthermore, it is possible to determine the required pumping speed at certain locations in order to achieve a desired pressure. The disadvantage, on the other hand, is the dependence on the conductance values which have to be known. Therefore, additional calculations with the Monte Carlo code MOLFLOW+ [137] are used to crosscheck the results – despite the related computational effort. The analysis requires a 3D-model of the vacuum system, in which a cloud of particles is launched and reflected from the wall segments, following a probability distribution for the reflectance angle. The main challenge for a Monte Carlo simulation in this case lies in the goal of a differential pumping segment: A significantly reduced particle density in the low pressure region – in the case of the REGAE upgrade six orders of magnitude. To achieve a statistical significant result, about 1000 particles should hit the polygons in the low pressure region, i.e., about 10^9 particles have to be launched. However, depending on the complexity of the system – measured in number of polygons – the launch rate can get as low as one particle per second. There are two ways to reduce the complexity of the system. Either the system is simulated in segments which are combined later on, or the number of polygons in the whole system has to be minimized. The first approach has the disadvantage that the beam line has a closure at the separation points. Additional assumptions have to be made to set an artificial pumping speed for the separating surface to the following segment. Since this would be based on the analytic method, such an approach is not suited to serve as independent crosscheck. However, by properly modeling the system, it has been made possible to simulate the whole REGAE beam line with a launch rate of more than 10 000 particles per second, so that a result can be expected within a finite time scale.

The results obtained with VAKTRAK and in particular with MOLFLOW+ are still only valid for molecular flow.

4.4.3 Pumps

The last piece to describe the differential pumping section of the upgraded REGAE beam line is the choice of suitable pumps. There are different types, each with advantages and disadvantages, depending on the vacuum environment they are exposed to.

The pump type which is probably most known, is a **T**urbo **M**olecular **P**ump (TMP) [136]: Particles are pushed out of the vacuum system by several rotors which add a small momentum to particles entering the pump. TMPs can be used at comparatively high pressure regions, and thus will be used close to the gas target. However, there are several disadvantages, especially when dealing with hydrogen. A TMP requires an additional backing pump which removes the gas at the outlet; it cannot pump against atmospheric pressure. The pumping speed for light gases is relatively low, since these have a high velocity at room temperature, so that the additional kick from the rotors has only a small effect. Also, the compression ratio, which is the ratio of the inlet pressure compared to the outlet pressure, is limited by this effect: The reference gas for the performance of a TMP is nitrogen, for which compression ratios on the order of 10^9 can be achieved. In contrast, this value is typically about 10^4 for hydrogen. Also the pumping speed is only about 70 % of that of nitrogen.

In addition, there are several safety issues. First of all, hydrogen is an explosive gas, as discussed in 4.2.2. Hence, additional infrastructure for the exhaust of the backing pump is required: A (monitored) dilution with nitrogen is necessary, as well as a controlled emission into the environment via a leak tight pipe system. Direct hazards derive from the tremendous rotational energy stored in the rotors of the pump. The pumps directly at the target chamber, for example, have a torque at failure of about 50 kNm, which in case of a crash could be released with devastating effects and with possibly lethal consequences for persons in the proximity of the disintegrating pump. The housing of the pump should resist such an event, but the mounting of the pump must also withstand such an impact – leading to bulky constructions for such big TMPs.

To avoid a crash, additional splinter guards have to be included in the setup, protecting the rotors from small parts like screws falling into the pump – and reducing the pumping speed by an additional 10 % [117]. Magnetic (stray) fields of surrounding magnets, for example used for the accelerator's beam optic, must be below a certain threshold at the TMPs location: Resulting eddy currents would heat up the rotors, leading to an expansion and ultimately a collision of the rotor with the casing [138].

On the other hand, there are also requirements for the pump stemming from the experiments themselves: Only magnetic bearings are allowed for the REGAE vacuum system, because of the danger of hydrocarbon contamination by lubricants [27, 138]. Thus, the pump is a source for magnetic fields, which could disturb the electron beam of comparatively low energy, so that a sufficient distance between the pump and the beam axis is mandatory. To avoid a backwards venting through a failing TMP– including particle and possible hydrocarbon contamination from the exhaust – a vacuum shutter should be installed at the inlet side of the pump. However, only full-metal sealed valves are allowed, which have a price in the range of the (expensive) pump itself and more. Finally, vibrations of the pump should be as low as possible, and ideally decoupled from the experiments – which is, however, in contrast to a rigid mounting of the pump due to the required bellows.

Another class of pumps are getter pumps. There are various types, three of which will be shortly introduced here. **I**on **G**etter **P**umps (IGPs) use the Penning discharge mechanism to trap an electron cloud [136]. The electrons ionize gas atoms and molecules by impact ionization. The ions are accelerated towards the cathodes and buried into the cathode material. On impact, the chemically active cathode material is sputtered onto the surrounding surfaces, acting as a fresh getter material which binds atoms and molecules by chemisorption and physisorption. By these mechanisms, IGPs are suited to reach vacuum pressures down to 10^{-11} mbar, but at pressures on the order of 10^{-4} mbar, saturation takes place very rapidly. In the case of hydrogen, the second binding mechanism is much more likely combined with a diffusion of the gas into the cathode material; a sputtering does not occur. The consequence is that the pumping rate does not reduce for hydrogen, in contrast to heavier gases where the cathode surface slowly becomes coated. Also, saturation takes much longer and can be delayed even further when thicker titanium cathodes are used. Hydrogen optimized versions can be operated for about 75 000 hours at a pressure of 10^{-6} mbar. For each order of magnitude less the operating time is increased by a factor of ten; this scaling is also valid in the opposite direction [117]. The Penning mechanism used has the side effect that one can determine the pressure inside an IGP by measuring the current in the pump. This is the standard method applied at DESY. For that purpose, small IGPs are even attached to segments which are pumped by different pump types [138].

The pumping speed of IGPs can reach about 1000 l/s for nitrogen, and is even higher by 50 % and more for hydrogen [117]. There are no moving parts inside and also, naturally, no lubricants, so that a contamination of the system with hydrocarbons cannot occur. But, due to the large volume occupied by the required cathodes and especially the big magnets, IGPs with such a high pumping speed are very heavy and bulky. Furthermore, the magnetic field is again a source for disturbances of the beam within an accelerator. For pumping of inert and especially noble gases, special material combinations are required.

Titanium **S**ublimation **P**umps (TSPs) also use chemisorption to bind particles [136]. A pump of this type consists of a titanium filament inside a chamber – typically a simple pipe. The filament can be heated by a high current so that the sublimation temperature of the metal is reached, which leads to a clean titanium layer coating at the wall of the surrounding chamber. This process has to be repeated when the pumping speed drops due to saturation. Pure titanium is excellent in binding reactive gases, but has a rather poor performance for noble gases. Hence, TSPs, which easily reach pumping speeds of 1000 l/s, are typically supported by another pump, for example a small (noble gas optimized) IGP [138].

TSPs are comparatively cheap and flexible due to the simple design. In addition, no magnetic or vibrating components are used, hence, a disturbance of the experiments or the beam is not possible – at least as long as there is no refreshing cycle in progress. In order to keep the refreshing rate low, the pressure should be well below 10^{-6} mbar. A disadvantage of TSPs is the coating process: They cannot be used in the vicinity of optical components since these would be coated as well, leading to a degradation in performance. In the case of a higher power laser, this in turn leads to the probability of severe damage to the component – and, thus, to a possible particle contamination of the vacuum system.

Non-**E**vaporable **G**etter pumps (NEGs) are similar to TSPs in terms of the pumping mechanism [136]. They, too, use the high chemisorption capability of pure metals. In these pumps, however, the metal is present in a porous alloy or powder. Since the pure metals are easily coated with oxygen, NEG pumps need to be activated by being heated to around 500 deg C. This allows the oxygen (and other bound atoms) to diffuse into the material, refurbishing the pump. As a consequence, a NEG cannot be switched off but simply pumps until saturation – which requires another activation cycle to restart the pump. NEGs provide the highest pumping speed per active volume and are especially efficient in pumping hydrogen, which directly diffuses into the material, forming a *solid solution* [136].

NEG pumps are very lightweight and compact considering their pumping speed. They have a mass of less then 10 kg even for a pump such as the one used at the upgraded REGAE beam line, which has a pumping speed of 3500 l/s for hydrogen. NEGs do not have any vibrating parts nor do they require any magnetic field. Their permeability is also negligible. But, in case of a machine venting, they simply pump until saturation – restricting access to NEG pumped segments to a minimum, since activation can only be done a few ten times. Also, these pumps cannot be used to pump noble gases, and, thus, need to be supported by additional pumps of a different kind [138].

In summary, TMPs are rather inefficient for pumping hydrogen and come with a lot of problems and hazards, leading to an overall bad cost-benefit-ratio. They are, however, indispensable in the regions of higher pressure. Getter pumps are a more convenient choice due to the better hydrogen pumping speed compared to the price, as well as the safer storage of hydrogen by trapping it in the getter material. All three discussed getter types will be used at the upgraded REGAE beam line, depending on the location and required pumping speed.

4.4.4 Concept

From the discussion of the previous sections it becomes clear that in order to reduce the pressure along a differential pumping section, the diameter of the connecting elements should be as small as possible, while the pumping speed should be maximized. Because the high-power laser is to be included into the beam line, there is a minimum pipe diameter which cannot be undercut.

This threshold is set to 1.65 times the $1/e^2$ diameter of the laser's intensity profile as pointed out in 4.2.2.

It follows that in the co-propagation sections, the pipe diameter will be several centimeters leading to conductance values of hundredths of liters per second. Hence, the differential pumping in the region upstream of the target – towards the accelerating cavities – will consist of two sections: one close to the target until the laser beam size requires too large beam pipes, so that an efficient pumping is rendered useless, and one between the cavities and the ICR, since there is no lower limit to the beam pipe diameter given by the laser beam.

Using the above-described methods, the following pumping concept has been developed; an overview of the pump locations is shown in figure 4.17: The target chamber is pumped by two 1500 l/s TMPs. In order to overcome the compression limit, these pumps are supported by an additional 300 l/s turbo pump which is added at the exhaust side of the TMPs at the chamber. Thus, an overall compression greater than 10^8 should be within reach – which is important in order to pump the chamber down to a reasonable pressures when the hydrogen supply is not in operation. (A compression limited TMP cannot reduce the pressure below the limit given by the compression rate, even if there is no more gas flow [87].) In order to achieve the desired pressure of $p_{\mathrm{gt}} = 0.2\,\mathrm{mbar}$ in the gas target, corresponding to a plasma density of $n_{\mathrm{e}} = 10^{16}\,\mathrm{cm}^{-3}$, a conservative estimate yields a required flow of $Q_{\mathrm{gt}} = 1\,\mathrm{mbar\,l/s}$, as determined by measurements using first prototype targets [87, 76].

The pressure inside *Sancho Panza* is, hence, expected to be $p_{\mathrm{SP}} = 3.3 \times 10^{-4}\,\mathrm{mbar}$ during operation, owing to the overall pumping speed of 3000 l/s of the attached TMPs. The flow to the next chamber (nEVOC3) is determined by the 21 mm beam pipe with a conductance of $C_{\mathrm{BAC}} = 10\,\mathrm{l/s}$. At nEVOC3 another 800 l/s TMP is installed, supported by another small TMP. The ratio of pumping speed and flow results in a pressure on the order of $p_{\mathrm{nE3}} \approx 10^{-5}\,\mathrm{mbar}$. The pressure is determined by a small IGP, which is the standard method at Desy. Hence, at the subsequent pumping point – NEGcross – it is already possible to place a strong NEG: This device has a pumping speed of 3500 l/s, so that it can maintain a pressure below $p_{\mathrm{Nc}} < 10^{-6}\,\mathrm{mbar}$, and thus does not saturate too quickly. The NEG section can be separated from the target area by a vacuum shutter, in order to keep the NEG in a vacuum environment if *Sancho Panza* is vented, for example in the case of a target change. Behind the NEGcross, the beam pipe diameter is too large to support an efficient differential pumping.

The next limiting aperture is thus at the holey mirror inside the ICR. Here, finally, the conductance can by efficiently reduced since the diameter of the hole is only 5 mm; it is extended by a hole with the same diameter in the collimator piece behind the reflector protecting the glass substrate. The conductance at this point is estimated to be less than 5 l/s. The mirror chamber is pumped by another NEG (2000 l/s) to capture particles reflected at the mirror and entering the system from the laser transport line. The pressure at the holey mirror is about $10^{-7}\,\mathrm{mbar}$. Behind the mirror-collimator, two TSPs (1000 l/s) separated by a 21 mm pipe are placed, followed by the unchanged Regae front-end. In this section, four more pumping ports are located: two right in front of the cavities at the rf couplers and two at the diagnostic stations DDC1/2. Each of these is equipped with a TSP-IGP combination. However, the respective pumping speeds are

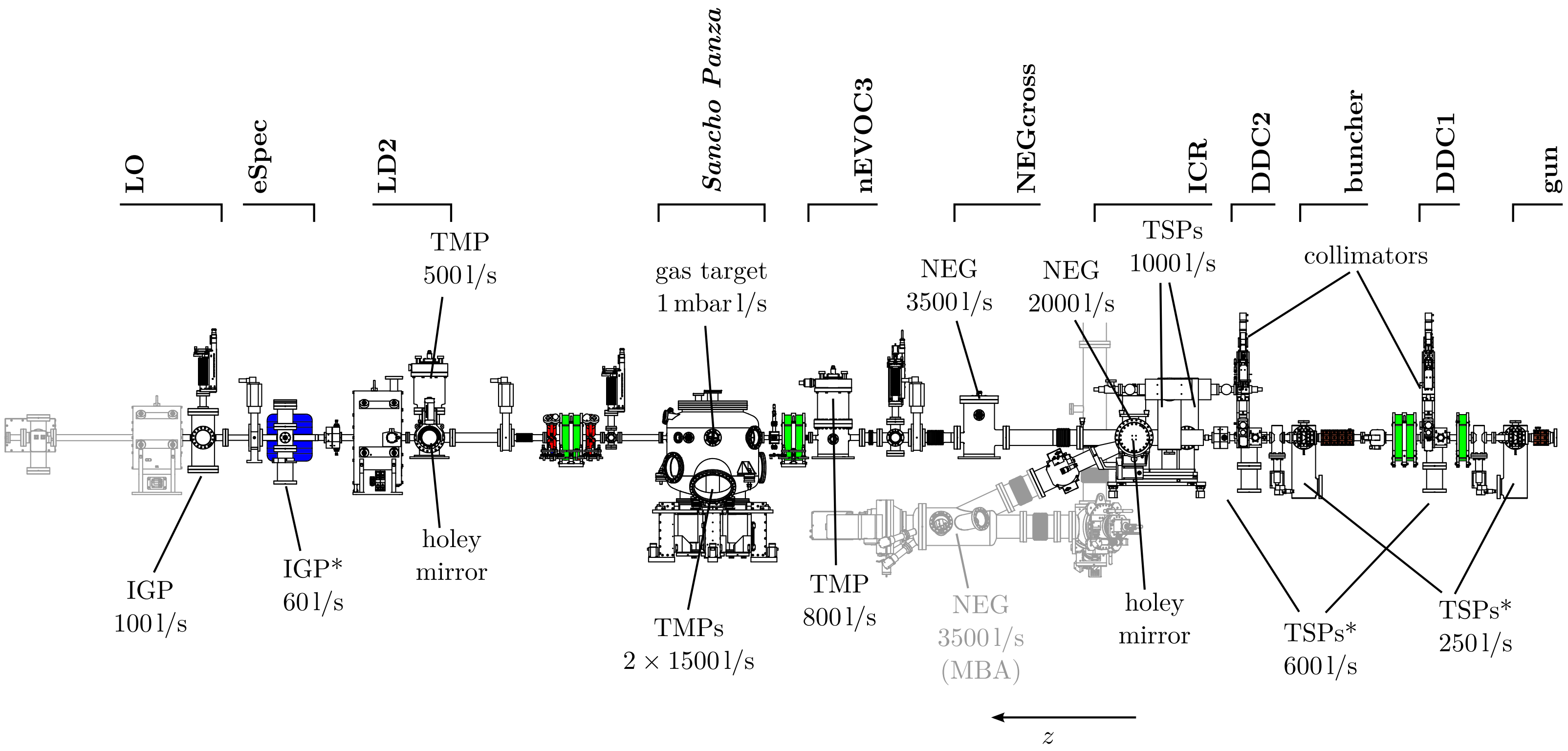

Figure 4.17 – Overview of the pumping scheme for the differential pumping concept at REGAE. The beam line is shown from the side. The values marked with * are corrected for the conductance of the pipes connecting the respective pump to the vacuum system, limiting the obtainable pumping speed.

IGP: **I**on **G**etter **P**ump — NEG **N**on-**E**vaporable **G**etter pump — TMP: **T**urbo **M**olecular **P**ump — TSP: **T**itanium **S**ublimation **P**ump

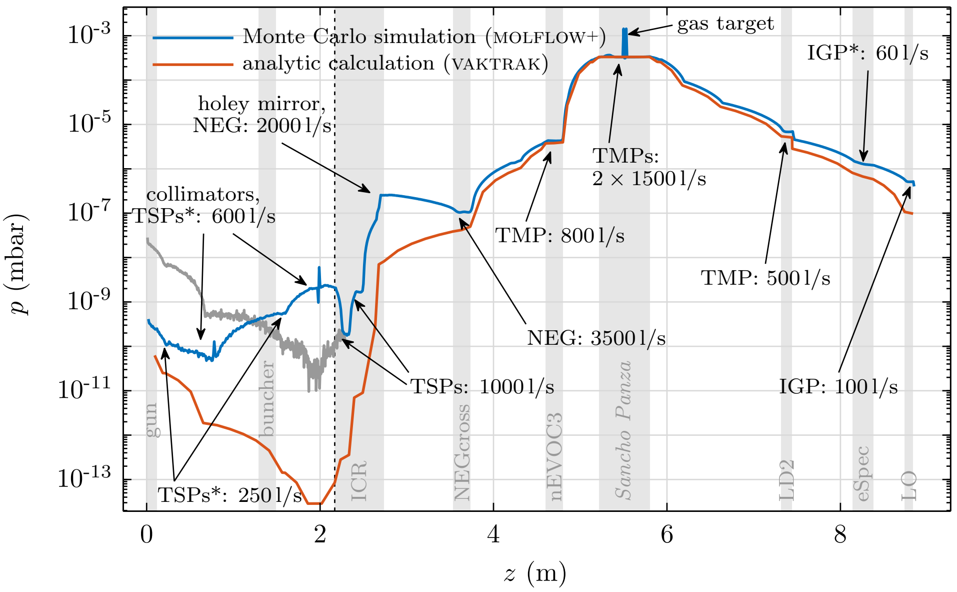

Figure 4.18 – Calculated pressure profiles for the REGAE beam line. In the low pressure regions, the analytic calculation shows a large deviation from the Monte Carlo simulation. This is caused by beaming effects which are not taken into account by that model: The Monte Carlo results show a pressure rise at the ICR, due to particles reflected at the holey mirror. In the accelerator sections it is necessary to use the collimators, which interrupt the beaming effect at this point. Without collimators a pressure above $p_{\text{gun}} > 10^{-8}$ mbar arises in the gun, depicted by the gray curve. With collimators, the pressure drops by more than six orders of magnitude along the beam line, so that the pressure inside the cavities is below $p = 10^{-9}$ mbar. The black dashed line depicts the position of DaMon1, i.e., the entrance into the REGAE front-end. The speed of the pumps marked with * has been adjusted to account for the conductance values towards the pump inlet.

reduced due to apertures limiting the conductance to the pumps. In addition, the collimators are also located at DDC1/2. In terms of the differential pumping, they are used as apertures, reducing the flow towards the cavities, so that a sufficiently low pressure, $p_{\text{gun}} < 10^{-9}$ mbar, can be achieved in the gun.

Upstream of the target chamber the pressure demands are more relaxed. Here only one TMP is used in order to reduce the pressure and flow to values allowing for IGPs to be used to maintain a pressure below $p < 10^{-6}$ mbar.

4.4.5 Results

The overall design of the differential pumping section is analyzed by two methods. First, the code VAKTRAK [135] is employed to determine and verify the estimated pumping speeds. Then, the result is crosschecked with the Monte Carlo simulation MOLFLOW+ [137].

The result of the VAKTRAK calculation can be seen in figure 4.18. The planned setup reduces the pressure towards the cavities below a value of $p = 10^{-9}\,\mathrm{mbar}$, which fulfills the design criterion. The values below $p = 10^{-10}\,\mathrm{mbar}$ as suggested by the analytic calculation are, however, not feasible: Outgassing of the vacuum pipes will lead to an equilibrium condition at higher pressures. Also, so-called beaming effects reduce the efficiency of the differential pumping setup. This will further be discussed below. The pressure rise towards the gun is due to the boundary conditions assumed for the solution of the differential equation system. In the downstream direction, the analytic model likewise predicts that the required parameters can be achieved.

The comparison with the MOLFLOW+ results shows a very good agreement in the higher pressure regions. However, at the ICR an unexpected pressure rise can be seen. It results from beaming effects [26, 136]: Since there is no offset of the apertures and tubes, which limit the conductance between the pumping sections, the whole setup works like a filter and rectifier: Particles which start at the target on trajectory close to the electron axis never hit a wall and thus cannot be deflected towards a pump, since there are no particle-particle interactions. Moreover, the thin pipes in the pumping sections redirect particles on that path: Inside a tube, atoms and molecules are scattered at the wall until they are on a path close to the beam axis which allows them to leave that tube. These atoms and molecules thus pass through the system until they hit the holey mirror and are reflected in a random direction. Therefore, the pressure drop at the NEGcross is overestimated: The particle flow is directed past the associated pump and these excess particles increase the pressure towards the ICR. A similar effect occurs at the gun cathode, caused by the apertures in the ICR, leading to a pressure rise above $p = 10^{-8}\,\mathrm{mbar}$ in the gun cavity. (This increase in pressure is indicated by the gray colored profile in figure 4.18 in the cavity region.)

An illustration of that effect is shown in figure 4.19. It shows the number N_1 of particles traveling on a trajectory which has an angular deviation of less then 1 deg from the z-axis, that is, the beam pipe direction. The value is taken at seven different positions between *Sancho Panza* and the gun, and normalized to the respective amount of all particles passing the various points, N_{tot}. As can be seen, at the height of the ICR, almost all particle trajectories are confined to that narrow cone. The same effect can be seen at DDC2, caused by the apertures of the ICR. If, however, the collimator is used, the majority of particles is reflected at this device, leading to a randomization of the propagation directions. The same effect occurs at the gun cathode in both the case with and without collimator, explaining the low value of the ratio $N_1/N_{\mathrm{tot}} < 0.2$ for either of the cases. However, the overall number of particles, N_{tot}, is much less at this point if the collimators are used.

In other words, the collimator reduces the acceptance angle of the filter. The randomization prior to the cavities at the same time increases the pumping efficiency at DDC1 and DDC2, while the pressure in the gun is reduced. Using both collimators with an aperture diameter of 1 mm results in a pressure of $p_{\mathrm{gun}} < 10^{-9}\,\mathrm{mbar}$, and is thus sufficiently low. As discussed, the incoming flow at the target ($Q_{\mathrm{gt}} = 1\,\mathrm{mbar\,l/s}$) is also estimated very conservatively, so that the real value at the gun should be even lower.

Please note: The outgassing of the beam line components has not been analyzed. In that sense, the pressure determined above is only the partial pressure contribution when the plasma experi-

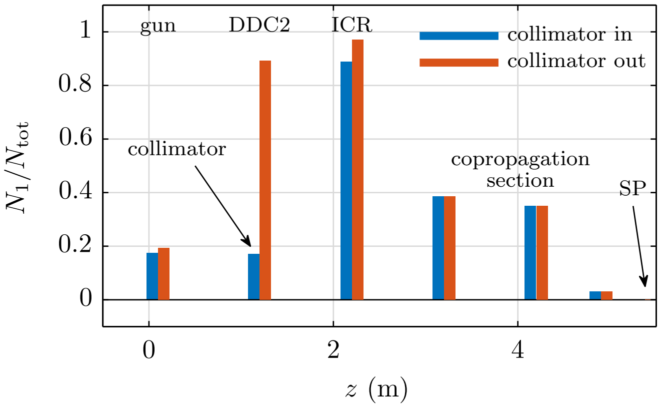

Figure 4.19 – Relative number of gas particles with a trajectory within an angular cone of 1 deg around the accelerator axis at various positions between gun cavity and *Sancho Panza*. Towards the cavities, almost all particles are confined to that narrow cone, that is, beaming occurs. Using the collimator at DDC2 interrupts that effect; the same is true for the gun cathode. The collimators increase the pumping efficiency at DDC1 and DDC2, so that the pressure in the REGAE front-end stays below $p = 10^{-9}$ mbar. Inside the gun the confinement to the 1 deg cone is not given in either case, since the particles are scattered at the cathode and reflected in a randomized way, so that the distribution is similar. The overall amount of particles is less with the use of collimators, though. Hence, the resulting pressure is lower in that case.

ment is carried out. However, since the first segment of the beam line is unchanged compared to the previous machine, it is known that in this segment part the outgassing rate is low enough to achieve the desired final pressure. In the new section, the surface area of the components is larger compared to the old machine and, consequently, the same holds true for the overall outgassing. But the pressure is on the order of 10^{-7} mbar in this region due to the partial pressure of the hydrogen gas so that the contribution from the properly cleaned and heated beam line segments is expected to be much lower. Furthermore, also for these effects the pumping stage is effective.

The contribution from the laser beam line can be treated as an additional outgassing. To keep this influence low, the MBA chamber, which is close to the joint of the beam lines – and close to the cavities –, is pumped with another 3500 l/s NEG pump, so that the flow contribution is negligible, or even better directed *towards* the MBA if the pressure in this is lower compared to the REGAE beam line, in particular the ICR; see figure 4.17. In addition, another IGP is located at this point to determine the pressure and, more importantly, to reduce the partial pressure of non-reactive gases in the co-propagation segment, mainly pumped by NEGs.

In conclusion, the differential pumping section described in this part is well-suited to reduce the partial pressure of hydrogen stemming from the plasma experiment. It is capable of a pressure reduction by more than six orders of magnitude, despite the continuous flow operation of the plasma cell. Since the incoming flow at the target is assumed with a large safety margin of more than one order of magnitude, the pressure rise at the cavities should be small enough for an undisturbed accelerator operation. Also, this overestimation could enable a possible operation at higher gas densities.

4.5 Summary

In this chapter, an overview of the whole experimental setup has been given. The external injection experiment requires a high-power laser (Angus), an accelerator (Regae), as well as the synchronization of these two systems on the level of few 10 fs. For the verification and analysis of the injection process, the Regae beam line has to be upgraded with various diagnostics and adapted for the needs of the laser propagation. Furthermore, Regae cannot be used exclusively for this purpose. Instead, two more experiments are planned and carried out at the machine and need to be taken into consideration when it comes to the beam line upgrade.

Therefore, a sophisticated target chamber (*Sancho Panza*) has been developed, respecting the various demands and restrictions. Furthermore, all relevant segments for the external injection experiment have been drafted in this chapter, such as the upgraded electron spectrometer or the various beam position diagnostics. An important part of the new electron beam line is the differential pumping section. It allows for the reduction of the pressure between the target chamber and the Regae front-end by six orders of magnitude. Hence, the pressure in the accelerating structures is low enough to allow for a stable operation – despite the gas flow from the plasma targets.

The upgraded beam line is scheduled to be commissioned in the second quarter of 2017. Apart from the ongoing diffraction projects and the newly introduced transmission electron microscope option, the machine will be well-suited to perform the external injection experiment under stable conditions, making use of the full repetition rate of Angus, especially due to the continuous flow operation.

This concludes the analysis and illustration of the external injection experiment and the requirements in order to achieve the project goals. In contrast, the next chapter is not purely focused on this special case, but deals with longitudinal electron beam dynamics. It is about the optimization of the bunch compression, especially in the case of the ballistic bunching method used at Regae – also in the case of external injection.

5 Linearization of the Longitudinal Phase Space Without Higher Harmonic Field

Modern particle accelerator applications, like FELs or time-resolved electron diffraction as performed at REGAE, require bunches of very short longitudinal extent. Likewise, the external injection experiment described in this thesis is reliant on an electron bunch duration which is only a small fraction of the plasma wavelength. A limit for the shortest achievable bunch length is set by space charge repulsion. However, another reason that hinders the maximal achievable longitudinal compression are nonlinear phase space correlations. At modern FEL facilities, like FLASH [43] or the European XFEL [44], the phase space is linearized using a dedicated cavity, which is operated at a higher harmonic frequency of the main rf system [45–47]. In the course of this Ph.D. work, another method has been developed, which is described in this chapter. It is based on a controlled beam expansion of the electron bunch after the gun. If the stretched bunch enters a cavity, operated at the fundamental rf frequency, this has similar effects to a bunch of unchanged length passing higher harmonic structure, i.e., a field of shorter wavelength. The novel method is denoted as *stretcher mode*.

The concept is described and analyzed in the following, largely based on the REGAE geometry which is used *exemplary* to test and demonstrate the approach. The derived formalism is based on the so-called ballistic bunching mechanism [51, 52]. However, the approach is not limited to that. Also, a compression using a magnetic chicane [139] can, in principle, be included in the description.

In the first part of the chapter, an analytic description of the process is derived, which is based on the longitudinal bunch kinetics in a free drift. This model is afterwards tested using ASTRA. According to the simulation, an optimization of the REGAE bunches by one order of magnitude is feasible, compared to the design value: A linearized bunch shorter than 1 fs is demonstrated – including space charge repulsion. In the context of such a third-order corrected bunch, a special case, the *overcompensation mode*, is introduced.

Another application of the stretcher mode is the compensation of the energy spread acquired in the gun cavity, using the buncher. The resulting electron distribution has a remarkably low energy spread of $T_{\text{RMS}}/\left\langle T\right\rangle < 10^{-5}$. A beam with such properties is very interesting for the transmission electron microscopy experiment planned at REGAE.

In the last section of this chapter, possibilities of applying the method detached from the REGAE geometry are explored. Varying the focus position, for example, allows for even shorter bunches, entering the attosecond regime for extremely low charges ($1\,\text{as} = 10^{-18}\,\text{s}$). Also, the option to produce electron bunches with a micro-bunching structure of high quality is discussed. Furthermore, the extension of the concept to larger machines in terms of a transport of such optimized bunches is addressed. And finally, an attempt is made to inject such a compressed bunch into a plasma wakefield, thus coming back to the previous discussions in this Ph.D. work.

The first part of the chapter is closely related to the publication, which emerged from the derivation of the concept [48].

5.1 Ballistic Bunching

Longitudinal beam dynamics is described in the longitudinal phase space. In the following, this subspace is constructed from the respective particle position in the co-moving frame, ζ, and the particles energy, expressed in terms of the Lorentz factor, γ. The bunch length is thus the width of the resulting distribution in ζ. Typically, the RMS value is chosen as a measure. The current profile associated with the bunch is a projection of the number of particles onto the ζ-axis.

In order to compress a bunch, a negative energy correlation must be imprinted. That is, the tailing electrons should have a higher energy than those in the front. Depending on the mean velocity of the bunch, there are then two options to shorten the bunch extent. Either – for high energy particles – a magnetic chicane must be used, or a simple drift can suffice. The magnetic structure makes use of different path lengths determined by the dispersion in dipoles (similar to an electron spectrometer, see section 4.2.2): Particles with higher energy have a more rigid trajectory and thus a shorter path, while those with less energy experience a larger offset and thus travel a longer path. Ideally, the distance between the particles is reduced after the chicane, i.e., the bunch is compressed.

The ballistic bunching works in a similar manner. However, in this case, the velocity difference compared to the mean velocity is large enough for the higher energy particles in the back to outrun the slower electrons in the front within a reasonably finite distance. This method is used at REGAE, and the subsequent sections will be based on this scenario.

The longitudinal shift, $\Delta\zeta$, between two particles within a drift $z_0 \to z$ to first order is given by

$$\begin{aligned}\Delta\zeta(z) &:= \Delta v(z)\Big(t(z) - t(z_0)\Big) = \frac{1}{\bar{\beta}}\Delta\beta(\gamma)(z - z_0)\\ &= \frac{1}{\bar{\beta}}\left[\frac{\mathrm{d}\beta}{\mathrm{d}\gamma}\Big|_{\bar{\gamma}}\delta\gamma\right]_{z_0}(z - z_0) = \left[\frac{1}{\bar{\gamma}^3\bar{\beta}^2}\delta\gamma\right]_{z_0}(z - z_0)\,.\end{aligned} \tag{5.1}$$

Here, β is again the velocity normalized to the speed of light, c, and $\gamma = 1/\sqrt{1-\beta^2}$ is the Lorentz factor, characterizing the particle energy. $\bar{\beta}$ and $\bar{\gamma}$ are these quantities, determined for the central particle of the bunch, located at $\zeta = 0$. That position also marks the center of the linear approximation. $\delta\gamma$ denotes the energy difference from $\bar{\gamma}$. $[\,\cdot\,]_{z_0}$ means that the expression has to be evaluated at $z = z_0$. Figure 5.1 shows the bunch length evolution for an exemplary case, as well as the phase space distributions at several points along the electron path. After

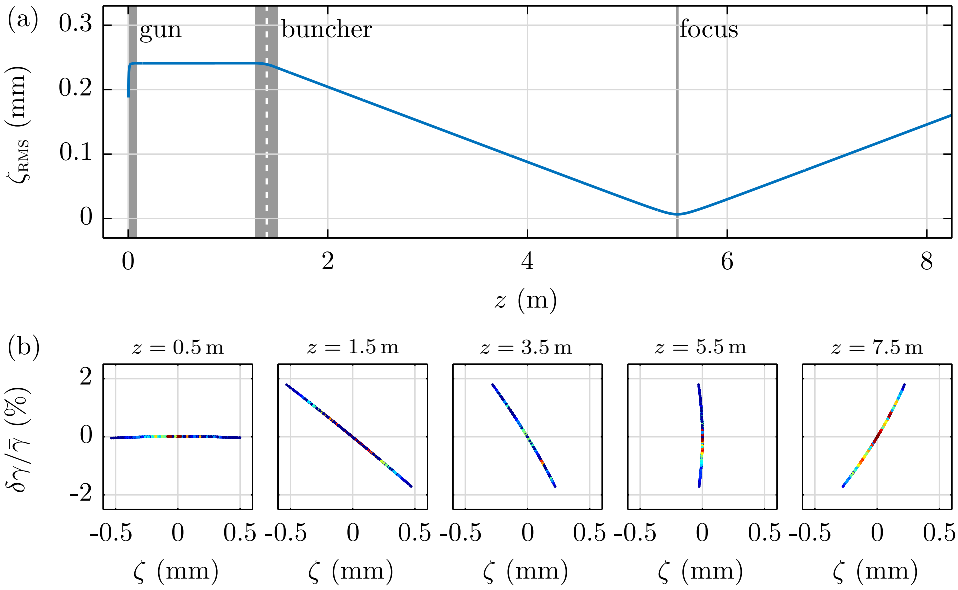

Figure 5.1 – Ballistic bunch compression: Figure (a) shows an exemplary bunch length evolution. Figures (b) depict the process in the longitudinal phase space. In the buncher cavity, a negative, almost linearly correlated energy spread is imprinted. In the subsequent drift, the bunch length reduces until the focus is achieved, and the bunch starts to lengthen again. Space charge effects are excluded in this ASTRA simulation.

the buncher cavity at about $z = 1.3\,\mathrm{m}$, an (almost) linear correlated energy spread is imprinted, leading to a longitudinal focus at $z_{\mathrm{f}} = 5.5\,\mathrm{m}$.

It is noteworthy that the shift between the particles scales with $1/\gamma^3$, i.e., for high energies and thus large γ-factors, the shift between the particles is strongly suppressed, and the bunch shape freezes out. In other words, ballistic bunching is no longer an efficient way for the bunch compression. Magnets must be employed, instead.

5.1.1 Higher Order Effects

The ideal distribution at the position of the longitudinal focus would be a straight, upright line. However, taking a closer look at the phase space at the location of the shortest bunch extent reveals a parabolic shape (see figure 5.2).

There are two reasons for this nonlinearity. First of all, the energy correlation is not linear, not even at the beginning. The bunch has a finite length and thus covers a finite phase interval in the gun. Since the accelerating field is curved, obeying a sinusoidal shape, and there is additionally considerable slippage of the bunch with respect to the phase of the field, a nonlinear energy correlation accumulates. This can already be seen in figure 5.1(b): The energy distribution decreases towards the edges of the bunch.

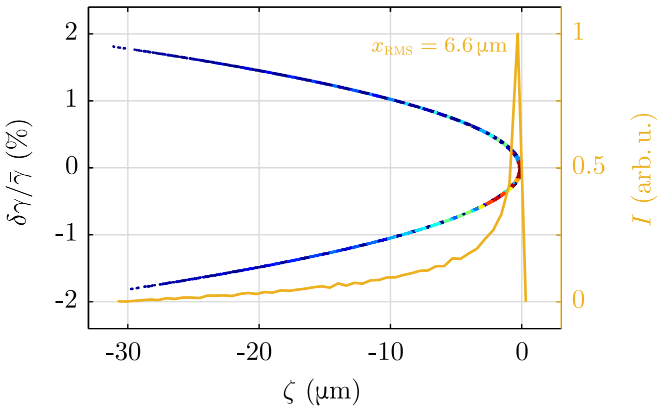

Figure 5.2 – Close up of the phase space in the longitudinal focus for the same case as in figure 5.1. As can be seen, the particle distribution has a parabolic shape, which limits the minimal bunch extent. The gray line depicts the corresponding current profile.

Moreover, even for a linearly correlated energy spread, a curvature will build up during the drift. This second effect is based on the nonlinear dependency of velocity and energy: $\gamma = 1/\sqrt{1-\beta^2}$. This means that for a more exact description, equation (5.1) has to be extended by means of a Taylor expansion around the energy of the central particle, $\bar{\gamma}$, i.e., at $\zeta = 0$. The equation then reads [51]:

$$\Delta\zeta(z) = \frac{1}{\bar{\beta}}\left[\frac{\mathrm{d}\beta}{\mathrm{d}\gamma}\bigg|_{\bar{\gamma}}\delta\gamma + \frac{1}{2}\frac{\mathrm{d}^2\beta}{\mathrm{d}\gamma^2}\bigg|_{\bar{\gamma}}(\delta\gamma)^2 + \frac{1}{6}\frac{\mathrm{d}^3\beta}{\mathrm{d}\gamma^3}\bigg|_{\bar{\gamma}}(\delta\gamma)^3 + \cdots\right]_{z_0}(z - z_0)\,. \tag{5.2}$$

The coefficients of this Taylor polynomial are given by:

$$\begin{aligned}
\eta_1(\bar{\gamma}) &:= \frac{1}{\bar{\beta}}\frac{\mathrm{d}\beta}{\mathrm{d}\gamma}\bigg|_{\bar{\gamma}} = \frac{1}{\bar{\gamma}^3\bar{\beta}^2},\\
\eta_2(\bar{\gamma}) &:= \frac{1}{2\bar{\beta}}\frac{\mathrm{d}^2\beta}{\mathrm{d}\gamma^2}\bigg|_{\bar{\gamma}} = \frac{2-3\bar{\gamma}^2}{2\bar{\gamma}^6\bar{\beta}^4},\\
\eta_3(\bar{\gamma}) &:= \frac{1}{6\bar{\beta}}\frac{\mathrm{d}^3\beta}{\mathrm{d}\gamma^3}\bigg|_{\bar{\gamma}} = \frac{2-5\bar{\gamma}^2+4\bar{\gamma}^4}{2\bar{\gamma}^9\bar{\beta}^6}.
\end{aligned} \tag{5.3}$$

From this kinetics, it is apparent that almost any energy distribution will generate higher order distortions in the longitudinal phase space, solely due to a free drift. As can be seen, the higher order terms rapidly vanish for large γ-values, so that the effects are strongly suppressed for high energies. However, in almost any conventional accelerator, there is a drift between electron source and first booster cavity, where the energy is in the order of a few MeV, so that an initial curvature will build up.

The effect of a cavity on the phase space curvature can be expressed in a similar manner. The bunch covers a finite phase intervall $\pm\delta\phi$ around the nominal accelerating phase ϕ. Hence, again a Taylor expansion in $\delta\phi$ can be employed around ϕ. An important prerequisite for this approach is that the uncorrelated energy spread is less than the correlated energy spread. If this is the case, the longitudinal phase space structure can be described by a function. (In other words, the phase space distribution can be treated as a line and does not have ambiguities in ϕ.) Since the central particle is located at $\zeta = 0$ in the longitudinal phase space, and this point corresponds to ϕ, the Taylor polynomial can be written in phase space coordinates, using $\delta\phi = -k\zeta$. Here, k is the wave number of the accelerating rf field.

The energy gain $\Delta\gamma$ in a cavity thus can be expressed as

$$\Delta\gamma\left(\zeta_{\mathrm{c}}\right) = \tilde{A}_0 + \tilde{A}_1\zeta_{\mathrm{c}} + \tilde{A}_2\zeta_{\mathrm{c}}^2 + \tilde{A}_3\zeta_{\mathrm{c}}^3 + \cdots. \tag{5.4}$$

The phase space coordinate, ζ_{c}, is taken at the position $z = z_{\mathrm{c}}$ of the cavity; the $\tilde{A}_i$ are the Taylor coefficients. The energy gain is added on top of the already present energy distribution of a bunch entering a cavity, marked by $\hat{\gamma}$. It is likewise expressed in ζ_{c}, and thus the resulting energy distribution behind the cavity is given by

$$\gamma\left(\zeta_{\mathrm{c}}\right) = \hat{\gamma}\left(\zeta_{\mathrm{c}}\right) + \Delta\gamma\left(\zeta_{\mathrm{c}}\right) = \underbrace{A_0}_{\bar{\gamma}} + \underbrace{A_1\zeta_{\mathrm{c}} + A_2\zeta_{\mathrm{c}}^2 + A_3\zeta_{\mathrm{c}}^3 + \cdots}_{\delta\gamma}. \tag{5.5}$$

Here the coefficients $A_i = \hat{A}_i + \tilde{A}_i$ are determined by the sums of the coefficients of $\hat{\gamma}\left(\zeta_{\mathrm{c}}\right)$ and the $\tilde{A}_i$. From this, the energy of the central particle, $\bar{\gamma}$, and the energy spread $\delta\gamma$ can now be inserted into equation (5.2), which describes the dynamics in the subsequent drift.

At this point, it is helpful to write out the square and cube of $\delta\gamma$, neglecting orders higher than ζ_{c}^3:

$$\begin{aligned}
\left[\delta\gamma(\zeta_{\mathrm{c}})\right]^1 &= A_1\zeta_{\mathrm{c}} + A_2\zeta_{\mathrm{c}}^2 + A_3\zeta_{\mathrm{c}}^3 + \mathcal{O}(\zeta_{\mathrm{c}}^4),\\
\left[\delta\gamma(\zeta_{\mathrm{c}})\right]^2 &= A_1^2\zeta_{\mathrm{c}}^2 + 2A_1A_2\zeta_{\mathrm{c}}^3 + \mathcal{O}(\zeta_{\mathrm{c}}^4),\\
\left[\delta\gamma(\zeta_{\mathrm{c}})\right]^3 &= A_1^3\zeta_{\mathrm{c}}^3 + \mathcal{O}(\zeta_{\mathrm{c}}^4).
\end{aligned} \tag{5.6}$$

Within the drift, the abscissa of a particle in phase space is hence shifted according to

$$\zeta\left(z\right) = \zeta_{\mathrm{c}} + \Delta\zeta,$$

where $\Delta\zeta$ is a polynomial in $\delta\gamma$ [equation (5.2)]. Inserting equations (5.6) yields an expression which maps the phase space coordinates, ζ_{c}, in the cavity onto the resulting particle positions at an arbitrary drift coordinate, z, behind the cavity – again as a third order polynomial:

$$\zeta(z) = \chi_1\left(z\right)\zeta_{\mathrm{c}} + \chi_2\left(z\right)\zeta_{\mathrm{c}}^2 + \chi_3\left(z\right)\zeta_{\mathrm{c}}^3. \tag{5.7}$$

The coefficients χ_i are obtained by rearranging and sorting according to powers:

$$\begin{aligned}
\chi_1(z) &= 1 + (z - z_0)\left[\eta_1 A_1\right],\\
\chi_2(z) &= (z - z_0)\left[\eta_1 A_2 + \eta_2 A_1^2\right],\\
\chi_3(z) &= (z - z_0)\left[\eta_1 A_3 + 2\eta_2 A_1 A_2 + \eta_3 A_1^3\right].
\end{aligned} \tag{5.8}$$

In order to cover the complete evolution of the phase space within a drift, one should keep in mind that each particle in the bunch has a coordinate pair $[\zeta(z), \gamma(z)]$. And, it is assumed that the energy $\gamma = \gamma(\zeta(z))$ can be treated as a function in ζ. The equations (5.7) and (5.8) describe the evolution of the abscissa in that sense. This might appear strange at first glance, and can spoil the functional description, since ambiguities can occur by this mapping of coordinate pairs. This typically happens in the focus of a beam, like in figure 5.2: Clearly, this curve cannot be described by a function in ζ. (Nevertheless, the mere mapping of coordinate pairs is still possible, as will be seen.) In the majority of cases, however, no ambiguities do occur.

In a drift, the energy of a particle does not change since space charge is neglected in this discussion. Hence, the magnitude of γ for each particle, that is, its ordinate, is unchanged – and known, since it results from the cavity. However, if γ can be expressed as a function of ζ, this *polynomial* function must reflect for the changes in the abscissa, in order to ensure the unchanged γ-value along the drift. Thus, the description at the end of a cavity [equation (5.5)] is a special case of a general solution:

$$\gamma(\zeta_\mathrm{c}) = A_0 + A_1\zeta_\mathrm{c} + A_2\zeta_\mathrm{c}^2 + A_3\zeta_\mathrm{c}^3 \equiv a_0 + \underbrace{a_1\zeta + a_2\zeta^2 + a_3\zeta^3}_{\delta\gamma} = \gamma(\zeta). \tag{5.9}$$

Here, the small letters are the coefficients of the general polynomial at an arbitrary position, while the capital letters describe the situation at the end of a cavity. This naming will be kept in the following.

The final step now is to insert the already obtained expression for ζ in the drift [equation (5.7)] into the right hand side of equation (5.9), which yields the general coefficients of the γ-polynomial:

$$\begin{aligned} a_0 &= A_0 = \bar{\gamma}, \qquad\qquad a_1 = \frac{A_1}{\chi_1}, \\ a_2 &= \frac{A_2 - a_1\chi_2}{\chi_1^2} = \cdots = \frac{A_2\chi_1 - A_1\chi_2}{\chi_1^3}, \\ a_3 &= \frac{A_3 - a_1\chi_3 - 2a_2\chi_1\chi_2}{\chi_1^3}. \end{aligned} \tag{5.10}$$

Thus, changes in ζ are compensated for by the coefficients a_i, keeping the magnitude of the γ-coordinates constant.

Equations (5.7) and (5.9) map the initial phase space coordinates of each particle in a bunch leaving a cavity – known and expressed by ζ_c and $\gamma(\zeta_\mathrm{c})$ – to the evolved phase space at an arbitrary point in the subsequent drift. The mapping functions only depend on cavity parameters, i.e., A_i and $\eta(A_0)$. Possible correlations present in the bunch prior to the cavity are included in that polynomial by equation (5.5).

Please note that by this formulation, the effect of the cavity is described by an instantaneous energy change, i.e., the spatial bunch evolution inside a cavity is neglected. This is analogous to the treatment of a thin lens in the transverse phase space. In contrast in the drift, the energy of the particles is kept constant, while the relative positions shift according to the equations derived. In other words, a cavity *only* changes the γ-coordinate, while the drift *only* affects the abscissa, i.e., the ζ-coordinates of the individual particles. The concept is illustrated in figure 5.3.

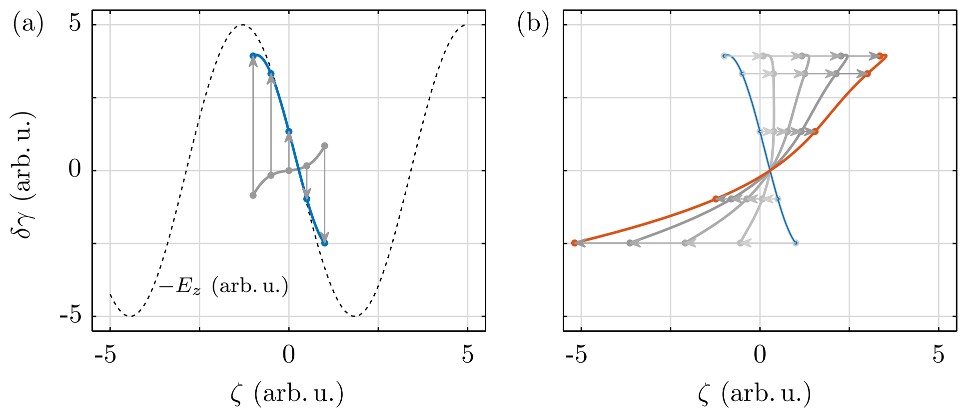

Figure 5.3 – Effects of a cavity field (a) and a drift (b) on an electron bunch described in the longitudinal phase space. The cavity instantaneously increases the particles' energy depending on the respective phase – imprinting its curvature. In the drift, the energy of each individual particle is unchanged, while the position is shifted according to equations (5.2), resulting in a change of the bunch length and an evolution of the curvature.

Iterative Application

By means of equations (5.4)–(5.10) also the phase space at the entrance of the next cavity can be described, of course. And thus, provided no ambiguities arise, the drift behind this accelerating structure can be expressed in an iterative manner. In the following, such a generalization for a machine like REGAE is done.

Hence, two cavities (gun and buncher) and two drift sections have to be treated. Therefore, A_i and a_i are replaced by G_i/g_i and B_i/b_i respectively. As mentioned, capital letters describe the cavity polynomials, and small letters the general formulation. The gun parameters, G_i are taken from a numerical simulation in the later analysis, so that the analytic treatment starts at the end of the gun cavity using these quantities as initial distribution.

Following the logic of the previous section, the bunch shape at the entrance of the buncher cavity, z_b, thus can be written in the respective phase space coordinates $[\zeta_\mathrm{b}, \hat{\gamma}(\zeta_\mathrm{b})]$, using

$$\hat{\gamma}\left(\zeta_\mathrm{b}\right) = g_0(z_\mathrm{b}) + g_1(z_\mathrm{b})\zeta_\mathrm{b} + g_2(z_\mathrm{b})\zeta_\mathrm{b}^2 + g_3(z_\mathrm{b})\zeta_\mathrm{b}^3. \tag{5.11}$$

In the cavity, an energy change is imprinted, which is incorporated by the application of equation (5.5), giving the energy polynomial after the action of the buncher:

$$\begin{aligned}\gamma_\mathrm{b}(\zeta_\mathrm{b}) &= \left(g_0 + \tilde{B}_0\right) + \left(g_1 + \tilde{B}_1\right)\zeta_\mathrm{b} + \left(g_2 + \tilde{B}_2\right)\zeta_\mathrm{b}^2 + \left(g_3 + \tilde{B}_3\right)\zeta_\mathrm{b}^3 \\ &= B_0 + B_1\zeta_\mathrm{b} + B_2\zeta_\mathrm{b}^2 + B_3\zeta_\mathrm{b}^3.\end{aligned} \tag{5.12}$$

Again applying the drift kinetics for the phase space distribution according to equation (5.11) finally yields

$$\zeta(z \geq z_\mathrm{b}) = \zeta_\mathrm{b} + \Delta\zeta(z \geq z_\mathrm{b}) = X_1\zeta_\mathrm{b} + X_2\zeta_\mathrm{b}^2 + X_3\zeta_\mathrm{b}^3, \tag{5.13}$$

where the coefficients X_i are defined as

$$\begin{aligned} X_1 &:= 1 + (z - z_\mathrm{b})\left[H_1 B_1\right], \\ X_2 &:= (z - z_\mathrm{b})\left[H_1 B_2 + H_2 B_1^2\right], \\ X_3 &:= (z - z_\mathrm{b})\left[H_1 B_3 + 2H_2 B_1 B_2 + H_3 B_1^3\right]. \end{aligned} \tag{5.14}$$

Here, H and X have to be treated as capital letters of η and χ respectively. This is to reflect that the parameters H are the functions η [equation (5.3)], evaluated for the total mean energy after the buncher cavity, $\bar{\gamma}_\mathrm{b} = B_0 = g_0 + \tilde{B}_0$. The coefficients X_i consequently have the same structure as χ_i in equations (5.8).

Finally, applying the same pattern as in equations (5.9) and (5.10), the energy polynomial in the second drift is determined. With that, a complete description of the bunch evolution along a Regae-like beam line is achieved within the limits of this method. The phase space coordinates $[\zeta, \zeta(\gamma)]$ are determined at any point within that system.

Even the focus can be calculated, despite the lack of a functional description. It is possible because the energy does not change, as employed several times: the γ-value in the particle coordinate vector $[\zeta, \gamma]$ is a constant. And, for the focus, it is not necessary to have a polynomial expression for the energy, since that is only required when the bunch is injected into a cavity, where the associated energy changes need to be added. That means, the phase space evolution can also be calculated in the focus and beyond – despite the breakdown of a functional description. The shift in ζ, which is the only relevant part here, is unspoiled: The description according to equation (5.13) is still valid. At the longitudinal focus, one, therefore, finds – analogously to equations (5.9) and (5.10):

$$\gamma_\mathrm{b}(\zeta) = b_0 + b_1\zeta + b_2\zeta^2 + b_3\zeta^3, \tag{5.15}$$

$$\begin{aligned} b_0 &= B_0 = \bar{\gamma}_\mathrm{b}, & b_1 &= \frac{B_1}{X_1}, \\ b_2 &= \frac{B_2 - b_1 X_2}{X_1^2} = \cdots = \frac{B_2 X_1 - B_1 X_2}{X_1^3}, \\ b_3 &= \frac{B_3 - b_1 X_3 - 2b_2 X_1 X_2}{X_1^3}. \end{aligned} \tag{5.16}$$

5.1.2 Phase Space Linearization

So far, the reasons for nonlinear phase space correlations have been explored. The general description of the phase space in the focus derived above – making use of the ballistic bunching scheme – is obviously nonlinear.

In the formalism, everything is dependent on the cavity coefficients, which are not fixed at this point in the discussion. In principle, each cavity in the system has two free parameters: amplitude and phase. The accelerating on-axis field in a standing wave cavity can be expressed as [51]

$$E_z(z,\phi) = \frac{1}{2}E_0\big[\sin(\phi) + \sin(\phi + 2kz)\big], \tag{5.17}$$

where the phase is defined as $\phi = \omega t - kz + \phi_0$. Here, E_0 is the amplitude and ω is the angular frequency of the rf field, and ϕ_0 is a constant phase offset. If the particle is at the speed of light, $\omega t - kz$, and thus ϕ becomes constant.

The energy gain in the case of constant phase ϕ for a cavity of length $L \propto \pi/(2k)$ can be written as

$$\Delta\gamma = \int_0^L \frac{e}{mc^2} E_z(z,\phi)\,\mathrm{d}z = \alpha k L \sin(\phi)\,, \tag{5.18}$$

using the normalized vector potential $\alpha := (eE_0)/(2mc^2k)$ for the field amplitude, similar as for the laser in equation (2.18) of chapter 2.2. The second term in $E_z(z)$, describing the counter-propagating part of the standing wave, has no contribution to the integral due to the restriction on L. To fix the phase offset ϕ_0, it is common practice to define $\phi = 0$ as the phase of maximum energy gain.

The central particle of a bunch is injected on a phase $\phi = \omega t - kz$, while a particle with a longitudinal offset enters the cavity at a later/earlier point in time. However, it still runs on a constant phase, $\tilde{\phi} = \omega(t + \delta t) - kz$. This leads to a constant phase offset $\delta\phi = \tilde{\phi} - \phi = \omega\delta t$.

The transfer from the laboratory frame (i.e., cavity frame) to the co-moving longitudinal phase space is achieved by a Galilean transformation, as in chapter 2.2 for the plasma wakefield: $\bar{\zeta} = \bar{z} - ct \equiv 0$. Again, $\bar{\zeta}$ and $\bar{z}$ describe the central particle of the bunch. Hence, the offset between the reference particle at $\bar{z}(t)$ and an arbitrary particle at location $z(t)$ is

$$\delta z = z - \bar{z} = \underbrace{(z - ct)}_{\zeta} - \underbrace{(\bar{z} - ct)}_{\bar{\zeta}\equiv 0} = \zeta \equiv -c\delta t. \tag{5.19}$$

The minus sign in $\delta z = -c\delta t$ reflects that a particle passing a certain position at a later point in time (i.e., a larger t) has a smaller initial position z, since the bunch travels in positive z-direction. It follows that $\delta\phi = -k\zeta$, making use of the fundamental relationship $\omega = ck$.

The phase deviation of a particle at ζ translates thus into a deviating energy gain,

$$\begin{aligned}\Delta\gamma &= akL\sin(\phi + \delta\phi)\\ &\approx akL\big[\sin(\phi) + \cos(\phi)\,(\delta\phi) - \frac{1}{2}\sin(\phi)\,(\delta\phi)^2 - \frac{1}{6}\cos(\phi)\,(\delta\phi)^3\big]\\ &= \underbrace{akL\sin(\phi)}_{\tilde{A}_0} + \underbrace{\left[-ak^2L\cos(\phi)\right]}_{\tilde{A}_1}\zeta_\mathrm{c} + \underbrace{\left[-\frac{1}{2}ak^3L\sin(\phi)\right]}_{\tilde{A}_2}\zeta_\mathrm{c}^2 + \underbrace{\left[\frac{1}{6}ak^4L\cos(\phi)\right]}_{\tilde{A}_3}\zeta_\mathrm{c}^3.\end{aligned} \tag{5.20}$$

The index c, and the coefficients $\tilde{A}_i$ are defined as in section 5.1.1. As a consequence, the cavity coefficients depend on the phase and frequency of the structure.

The system in the REGAE scenario consists of two cavities, resulting in four parameters which can be chosen almost freely. In order to linearize the phase space – and thus optimize the focus – an elegant approach is the introduction of a higher harmonic cavity [45–47]. To illustrate the principle, the kinetic curvature evolution according to equation (5.3) is neglected for a moment, so that only the field curvature is present. Having two cavities in the system, the idea is now to choose the cavity phases and amplitudes in such a way that the nonlinear terms cancel each other out exactly. That is, $\tilde{G}_2 \equiv -\tilde{B}_2$ and $\tilde{G}_3 \equiv -\tilde{B}_3$, where G and B are used for the gun and buncher cavity again.

Breaking that down, two equations have to be fulfilled:

$$\begin{aligned} L_\mathrm{g} E_\mathrm{g} k^2 \sin\left(\phi_\mathrm{g}\right) &= -L_\mathrm{b} E_\mathrm{b} k^2 \sin\left(\phi_\mathrm{b}\right), \\ L_\mathrm{g} E_\mathrm{g} k^3 \cos\left(\phi_\mathrm{g}\right) &= -L_\mathrm{b} E_\mathrm{b} k^3 \cos\left(\phi_\mathrm{b}\right). \end{aligned} \tag{5.21}$$

Taking the ratio of these, results in

$$\frac{1}{k} \tan\left(\phi_\mathrm{g}\right) = \frac{1}{k} \tan\left(\phi_\mathrm{b}\right), \tag{5.22}$$

which leads to $L_\mathrm{g} E_\mathrm{g} = -L_\mathrm{b} E_\mathrm{b}$. In other words, the solution results in either a phase shift of π between the cavities in combination with the same magnitude and sign of amplitudes, which are proportional to LE, or equivalently the same frequency and same magnitude of the amplitude, but of opposite sign. Put differently, the energy gain from the first cavity is completely absorbed by the second one, so that the bunch would be entirely decelerated.

The situation changes, however, if k is not equal for the cavities. Motivated by a Fourier series approach, for example, a cavity operated at triple the frequency can be used [45–47]: The curvature in this reduced model is only determined by the sum of acting fields. Thus, it would be ideal to use a flat profile, which can be achieved by the sum of uneven harmonics like for a square pulse. Free-electron lasers, like for example FLASH [43] and the upcoming European XFEL [44] use exactly this approach to optimize the peak current. Such a decelerating structure is typically included in the accelerator *in addition* to the main cavities. I.e., in the case of REGAE, the structure would be placed between the gun and buncher cavities, or behind the buncher – which is still required in order to imprint the linearly correlated energy spread. An ASTRA simulation of REGAE with an added third harmonic structure shows the feasibility of bunches with a length of 700 as [51].

The disadvantage of a higher harmonic structure is the requirement of a separate and costly rf system, which for REGAE would for example be an expensive X-band structure. Also, there is no space left for the inclusion of an additional cavity in the beam line. (Compare chapter 4.2.2.)

Therefore, another method has been developed in the course of this work, suggested by [57]. Instead of the inclusion of a higher harmonic structure, a similar effect can be introduced if the bunch is expanded in a controlled way between the electron gun and the buncher cavity: The increase in the bunch length reduces the phase space curvature. This means that in reference to the bunch, the curvature of the buncher cavity field is increased compared to the evolved bunch shape, although this cavity is operated at the same frequency as the gun. Thus, the buncher

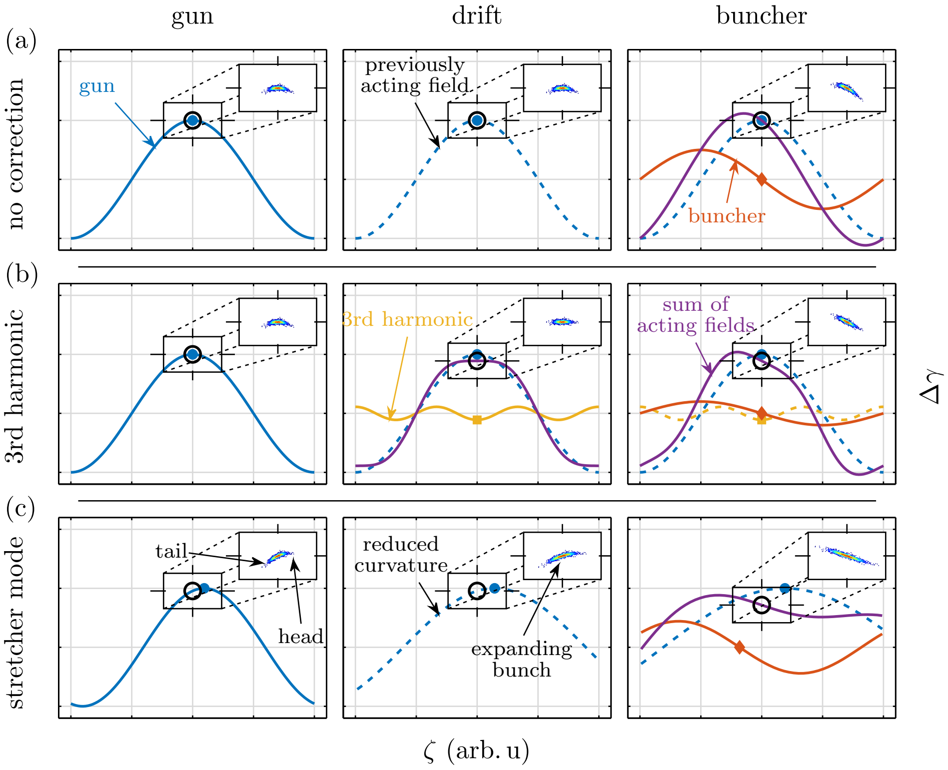

Figure 5.4 – Schematic overview of the *uncorrected* ballistic bunching technique (a), the *third harmonic* concept (b), and the new *stretcher mode* method (c). Each row shows snapshots of the longitudinal phase space evolution at important points in the respective method, starting on the left. Phase slippage in the cavities, especially the gun is ignored for the sake of simplicity in this illustration. Also, nonlinear bunch evolution in the drifts is neglected in this sketch depicting the principle of the concepts. Fields acting on the bunch in a previous section are marked by dashed lines; the violet line indicates the sum of all fields acting so far. The bunch shape is shown in the insets. In figure (a), the distribution acquires a curvature in the gun, which is transported almost unchanged towards the buncher. Due to the linear slope at the zero crossing of the latter cavity, the curvature is still present in the focus distribution. In (b), the curvature of the gun is compensated by the deceleration in the third harmonic cavity. Hence, the distribution towards the focus is much more linear. Finally, the stretcher mode in (c) shows the reduction of the curvature during the drift due to the expansion of the beam. Hence, a bunching and correcting phase can be found by the application of the formalism. Again, a linearly correlated distribution is created. Figure adapted from [48].

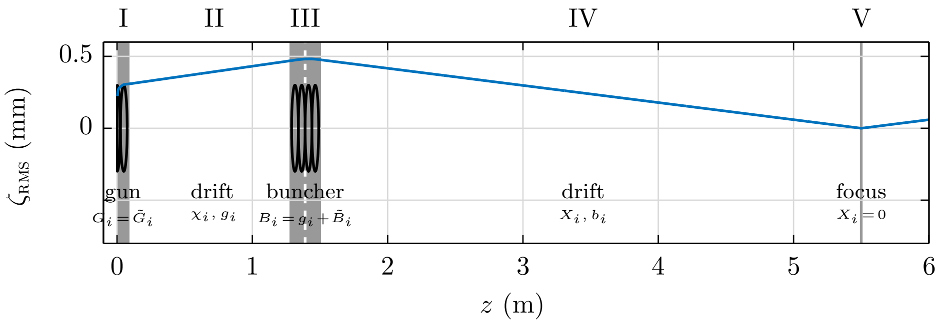

Figure 5.5 – Segments I–V used in the linearization scheme. The bunch leaves the gun, I, on an expanding phase, so that the bunch length increases in the first drift section, II. Using the formalism derived in section 5.1.1, the expansion can be described precisely. In the buncher cavity, III, the energy spread is changed in such a way that a bunching configuration is achieved; the dashed white line marks the thin lens approximation of the cavity. Hence, ζ_{RMS} reduces in the second drift, IV, until the beam reaches the focus V. Ideally, all nonlinearities vanish at this point. The shaded zones, marking the segments, will be used throughout this chapter. To illustrate the relevant quantities for the analytic description, the symbols used in the respective zones are given as well. Figure adapted from [48].

cavity provides an option to eliminate higher order effects similar to a higher harmonic system. By this approach, which requires an operation of the gun at an off-crest phase, the assumptions which lead to equations (5.21) and (5.22) are no longer valid. It is thus possible, to find a solution for a linearized focus without a higher harmonic field by this method, which is called *stretcher mode*. The basic principle of these two methods are sketched in figure 5.4.

Importantly, a *controlled* expansion of the bunch is required for this approach. It is enabled by the analytic description of the beam evolution derived in chapter 5.1.1 of this thesis.

5.1.3 Linearization Strategy

To find a mathematical solution for the linearization method sketched above, the formalism derived in section 5.1.1 is used. Five steps need to be taken up to the focus, located at $z = z_{\mathrm{f}}$. They are illustrated in figure 5.5 and summarized in the following; the numbers I–V correspond to the respective zones in the figure. The REGAE geometry is used as an exemplary case in the evaluation.

I. The bunch starts at the gun. The dynamics in the gun cavity is quite complex due to the strong phase slippage. The energy gain in the gun is, therefore, obtained numerically by an ASTRA phase scan. The longitudinal coordinates ζ_{g} and the energy coefficients G_i are derived from a polynomial fit and a Taylor expansion around the phase of the central particle, respectively. An analytic approach to describe the dynamics including phase slippage can be found in [140]; the accuracy of this description is, however, not sufficient for the delicate analysis discussed here. The phase space at the end of the gun is given by

$$\left[\zeta_\mathrm{g},\ \sum G_i \zeta_\mathrm{g}^i\right].$$

II. Behind the gun, the bunch is expanding, which leads to an additional curvature acquisition due to the drift effects characterized by η_i, equations (5.3). It leads to a relative shift of particles in the longitudinal phase space which manifests in the $\zeta(z)$ coordinate, described by $\chi_i(z)$ (equations (5.7) and (5.8)). The magnitude of the energy coordinate of each particle is unchanged. However, the function describing $\gamma(\zeta; z)$ depends on the changing longitudinal coordinate, so that the coefficients in the energy polynomial must be adapted to compensate for the drift kinetics, maintaining the value of the individual γ-coordinates: The special solutions G_i at the gun exit are replaced by general expressions $g_i(z)$ [equations (5.9), (5.10)]. The phase space coordinates in the interval $z_\mathrm{g} \leq z \leq z_\mathrm{b}$ are:

$$\left[\underbrace{\sum \chi_i(z) \zeta_\mathrm{g}^i}_{\zeta(z)},\ \sum g_i(z) \zeta(z)^i\right].$$

III. The transportation of the phase space to the buncher cavity at $z = z_\mathrm{b}$ by means of II leads to an expression of the bunch structure in the respective longitudinal coordinates $\zeta_\mathrm{b} = \zeta(z_\mathrm{b})$. Likewise, the γ-polynomial is determined. The energy gain caused by the buncher is described by a Taylor series around the injection phase of the central particle, which yields the coefficients $\tilde{B}_i$, equation (5.11). They can simply be added to the incoming particle distribution, since that energy polynomial, $\hat{\gamma}(\zeta_\mathrm{b}) = \sum g_i(z_\mathrm{b}) \zeta_\mathrm{b}^i \equiv \sum \hat{B}_i \zeta_\mathrm{b}^i$, is expressed in the same longitudinal coordinates; $B_i = \hat{B}_i + \tilde{B}_i$. The approximation of the buncher cavity as a thin lens is important for this approach, i.e., the energy change is instantaneously applied and the longitudinal bunch distribution does not evolve: The individual particle coordinates ζ_b are constant in the cavity. The phase space coordinates are thus:

$$\left[\underbrace{\sum \chi_i(z_\mathrm{b}) \zeta_\mathrm{g}^i}_{\zeta_\mathrm{b}},\ \sum B_i \zeta_\mathrm{b}^i\right].$$

IV. The description of the second drift segment towards the focus, $z_\mathrm{b} \leq z \leq z_\mathrm{f}$, replicates the mathematical structure of II. The longitudinal coordinate changes are now described as polynomial in ζ_b. The corresponding coefficients X_i are given by equations (5.8), evaluated for the phase space at the end of the buncher. The energy polynomial with the respective coefficients $b_i(z)$ are determined by the same strategy: Keeping the magnitude of the individual γ-values constant by compensating for changes in ζ with adaptions in b_i.

$$\left[\underbrace{\sum X_i(z) \zeta_\mathrm{b}^i}_{\zeta(z)},\ \sum b_i(z) \zeta(z)^i\right].$$

V. The longitudinal focus marks the end of segment IV. The longitudinal coordinates are determined by the polynomial evaluated at $z = z_\mathrm{f}$. In order to achieve maximal bunch compression, $\zeta(z_\mathrm{f})$ should be zero for each individual particle, i.e., all electrons are simultaneously located at the same position $z = z_\mathrm{f}$. The energy can no longer be expressed as a function of $\zeta(z_\mathrm{f})$ at this point, since multiple particles at one position make for an ambiguous mapping. But, during the drift in segment IV the magnitude of γ has not changed for each individual particle. Thus, this coordinate can simply be expressed by the value at the exit of the buncher cavity. (A functional description is only important if an energy change of a subsequent cavity must be applied.) Thus, the phase space in focus is characterized by

$$\Big[\underbrace{\sum X_i(z_\mathrm{f})\zeta_\mathrm{b}^i}_{\zeta(z_\mathrm{f})\overset{!}{=}0},\ \sum B_i\zeta_\mathrm{b}^i\Big].$$

With these five steps, a start-to-end description from the electron gun to the longitudinal focus is accomplished: The phase space coordinates from the beginning of the beam line are mapped to those at the focus, $z = z_\mathrm{f}$. Setting $X_i = 0$ yields an upright line in the phase space at the focus position, i.e., the nonlinearities up to the third order vanish; the minimal bunch length is improved. Please note that there is no restriction on the start distribution so far, except for the demands that it can be approximated by a line. Furthermore, the formalism can be extended to more then two cavities, also employing different frequencies – as for example a third harmonic system. Apart from the numerical effort that comes along with more free parameters, it should be possible to calculate even higher order corrections by using this method

5.1.4 Longitudinal Emittance

As already mentioned in chapter 2.1, nonlinear phase space correlations increase the magnitude of the associated RMS emittance. This is also true for the longitudinal phase space, of course. Hence, ε can be used as a measure for the nonlinearities.

Following equation (2.5), the longitudinal RMS emittance is determined by

$$\varepsilon = \sqrt{\langle\zeta^2\rangle\,\langle T^2\rangle - \langle\zeta T\rangle^2}. \tag{5.23}$$

The symbol ε is used in the subsequent discussions to denote this quantity.

It can be shown that this expression is proportional to the product of the RMS bunch length and the nonlinear energy spread [140]. That is,

$$\varepsilon \propto \sqrt{\langle\delta\gamma_\mathrm{nl}^2\rangle\,\langle\zeta^2\rangle} = \delta\gamma_{\mathrm{nl,RMS}}\,\zeta_\mathrm{RMS}, \tag{5.24}$$

where the nonlinear energy spread $\delta\gamma_\mathrm{nl}$ is defined as:

$$\delta\gamma_\mathrm{nl} := \delta\gamma - \frac{\langle\zeta\delta\gamma\rangle}{\langle\zeta^2\rangle}\zeta. \tag{5.25}$$

Going back to equations (5.9) and (5.10), there is an expression for $\delta\gamma$ as a function of ζ. Thus, the only thing left to evaluate ε is the density distribution, $\rho(\zeta)$. Assuming, for example, a uniform density distribution,

$$\rho(\zeta) = \begin{cases} \frac{1}{2\zeta_\mathrm{m}} & \text{for } |\zeta| \leq \zeta_\mathrm{m}, \\ 0 & \text{else}, \end{cases} \tag{5.26}$$

equation (5.25) can be applied, and the integration according to equations (2.3) and (2.4) can be performed. It results in

$$\delta\gamma_\mathrm{nl} = a_2\zeta^2 + a_3\zeta^3 - \frac{3}{5}a_3\zeta_\mathrm{m}^2\zeta, \tag{5.27}$$

which are exactly the nonlinear elements of the γ-polynomial [equation (5.9)], except for the last item. This term removes a *linear* correlation which results from the cubic term and thus does not contribute to the emittance.

The mean of this expression calculates to $\langle\delta\gamma_\mathrm{nl}\rangle = a_2\zeta_\mathrm{m}^2/3$; this value is required for the calculation of the variance and denotes the difference to the energy of the central particle of the distribution, $\bar{\gamma}$. Combining all this, the nonlinear RMS energy spread according to the definition above [equation (5.25)] yields

$$\begin{aligned} \delta\gamma_\mathrm{nl,RMS} = \sqrt{\langle\delta\gamma_\mathrm{nl}^2\rangle} &= \left[\frac{1}{2\zeta_\mathrm{m}}\int\limits_{-\zeta_\mathrm{m}}^{\zeta_\mathrm{m}} \left(a_2\zeta^2 + a_3\zeta^3 - \frac{3}{5}a_3\zeta_\mathrm{m}^2\zeta\right)^2 \mathrm{d}\zeta - \left(\frac{1}{3}a_2\zeta_\mathrm{m}^2\right)^2\right]^{\frac{1}{2}} \\ &= \sqrt{\frac{4}{45}a_2^2\zeta_\mathrm{m}^4 + \frac{4}{175}a_3^2\zeta_\mathrm{m}^6}\,. \end{aligned} \tag{5.28}$$

The RMS value of the distribution $\rho(\zeta)$, i.e., the bunch length, is calculated to $\zeta_\mathrm{RMS} = \sqrt{1/3}\,\zeta_\mathrm{m}$. Hence equation (5.28) to first order gives

$$\delta\gamma_\mathrm{nl,RMS} \approx \frac{2}{\sqrt{5}}|a_2|\zeta_\mathrm{RMS}^2. \tag{5.29}$$

The scaling with $|a_2|\zeta_\mathrm{RMS}^2$ to leading order is valid for any particle distribution which is symmetric in ζ. Only the proportionality factor depends on the explicit shape of $\rho(\zeta)$ in this cases. As a consequence, the emittance evolution along the beam line can be characterized by

$$\begin{aligned} \varepsilon(z) = D(z)|a_2(z)|\zeta_\mathrm{RMS}(z)^3 &\approx D(z)|a_2(z)\chi_1(z)^3|\zeta_\mathrm{c,RMS}^3 \\ &\equiv D(z)|A_2\chi_1(z) - A_1\chi_2(z)|\zeta_\mathrm{c,RMS}^3, \end{aligned} \tag{5.30}$$

where $D(z)$ in this expression is the proportionality factor, and $\zeta_\mathrm{c,RMS}$ denotes the bunch length at the cavity, according to the naming convention used above.

Strictly speaking, the assumption $\zeta_\mathrm{RMS}(z) = \chi_1(z)\zeta_\mathrm{c,RMS}$ is only valid for linear changes of the particle positions. That is, the particle at location $\zeta_\mathrm{c,RMS}$ always stays at the RMS position throughout the evolution. This also implies that the kind of the distribution is unchanged in the drift, i.e., $D(z) \equiv D$ is a constant. Nonlinear changes, however, are of order $\mathcal{O}(\zeta^4)$ which justifies the assumption. The linear particle shifts are exactly described by $\chi_1(z)$.

As long as the symmetry is preserved, one can also include the nonlinear changes to the distribution in $D(z)$. Thus, the derivation entails that the changes to the RMS emittance due to the drift are to a certain degree independent of the initial distribution. This, of course, traces back to the fact that the particle shifts themselves do not depend on a distribution at all, according to the derived formalism.

The behavior of the emittance by means of equation (5.30) is no longer valid close to the longitudinal focus, because the symmetry of ρ breaks down. Nevertheless, the expression provides a useful tool for the determination of a linearized focus: In such a case, the right hand side of equation (5.30) must vanish, since $\chi_1 = \chi_2 = 0$, as discussed. And thus, the emittance is zero as well at that point if only second order effects are treated. More precisely, if χ_2 vanishes, it must be zero independently of the bunch position, z, according to equations (5.8)[1]. In this case, the emittance evolution is hence described by $\varepsilon(z) \propto |A_2\chi_1(z)| = |A_2\,[1 + (z - z_0)\,\eta_1 A_1]|$, i.e., it is linear in z and proportional to the (linear) bunch length evolution, and thus both curves have to vanish at the position of the linearized longitudinal focus.

A vanishing emittance is, of course, only possible in the line model. A line in phase space does not have a volume, and thus no emittance in the sense of Liouville, which is a lower limit to the RMS emittance. This, in addition to uncorrected higher order effects, as well as the mentioned asymmetry of the distribution in the focus, will lead to a deviating value.

However, the important point in this discussion is not the absolute value $\varepsilon = 0$. Instead, it is the general behavior of the emittance function: $\varepsilon \propto |a_2|$ implies that a local minimum exists in the case of vanishing second order, a_2, which dominates ε. Hence, the formalism also reflects that the RMS emittance is basically the sum of Liouville's contribution and higher order correlations.

For the case of a focus, i.e, $\chi_1(z_\mathrm{f}) = 0$, however, $a_2 \propto 1/\chi_1^3$ diverges. This is also a consequence of the functional formalism, $\gamma = \gamma(\zeta)$, breaking down: The phase space is given by an upright line in this case. The emittance, in contrast, is still well defined due to the combination of $a_2\chi_1^3$ being present in equation (5.30), which removes the singularity. The dominating influence of the second order in the emittance is here indicated by the discussed minimum in ε – for the case that $\chi_2 = 0$. A vanishing χ_1 does not suffice.

Thus, if the second order should be corrected in the focus, one needs to match the position of minimal bunch length and the position of the (local) minimum of the longitudinal RMS emittance to the location of the desired focus. This allows, for example, the construction of numerical optimization algorithms to adjust the machine settings – at least in simulations.

5.2 Applications

The next step to be taken is the verification of the applicability of the derived formalism and, more importantly, the demonstration of the new linearization concept, using ASTRA simulations.

---

[1] This does not imply a vanishing second order along the whole drift, since the evolution of the second order is described by $a_2(z)$ in the function $\gamma(\zeta)$.

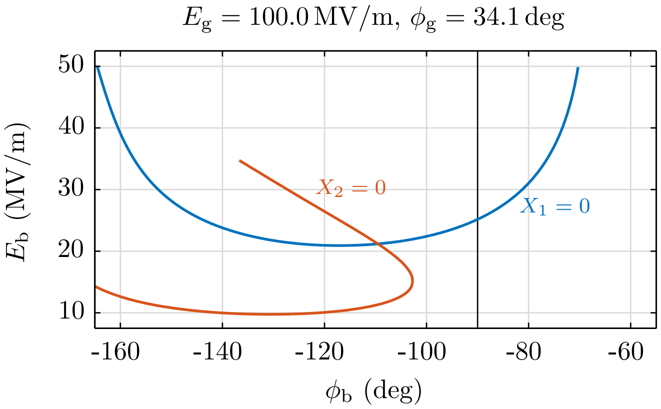

Figure 5.6 – Solutions for $X_1 = 0$ and $X_2 = 0$, depending on the buncher parameters. The gun is set to $E_\mathrm{g} = 100.0\,\mathrm{MV/m}$ and $\phi_\mathrm{g} = 34.1\,\mathrm{deg}$ in this exemplary case. The parameters determined by the intersection of the lines yield a second order corrected focus. The black line marks the typical bunching phase, $\phi_\mathrm{b} = -90.0\,\mathrm{deg}$.

As described earlier, it is necessary to solve the following system of equations in order to achieve a linearized focus:

$$\begin{aligned} X_1 &= 1 + (z_\mathrm{f} - z_\mathrm{b})\,[H_1 B_1] \equiv 0, \\ X_2 &= (z_\mathrm{f} - z_\mathrm{b})\left[H_1 B_2 + H_2 B_1^2\right] \equiv 0, \\ X_3 &= (z_\mathrm{f} - z_\mathrm{b})\big[H_1 B_3 + 2 H_2 B_1 B_2 + H_3 B_1^3\big] \equiv 0. \end{aligned} \tag{5.31}$$

Since there are two cavities present, four free parameters can be used: phases and amplitudes of the rf fields. Thus, the system can in principle be solved, leaving one parameter to fix, for example, the energy. (However, the parameters can be varied in restricted domains only, so that the energy cannot be set entirely arbitrarily.) The system cannot be solved analytically, though. The phase in equations (5.31) enters in trigonometric functions, while the amplitude is linearly included, i.e., the equations are transcendent.

Instead, a numerical approach is developed, which is based on the idea of a graphic solution: The equations for X_1 and X_2 are evaluated in a parameter space determined by the buncher variables ($0\,\mathrm{MV/m} < E_\mathrm{b} \leq 50\,\mathrm{MV/m}$, $-180\,\mathrm{deg} \leq \phi_\mathrm{b} \leq 0\,\mathrm{deg}$). From these solutions, the parameter combinations which yield $X_1 = 0$ or $X_2 = 0$ are derived; typically the points lie on a line; see figure 5.6. In a next step, the intersection of the lines is determined, which yields the parameters for a second order corrected focus: X_1 determines the linear energy correlation required for a focus at position $z = z_\mathrm{f}$, while $X_2 = 0$ eliminates the second order.

For an elimination of the third order, one must also solve $X_3 = 0$, using the gun parameters, and determine the solution for which the three lines intersect at one point – now in a three-dimensional parameter space. Therefore, a second order correction is attempted in the beginning.

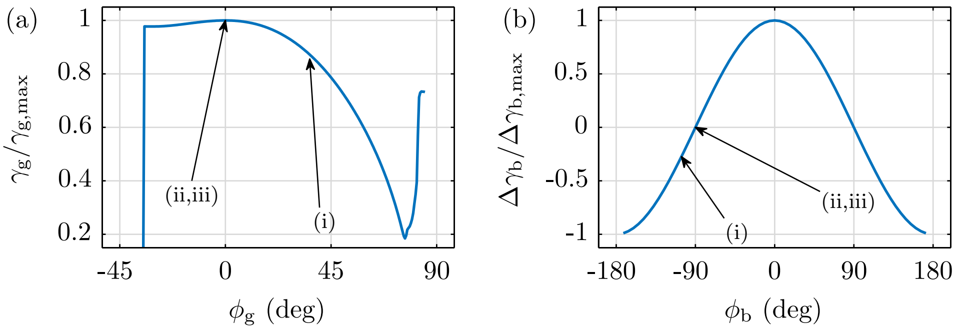

Figure 5.7 – Cavity phase settings for the cases (i–iii). The peculiar shape of the energy gain curve for the gun (a) is due to phase slippage effects, since particles released at the cathode have almost zero kinetic energy. The respective maximum energy gain phases define $\phi = 0$. Cases (ii,iii) are accelerated on this phase in the gun, while in the buncher (b) no net energy is gained. Only the required energy correlation is imprinted. In Contrast, case (i) is set to an expanding phase, which is accompanied by a slightly decelerating setting for the buncher. Figures adapted from [48].

5.2.1 Second Order Correction

There exists a whole set of solutions for the correction of the second order, since the gun phase is not fixed. For reasons of simplicity, the case solved in figure 5.6 is picked out of the numerical solutions derived above. It is marked with (i), for comparison with two reference cases. The calculated cavity parameters are $E_g(\mathrm{i}) = 100.0\,\mathrm{MV/m}$, $\phi_g(\mathrm{i}) = 34.1\,\mathrm{deg}$ and $E_b(\mathrm{i}) = 21.2\,\mathrm{MV/m}$, $\phi_b(\mathrm{i}) = -109.3\,\mathrm{deg}$. As mentioned above, the phases are defined in such a way that $\phi_g = \phi_b = 0$ yields the maximal energy gain in the respective cavity. The resulting bunch has an energy of $\langle T\rangle(\mathrm{i}) = 3.2\,\mathrm{MeV}$. So, like in the case of a third harmonic structure, the bunch is decelerated.

The scenarios for the comparison are defined as follows: For case (ii), the gun is set to the maximum acceleration phase ($\phi_g(\mathrm{ii}) = 0.0\,\mathrm{deg}$) while keeping the gradient of $E_g(\mathrm{ii}) = 100.0\,\mathrm{MV/m}$. For (iii) on the other hand, the amplitude is reduced to $E_g(\mathrm{iii}) = 70.0\,\mathrm{MV/m}$. In addition, the on-crest phase is chosen again, $\phi_g(\mathrm{iii}) = 0.0\,\mathrm{deg}$. Hence, for both cases, the bunch does not expand towards the buncher cavity, which is operated at the zero crossing: $\phi_b(\mathrm{ii,iii}) = -90.0\,\mathrm{deg}$. To achieve a focus at the same position, the amplitudes have to be set to $E_b(\mathrm{ii}) = 17.6\,\mathrm{MV/m}$ and $E_b(\mathrm{iii}) = 6.6\,\mathrm{MV/m}$, respectively. The energy in focus for the bunches of the cases (ii,iii) is $\langle T\rangle(\mathrm{ii}) = 4.6\,\mathrm{MeV}$ and $\langle T\rangle(\mathrm{iii}) = 3.2\,\mathrm{MeV}$.

Figures 5.7 depict the phase settings. A comparison of the analytically calculated phase spaces in the focus is shown in figure 5.8. Cases (ii) and (iii) clearly show the parabolic dependence of the second order, limiting the minimal bunch extent to $\zeta_{\mathrm{RMS}}(\mathrm{ii}) = 6.6\,\mu\mathrm{m} \mathrel{\widehat{=}} 22\,\mathrm{fs}$ and $\zeta_{\mathrm{RMS}}(\mathrm{iii}) = 5.9\,\mu\mathrm{m} \mathrel{\widehat{=}} 20\,\mathrm{fs}$. Case (i), in contrast, is no longer limited by the second order contribution. Instead, a clear signature of the third order is visible. The bunch length in this case is $\zeta_{\mathrm{RMS}}(\mathrm{i}) = 230\,\mathrm{nm} \mathrel{\widehat{=}} 770\,\mathrm{as}$.

For the calculation of the explicit bunch length, an initial particle distribution is required, which

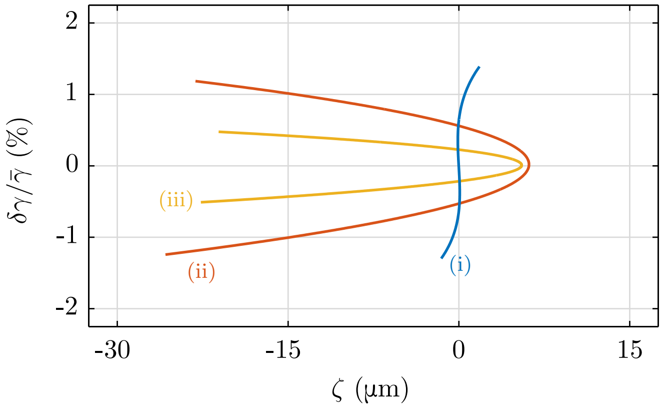

Figure 5.8 – Phase space distributions in focus for the three cases (i–iii). The standard bunching scenarios (ii,iii) clearly show a second order signature, while the optimized case has a much shorter longitudinal extent, limited by the third order, which manifests in the S-shaped structure. Figure adapted from [48].

Case	**Method**	**Space Charge**	E_g (MV/m)	ϕ_g (deg)	E_b (MV/m)	ϕ_b (deg)	T (MeV)	$\zeta_\mathrm{RMS}(z_\mathrm{F})$ (µm)	$\sigma_t(z_\mathrm{F})$ (fs)
(i)	analytic	—	100.00	34.13	21.21	-109.29	3.17	0.23	0.77
(i)	simulation	no	100.00	34.13	21.66	-111.99	3.12	0.19	0.63
(ii)	analytic	—	100.00	0.00	17.60	-90.00	4.60	6.58	21.95
(iii)	analytic	—	70.00	0.00	6.60	-90.00	3.19	5.89	19.66
(iv)	analytic	—	100.00	42.75	20.94	-94.45	3.35	0.01	0.04
(iv)	simulation	no	100.00	38.00	21.77	-104.15	3.25	0.11	0.38
(iv)	simulation	50 fC	100.00	42.00	21.63	-97.42	3.32	0.24	0.80

Table 5.1 – Summary of the cavity parameters and resulting bunch lengths for the different cases treated.

is transported using the method derived in section 5.1. For all cases treated in this discussion, an inverted parabolic distribution at the gun is used. It is assumed that the released electron cloud in the gun mimics the shape of the gun laser pulse. The advantage of the inverted parabolic distribution is the reduction of space charge influences on the curvature in the focus [51]: Combined with a transversely uniform density, this distribution develops similarly to an ellipsoidal density profile where space charge forces are entirely linear. If not stated otherwise, the laser pulse length at the cathode is set to $\tau_\mathrm{RMS} = 1\,\mathrm{ps}$. (Since the analytic treatment starts at the end of the gun, bunch length changes inside that cavity are taken into account, leading to an adapted start parameter.)

In order to crosscheck and verify the method, ASTRA simulations have been performed. The calculated values from case (i) have been used as seed parameters for the tracking code. Also, the initial bunch length has been set to the identical value. Though the distribution is optimized for space charge effects, the second order simulations have been performed without Coulomb interaction. Since the buncher cavity has a significant length, deviations from the analytic calculation are to be expected: The thin lens approximation used in the analytic description is, of course, not fulfilled. Hence, an optimization algorithm based on the emittance minimization has been developed to tweak the buncher parameters towards an overlap of the minimum in $\varepsilon(z)$ and $\zeta_{\text{RMS}}(z)$ at $z = z_\text{f}$.

Figure 5.9 shows the bunch length evolution for the ASTRA output, compared to the analytic solution (i) and the reference case (iii), which is set to the same energy after the buncher. The simulation of (i) requires a slight adaption of about $\Delta\phi_\text{b} = -2\,\text{deg}$, as well as a minimal correction of the amplitude; the parameters are given in table 5.1. As can be seen, the curves depicting the stretcher mode are in excellent agreement. As desired, the bunch length firstly extends up to the buncher, where the energy correlation is set to compression. Due to the controlled lengthening, the rf curvature of the buncher is larger than the evolved second order originating from the gun – nonlinearities can be corrected, similar to a higher harmonic system. Compared to the reference case using standard phases, the minimal bunch extent is much less for cases (i). As already mentioned, the analytic calculation of (i) results in $\zeta_{\text{RMS}} = 230\,\text{nm}$, while the simulation predicts an even better value of $\zeta_{\text{RMS}} = 190\,\text{nm} \mathrel{\widehat{=}} 630\,\text{as}$. Taking the initial value of 1 ps, the achieved compression ratio is thus larger than 1000. Also, the longitudinal emittance shows the required minimum at the focal spot, i.e., the second order vanishes at this point. As can be seen from the analytic curve, the emittance in the buncher goes through a minimum. This means, that the curvature has to be overcompensated by the buncher. That is, the drift effect [equations (5.3)] on the second order alone is strong enough to achieve the minimum even before $z = z_\text{f}$. The buncher, therefore, increases the curvature and, consequently, the emittance (please refer also to [51]). The price for this optimized focus is a deceleration of the particles in the buncher.

In figure 5.10, four phase space distributions of case (i) around the focus are depicted. Simulation and analytic calculation agree very well. Thus, the kinetic model and mechanism derived in section 5.1 yield a good applicability. Please note that the RMS based focus is actually at distance $\Delta z = -2\,\text{mm}$ compared to the focus according to the analytical model: The presence of the negative slope compensates partly for the third order wings, which determine the S-shape. The RMS value at this point is hence less than that of the case at $\Delta z = 0\,\text{mm}$. The latter case, in contrast, yields a focus in the sense of the model: An upright distribution – at least up to the second order. Resulting from the minor adjustment of the buncher cavity parameters (see table 5.1), the mean energy of the ASTRA bunch is about 80 keV less compared to the mathematical description.

5.2.2 Third Order Correlations and Space Charge

So far, the method derived in section 5.1 has not been used to its full potential, though. The stretcher concept is also capable of eliminating even the third order, which dominates the phase space distribution obtained in the previous chapter by its prominent S-shape.

As discussed earlier, the solution of $X_3 \overset{!}{=} 0$ – for likewise vanishing X_1 and X_2 [equations (5.31)]– is the determination of an intersection of three lines in a three-dimensional parameter

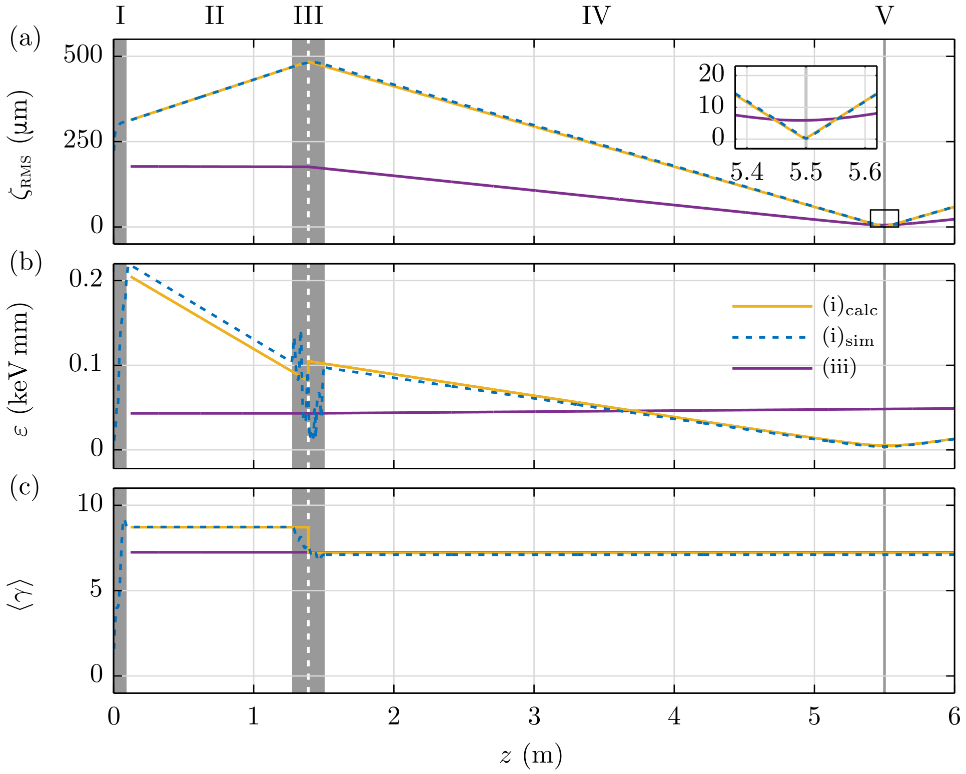

Figure 5.9 – Comparison of the bunch length (a) and emittance evolution (b) for a second order optimized case (i) – analytically calculated and simulated – and a reference case (iii) using standard bunching settings. The bunch length for case (i) increases, reflecting the controlled beam expansion, while case (iii) does not show a significant change in ζ_{RMS} up to the buncher. Behind the longitudinal lens, the bunch length reduces towards the focus. As can be seen from the inset, the minimal bunch extent is much less for case (i). As discussed, the emittance (b) also has a minimum at the focus position for the linearized case (i). The energy curve (c) shows that the beam is decelerated in the stretcher mode (i), while (iii) does not show an energy change due to operation on the zero crossing. The simulation results are in very good agreement with the analytic calculations. Figure adapted from [48].

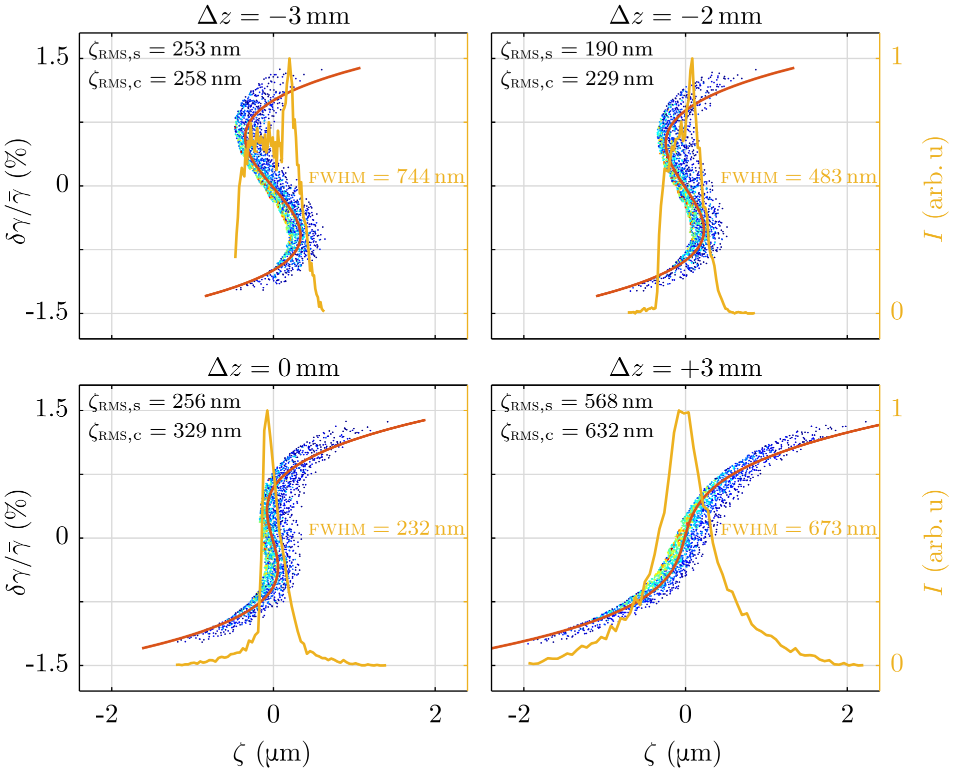

Figure 5.10 – Evolution of the longitudinal phase space around the focus for case (i). The particle distributions result from an ASTRA simulation, while the red lines are calculations according to the mathematical description of the previous chapter. For both cases, the same longitudinal initial distribution has been assumed. The analytic model accurately reproduces the phase space structure obtained with the simulation; the curve is not fitted. The S-shaped distribution is a clear sign of the dominating third order. The yellow line marks the current profile associated with the respective electron density. At $\Delta z = 0\,\mathrm{mm}$, the bunch is in the focus according to the definition in the analytical model: The slope is almost infinite, while the second order is eliminated, that is, all particles occupy the same ζ-coordinate, except for third order deviations, which are not corrected in this case. The FWHM of the current profile is minimal at this location, corresponding to an FWHM bunch length of 780 as; since the RMS value at this point is about the same as the FWHM, one can conclude that the amount of particles in the wings is comparatively small. However, the minimal RMS bunch length, ζ_{RMS}, is obtained shortly before that point at $\Delta z = -2\,\mathrm{mm}$: The third order effects are partly compensated for by the negative slope. Figure adapted from [48].

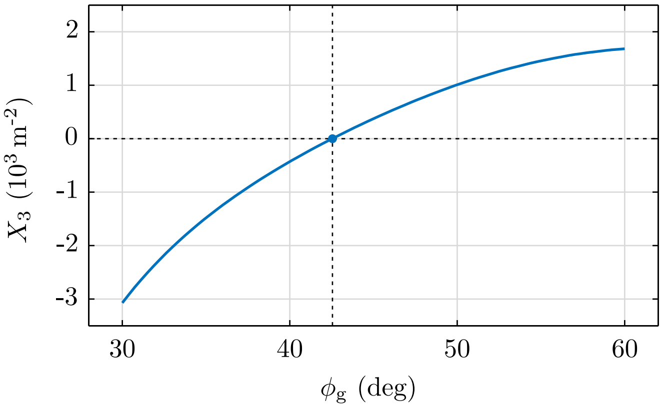

Figure 5.11 – Evaluation of X_3 depending on the gun phase ϕ_g. For each gun phase setting, the buncher parameters are tuned to eliminate X_1 and X_2. At $\phi_g \approx 43\,\mathrm{deg}$ the third order coefficient changes its sign. Hence, all three coefficients X_i vanish simultaneously at this point. The gun amplitude is kept at $E_g = 100\,\mathrm{MV/m}$. Figure adapted from [48].

space. Since this is rather complex, a reduced variant is applied. For the minimization up to the second order, only the buncher cavity has been used. Thus, the third order will be adjusted by the gun, namely the phase ϕ_g. In order to solve the system, the strategy for the first and second order is kept, but, the parameters for $X_1 = X_2 = 0$ are now solved for in a range of gun phases: $0\,\mathrm{deg} < \phi_g \leq 60\,\mathrm{deg}$. For all of these solutions, the magnitude of X_3 is evaluated. The result is depicted in figure 5.11. Thus, the system is not solved in the complete parameter space and the numerical effort is reduced.

As can be seen from the plot in figure 5.11, X_3 is negative at low gun phases but increases towards larger values of ϕ_g. At about $\phi_g = 43\,\mathrm{deg}$, the sign changes, i.e., $X_3 \approx 0\,\mathrm{m}^{-2}$. The gun amplitude is kept at $E_g = 100.0\,\mathrm{MV/m}$ for this parameter set which marks this new case, (iv). Also, the focus position is unchanged, $z_f = 5.50\,\mathrm{m}$.

According to the mathematical model, the exact cavity parameters for case (iv) are $E_g = 100.0\,\mathrm{MV/m}$, $\phi_g = 42.8\,\mathrm{MV/m}$, and $E_b = 20.9\,\mathrm{MV/m}$, $\phi_b = -94.5\,\mathrm{deg}$. In contrast, the gun phase in case (i) obtained in the previous section is at $\phi_g = 34.1\,\mathrm{deg}$ and thus has a much larger magnitude of $X_3(i) \approx -1600\,\mathrm{m}^{-2}$.

Figure 5.12 shows the resulting phase space curves in the focus for the analytic calculation of case (i) compared to case (iv). As can be seen, the new parameter set yields a much shorter bunch: The prominent S-shape is no longer visible, instead a slight Z-shape can be seen indicating a change of sign has indeed taken place in the third order. The associated bunch length is reduced by more than one order of magnitude to about 10 nm in the idealized mathematical method. The ideal focus in that model approaches zero. In a simulation, the bunch length for such a configuration is entirely determined by the uncorrelated energy spread, and possible fourth and higher order effects: Using ASTRA without space charge as a comparison, yields a bunch compressed to $\zeta_{\mathrm{RMS}} = 115\,\mathrm{nm} \mathrel{\widehat{=}} 380\,\mathrm{as}$ – which is about half of value previously obtained in

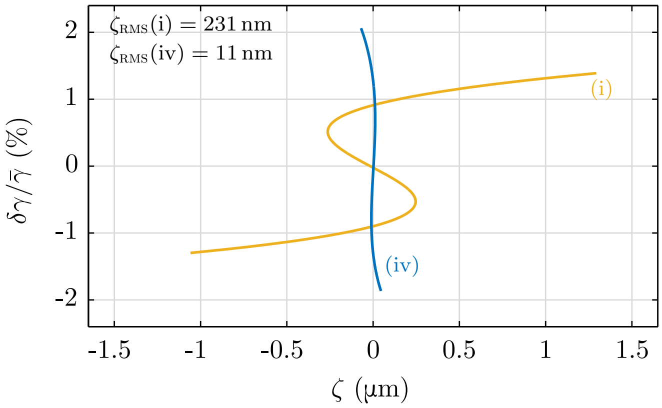

Figure 5.12 – Phase space curvature for cases (i) and (iv) in the focus according to the mathematical model. Case (iv) no longer exhibits an S-shaped structure in contrast to (i). Instead, a slight Z-shape can be seen. This means that the third order contribution, X_3, changed sign. Also, the bunch length in case (iv) is much shorter. Figure adapted from [48]

case (i). The gun phase in the simulation without space charge deviates about 10 % from the calculated value, which leads to a similar shift in the buncher phase.

Finally, space charge is included in another simulations of case (iv). The amount of charge is set to $Q = 50\,\mathrm{fC}$ to keep the influence of the associated repulsion effects low. The value is in the range of typical REGAE bunches used for the diffraction experiments [42], as well as for the planned injection campaign (see chapter 3). The space charge forces also require an adaption of the cavity parameters. Interestingly, these are closer to the calculated values than those resulting from the ASTRA simulations without particle interaction. The minimal bunch length obtained *with* space charge is about 240 nm, i.e., about 800 as. This is a considerable improvement compared to the design value of the machine, which is on the order of $\zeta_{\mathrm{RMS}} \approx 3\,\mu\mathrm{m} \mathrel{\widehat{=}} 10\,\mathrm{fs}$. The phase space of the third order compensated bunch, including space charge effects, is depicted in figure 5.13. Since the bunch is launched with $\tau_{\mathrm{RMS}} = 1\,\mathrm{ps}$, the compression factor – even with space charge – is still larger than 1 000. The side wings and bumps in this distribution can be attributed to the Coulomb repulsion during the emission process in the gun [51]. The inverted parabolic particle distribution used for the initial bunch formation minimizes this effect.

5.2.3 Overcompensation Mode

Associated with the higher gun phase required for the correction of the third order, the longitudinal RMS emittance has a first local minimum prior to the buncher cavity. This is no coincidence. In fact, it is necessary that the coefficient of the second order in the energy polynomial, g_2, changes its sign in order to eliminate the third order, X_3, at the focus, at least for the case that the second order should vanish at the same time. The immediate consequence of this is a local minimum in the emittance, as discussed in 5.1.4.

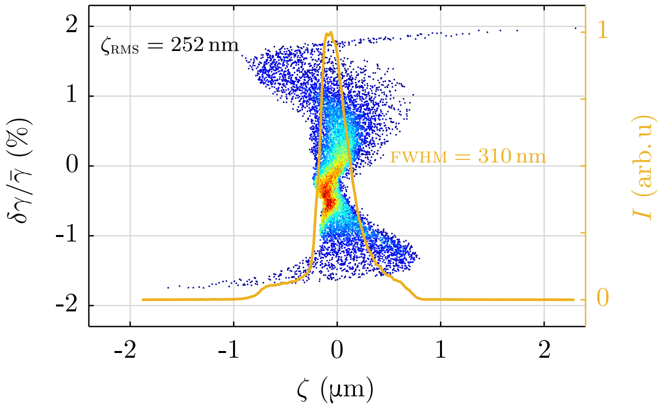

Figure 5.13 – Longitudinal phase space of case (iv) resulting from an ASTRA simulation. The depicted distribution is determined close to the focus. In the focus, the bunch has an extent of $\zeta_{\text{RMS}} \approx 240\,\text{nm} \mathrel{\widehat{=}} 800\,\text{as}$. The charge in this simulation is $Q = 50\,\text{fC}$. The nonlinearities up to the third order are compensated. The bumps and wings in the distribution can mainly be attributed to space charge effects happening in the electron gun. Figure adapted from [48].

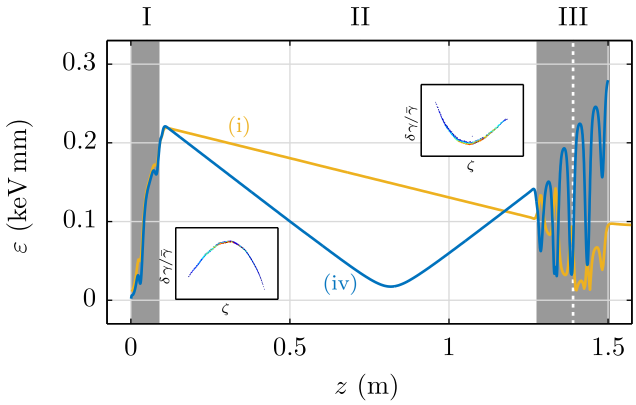

Figure 5.14 – Longitudinal RMS emittances for cases (i) and (iv); both results are taken from the respective ASTRA simulation. In case (i), space charge is not considered and only the second order is corrected. In contrast, case (iv) is simulated with space charge forces and a compensation up to the third order. The emittance evolution of case (iv) has a minimum, attributed to the change of sign in the second order correlation – illustrated in the insets. It can be shown, that this effect is mandatory in order to eliminate the third order.

Starting with $X_3 = 0$, it follows that

$$X_3 = 0 = H_1 B_3 + 2H_2 B_1 B_2 + H_3 B_1^3 = \underbrace{H_1}_{>0} \underbrace{B_3}_{<0} + \underbrace{\left(H_3 - 2\frac{H_2^2}{H_1} \right)}_{<0} \underbrace{B_1^3}_{<0}, \tag{5.32}$$

where the last step is a direct consequence of the vanishing second order: $X_2 = 0 = H_1 B_2 + H_2 B_1^2$. The coefficients η_i and H_i are combinations of β and γ [see equations (5.3)], so that $\eta_1 > 0$, $\eta_2 < 0$, and $\eta_3 > 0$, since $\gamma \geq 1$; the same is true for H_i due to the same structure. The expression in brackets is negative, since the term can be explicitly expressed as

$$H_3 - 2\frac{H_2^2}{H_1} = \frac{-2 + 7\gamma^2 - 5\gamma^4}{2\gamma^9 \beta^6} < 0 \quad \forall\, \gamma > 1. \tag{5.33}$$

The coefficient B_1 in equation (5.32) is negative, since this value describes the slope of the energy polynomial behind the buncher, i.e., the linear contribution to the ballistic bunching process, which requires $B_1 = \partial\gamma/\partial\zeta < 0$. Consequently B_3 must be negative as well in order to achieve $X_3 = 0$, since $H_1 = \gamma^{-3}\beta^{-2} > 0$.

Furthermore, $B_1 = g_1 + \tilde{B}_1$ and $g_1 > 0$, since the beam is expanding between gun and buncher, and g_1 is the slope describing this effect. Thus, the slope of the field applied in the buncher, $\tilde{B}_1$ must be negative to compensate for $g_1 > 0$. This has a direct consequence on $B_3 = g_3 + \tilde{B}_3$: Since the buncher field is of sinusoidal shape, $E_\mathrm{b} \propto \sin(-k\zeta)$, $\tilde{B}_3$ always has the opposite sign of $\tilde{B}_1$:

$$\tilde{B}_1 = \frac{\partial E_\mathrm{b}}{\partial \zeta} \propto -\cos(-k\zeta), \qquad \tilde{B}_3 = \frac{\partial^3 E_\mathrm{b}}{\partial \zeta^3} \propto \cos(-k\zeta). \tag{5.34}$$

Hence, $\tilde{B}_3$ must be positive, and therefore $g_3 < 0$ to ensure $B_3 = g_3 + \tilde{B}_3 < 0$ as required by equation (5.32).

Now, the third order of the energy gain curve at the end of the gun [figure 5.7(a)] is positive according to a numerical differentiation of γ resulting from ASTRA at that point. That is, $G_3 = g_3(z = z_\mathrm{g}) > 0$. Hence, g_3 starts positive and has to change sign in the drift up to the buncher cavity. However, to satisfy this requirement, g_2 must cross zero as well: Using equations (5.10), the coefficient is given by

$$g_2 = (G_2 - g_1\chi_2)/\chi_1^2.$$

The curvature of the gun polynomial, G_2, is negative, as can be deduced from figure 5.7(a) again. The coefficient

$$\chi_2(z) = (z - z_\mathrm{g}) \left[\eta_1 G_2 + \eta_2 G_1^2 \right]$$

is thus likewise less than zero, since $\eta_1 > 0$ and $\eta_2 < 0$. Moreover, the magnitude of $\chi_2(z)$ increases with z. Therefore, g_2 starts with a negative value at $z = z_\mathrm{g}$, where it is equal to G_2, but gradually increases towards zero due to the change in χ_2, since $g_1 > 0$, as pointed out.

Finally, as deduced, g_3 starts with a positive value but needs to be negative in the segment from buncher to focus. This switch must be achieved prior to the buncher, since the coefficients g_i are constant in the compression section afterwards. In short, g_2 is growing with z, while g_3 is decreasing. Furthermore, g_2 also enters the expression for g_3. Thus, an evaluation of the third order at the point where $g_2 = 0$ reveals

$$g_3 = \frac{G_3 - g_1\chi_3 - 2g_2\chi_1\chi_2}{\chi_1^3} \overset{g_2=0}{=} \frac{G_3 - g_1\chi_3}{\chi_1^3} = \frac{G_3 + G_2\chi_3/\chi_2}{\chi_1^3} > 0, \tag{5.35}$$

since G_3, χ_3 and χ_1 are positive for the expanding case, and G_2 and χ_2 are negative. This means that at the point where g_2 crosses zero, the respective third order coefficient is still positive. And since g_3 has to change its sign as well, both zero crossings must happen prior to the buncher cavity. Important for this conclusion is the fact that both functions, g_2 and g_3 should be monotone: More than one change of sign in the second or third order within a free drift are physically impossible.

Hence, the longitudinal RMS emittance, which is dominated by g_2 in the segment between gun and buncher – see above – has to have a minimum within that region. This effect, necessary for a third order compensation according to the mathematical model, is subsequently denoted as *overcompensation mode*. Figure 5.14 depicts the process, indicating the associated swap of the curvature in the phase space distribution.

5.2.4 About Tolerances

The phases and amplitudes of accelerator cavities are subject to jitter in certain boundaries around the respective set points. At REGAE, the goal is to reach a phase stability of $\delta\phi \leq 10^{-2}$ deg and a relative amplitude stability of $\delta E/E \leq 10^{-4}$. With these values, which are achievable parameters for state-of-the-art accelerators [57], the arrival time jitter on target for the design values of the UED experiments is less than 10 fs. To analyze the sensitivity of the linearization method with respect to these fluctuations, ASTRA simulations have been performed. Five sets of 999 runs each have been employed, using the parameters of case (iv) as set points. Space charge is included in this analysis. In four of these sets, an isolated jitter source has been used, that is, only one of the four parameters varies in the above limits. In the fifth set, all cavity parameters are subject to fluctuations.

The results of the latter set are depicted in figure 5.15. It shows that the minimal achievable bunch length $\zeta_{\text{RMS,f}}$ is very robust and insensitive to the input fluctuations. The mean of this shortest extent along the drift, $\langle\zeta_{\text{RMS,f}}\rangle = 266$ nm, is slightly higher than the value obtained in the previous chapter. This is, however, mainly attributed to the reduced number of particles in the simulation, compared to the above simulation. A number of 10 000 macro particles have been employed in the tolerance runs, in contrast to 300 000 used for the result in the previous section; this step was necessary to reduce the computational effort. The standard deviation within the combined set is only about

$$\sigma_{\zeta_{\text{RMS,f}}} = \sqrt{\left\langle \zeta_{\text{RMS,f}}^2 \right\rangle} \approx 1\,\text{nm}. \tag{5.36}$$

However, the shortest bunch extent is not reached at the nominal focus position $z_\text{f}^* = 5.500$ m. Instead, the position fluctuates by several millimeters, with a standard deviation of $\sigma_{z_\text{f}} \approx 4$ mm, as can be seen in figure 5.15. The mean bunch length obtained at the nominal focus position is

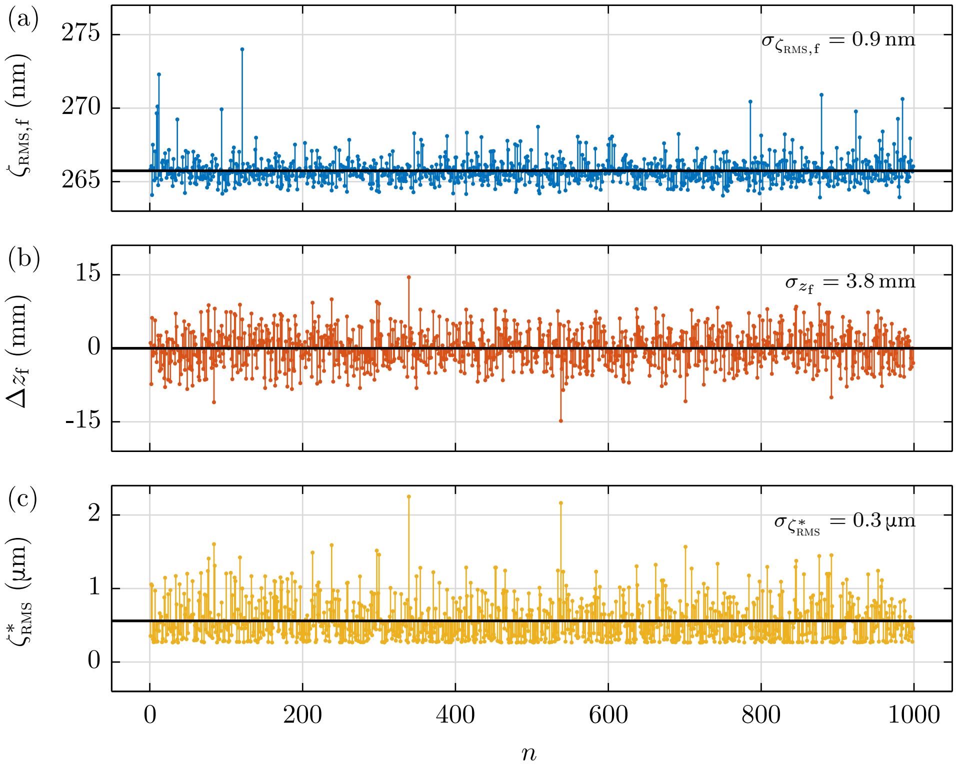

Figure 5.15 – Tolerance analysis of the achievable bunch length with respect to fluctuating cavity phases and amplitudes. Minimal bunch length (a), position of the longitudinal focus (b), and bunch length ζ^*_{RMS} at the nominal focus position $z_{\mathrm{f}} = 5.500\,\mathrm{m}$ (c) are analyzed. A phase stability of $\delta\phi \leq 10^{-2}$ deg and a relative amplitude stability of $\delta E/E \leq 10^{-4}$ has been assumed for both cavities; 999 runs have been performed. The relative bunch length in focus (a) and the relative focal length variation (b) are on the order of 10^{-3}, which in the latter case results in variations of a few millimeters due to the focal length of 4 m. Consequently, the bunch length at the nominal focus position (c) is subject to larger fluctuations, since it is dominated by the slope being present in the case of shifted minimum position.

Set	**1**	**2**	**3**	**4**	**1–4**	**5**	**Relative Errors**
Parameter	E_g	ϕ_g	E_b	ϕ_b	$\sqrt{\sum\sigma_k^2}$	all	— set 5 —
$\sigma_{\zeta_{\mathrm{RMS,f}}}$ (nm)	0.8	0.3	0.1	0.4	0.9	0.9	3.5×10^{-3}
σ_{z_f} (mm)	2.7	2.3	1.2	1.1	3.9	3.8	0.9×10^{-3}

Table 5.2 – Results from the numerical tolerance analysis using ASTRA. The bunch length in focus, $\sigma_{\mathrm{RMS,f}}$, is only mildly affected by the input fluctuations. The focus position itself, however, varies by several millimeters. The relative errors are comparable, though, and can be explained by error propagation using the mathematical model.

$\langle\zeta^*_{\mathrm{RMS}}\rangle\approx560\,\mathrm{nm}$. This value corresponds to about 2 fs, and is about double the minimal bunch length achieved in the focus. The standard deviation of the fluctuations at the nominal focus is $\sigma_{\zeta^*_{\mathrm{RMS}}}=289\,\mathrm{nm}$, and thus much larger than at the actual focus. Nevertheless, the results at z^*_f are still below 1 µm, which is a remarkable value. Furthermore, as can be seen in figure 5.15(c), in many cases, the lower boundary given by the optimal focus at z^*_f is achieved.

In table 5.2, the results for the actual focus are summarized. As can be seen, all four parameters have a similar effect on fluctuations of the minimal bunch length, $\sigma_{\zeta_{\mathrm{RMS,f}}}$, and fluctuations of the respective focus position, σ_{z_f}. For the focus position, the influence of the gun is about double that of the buncher, while for the minimal length achieved the gun amplitude and the buncher phase are pronounced in comparison to the respective other cavity parameters. The square root of the quadratic sum over these four sets, $\sqrt{\sum\sigma_k^2}$ is very close to the results of set 5, where all parameter deviations are combined. Hence, the single fluctuations enter into the final result statistically independently.

To understand the strong influence of the parameter jitters on the focus position, compared to the mild influence on the actual bunch length in focus, it is helpful to once more employ the mathematical model of the process, as described above. The fluctuations enter the coefficients of the cavity polynomials, general described by A_i [equations (5.5)]. They are proportional to the amplitude and in a linear approximation likewise proportional to the phase-deviations [equation (5.20)]. The phase fluctuations of $\delta\phi=0.01\,\mathrm{deg}\;\widehat{=}\;2\times10^{-4}\,\mathrm{rad}$ thus leads to a similar relative fluctuation of $\delta A_i/A_i\approx10^{-4}$. As can be deduced from the evolution of the cavity coefficients, a_i, described in equation (5.10), the evolved coefficients g_i will also follow that scaling to leading order.

The bunch length in focus is described by the expressions X_i, equations (5.14), which are explicit functions of $B_i=g_i+\tilde{B}_i$ $(i\in1,2,3)$, that is, the (partly evolved) higher order cavity coefficients, and H_i, which are functions of $B_0=g_0+\tilde{B}_0$. As in the case above, the tilde marks the coefficients of the energy gain in the buncher. The scaling of the relative fluctuations in the summed cavity parameters B is still on the order of 10^{-4}. The same holds true for the functions H_i:

$$\frac{\delta H_i}{H_i}=\frac{1}{H_i}\frac{\partial H_i}{\partial\bar{\gamma}}\delta\bar{\gamma}\approx n\frac{\delta\bar{\gamma}}{\bar{\gamma}}\approx n\times10^{-4}\lesssim10^{-3}. \tag{5.37}$$

This claim is justified as follows: In a rough estimate, the derivative $\partial_{\bar{\gamma}} H_i(\bar{\gamma}) \approx nH_i/\bar{\gamma}$ will be dominated by the term of highest exponent, n, of $\bar{\gamma}$ in H_i – see equations (5.3) on page 126. Hence, the relative quantity $(\partial_{\bar{\gamma}} H_i)/H_i$ to leading order yields $(\partial_{\bar{\gamma}} H_i)/H_i \approx n/\bar{\gamma}$. Since $\bar{\gamma} = B_0$, the deviations scale as $\delta\bar{\gamma}/\bar{\gamma} \approx 10^{-4}$. The magnitude of the leading order exponent is $|n| \leq 5$ for H_i $(i \in 1, 2, 3)$, so that equation (5.37) holds.

The focus position is determined by $X_1^* = 1 + (z_\mathrm{f} - z_\mathrm{b})\,[H_1 B_1] \equiv 0$ from equations (5.14). The asterisks denotes the design focus position $z = z_\mathrm{f}^*$, which would be $z_\mathrm{f}^* = 5.500\,\mathrm{m}$ for Regae. A deviation in A_i then results in

$$X_1 = 1 + (\underbrace{z_\mathrm{f} - z_\mathrm{b}}_{\Delta z} + \delta z)\,[(H_1 + \delta H_1)(B_1 + \delta B_1)] \equiv 0, \tag{5.38}$$

i.e., the focus position must shift by δz to compensate for the cavity fluctuation. Rearranging the equation yields:

$$\begin{aligned} \frac{-1}{\Delta z + \delta z} \approx -\frac{1 + \delta z/\Delta z}{\Delta z} &= \left[H_1 \left(1 + \frac{\delta H_1}{H_1}\right) B_1 \left(1 + \frac{\delta B_1}{B_1}\right)\right] \\ &\approx \underbrace{H_1 B_1}_{-1/\Delta z} \left(1 + 2 \times 10^{-4}\right) \left(1 + 1 \times 10^{-4}\right) \approx \frac{-1}{\Delta z} \left(1 + 4 \times 10^{-4}\right), \end{aligned} \tag{5.39}$$

using the more accurate value for $\delta H_1/H_1 \approx 2\delta\bar{\gamma}/\bar{\gamma}$. Thus, the focus position varies on the order of

$$\frac{\delta z}{\Delta z} \lesssim 2 \times 10^{-3}, \tag{5.40}$$

which is in the range of a few millimeters for $\Delta z \approx 4\,\mathrm{m}$ as for Regae, and in line with the values obtained in the simulations.

A similar calculation can be performed for $X_{2/3}$, showing an analogous behavior, with a slightly increased impact due to the scaling of $\delta H_2/H_2 \propto 4\bar{\gamma}$ and $\delta H_3/H_3 \propto 5\bar{\gamma}$. Also, an increased number of error terms contributes to the overall resulting deviations. However, $X_{2/3}$ do not influence the focus position, as can be deduced from the different structure. In contrast to X_1 which has an additional term $(+1)$, the nonlinear coefficients $X_{2/3}$ are just proportional to Δz. That is, their magnitude fluctuates with the same error level, which likewise contributes to the fluctuation in bunch length on that level. In the actual (shifted) focus, X_1 is zero, the bunch length is determined by the slightly varying X_2 term with $\delta X_2/X_2$ being on the order of 10^{-3}.

At the nominal focus position z_f^* the bunch length is determined due to the linear evolution given by the slope to achieve the focus, $H_1 B_1 \approx -1/4\,\mathrm{m}^{-2}$, the distance $\Delta z_\mathrm{f} = z_\mathrm{f} - z_\mathrm{f}^* \approx 4\,\mathrm{mm}$, and the bunch length at the buncher which is about $\zeta_{\mathrm{RMS,b}} \approx 600\,\mathrm{\mu m} \mathrel{\widehat{=}} 2\,\mathrm{ps}$, assuming a beam expansion from gun to buncher by a factor of two. That is, $\zeta_{\mathrm{RMS,f}}^* = \Delta z_\mathrm{f} H_1 B_1 \zeta_{\mathrm{RMS,b}} \approx 600\,\mathrm{nm}$, which is about the same value as the mean obtained in the jitter analysis, shown in figure 5.15(c): $\langle \zeta_{\mathrm{RMS}}^* \rangle = 560\,\mathrm{nm}$, depicted by the black line. In other words, the average bunch length at the nominal focus is entirely dominated by the error propagation of the relative fluctuation in the focal length.

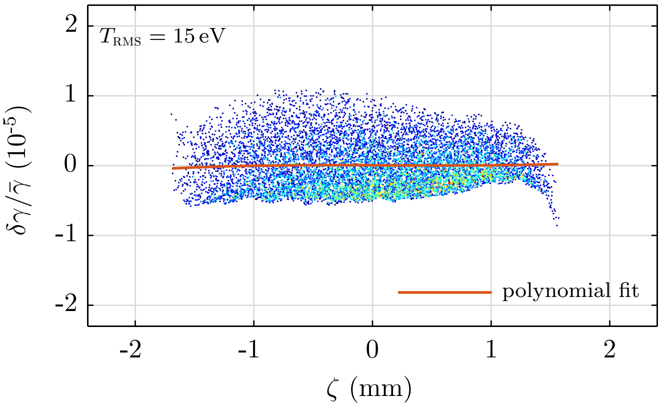

Figure 5.16 – Compensation of the energy spread imprinted by the gun, using the buncher cavity. By the application of the stretcher concept, the beam is not compressed in this case. Instead, a flat line is created by the correction of the higher orders directly at the buncher. The resulting energy spread in this case, using the parameters described in the text, is $T_{\mathrm{RMS}} = 15\,\mathrm{eV}$ for a beam of $\langle T \rangle = 3.9\,\mathrm{MeV}$. That is, $T_{\mathrm{RMS}} / \langle T \rangle < 10^{-5}$; please note the scale of the energy axis. As can be seen from the polynomial fit, the curvature is eliminated. Figure adapted from [48].

In conclusion, fluctuations in the cavity parameters mainly manifest in a shift of the focus. This is intrinsic to any bunching scheme: The focal length determined by the linear correlation fluctuates on the level of the (combined) instabilities. The linearization method itself is only slightly affected. This is also sustained by the formalism derived in sections 5.1 and 5.1.1, which yields similar error estimates.

5.2.5 Energy Spread Compensation

Phase space linearization does not necessarily mean that the distribution is resembled by an *upright* line in phase space, resulting in a strongly compressed bunch. Other configurations can be thought of as well. A particular application of the above-mentioned method that is also usable at REGAE is the compensation of the energy spread resulting from the gun curvature by means of the buncher cavity. Of course, this will not lead to a maximal compressed bunch. Instead, a flat line in phase space is now produced.

Such a configuration is very interesting for the planned TEM experiments [42]. In the case of real space imaging, the resolution is limited by the quality of the solenoid lenses and, especially, their chromaticity, i.e., the energy dependence of the focal length. (The focusing strength of a solenoid scales with $1/\gamma^2$ [53].) Hence, an electron bunch with a small energy spread reduces aberrations in the imaging process of the instrument. To achieve this, one can start with a short bunch, reducing the influence of nonlinearities. However, space charge repulsion at the sample position of the TEM severely limits the resolution due to the high charge density at the transverse focus in this case.

The linearization approach offers a method to start with a comparatively long bunch at the gun, which expands even further, so that space charge effects in the transverse focus are reduced. Using the stretcher mode concept, the considerable rf-based energy spread, which is imprinted during the emission, can be compensated in the buncher, so that image degradations due to both solenoid chromaticity *and* space charge repulsion are reduced.

In this case, it is sufficient to describe the beam transport up to the buncher cavity, applying equations (5.7)–(5.11). At that point, the coefficients g_i can be canceled by a choice of corresponding factors $\tilde{B}_i$. That is, $B_1 = B_2 = B_3 \equiv 0$ for $i \in \{1, 2, 3\}$, defined in equation (5.12).

An example of such settings can be seen in figure 5.16. Here, the parameters according to the formalism are $E_\mathrm{g} = 100.0\,\mathrm{MV/m}$, $\phi_\mathrm{g} = 48.1\,\mathrm{deg}$ and $E_\mathrm{b} = 13.5\,\mathrm{MV/m}$, $\phi_\mathrm{b} = -64.8\,\mathrm{deg}$, which have been refined using ASTRA. Space charge forces are considered, using a charge of $Q = 50\,\mathrm{fC}$. Despite this degrading influence, the resulting bunch shows an extremely small energy spread of $T_\mathrm{RMS} = 15\,\mathrm{eV}$. Compared to the kinetic energy of the bunch, $\langle T \rangle = 3.9\,\mathrm{MeV}$, the relative energy spread is thus $T_\mathrm{RMS}/\langle T \rangle = 4 \times 10^{-6}$. The bunch length is still on the order of a few picoseconds. The refined ASTRA parameters are $E_\mathrm{g} = 100.0\,\mathrm{MV/m}$ and $\phi_\mathrm{g} = 45.7\,\mathrm{deg}$, while the buncher is set to $E_\mathrm{b} = 14.1\,\mathrm{MV/m}$ and $\phi_\mathrm{b} = -69.9\,\mathrm{deg}$.

Furthermore, this case is also an application of the overcompensation mode. The second order flips and changes its sign along the drift. An immediate consequence of this is, that the buncher cavity does not decelerate the bunch. Instead, the compensation of the energy spread is achieved at an accelerating phase. Please refer to figure 5.17.

In order to get an estimate on the influence of the parameter fluctuations, a sequence of 999 ASTRA runs with jittering cavity settings has been performed once more. As in the tolerance study above, an RMS phase jitter of 0.01 deg has been assumed, as well as a relative amplitude stability of $\delta E/E = 10^{-4}$. The result is shown in figure 5.18. The mean energy spread is $\langle T_\mathrm{RMS} \rangle = 24\,\mathrm{eV}$ with a standard deviation of $\sigma_{T_\mathrm{RMS}} = 10\,\mathrm{eV}$. That is, the majority of cases is well below 50 eV; all cases result in a relative RMS energy spread of $T_\mathrm{RMS}/\langle T \rangle < 10^{-5}$.

5.3 Beyond REGAE

So far, the stretcher mode concept has been applied to the REGAE geometry, resulting in bunches of a length less than 1 fs for typical REGAE parameters. Also, the energy spread compensation is an interesting concept usable at that accelerator. To explore more aspects of the method, the constraints given by the layout of this machine are relaxed in the following.

The purpose of this last section is to introduce ideas for additional applications. The examples are mostly analyzed without space charge forces, demonstrating the underlying principle. The considerations are of an exemplary and preliminary character, meaning that further studies are required to examine the experimental feasibility.

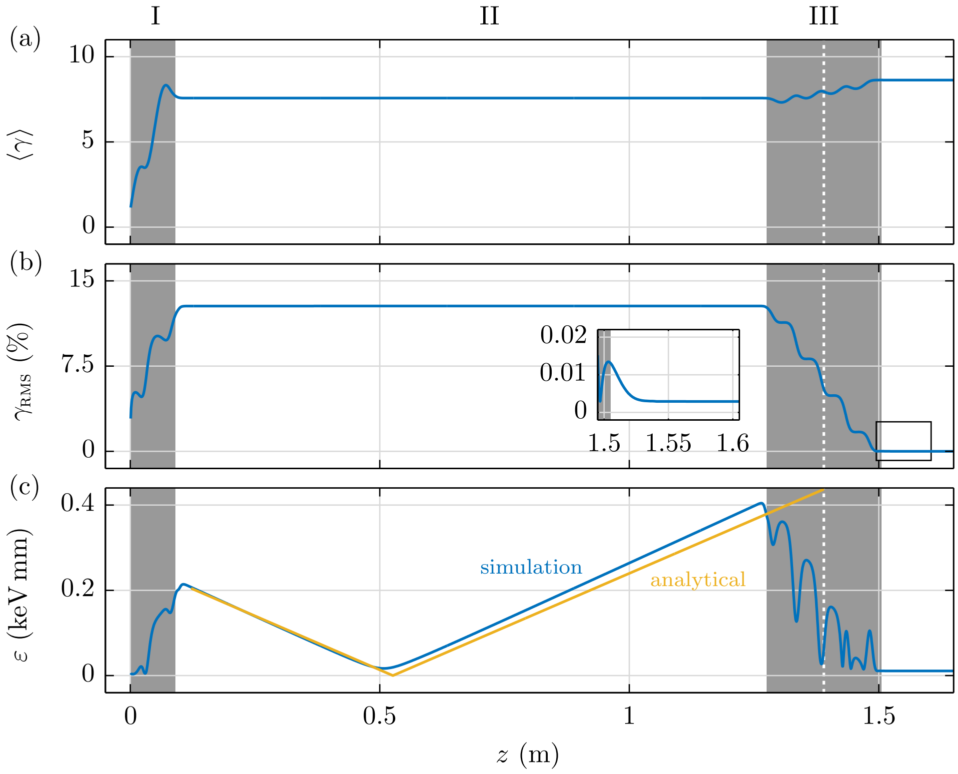

Figure 5.17 – Mean energy (a), RMS energy spread (b), and longitudinal RMS emittance (c) during the drift from gun to the buncher cavity for the discussed energy compensation settings. As can be seen in figure (c), the parameters are such that the machine is set to overcompensation mode. As a consequence, the energy spread compensation is achieved on an accelerating phase. Behind the buncher, the energy spread is eliminated almost entirely. Figure adapted from [48].

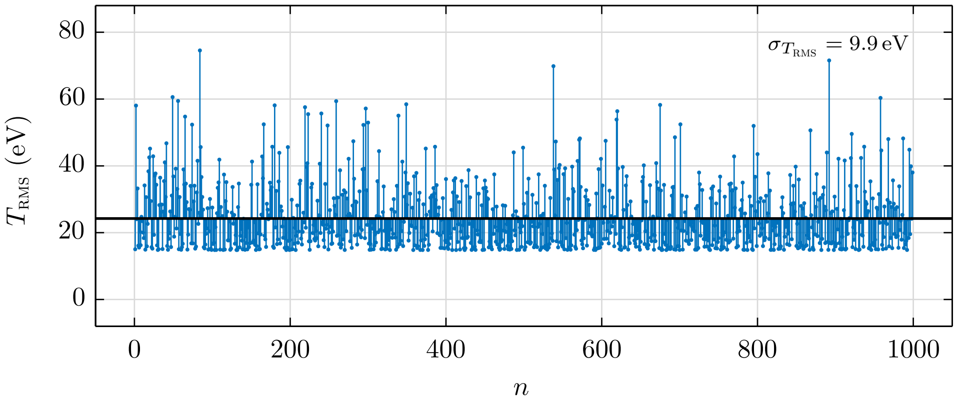

Figure 5.18 – Jitter analysis for the energy spread compensation settings described in the text. A fluctuation of of the cavity parameters of 0.01 deg for the phases and 10^{-4} for the relative amplitudes has been assumed. The resulting RMS energy spread is well below 100 keV for all cases, which results in a relative RMS energy spread of $T_{\mathrm{RMS}}/\langle T\rangle < 10^{-5}$.

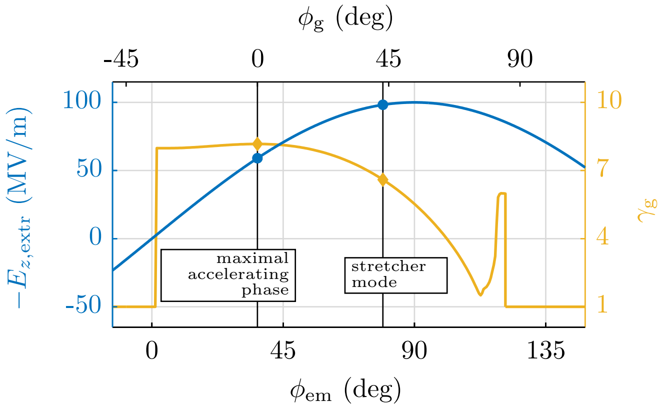

Figure 5.19 – Definition of the emission phase, ϕ_{em}, in comparison to the gun phase, ϕ_{g}. In this example, these two phase definitions are shifted by a constant offset of about 40 deg with respect to each other. The maximum energy gain is obtained at $\phi_{\mathrm{g}} = 0$ deg (following the definition in section 5.1.2). The extraction field is about $E_{z,\mathrm{extr}} \approx 60\,\mathrm{MV/m}$ at this point and increases towards larger gun phases. Figure adapted from [48].

5.3.1 Transverse Emittance

The stretcher mode approach relies on phase settings in the gun that lead to the expansion of the beam in the subsequent drift. To achieve that, the gun is not operated at the maximal accelerating phase. Instead, a phase around $\phi_{\mathrm{g}} \approx 40\,\mathrm{deg}$ is used in the examples above. Due to phase slippage of the initially (almost) resting electron emitted by the cathode and the field, a certain offset exists between the maximum energy gain, which is used as reference for the definition of $\phi_{\mathrm{g}} = 0$, and the maximum extraction field $E_{z,\mathrm{extr}}$ at the cathode. The emission phase ϕ_{em} describes the rf field at the cathode and is defined such that the field reaches its maximum E_0 at $\phi_{\mathrm{em}} = 90\,\mathrm{deg}$, i.e., $E_{z,\mathrm{extr}} \propto E_0 \sin(\phi_{\mathrm{em}})$.

However, this maximum emission phase does not coincide with the maximal accelerating phase, $\phi_{\mathrm{g}} = 0$. Instead, the emission phase is about $\phi_{\mathrm{em}} \approx 40\,\mathrm{deg}$ at the point of maximum energy gain, which means that the extracting field is only about $60\,\%$ of the maximum field. In contrast, the phase is shifted by $40\,\mathrm{deg}$ in the stretcher mode configuration, i.e., $\phi_{\mathrm{em}} \approx 80\,\mathrm{deg}$. As a consequence, the extracting field is larger than in the standard operation where $\phi_{\mathrm{g}} = 0$, corresponding to $\phi_{\mathrm{em}} = 40\,\mathrm{deg}$. The phase offsets are illustrated in figure 5.19.

In order to optimize the electron emission in the gun for a minimized transverse emittance, one has to balance the beam spot size of the laser against space charge forces. The laser spot should be focused as tight as possible, since the initial transverse bunch extent defines the minimal emittance. However, space charge repulsion, which pushes the electrons apart and increases the emittance, gets stronger, the smaller the initial bunch volume gets – especially for these low energy particles. Hence, there is an optimum. The higher extraction field of the stretcher mode shifts this optimum to smaller spot sizes, since an increased initial phase space density can be utilized due to the more rapid acceleration. Also, the linearization makes it possible to increase the bunch length at emission, because the associated curvature effects are compensated at a later stage. This leads to a further reduction of the Coulomb repulsion and, in addition, to a more linear behavior of the space charge forces due to the beam aspect ratio. Hence, the stretcher mode could possibly allow for a better transverse emittance for the gun.

For cases of high bunch charges, which require an emittance compensation scheme [141, 142], the associated energy spread conflicts with this concept, though. The concept relies on controlled refocusing of the beam which is defocused by the space charge forces. The defocusing effect is described by the so-called perveance [143], which describes the space charge repulsion in the beam envelope equation, analogous to a focusing strength. The perveance scales with $1/\gamma^3$ [142]. Hence, it changes along the bunch, if a large correlated energy spread is present, so that a controlled compensation of the space charge driven emittance increase seems no longer feasible. Further studies are required to examine the effects in detail, though.

Apart from this, there might be an increased space charge influence in the free drift, resulting from the reduced overall energy. Also, the transverse divergence combined with the energy spread will lead to an increased emittance in free drifts [30]. Furthermore, due to the long bunch, rf-induced emittance effects also need to be analyzed: So-called chromatic emittance variation caused by different transverse cavity fields along the bunch and the high energy spread especially in the first gun half-cell can also drive an emittance growth. The effect is getting stronger for higher emission phases [140] and thus needs to be explored for the stretcher mode.

A comprehensive treatment of gun dynamics and the emittance effects is beyond the scope of this thesis. More studies on this topic are required.

5.3.2 Varying Focus Position

An extension to the parameters emerging from the REGAE geometry is the variance of the focus position. Like for a laser beam, or the transverse focusing of an electron bunch, a shorter focal length should yield shorter bunches – at least if it is limited by the emittance.

Similar to the beam size evolution for a Gaussian laser beam via the Rayleigh length, the behavior can be expressed by the beta function for an electron bunch. Here, the beta function in the longitudinal space is required, which can be treated analogously to the transverse case. In a free drift of length s, the evolution of $\beta(s)$ starting at a waist with $\beta(0) =: \beta^*$ is given by [64, 65]:

$$\beta(s) = \beta^* + \frac{s^2}{\beta^*}. \tag{5.41}$$

Starting with a fixed beta function at the buncher, β_b, which is not in the waist, and replacing the distance to the waist by Δz, as used above, this expression can be rearranged to describe β^* depending on Δz,

$$\beta^*_{1/2} = \frac{1}{2}\left(\beta_\mathrm{b} \pm \sqrt{\beta_\mathrm{b}^2 - 4(\Delta z)^2}\right). \tag{5.42}$$

The smaller solution describes the reduction of β^* by shorter distances Δz to the focus, i.e., stronger focusing. Also, the larger the beta function β_b in the buncher for constant focal length Δz, the more dominant does the first term in the square root become, so that β^* likewise decreases. Again, comparisons can be drawn to optics: A larger beam can be focused to smaller spot sizes.

In order to analyze the influence of the focus position, it has been varied in a range of $2.0\,\mathrm{m} \leq z_\mathrm{f} \leq 8.0\,\mathrm{m}$, using ASTRA; the cavity positions are unchanged with respect to the REGAE geometry, i.e., $z_\mathrm{g} = 0.00\,\mathrm{m}$ and $z_\mathrm{b} = 1.29\,\mathrm{m}$. A first scan has been performed without space charge. As expected, the minimal bunch length gets smaller, the closer the longitudinal focus is located with respect to the buncher's position. However, for very short focal length, the beam extent increases again, so that there is an optimum around $z_\mathrm{f} = 3.5\,\mathrm{m}$; see figure 5.20.

The behavior can be attributed to two effects. First, having a look at the shape of the longitudinal phase space for the short focal length – figures 5.21 – one finds that a third order is present for $z_\mathrm{f} < 3.5\,\mathrm{m}$, in contrast to the shortest bunch length achieved at $z_\mathrm{f} = 3.5\,\mathrm{m}$. In the latter case, a W-shape can be seen, indicating the fourth order; this bunch has an extent of 17 nm. Space charge effects are excluded. A comparison of the start phases of the different cases shows that for shorter focal length, ϕ_g gets closer to the maximum accelerating phase. As a consequence of this, the bunches which are focused closely behind the buncher cavity slip out of the overcompensation

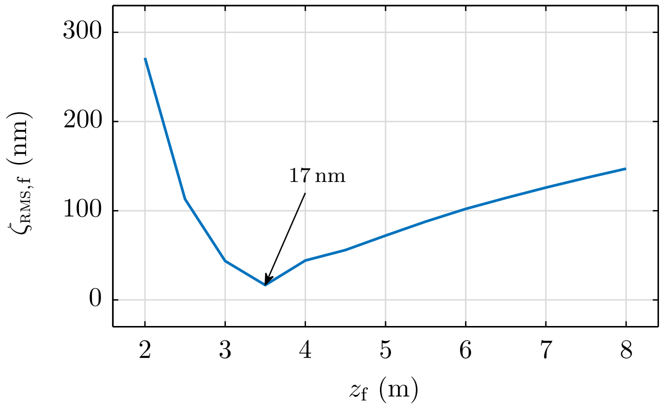

Figure 5.20 – Minimal bunch length for different focus positions. The resulting bunches get shorter with decreasing focal length, except for very close focus settings. The optimum is around $z_{\mathrm{f}} = 3.5\,\mathrm{m}$, having a bunch length of $\zeta_{\mathrm{RMS}} = 17\,\mathrm{nm}$. The ASTRA simulations have been performed without space charge forces.

mode. Thus, the third order dominates the bunch length for these cases, hindering a further compression. Shifting the buncher cavity further downstream should hence enable even shorter bunches, since this recovers the overcompensation mode even for shorter focal length.

A second reason which leads to the increased bunch length is found in transverse effects: Figure 5.21(b) shows the radial particle distribution in r-ζ space of bunches in the focus for different cases. As can be seen, for very short focal length, the off-axis particles fall behind. In other words, due to the high focus quality, differences in path length based on the transverse focusing of the beam start to influence the longitudinal structure of the bunch. The effect can also be seen from the layering in the longitudinal phase space plots according to the initial radial particle position.

For illustration one can assume two particles at the same longitudinal position behind the gun and with the same energy, but one on the central axis of the beam while the other one lies on a divergent trajectory. If the latter electron increases its transverse offset by 200 µm in the drift of 1 m from the gun to the buncher cavity, a longitudinal separation of the two particles of about

$$\delta z = \left[\sqrt{1^2 + (2\times 10^{-4})^2} - 1\right]\,\mathrm{m} \approx 2\times 10^{-8}\,\mathrm{m} = 20\,\mathrm{nm}, \tag{5.43}$$

builds up. For typical electron bunches such a small value is negligible. However, the bunches treated here are likewise on the order of a few 10 nm, and thus, the lengthening is significant.

This gets even more interesting when looking at the longer focal length. Suddenly, off-axis particles which have to travel a *longer* distance surpass the on-axis electrons. This counter-intuitive result can also be explained by off-axis effects. Particles starting with a larger divergence at the gun travel a longer distance towards the buncher. Here, the delayed particles gain more energy than expected, since they arrive at a later phase compared to the reference particle from their initial longitudinal bunch slice. However, this means that these particles are now faster.

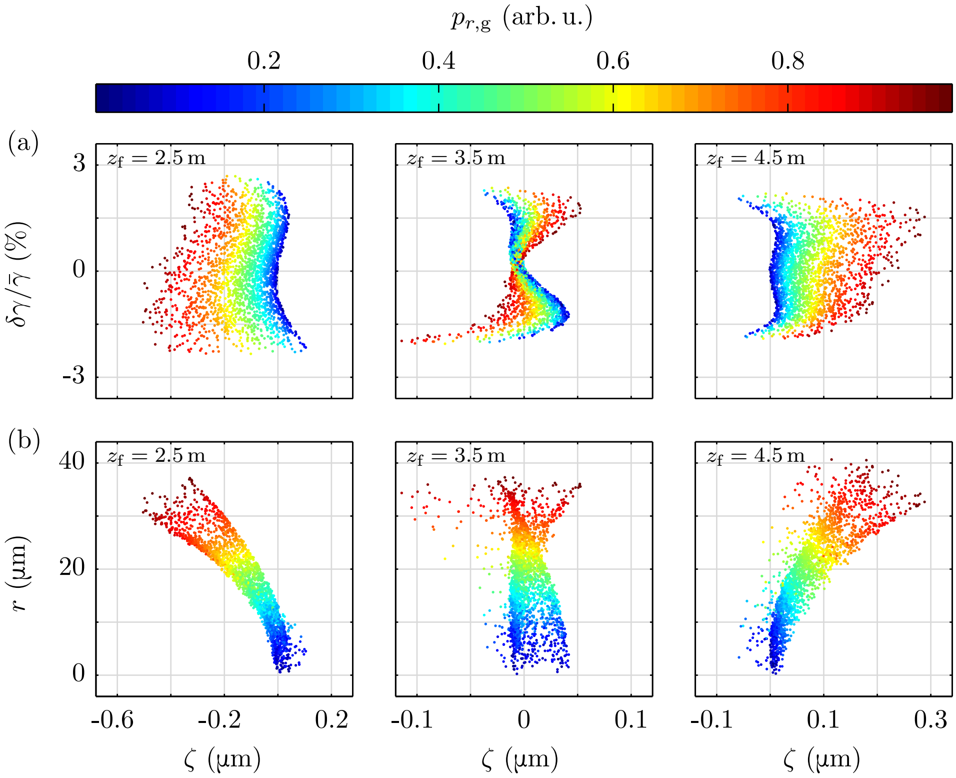

Figure 5.21 – (a) Longitudinal phase space distributions in the focus for three different focal lengths. For the case of $z_\mathrm{f} = 2.5\,\mathrm{m}$, a third order contribution is still present, in contrast to the larger focal length: The W-shape indicates a dominating fourth order. The color code depicts the radial particle momenta $p_{r,\mathrm{g}}$ at the end of the electron gun at $z = 0.1\,\mathrm{m}$. The phase space distribution shows a layering according to the associated initial particle divergence. The same effect can be seen in figures (b), where the radial position at the focus is compared to the longitudinal particle coordinate. Transverse effects start to influence the achievable bunch length.

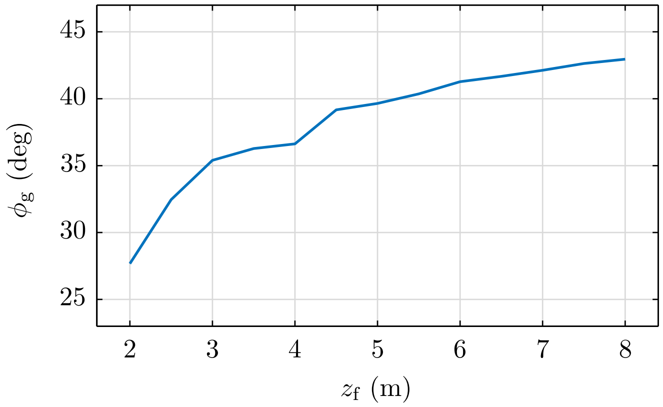

Figure 5.22 – Gun phase ϕ_g as function of the focus position. The closer the longitudinal focus is shifted to the buncher cavity, the more ϕ_g is reduced. For focus positions $z_f < 3.5\,\mathrm{m}$, the machine settings slip out of the overcompensation mode, leading to the third order effect visible in figure 5.21.

And thus, the off-axis particles can compensate for the loss and even outrun the on-axis electrons, despite the longer way they have to travel again in the second section. In the case of the shortest bunch extent, both effects cancel each other out, leading to a bunch length of $\zeta_{\mathrm{RMS}} = 17\,\mathrm{nm}$. Thus, a compression ratio greater than 2.5×10^4 is reached, taking into account the fully expanded beam of about 450 µm.

By this effect the complexity of the bunch compression scheme increases, giving room to optimize the bunch structure in focus even further. It now depends also on the settings of the beam optics, and with that comes an additional dependency on the energy, apart from the kinetic factors η_i defined in equations (5.3). Furthermore, the cavities also exert (de-)focusing forces on the bunch, depending on the phase [140]. However, one should keep in mind that space charge is excluded in the presented simulations, which, of course, is bound to have additional effects.

Finally, shifting the focus to positions further away from the buncher yields another option: The buncher phase approaches the zero crossing more and more until, eventually, a bunching and accelerating configuration is found. For the parameter set used here, this happens at about $z_f = 10\,\mathrm{m}$. Of course, coupled to the long focal length, the minimal bunch length achieved is larger than in the case of a hard focus.

Space Charge and Initial Bunch Length

Adding space charge and sampling the focal length in finer steps, slightly shifts the position of the shortest bunches towards $z_f = 3.25\,\mathrm{m}$. The minimal bunch length achieved increases due to the repulsing effects and the associated increase in the longitudinal emittance by this uncorrelated effect.

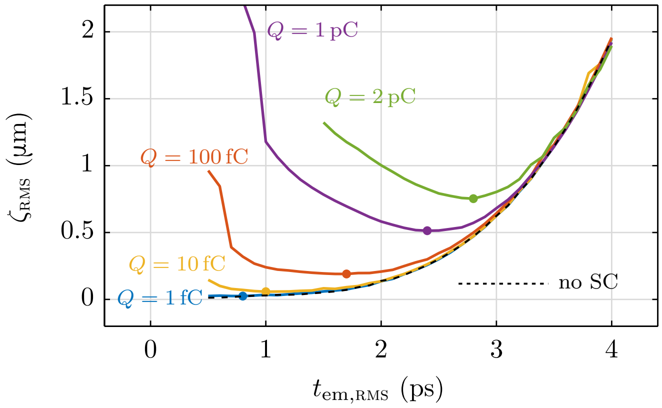

Figure 5.23 – Minimal bunch length in the focus versus emission time at the gun, $t_{\mathrm{em}}, \mathrm{RMS}$, evaluated for different bunch charges. With a lower charge, the optimum shifts towards shorter emission times, while higher charged bunches require a longer emission time. The optimum results from balancing the Coulomb repulsion in the gun against the cavity- and drift-based nonlinearities in phase space. For long emission times, the results converge to the case without space charge. For very short emission times, the high charge cases do not lead to stable beams.

Most of the influence of the Coulomb interaction happens at the electron emission and acceleration in the first half-cell of the gun, while space charge effects are decreasing with larger energies. Also, the charge density at the cathode is comparatively large due to the small beam spot of the laser, as discussed in 5.3.1. In order to further optimize the results one can try to increase the initial bunch length, i.e., vary the length of the cathode laser pulse, τ_{RMS}, reducing the charge density and thus the influence of the Coulomb interaction. Going back to the ballistic bunching formalism, equations (5.19), it is apparent that $\zeta_{\mathrm{g,RMS}}$ enters directly the description of the bunch length in focus. In other words, the minimal achievable bunch length in focus increases with larger τ_{RMS} due to uncorrected higher order nonlinearities, and possible remainders of not perfectly eliminated second and third order contributions. Hence, there should be an optimum of the competing effects.

Figure 5.23 shows a scan for different space charge scenarios. As expected, there is an optimal setting, between $0.5\,\mathrm{ps} \leq \tau_{\mathrm{RMS}} \leq 3.0\,\mathrm{ps}$, depending on the charge. For longer initial pulses, all cases converge to the same final bunch extent, since here the contribution of $\zeta_{\mathrm{g,RMS}}$ in the polynomials becomes dominant, while space charge effects can be neglected.

Please note that for very low charges of $Q = 1\,\mathrm{fC}$, bunch length below 100 as are predicted by the simulation, which is on the level of the shortest light pulses created in attosecond-science [144, 145]. However, only about 5 000 particles contribute to such an electron bunch. Hence, if the linearization technique can be pushed to these limits, this could, for example, result in an increase of time-resolution for ultra-fast electron diffraction to this level. However, prior to such claims, an electron bunch of this type needs to be demonstrated first. This requires a suitable measurement concept for such short structures with so little charge. Furthermore, if the method

Q (fC)	$t_{\text{em,RMS}}$ (ps)	ζ_{RMS} (nm)	t_{RMS} (fs)	I_{pk} (A)
1	0.8	24	0.1	7
10	1.0	58	0.2	40
100	1.7	190	0.6	150
1000	2.4	513	1.7	400
2000	2.8	753	2.5	550

Table 5.3 – Parameters for electron bunches focused at $z_{\text{f}} = 3.25\,\text{m}$, employing different bunch charges. The emission time is balanced for the shortest bunch length depending on the charge, as depicted in figure 5.23. For very low charges, bunches on the order of 100 as are predicted, while high charge cases produce (local) peak currents of several hundred Amperes.

proves viable, the timing fluctuations need to be reduced to a similar level, especially for an external pump pulse. In addition, the target has to be positioned precisely in the extremely localized focus, due to the strong focusing.

In contrast, for much higher charges, peak currents of several hundred amperes can be achieved. Using for example a 2 pC bunch, a compression to about 750 nm can still be achieved, which corresponds to $I_{\text{pk}} \approx 550\,\text{A}$. The bunch length and peak currents for the various cases are summarized in table 5.3.

An analytic estimate for the achievable bunch length at the focus depending on the charge is complex. It is limited by the non-correlated contributions to the longitudinal emittance by the Coulomb repulsion, mostly happening in the gun. It thus requires the description of the influence of space charge effects on the longitudinal emittance inside the gun, which is tied to additional dynamics due to the large change in energy in the gun and other effects like mirror charges at the cathode during the emission process. The description of the gun dynamics, however, is not covered by the analytical model derived in section 5.1.2. Furthermore, space charge effects in the longitudinal focus need to be considered, which also needs an extension of the analytic model. Interestingly, the values obtained for the bunch length at the focus, given in table 5.3 suggests a scaling like $\zeta_{\text{RMS}} \propto \sqrt{Q}$, see figure 5.24, which requires further investigations beyond the scope of this thesis.

5.3.3 Energy Modulation

The energy spread compensation and the linearized bunch compression scheme are only two special cases of a linearized phase space. In principle, there must also be solutions eliminating these higher orders, but resulting in a skew line in phase space.

An interesting option making use of that is the creation of a periodically structured electron density, i.e., a micro-bunched beam. The idea itself is not new, see for example [146–149]. However, the quality of the resulting spike pattern can be improved employing the overcompensation mode: One can add a modulation to the bunch in the first emittance minimum which evolves into a spiked current pattern in the subsequent drift. The energy modulation develops into a density

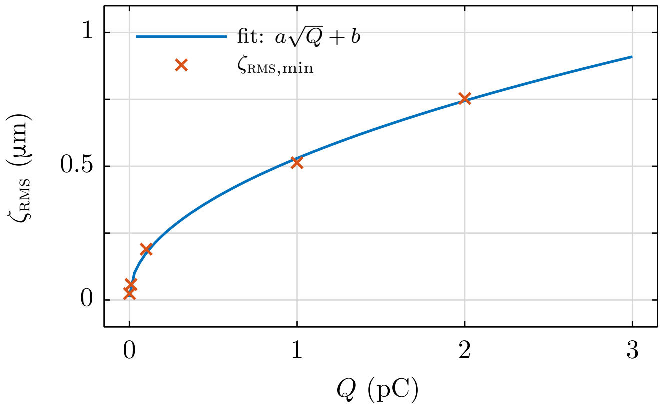

Figure 5.24 – Numerical fit to the minimal bunch length obtained depending on the bunch charge. The fit model used is $\zeta_{\mathrm{RMS}} = a\sqrt{Q} + b$. The resulting fit parameters are $a = 0.52\,\mu\mathrm{m}/\sqrt{C}$ and $b = 0.01\,\mu\mathrm{m}$.

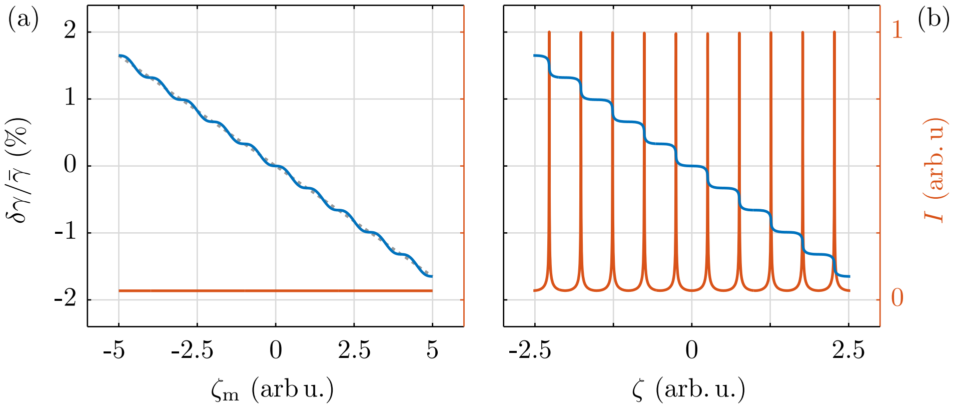

Figure 5.25 – Concept of the micro-bunch evolution based on a modulation of the initial electron bunch. In (a) the initial bunch has a uniform current profile and a negatively correlated energy spread, i.e., it is set for bunch compression. A sinusoidal modulation is added to the distribution, which evolves into the staircase pattern depicted in (b), according to equation (5.47). The associated current distribution develops evenly spaced spikes in this linear model.

modulation, while the global energy spread compresses the whole bunch structure. If the parameters are chosen in such a way that the second emittance minimum and the maximal micro-bunch pattern coincide, the resulting spikes in the current distribution are spaced very evenly and are of similar magnitude. The first of these properties is achieved, because the emittance values at the locations of the two minima are of comparable magnitude, so that a linear mapping between the two points is ensured [57]. The second property is resulting from a (more or less) uniform charge density at the modulation point and the underlying phase space linearization, which – on average – yields a likewise uniform density distribution in the second emittance minimum.

Employing a radiation emission process at the location of maximum modulation, for example by making use of a foil, will hence yield a coherent emission at the wave length of the spacing [147, 150] – which is determined by the overall compression of the bunch. Possible processes to imprint the modulation in the first emittance minimum are not explored here; see for example [148, 149], where the modulation is induced by the wakefields of the bunch in a dielectric structure. In the following, only the basic concept of applying the overcompensation mode to the modulation-based micro-bunch formation is demonstrated.

At the modulation spot z_m, the bunch is linear in the sense that the second order, g_2 vanishes. Following the notation in equations (5.4) and (5.5), the incoming energy at this point can be expressed as

$$\hat{\gamma}_\mathrm{m} = g_0 + g_1(z_\mathrm{m})\zeta_\mathrm{m} + \underbrace{g_2(z_\mathrm{m})}_{\equiv 0}\zeta_\mathrm{m}^2 + \cdots =: \hat{M}_0 + \hat{M}_1\zeta_\mathrm{m}. \tag{5.44}$$

The modulation is added by a sine function:

$$\tilde{\gamma}_\mathrm{m} = \Gamma \sin\left(\kappa\zeta_\mathrm{m}\right), \tag{5.45}$$

where Γ is the amplitude describing the modulation depths, and $\kappa = 2\pi/\lambda_\mathrm{m}$ is the respective wave vector. It is chosen such that the modulation wavelength is shorter than the bunch length, i.e., $\lambda_\mathrm{m} < \zeta_{\mathrm{m,RMS}}$. The energy function then reads

$$\gamma_\mathrm{m} = \hat{\gamma}_\mathrm{m} + \tilde{\gamma}_\mathrm{m} = \underbrace{M_0}_{\gamma_0} + \underbrace{M_1\zeta_\mathrm{m} + \Gamma\sin\left(\kappa\zeta_\mathrm{m}\right)}_{\delta\gamma}. \tag{5.46}$$

Here, M_i=$\hat{M}_i$, since the effect of the modulation is entirely contained in the sine term.

To first order, the position change of a particle in the bunch is given by

$$\begin{aligned}\zeta(z) &= \zeta_\mathrm{m} + \eta_1\delta\gamma\,(z - z_\mathrm{m}) \\ &= \zeta_\mathrm{m}\left[1 + \eta_1 M_1\,(z - z_\mathrm{m})\right] + \eta_1\Gamma\sin\left(\kappa\zeta_\mathrm{m}\right)(z - z_\mathrm{m}),\end{aligned} \tag{5.47}$$

analogously to equation (5.1). The evolution of a modulated bunch described by equation (5.47) can be seen in figure 5.25. In this case, M_1 is negative, so that the bunch length decreases. As can be seen, the sine structure leads to a stair case pattern at a later point, and hence the particle density develops spikes.

The location of this micro-bunching is determined by the amplitude Γ. In this case, it is adjusted such that the micro-bunch pattern builds up at the second emittance minimum behind

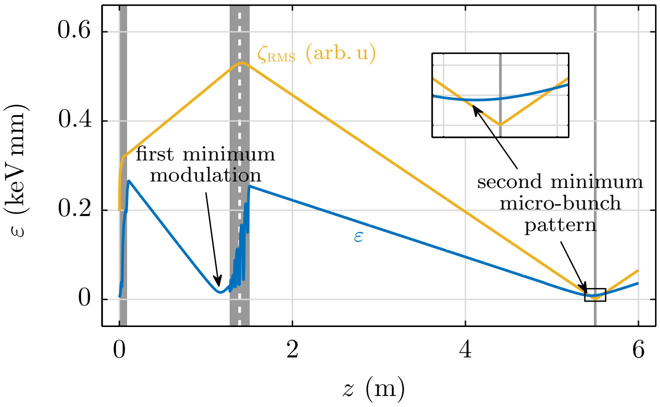

Figure 5.26 – Application of the micro-bunching concept in the case of the overcompensation mode: The bunch is modulated in the first emittance minimum, where the phase space distribution is linear. The micro-bunch pattern is achieved in the second minimum, shortly in front of the longitudinal focus.

the buncher. Contrary to the previous cases, the parameters for the compression behind the buncher are chosen such that this emittance minimum itself is slightly in front of the actual focus, defined by $X_1 = 0$; see figure 5.26. Thus the distribution is linear again, but the line is not upright. Moreover, the emittance values at the two points are of comparable magnitude, and hence, the mapping between the phase spaces at the two points is close to linear. In consequence, the micro-bunch pattern is spread evenly and thus the bunch can be turned into a coherent radiation source, for example making use of light emission from transition radiation.

The radiation process should happen localized, due to the constant changing bunch length and nonlinear contributions which build up again in a longer drift section. That is, an undulator, for example, would not be a suitable tool. The emitted photons have a wavelength that is given by the modulation period divided by the compression factor of the associated ballistic bunching. It can be calculated from the bunch form factor (BFF), which is the Fourier transform of the line charge density [147, 150]. Since the beam is not in focus, the bunching factor will be on the order of 100, rather than 1 000. A modulation at optical wavelengths could thus be transferred into extreme ultra-violet radiation or even soft-x-rays. Also (and more likely), THz radiation could be produced [147–150]. And, due to the high quality associated with the linearization, higher orders of the emission process could also be employed, either further reducing the produced wavelength, or relaxing the demands on the modulation period.

The result from an ASTRA simulation for such a case is shown in figure 5.27; the simulation has been performed without space charge forces. The RMS bunch length at the modulation point is $\zeta_{\mathrm{RMS,mod}} \approx 0.9\,\mathrm{mm} \mathrel{\widehat{=}} 3\,\mathrm{ps}$. Since the distribution is still an inverted parabola, the maximum bunch extent is given by $\Delta\zeta_{\mathrm{max}} = 2\sqrt{5}\,\zeta_{\mathrm{RMS,mod}} \approx 4.2\,\mathrm{mm}$. The modulation wavelength is 267 µm, so that the bunch covers 15 full periods. The amplitude of the modulation is $\delta p_z = 150\,\mathrm{eV/c}$, which is about 3.6×10^{-5} of the mean longitudinal momentum $\langle p_z \rangle = 4.2\,\mathrm{MeV/c}$.

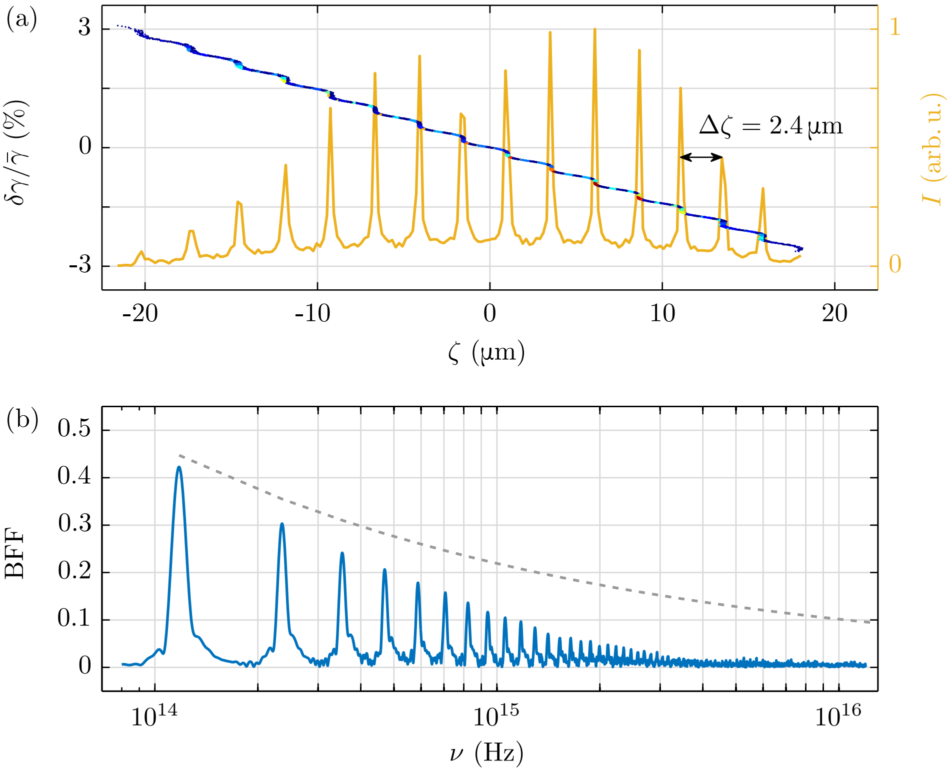

Figure 5.27 – ASTRA simulation of a bunch modulated in the first emittance minimum and tracked to the second minimum. As can be seen from the phase space pattern and the current profile depicted in figure (a), a spiked charge density builds up. Figure (b) shows the expected bunch form factor. The separation of the micro-bunches in figure (a), $\Delta\zeta = 2.4\,\mu\text{m}$ corresponds to the fundamental wavelength of $\lambda = 2.4\,\mu\text{m} \mathrel{\widehat{=}} 1.25 \times 10^{14}\,\text{Hz}$ in figure (b). The calculation of the BFF has been performed using the ASTRA post-processing tool [56].

As pointed out above, a micro-bunch pattern evolves with a spacing of $\Delta\zeta = 2.4\,\mu\text{m}$, corresponding to a compression factor of about 100. In figure 5.27(b), the corresponding bunch form factor is shown. The fundamental frequency of $\nu_1 = 1.25 \times 10^{14}\,\text{Hz}$ corresponds to a wavelength $\lambda_1 = 2.4\,\mu\text{m} = \Delta\zeta$. The high accuracy of the spacing in the micro-bunch pattern is demonstrated by the more than 20 harmonics that can be identified. This is made possible by the linearity of the mapping. The bunch form factor does not reach the theoretical optimum, which can be estimated for a perfect structure with zero emittance to $0.4473\,n^{-1/3}$ [146], where n is the harmonic number.

To evaluate the applicability of the concept, an analysis with space charge is required. However, since the beam is not set for maximal compression, one could start with a long bunch of higher charge. This way, the local electron density is low enough to reduce the influence of the Coulomb repulsion on the spike formation and the linearity of the process. It is also important that the transverse beam diameter is small enough for a coherent emission: $r_{\text{RMS}} \ll \zeta_{\text{RMS}}/\gamma$ must be fulfilled in order to apply the line charge model [147], leading to the bunch form factor. Also, suitable modulation concepts and compression ratios are required to shift the resulting radiation towards the THz or extreme ultra-violet (EUV) frequency bands. For EUV radiation, thus modulation concepts in the optical to ultra-violet are required, assuming a compression ratio of 100. Please note that the compression ratio can be adjusted within certain limits, allowing for a tunable radiation source.

5.3.4 Freeze-Out

The ballistic bunching mechanism leads to short bunches, but only at a specific location. However, the bunching factors η_i scale with $1/\gamma^3$, and higher powers for the nonlinear coefficients. Hence, an injection of a linearized and focused bunch into a subsequent cavity could effectively freeze out the bunch structure due to the increasing γ value. Especially the second and third order nonlinearities, which are proportional to $1/\gamma^4$ and $1/\gamma^5$ respectively, can be eliminated by this approach. The resulting bunch would keep the short extent over a longer distance, ideally over the entire length of the accelerator.

A simulation of this concept has been done, using the REGAE geometry once more, but adding a 5 m S-band **T**raveling **W**ave **S**tructure (TWS) with an average accelerating gradient of about 28 MV/m, resulting in an energy gain of about $\Delta T \approx 140\,\text{MeV}$. As can be seen in figure 5.28, the absolute energy spread is even reduced in this case, due to the short phase interval covered by the injected bunch. The correlated energy spread is almost eliminated at the end of the TWS, meaning that the bunch is injected such that the focus is nearly reached during acceleration, while the ballistic bunching is more and more suppressed. The actual focus is achieved at about two meters behind the TWS. The longitudinal bunch evolution is negligible, though, as it is less than 1 nm within five meters of drift. Also, the longitudinal emittance freezes at the minimal value, meaning that the higher order correlations are suppressed, which has been as assumed beforehand: The nonlinear coefficients are suppressed by a factor of 8×10^5 and 2×10^7, compared to a bunch with $\gamma = 10$. The linear term is likewise suppressed more, namely by a factor of 3×10^4. Space charge forces have not been considered in the simulation.

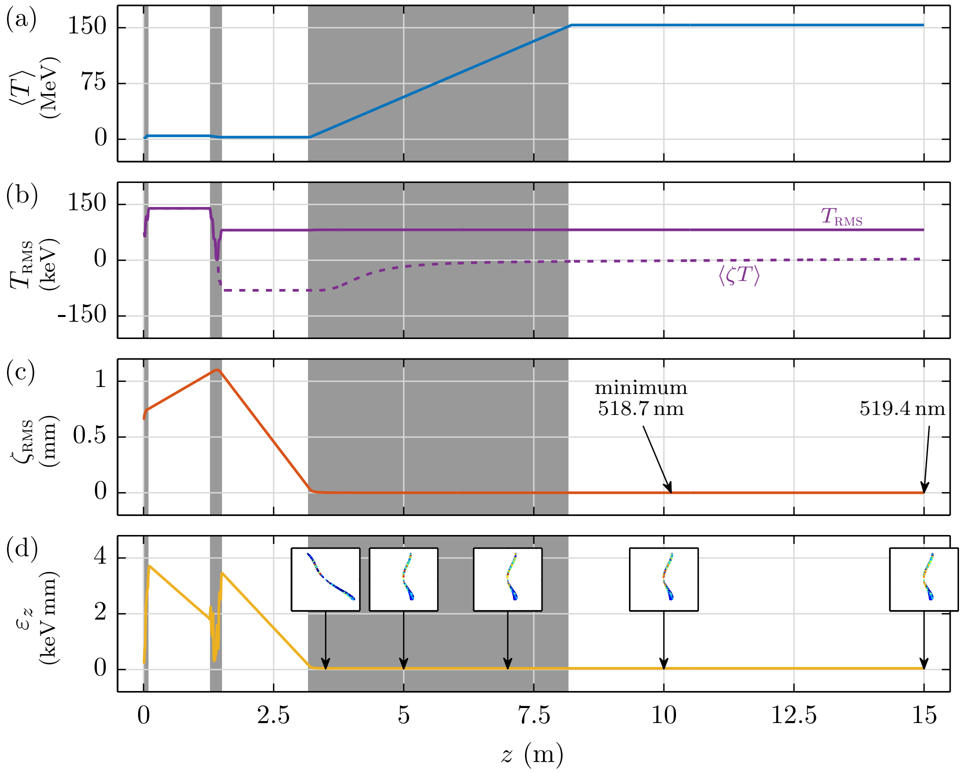

Figure 5.28 – Evolution of the mean kinetic energy (a), the energy spread (b), as well as the bunch length (c) and the longitudinal emittance (d) for the injection of a linearized bunch into a TWS. Behind the additional cavity, the ballistic bunch compression mechanism is strongly suppressed, so that the correlated energy spread $\langle \zeta T \rangle$ is close to zero, and $\zeta_{\rm RMS}$ and ε are frozen at their minimal values. The insets depict the longitudinal phase space distribution at various points along the beam line. The axis limits of the scatter plots are set to identical values, that is, the bunch evolution is frozen. Space charge forces were disabled in the simulation.

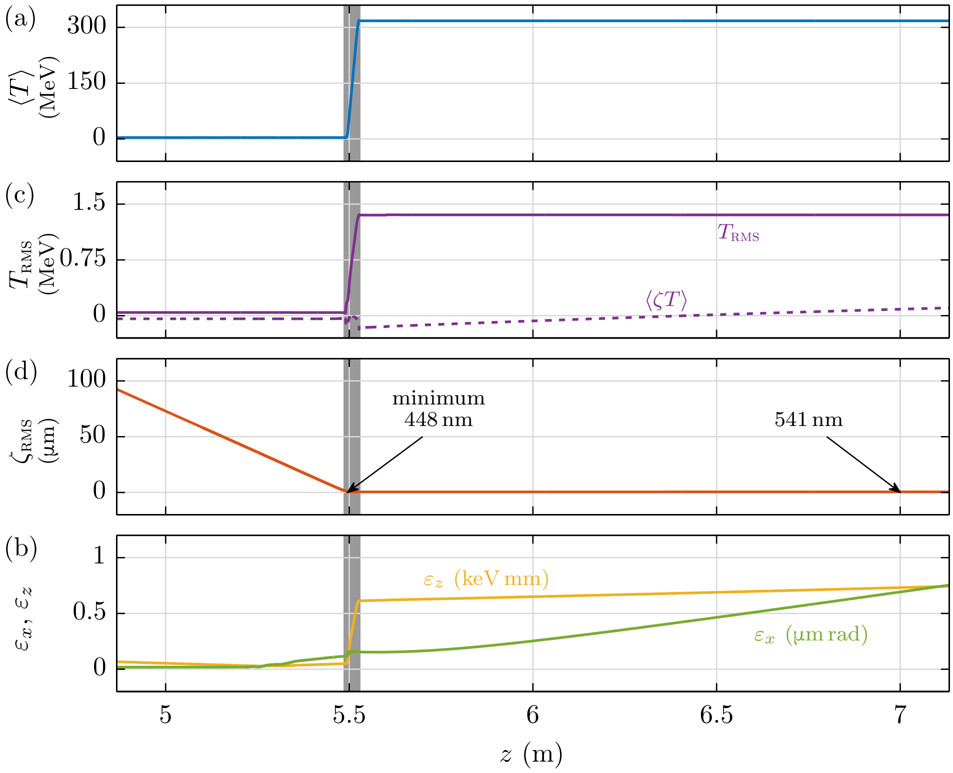

Figure 5.29 – Evolution of a linearized bunch injected into a plasma wakefield. Mean energy (a), RMS energy spread (b), bunch length (c), and longitudinal as well as transverse emittance (d) are depicted. Due to the short plasma wavelength, a significant energy spread is acquired. As a consequence, the ballistic bunching process is not entirely suppressed. The transverse emittance is increased inside the plasma due to a mismatched beta function, and grows further in the subsequent drift due to the acquired energy spread combined with the divergence of the beam. The longitudinal emittance is increased due to nonlinearities caused by the wakefield.

The ideal is to carefully optimize each order so that it gets frozen at the desired position. In some cases, it will even be necessary to achieve and maintain a certain curvature setting. For example, if a magnetic chicane compressor is additionally used, one can pre-compensate for the curvature acquired in that device. Another option is to freeze a micro-bunched configuration as discussed above. In this case, it would be possible to use an undulator for the radiation process. However, the linear energy spread along the whole bunch must be taken into account and compensated by the TWS for such a setup. Also, the curvature applied by the booster cavity needs to be considered. Please note that since the longitudinal bunch evolution is eliminated in the drift behind the booster, the curvature does not change the current density. Hence, a compensation is possibly not required, as long as no dispersive elements are used.

Another candidate for the freeze-out scheme would be a plasma booster. Due to the shortness of the bunch, the relative energy spread acquired inside the plasma remains within reasonable bounds, while the high gradient rapidly suppresses the ballistic bunching process and the evolution of the nonlinearities. Depending on the associated plasma wavelength, a curvature similar to that in an rf-like structure will build up, though. Also, due to the small beam spots required because of the matching, transverse effects can reduce the longitudinal focus quality. Likewise, space charge in a transversely and longitudinally focused bunch poses a problem for such a delicate technique. However, even a second order corrected bunch would further improve the results of the experiment described in chapter 3.

A simulation of the injection of a linearized bunch into a plasma wakefield has been performed. The plasma density in this case was set to $n_\mathrm{e} = 10^{17}\,\mathrm{cm}^{-3}$, using a 35 mm plateau, and 5 mm ramps. Laser guiding has been assumed, that is, the laser beam envelope was constant over the last 20 mm of the plateau. Specific numbers for the self-focusing threshold have not been calculated for this case. The injected electron bunch results from a similar case to case (iv) depicted in section 5.2. However, the gun amplitude has been increased to 120 MV/m and the transverse focus has been set to the plasma position. The bunch has an energy of about 3.7 MeV, a charge of $Q = 50\,\mathrm{fC}$, and a length of about 1 µm. The increase in the bunch extent by a factor of more than three is attributed to space charge repulsion and a slight longitudinal mismatch, so that the injection happens prior to the longitudinal focus. The bunch is further compressed in the plasma. Transverse effects have not been analyzed and could contribute to the lengthening.

Within the plasma, the beam is accelerated to $\langle T \rangle = 300\,\mathrm{MeV}$. As can be seen in figure 5.29, a freezing effect can be achieved. However, the effect is not as strong as the one in the TWS case. This is a result of the additional correlated energy spread acquired in the plasma, due to the shortness of the plasma wave length. Also, the longitudinal emittance is strongly increased due to the energy spread, as well as nonlinearities imprinted by the plasma. The transverse emittance is increased by a about 50 % in the plasma, meaning that the beam is not ideally matched. The divergence in combination with the large energy spread leads to an additional growth of this quantity in the subsequent drift, which could be reduced if a focusing element were to be included. The same effect already leads to an increased emittance during the focusing into the plasma.

Figure 5.30 depicts the phase space of the accelerated beam. It shows a complex structure and also some curvature effect in the high charge region. An in-depth analysis of this particular injection has not been performed. Nevertheless, this last case shows that an injection of low energy electrons into a plasma wakefield can be achieved even at shorter plasma wavelength. The parameters of the plasma profile as well as the machine settings of Regae can be further improved to optimize the result of this exemplary case.

5.4 Summary

In this chapter, a novel linearization scheme of the longitudinal phase space has been described. Instead of using a shorter wavelength cavity for that purpose, like in a higher harmonic structure, the method takes advantage of the beam dynamics itself by stretching the bunch, thus achieving

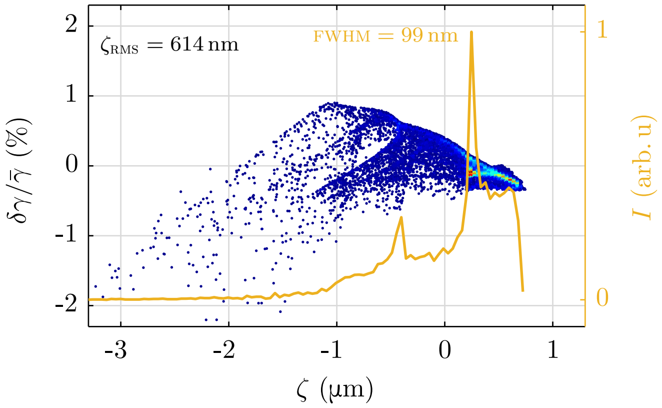

Figure 5.30 – Longitudinal phase space of a linearized bunch injected into a plasma wakefield. Despite the shorter bunch extent, the smallness of the plasma features lead to a complex structure.

a similar effect with an accelerating field at the fundamental frequency of the rf system. The technique is called *stretcher mode*.

For the application of the stretcher mode, a controlled beam expansion is mandatory. Therefore, an analytic model has been developed in the course of this thesis, describing the process. It is very well supported by ASTRA simulations. If the special case of the *overcompensation mode* is applied, even the third order nonlinearity can be eliminated. The results of the simulations in this case suggest an improvement of the bunch compression ratio at REGAE by a factor of ten compared to the design parameters, i.e., possible bunch durations below 1 fs – including space charge. As an alternative, bunches with a relative energy spread below $T_{\mathrm{RMS}}/\left\langle T\right\rangle < 10^{-5}$ can be produced.

Even shorter bunches can be generated when the focal length is reduced. Further possible applications are the freeze-out scheme or the generation of evenly spaced micro-bunch patterns in a long electron bunch. However, more investigations – including a treatment of space charge forces – are required on these topics.

The general method provides a broad applicability, since an additional higher harmonic cavity as well as the associated rf system are not required. At REGAE, for example, a third harmonic system would be a 9 GHz structure, which results in high acquisition costs – apart from the fact that there is no space to include such an X-band device and the demands from the ANGUS beam into the drift section between buncher cavity and interaction chamber.

The experiments drafted for REGAE can in principle be conducted with the machine as it is. The first step for that demonstration will be the energy spread compensation, since it is relatively insensitive to fluctuations and more importantly, the bunch evolution is stopped behind the buncher cavity. This makes the measurement more accessible, since it only relies on a high resolution electron spectrometer. The additional klystron to be installed at REGAE is essential for the measurement, though. In order to demonstrate the improved bunch compression, a transverse deflecting structure is required and planned. It could, however, also be measured using a plasma-based concept [96].

The ultimate goal is the acceleration of such a linearized bunch by an (emittance conserving) injection into a laser-driven plasma wakefield, thus combining the concepts developed and described in this Ph.D. work.

6 Discussion and Outlook

The preceding chapters of this work have dealt with two major topics. In the first part, the external injection of conventionally generated electron bunches into a laser-driven plasma wakefield has been explored, while the last chapter has been dedicated to a novel method to further improve the beam quality of conventional sources in terms of longitudinal beam dynamics – holding the promise to extend this also to laser wakefield acceleration.

The external injection experiment is designed as a diagnostic tool for the plasma fields. The electrons emitted by REGAE are injected into the plasma at varying time delays with respect to the driving laser pulse and thus at different phases of the plasma wakefield. By analyzing the resulting energy spectrum, the strength of the accelerating field can be determined and correlated to the injection phase. Thus, it allows for the mapping of the wakefield.

The simulations performed and presented in this thesis show that an injection into a laser-driven plasma wakefield at REGAE is possible. In particular, it is feasible to transport electron bunches through the plasma for phase settings which cover about one third of the plasma wavelength, despite the low injection energy and the accordingly large phase slippage. The emittance growth within the plasma can be limited to less than 50 %, using the standard focusing optics to adjust the beam parameters at the plasma entrance according to the matched beta function.

The back-calculation of the accelerating field structure from the resulting spectra – the goal of the experiment – can be performed in the case of an on-axis injection in the accelerating and focusing phase region. However, only the *integrated* field is accessible by the measurement of the resulting energy, so that a model has to be assumed in an iterative method: If the model is correct, measurement and calculation result in the same energy gain curve. However, it is not proven that the *local* field reconstruction, i.e., the model, is unique. Furthermore, for the integration performed in the case analyzed in this thesis, the less important decelerating phase region is not well reconstructed. As a result, it requires a more exact treatment of the phase slippage, which is asymmetric around the peak of the field.

An issue with this approach is the combination of the phase slippage and the varying wakefield amplitude caused by the evolution of the laser intensity. A simplification could thus be obtained if a guiding channel were used. In that case, the laser beam envelope stays constant, and hence the wakefield amplitude does not change, either.

The mapping of the wakefield can also be extended to transverse offsets, so that a three-dimensional wakefield profile is obtained. In this case, however, the bunch performs betatron oscillations around the symmetry axis defined by the laser's path. Since the accelerating field strength depends on the radial position, this leads to an additional amplitude variation of the accelerating field – on top of the phase slippage and laser envelope issues. The magnitude of this effect requires further investigations.

The betatron oscillations also lead to an increase of the RMS emittance of the bunch and thus raises questions about the beam transport to the spectrometer, i.e., the measurement of an off-axis injected beam. Since the emittance growth, however, is based on the described phase space mixing, the slice emittance is affected far less by this *spiralization* effect. In combination with the imprinted energy correlation, this means that an oscillating pattern is created at the spectrometer screen. The image might be clipped, but it should be possible to attribute the fragments to the off-axis injection. The combination of slice emittance and energy chirp thus mitigates the influence of transverse offset jitters of laser and electrons, which is one of the main issues identified in terms of parameter tolerance along with the timing jitter between REGAE and the laser. Both uncertainties are based on statistical fluctuations, so that a large statistics leads to a reduction of the impact.

Another uncertainty not treated in the course of this work stems from variations of the plasma density. An overall deviating density leads to different accelerating fields and a different plasma period. Hence, the periodicity in the measured signal changes accordingly, so that this case can be deduced directly from the phase scan performed in the laser-pump electron-probe experiment. A fluctuation of the plasma density on top of a constant plateau is more challenging. The electrons pass through varying phases and amplitudes, depending on the strength of the density fluctuations. The effect is further complicated by the laser evolution, i.e., the local driver strength of the wake. Further investigations are required to judge the impact of such uncertainties. In addition, a precise characterization of the plasma density in the experiment is required in order to avoid these instabilities.

ASTRA uses the analytic equations of the linear regime of laser wakefield acceleration. Thus, there can be deviations from that model if, for example, nonlinear plasma fields occur. A way to identify a nonlinear behavior is to look at the period length of the plasma, which gets elongated in the nonlinear case. To distinguish this lengthening from a linear wake at lower density, which also has a longer plasma wavelength, one could compare the range of phases that allow for a passage of the electrons. Since the focusing phase interval in the nonlinear regime is increased compared to the increasingly reduced defocusing section, the overall phase range in which a passage of electrons through the plasma is possible increases, broadening the detectable phase range, and thus shifting the ratio to values larger than 1/3, as deduced from the simulations of the linear case.

An explicit deviation of the ASTRA simulations in this thesis from the later experiment is the description of the laser beam during the *overtaking process*. The laser profile of the ANGUS laser system is different from the Gaussian model, which has been used in the analysis, since the implementation of a super-Gaussian beam propagation model into the particle tracking code has not been finalized, yet. Hence, further investigations and measurements of the laser's effect on the electrons during the overtaking are required and planned [62].

The wakefield reconstruction should also yield a description of the emittance behavior, i.e., the emittance changes due to the beam dynamics induced by the plasma must be derivable from the fields and thus covered by the model. The emittance in turn must be measured to refine the model and understand the plasma effects. Analysis on this topic can also be found in [29]. Such a measurement requires stable experimental conditions, since the concepts to determine the emittance typically rely on a multi-shot method. To mitigate additional emittance effects in the drift behind the plasma, a beam optics closely behind the plasma targets is required to reduce the divergence. At REGAE, an additional permanent solenoid is included in the target chamber, which can be used for this purpose. By this approach, concepts to mitigate plasma induced emittance growth [31, 32, 79] by matched injection and controlled (transverse) beam expansion at the plasma exit can be tested and analyzed with the external injection experiments at REGAE.

An emittance-conserving beam transport is of utmost importance for staged laser wakefield accelerators and hybrid machines using a plasma-based booster. The bunch charge of such machines is typically on the order of several pico-Coulombs and more. In order to compress and focus an electron bunch of this kind, a dedicated photo injector with a higher injection energy than provided by REGAE is required. Since space charge forces scale inversely with the energy, their effect is reduced by higher energies.

Coulomb repulsion is not the only effect which hinders bunch compression. Nonlinear correlations in the longitudinal phase space lead to a lower limit for the minimal bunch extent, too. In order to eliminate the contribution at REGAE, a new method has been derived in the course of this thesis. This *stretcher mode* concept relies on the controlled beam expansion after the electron gun, such that the evolved nonlinearities can be corrected by the subsequent buncher cavity. The idea is to mimic a higher harmonic structure by this expansion: The reference for the curvature and higher order effects is the bunch length. That is, nonlinearities in a bunch of unchanged length which can be corrected by a higher harmonic structure can likewise be eliminated in an expanded beam which is sent through a cavity operated at the fundamental frequency of the rf system.

The concept described and mathematically derived in the second part of this thesis works exceptionally well according to ASTRA simulations. For the case of REGAE, a bunch length well below 1 fs can be obtained, compared to 7 fs without linearization. Using less charge and a shorter focal length, even shorter bunches down to a 100 fs level are suggested by the simulations. Alternatively, an energy spread compensation to relative values of $T_{\mathrm{RMS}}/\langle T\rangle < 10^{-5}$ can be obtained.

Further improvements of the model could include an analytic formulation which incorporates space charge forces. However, the treatment of Coulomb forces changes the drift description from a purely kinetic to a dynamic problem. In addition, the calculation of the Coulomb fields in an electron bunch is complex [142]: The scaling of the space charge fields depends on the longitudinal (L) and radial size (R) of the bunch, since the behavior of the space charge fields differs for various aspect ratios $A = R/L$. A radial dependency has not been considered in the formalism so far. The longitudinal space charge field, E_z, shows a nonlinear behavior along the ζ-coordinate towards the edges of a long bunch ($A < 1$), whilst this dependency is linear in the case of a short bunch ($A > 1$), converging to a constant field strength given by an infinitesimally thin sheet of charge for extremely short bunches ($A \gg 1$). That is, the behavior can change during the compression process, where the bunch shape evolves from a long, cylindrical shape to a pancake like structure in the focus. Since the aspect ratio is given in the rest frame of the bunch, there is an additional dependence on the energy, γ. Also, since the transverse beam size is not constant, A shows another variation along the beam line, given by the focusing elements and possible transverse space charge forces. On top of this complications, the fields depend on the type of the charge density distribution – which can evolve and change along the drift as well.

Another improvement would be the inclusion of the gun dynamics in the mathematical formulation. In the work presented here, the bunch structure at the end of the gun is taken from an ASTRA simulation. Due to the large phase slippage in the first half cell of the gun, an analytic description can only be achieved by an approximation [140]. To extend the stretcher mode model to this gun dynamics description, it is hence important to analyze the calculated bunch structure at the end of the gun up to the third order and compare it to the corresponding Taylor polynomial obtained by an ASTRA simulation. For too large deviations, an adaption of the gun dynamics description is required. A stretcher mode model which includes both, space charge effects and phase slippage in the gun, would be beneficial, since it should provide a scaling of the minimal bunch length obtainable with the charge carried by the bunch.

The linearization concept can be adapted to different machine configurations. For example by the inclusion of a third harmonic structure, which could be used to even correct for forth and fifth order nonlinearities. This is important in the case of very long bunches. Also, a chicane formalism can be developed. Ballistic bunching is limited to energies on the order of 10 MeV, since the linear bunching factor scales with $1/\gamma^3$. That is, an energy doubling at REGAE from 5 MeV to 10 MeV already reduces the efficiency by one order of magnitude, meaning that the focal length increases to about 40 m. This can be partly reduced by an increased gradient of the buncher cavity, and/or an increased length of that structure. Both of these counter measures, however, scale linearly only and are limited, meaning the ballistic bunching concept is rendered inefficient for higher energies.

Instead, chicane-based bunching schemes are required. The dispersion in a magnetic chicane leads to different path lengths for different energies, so that a longitudinal shift between particles of different longitudinal momentum occurs. Similar to the kinetic evolution described in chapter 5.1.1, this shift is subject to a nonlinear evolution. The description of chicane-based bunching is typically done via the matrix formalism. The linear matrix element is denoted by R_{56}. The higher orders are described in that formalism by the matrix element T_{566} for the second order and the matrix element U_{5666} for the third order [46]. Since the same polynomial structure underlies formulations of both concepts, a chicane can be included into the stretcher mode formalism – or, alternatively, the stretcher mode concept can be included in the matrix formalism. Hence, chicane effects in principle can be (pre-)compensated by the stretcher mode. Lastly, the novel concept effectively does the same as higher harmonic structures, which are successfully operated at various accelerator facilities.

The stretcher mode concept can also be applied to improve the micro-bunch formation obtained from an upstream modulation: The sinus pattern added at the modulation point develops into a staircase structure in phase space, resulting in a spiked current profile. In the case of the stretcher concept, or more precisely the special case of the *overcompensation mode*, the quality of the pattern can be improved, resulting in an evenly spaced spiked current profile. Hence, in a radiation process, coherent radiation is emitted. The simulation performed in the context of this thesis to demonstrate the concept contains more than ten harmonics. However, the case has not been analyzed with space charge forces enabled, which must be considered for such delicate structures. Hence, further investigations are needed.

Two factors determine the spacing of the current spikes, and thus the radiation frequency: The modulation wavelength and the compression ratio. The compression ratio cannot be too large, i.e., it will be on the order of 100 and less, because the bunch must not be in the longitudinal focus at the point where the full micro-bunch pattern unfolds; in the focus all particles are at the same longitudinal position, so that the spikes would be on top of each other. In the example given, the wavelength of the emitted radiation, would be in the infrared region. To produce radiation in the nanometer range, e.g., the water window below 4 nm, either a modulation in the ultraviolet region is required, or the usage of a large harmonic of the radiation is chosen, which in turn requires a very high quality micro-bunch pattern. At this point in time, the concept thus seems more feasible for THz radiation, where similar sources already exist.

Radiation of 1 THz corresponds to 300 µm $\widehat{=}$ 1 ps. The modulation thus would be in the millimeter range and can be obtained for example by wakefield induced energy modulations in a dielectric structure [149]. The bunch length at the modulation point consequently needs to be on the order of several millimeters. The wavelength emitted by the source can be tuned by adapting the compression ratio. Shifting the radiation to the optical band could be an interesting option for diagnostics and the demonstration of the linearization concept in the context of the micro-bunch formation.

Alternatively, one could think about a combination with a booster cavity, so that the micro-bunched beam is injected into that subsequent accelerating structure, where the pattern is frozen. The ballistic bunching process which underlies the compression and the micro-bunching process is suppressed with $1/\gamma^3$. In that case, the emission angle $\theta = 1/\gamma$ of the radiation reduces, too, due to this scaling associated with synchrotron radiation. If the booster cavity at the same time corrects for the linear energy correlation, the bunch could even be sent through an undulator, i.e., the requirement for a *local* emitter is no longer valid. Depending on the number of micro-bunches, the modulation could possibly even seed an FEL process.

A long bunch cannot be injected into a plasma. However, the micro-bunching concept yields an interesting option here, as well. If the spacing of the current spikes is tuned to the plasma wavelength, an injection in a way that each micro-bunch is accelerated in a separate bucket can be obtained. The resulting multi-bunch train can for example be further compressed in a downstream chicane, since an energy correlation is still present: Each micro-bunch is assumed to be injected into an accelerating field of the same magnitude, so that ideally the energy correlation from the preceding ballistic bunching process is maintained. At the same time, the defocusing fields of the plasma filter out a fraction of the electrons between the spikes, thus reducing the associated background signal. The length of the micro-bunch pattern, i.e., the maximum number of current spikes, depends also on the number of stable buckets formed by the plasma in that case, which might limit the applicability as an FEL driver due to slippage of the bunch with respect to the emitted light field. This, however, needs to be further explored. In any case, the approach poses an interesting concept for plasma injection.

Including the stretcher-mode linearization scheme into the photo-injector line for a hybrid accelerator described above allows for maximum compression to operate the plasma-booster at a density of $n_\mathrm{e} = 10^{17}\,\mathrm{cm}^{-3}$. This results in higher accelerating gradients of up to 30 GV/m, depending on the driver laser strength. At the same time, the use of bunch charges of a few pico-Coulombs is possible due to the higher injection energy. Thus, with such an injection-optimized pre-accelerator, an emittance conserving beam transport and acceleration as suggested in [32] could be obtained.

The REGAE studies, which are conceptually described in this thesis, and the insights gained from the experiments are first steps to test the applicability of the advanced concepts described in this chapter. The required beam line upgrade at REGAE, which has been developed in the course of this thesis, is planned for the near future. The experiments are scheduled for 2017. Since the experiments at the LUX project are in the starting phase, experiences gained with the ANGUS laser system and experimental insights – like for example optimized alignment procedures – can be transferred and adapted to the REGAE side arm, leading to possible changes and adaptions of the systems illustrated here.

When the external injection experiment at REGAE is finally executed, the knowledge and results gained from that wakefield diagnostic will be transferred to LUX and combined with the findings at this beam line. Despite the low charge, the results obtained in terms of the field distribution and, in particular, matching and beam transport through the plasma are cornerstones for any plasma booster scenario. No matter whether it is the staging of several plasma cells, or the external injection from a conventional source: In order to produce a usable bunch, a controllable and emittance conserving beam transport through the plasma is inevitable. The linearization concept can be applied to various low- and mid-charge accelerators, including photo injectors for novel hybrid machines, which are possible candidates for FEL operations due to their compactness based on the large acceleration gradients of the plasma fields and the high level of beam control obtained with conventional techniques.

List of Figures

List of Tables

Bibliography

[1] T. Tajima and J. M. Dawson, "Laser electron accelerator," *Phys. Rev. Lett.*, vol. 43, pp. 267–270, 1979.

[2] D. Strickland and G. Mourou, "Compression of amplified chirped optical pulses," *Opt. Commun.*, vol. 56, no. 3, pp. 219–221, 1985.

[3] E. Esarey, C. B. Schroeder, and W. P. Leemans, "Physics of laser-driven plasma-based electron accelerators," *Rev. Mod. Phys.*, vol. 81, no. 3, pp. 1229–1285, 2009.

[4] J. Faure, Y. Glinec, A. Pukhov, S. Kiselev, S. Gordienko, E. Lefebvre, J.-P. Rousseau, F. Burgy, and V. Malka, "A laser-plasma accelerator producing monoenergetic electron beams.," *Nature*, vol. 431, no. 7008, pp. 541–544, 2004.

[5] C. G. R. Geddes, C. S. Toth, J. van Tilborg, E. Esarey, C. B. Schroeder, D. Bruhwiler, C. Nieter, J. Cary, and W. P. Leemans, "High-quality electron beams from a laser wakefield accelerator using plasma-channel guiding.," *Nature*, vol. 431, no. 7008, pp. 538–541, 2004.

[6] S. P. D. Mangles, C. D. Murphy, Z. Najmudin, A. G. R. Thomas, J. L. Collier, A. E. Dangor, E. J. Divall, P. S. Foster, J. G. Gallacher, C. J. Hooker, D. A. Jaroszynski, A. J. Langley, W. B. Mori, P. A. Norreys, F. S. Tsung, R. Viskup, B. R. Walton, and K. Krushelnick, "Monoenergetic beams of relativistic electrons from intense laser-plasma interactions.," *Nature*, vol. 431, no. 7008, pp. 535–538, 2004.

[7] W. P. Leemans, B. Nagler, A. J. Gonsalves, C. Toth, K. Nakamura, C. G. R. Geddes, E. Esarey, C. B. Schroeder, and S. M. Hooker, "Gev electron beams from a centimetre-scale accelerator," *Nature Phys.*, vol. 2, pp. 696–699, 2006.

[8] W. P. Leemans, A. J. Gonsalves, H.-S. Mao, K. Nakamura, C. Benedetti, C. B. Schroeder, C. Tóth, J. Daniels, D. E. Mittelberger, S. S. Bulanov, J.-L. Vay, C. G. R. Geddes, and E. Esarey, "Multi-GeV Electron Beams from Capillary-Discharge-Guided Subpetawatt Laser Pulses in the Self-Trapping Regime," *Phys. Rev. Lett.*, vol. 113, pp. 245002–5, 2014.

[9] A. J. Gonsalves, K. Nakamura, J. Daniels, H. S. Mao, C. Benedetti, C. B. Schroeder, C. Tóth, J. van Tilborg, D. E. Mittelberger, S. S. Bulanov, J. L. Vay, C. G. R. Geddes, E. Esarey, and W. P. Leemans, "Generation and pointing stabilization of multi-GeV electron beams from a laser plasma accelerator driven in a pre-formed plasma waveguidea)," *Phys. Plasmas*, vol. 22, no. 5, pp. 056703–9, 2015.

[10] S. Bulanov, N. Naumova, F. Pegoraro, and J. Sakai, “Particle injection into the wave acceleration phase due to nonlinear wake wave breaking,” *Phys. Rev. E*, vol. 58, no. 5, pp. R5257–R5260, 1998.

[11] J. Faure, C. Rechatin, A. Norlin, A. Lifschitz, Y. Glinec, and V. Malka, “Controlled injection and acceleration of electrons in plasma wakefields by colliding laser pulses.,” *Nature*, vol. 444, no. 7120, pp. 737–739, 2006.

[12] V. Malka, J. Faure, C. Rechatin, A. Ben-Ismail, J. K. Lim, X. Davoine, and E. Lefebvre, “Laser-driven accelerators by colliding pulses injection: A review of simulation and experimental results,” *Phys. Plasmas*, vol. 16, no. 5, p. 056703, 2009.

[13] R. Weingartner, S. Raith, A. Popp, S. Chou, J. Wenz, K. Khrennikov, M. Heigoldt, A. R. Maier, N. Kajumba, M. Fuchs, B. Zeitler, F. Krausz, S. Karsch, and F. Grüner, “Ultralow emittance electron beams from a laser-wakefield accelerator,” *Phys. Rev. ST Accel. Beams*, vol. 15, p. 111302, 2012.

[14] G. R. Plateau, C. G. R. Geddes, D. B. Thorn, M. Chen, C. Benedetti, E. Esarey, A. J. Gonsalves, N. H. Matlis, K. Nakamura, C. B. Schroeder, S. Shiraishi, T. Sokollik, J. van Tilborg, C. Tóth, S. Trotsenko, T. S. Kim, M. Battaglia, T. Stöhlker, and W. P. Leemans, “Low-Emittance Electron Bunches from a Laser-Plasma Accelerator Measured using Single-Shot X-Ray Spectroscopy,” *Phys. Rev. Lett.*, vol. 109, p. 064802, 2012.

[15] O. Lundh, J. Lim, C. Rechatin, L. Ammoura, A. Ben-Ismail, X. Davoine, G. Gallot, J.-P. Goddet, E. Lefebvre, V. Malka, and J. Faure, “Few femtosecond, few kiloampere electron bunch produced by a laser-plasma accelerator,” *Nature Phys.*, vol. 7, pp. 219–222, 2011.

[16] A. Buck, M. Nicolai, K. Schmid, C. M. S. Sears, A. Sävert, J. M. Mikhailova, F. Krausz, M. C. Kaluza, and L. Veisz, “Real-time observation of laser-driven electron acceleration,” *Nature Phys.*, vol. 7, pp. 543–548, 2011.

[17] M. Fuchs, R. Weingartner, A. Popp, Z. Major, S. Becker, J. Osterhoff, I. Cortrie, B. Zeitler, R. Hörlein, G. D. Tsakiris, U. Schramm, T. P. Rowlands-Rees, S. M. Hooker, D. Habs, F. Krausz, S. Karsch, and F. Grüner, “Laser-driven soft-X-ray undulator source,” *Nature Phys.*, vol. 5, no. 11, pp. 826–829, 2009.

[18] M. Fuchs, *Laser-Driven Soft-X-Ray Undulator Source.* Ph.D. thesis, Ludwig-Maximilians-Universitäat München, München, Germany, 2010.

[19] A. R. Maier, *Generation and Characterization of Few-Fs X-Ray Pulses.* Ph.D. thesis, University of Hamburg, Hamburg, Germany, 2012.

[20] A. R. Maier, N. Kajumba, A. Guggenmos, C. Werle, J. Wenz, N. Delbos, B. Zeitler, I. Dornmaier, J. Schmidt, E. M. Gullikson, F. Krausz, U. Kleinerberg, S. Karsch, and F. Grüner, “Water-Window X-Ray Pulses from a Laser-Plasma Driven Undulator,” *submitted*, 2016.

[21] F. Grüner, S. Becker, U. Schramm, T. Eichner, M. Fuchs, R. Weingartner, D. Habs, J. Meyer-ter Vehn, M. Geissler, M. Ferrario, L. Serafini, B. van der Geer, H. Backe,

W. Lauth, and S. Reiche, “Design considerations for table-top, laser-based VUV and X-ray free electron lasers,” *Appl. Phys. B*, vol. 86, no. 3, pp. 431–435, 2007.

[22] A. R. Maier, A. Meseck, S. Reiche, C. B. Schroeder, T. Seggebrock, and F. Grüner, “Demonstration Scheme for a Laser-Plasma-Driven Free-Electron Laser,” *Phys. Rev. X*, vol. 2, p. 031019, 2012.

[23] Z. Huang, Y. Ding, and C. B. Schroeder, “Compact x-ray free-electron laser from a laser-plasma accelerator using a transverse-gradient undulator.,” *Phys. Rev. Lett.*, vol. 109, no. 20, p. 204801, 2012.

[24] `laola.desy.de`.

[25] `lux.cfel.de`.

[26] N. Delbos. Ph.D. thesis in preparation, University of Hamburg, Hamburg, Germany, 2017.

[27] U. Hahn and K. Zapfe, *Richtlinien für UHV-Komponenten bei DESY.* Deutsches Elektronen-Synchrotron DESY, Hamburg, Germany. (Version 1.6 / 22.09.2010).

[28] B. Zeitler, I. Dornmair, T. Gehrke, M. Titberidze, A. R. Maier, B. Hidding, K. Flöttmann, and F. Grüner, “Merging conventional and laser wakefield accelerators,” in *SPIE Optics + Optoelectronics* (E. Esarey, C. B. Schroeder, W. P. Leemans, K. W. D. Ledingham, and D. A. Jaroszynski, eds.), vol. 8779, (Prague, Czech Republic), p. 877904, SPIE, 2013.

[29] M. Hachmann, *High precision transverse emittance measurement for novel plasma accelerators.* Ph.D. thesis in preparation, University of Hamburg, Hamburg, Germany, 2017.

[30] K. Floettmann, “Some basic features of the beam emittance,” *Phys. Rev. ST Accel. Beams*, vol. 6, no. 3, p. 034202, 2003.

[31] K. Floettmann, “Adiabatic matching section for plasma accelerated beams,” *Phys. Rev. ST Accel. Beams*, vol. 17, p. 054402, 2014.

[32] I. Dornmair, K. Floettmann, and A. R. Maier, “Emittance conservation by tailored focusing profiles in a plasma accelerator,” *Phys. Rev. ST Accel. Beams*, vol. 18, p. 041302, 2015.

[33] M. Titberidze, *Pilot Study of Synchronization on a Femtosecond Scale between the Electron Gun REGAE and a Laser-Plasma Accelerator.* Ph.D. thesis, University of Hamburg, Hamburg, Germany, 2016.

[34] A. Pukhov and J. Meyer-ter Vehn, “Laser wake field acceleration: the highly non-linear broken-wave regime,” *Appl. Phys. B*, vol. 74, no. 4-5, pp. 355–361, 2002.

[35] C. B. Schroeder, E. Esarey, C. G. R. Geddes, C. Benedetti, and W. P. Leemans, “Physics considerations for laser-plasma linear colliders,” *Phys. Rev. ST Accel. Beams*, vol. 13, p. 101301, 2010.

[36] S. Steinke, J. van Tilborg, C. Benedetti, C. G. R. Geddes, C. B. Schroeder, J. Daniels, K. K. Swanson, A. J. Gonsalves, K. Nakamura, N. H. Matlis, B. H. Shaw, E. Esarey, and W. P. Leemans, "Multistage coupling of independent laser-plasma accelerators," *Nature*, vol. 530, no. 7589, pp. 190–193, 2016.

[37] A. R. Rossi, A. Bacci, M. Belleveglia, E. Chiadroni, A. Cianchi, G. Di Pirro, M. Ferrario, A. Gallo, G. Gatti, C. Maroli, A. Mostacci, V. Petrillo, L. Serafini, P. Tomassini, and C. Vaccarezza, "The External-Injection experiment at the SPARC_LAB facility," *Nucl. Instr. Meth. Phys. Res. A*, vol. 740, pp. 60–66, 2014. Proceedings of the first European Advanced Accelerator Concepts Workshop 2013.

[38] R. Assmann, C. Behrens, R. Brinkmann, U. Dorda, K. Flöttmann, B. Foster, J. Grebenyuk, M. Gross, I. Hartl, M. Hüning, F. Kärtner, B. Marchetti, Y. Nie, J. Osterhoff, A. Rühl, H. Schlarb, B. Schmidt, F. Stephan, A. S. Müller, M. Schuh, F. Grüner, B. Hidding, A. R. Maier, and B. Zeitler, "SINBAD - A Proposal for a Dedicated Accelerator Research Facility at DESY," in *Proceedings of IPAC2014*, (Dresden, Germany), pp. 1466–1469, 2014. TUPME047.

[39] I. Dornmair. Private communication.

[40] R. J. D. Miller, R. Ernstorfer, M. Harb, M. Gao, C. T. Hebeisen, H. Jean-Ruel, C. Lu, G. Moriena, and G. Sciaini, "dynamical structural science 'Making the molecular movie': first frames," *Acta Cryst.*, vol. 66, no. 2, pp. 137–156, 2010.

[41] G. Sciaini and R. J. D. Miller, "Femtosecond electron diffraction: heralding the era of atomically resolved dynamics," *Rep. Prog. Phys.*, vol. 74, no. 9, pp. 096101–37, 2011.

[42] S. Manz, A. Casandruc, D. Zhang, Y. Zhong, R. A. Loch, A. Marx, T. Hasegawa, L. C. Liu, S. Bayesteh, H. Delsim-Hashemi, M. Hoffmann, M. Felber, M. Hachmann, F. Mayet, J. Hirscht, S. Keskin, M. Hada, S. W. Epp, K. Flöttmann, and R. J. D. Miller, "Mapping atomic motions with ultrabright electrons: towards fundamental limits in space-time resolution," *Faraday Discuss.*, vol. 177, pp. 467–491, 2015.

[43] E. Vogel, C. Albrecht, N. Baboi, C. Behrens, T. Delfs, J. Eschke, C. Gerth, M. G. Hoffmann, M. Hoffmann, M. Hüning, R. Jonas, J. Kahl, D. Kostin, G. Kreps, F. Ludwig, W. Maschmann, C. Müller, P. Nommensen, J. Rothenburg, H. Schlarb, C. Schmidt, J. Sekutowicz, H. Edwards, E. R. Harms, A. Hocker, T. N. Khabiboulline, and M. Kuhn, "Test and Commissioning of the Third Harmonic RF System for FLASH," in *Proceedings of IPAC'10*, (Kyoto, Japan), pp. 4281–4283, 2010. THPD003.

[44] R. Brinkmann, K. Flöttmann, J. Roßbach, P. Schmüser, N. Walker, and H. Weise, eds., *TESLA - Technical Design Report, Part II*. Hamburg, Germany: DESY, 2001. Report No. DESY 2001-011.

[45] T. I. Smith, "Intense Low Emittance Beams for Free Electron Lasers," in *Proceedings of the 1986 Linear Accelerator Conference (LINAC86)*, (Stanford, CA, USA), pp. 421–426, SLAC, 1986. SLAC-R-PUB-303.

[46] K. Floettmann, T. Limberg, and P. Piot, "Generation of ultrashort electron bunches by cancellation of nonlinear distortions in the longitudinal phase space," TESLA-FEL Report 2001-06, DESY, Hamburg, Germany, 2001.

[47] F. Fu, R. Wang, P. Zhu, L. Zhao, T. Jiang, C. Lu, S. Liu, L. Shi, L. Yan, H. Deng, C. Feng, Q. Gu, D. Huang, B. Liu, D. Wang, X. Wang, M. Zhang, Z. Zhao, G. Stupakov, D. Xiang, and J. Zhang, "Demonstration of Nonlinear-Energy-Spread Compensation in Relativistic Electron Bunches with Corrugated Structures," *Phys. Rev. Lett.*, vol. 114, p. 114801, 2015.

[48] B. Zeitler, K. Floettmann, and F. Grüner, "Linearization of the longitudinal phase space without higher harmonic field," *Phys. Rev. ST Accel. Beams*, vol. 18, p. 120102, 2015.

[49] `regae.desy.de`.

[50] M. Hada, J. Hirscht, D. Zhang, S. Manz, K. Pichugin, D. Mazurenko, S. Bayesteh, H. Delsim-Hashemi, K. Floettmann, M. Huening, S. Lederer, G. Moriena, C. Mueller, G. Sciaini, and D. Miller, "REGAE: New Source for Atomically Resolved Dynamics," in *Research in Optical Sciences*, (Washington, D.C.), p. JT2A.47, 2012.

[51] K. Floettmann, "Generation of sub-fs electron beams at few-MeV energies," *Nucl. Instr. Meth. Phys. Res. A*, vol. 740, pp. 34–38, 2014. Proceedings of the first European Advanced Accelerator Concepts Workshop 2013.

[52] X. H. Lu, C. X. Tang, R. K. Li, H. To, G. Andonian, and P. Musumeci, "Generation and measurement of velocity bunched ultrashort bunch of pC charge," *Phys. Rev. ST Accel. Beams*, vol. 18, p. 032802, 2015.

[53] T. Gehrke, "Design of Permanent Magnetic Solenoids for REGAE," Master's thesis, University of Hamburg, Hamburg, Germany, 2013.

[54] T. Lamb, M. K. Bock, M. Bousonville, M. Felber, P. Gessler, F. Ludwig, S. Ruzin, H. Schlarb, B. Schmidt, S. Schulz, and E. Janas, "Femtosecond stable laser-to-RF phase detection using optical modulators," in *Proceedings of FEL2011*, (Shanghai, China), pp. 551–554, 2011. THPA32.

[55] K. Floettmann, "ASTRA – A space charge tracking algorithm." `http://www.desy.de/~mpyflo`.

[56] K. Floettmann, *ASTRA – A Space Charge Tracking Algorithm*, 2014. User manual. Version 3.0.

[57] K. Flöttmann. DESY MPY. Private communication.

[58] A. E. Siegmann, *Lasers*. Sausalito, CA, USA: University Science Books, 1971.

[59] K. T. McDonald, "A Relativistic Electron Can't Extract Net Energy from a Long Laser Pulse." Accessed online June 03, 2016, 1997.

[60] R. Paschotta, "M2 factor." *Encyclopedia of Laser Physics and Technology*. Accessed online June 11, 2016. URL: `https://www.rp-photonics.com/m2_factor.html`.

[61] V. Leroux. Private communication.

[62] V. Leroux. Ph.D. thesis in preparation, University of Hamburg, Hamburg, Germany, 2017.

[63] I. Dornmair, *Advanced Beam Dynamics and Diagnostics Concepts for Laser-Plasma Accelerators* . Ph.D. thesis, University of Hamburg, Hamburg, Germany, 2016.

[64] B. Schmidt, "Accelerator Physics." Lecture Notes (WiSe 2013/14), 2014.

[65] S. Y. Lee, *Accelerator Physics.* Singapore, Singapore: World Scientific Publishing Co. Pte. Ltd, second ed., 2004.

[66] H. Golstein, C. Poole, and J. Safko, *Classical Mechanics.* San Francisco, CA, USA: Addison Wesley, third ed., 2002.

[67] "Covariance." Encyclopedia of Mathematics. Accessed online June 05, 2016. URL: `http://www.encyclopediaofmath.org/index.php?title=Covariance_matrix&oldid=13365`.

[68] K. Floettmann, "Erratum: Some basic features of the beam emittance [Phys. Rev. ST Accel. Beams 6, 034202 (2003)]," *Phys. Rev. ST Accel. Beams*, vol. 6, no. 7, p. 079901, 2003.

[69] E. D. Courant and H. S. Snyder, "Theory of the alternating gradient synchrotron," *Ann. Phys.*, vol. 3, no. 1, pp. 1–48, 1958.

[70] P. Gibbon, *Short Pulse Laser Interactions with Matter: An Introduction.* London, UK: Imperial College Press, 2005.

[71] M. Titberidze, F. Grüner, A. R. Maier, B. Zeitler, M. Felber, K. Flöttmann, T. Lamb, H. Schlarb, C. Sydlo, and E. Janas, "Novel Femtosecond Level Synchronization of Titanium Sapphire Laser and Relativistic Electron Beams," in *Proceedings of IBIC2014*, (Monterey, CA, USA), pp. 174–178, 2014. MOPD12.

[72] T. Weineisen, "Density Measurement inside a Sapphire Capillary for Laser Wakefield Acceleration," diploma thesis, Ludwig-Maximilians-Universitäat München, München, Germany, 2009.

[73] T. Weineisen, B. Göppner, K. Schmid, M. Fuchs, H. Schröder, S. Karsch, and F. Grüner, "Density measurement in a laser-plasma-accelerator capillary using Raman scattering," *Phys. Rev. ST Accel. Beams*, vol. 14, no. 5, pp. 050705–5, 2011.

[74] B. Göppner, "Density Gradients in Discharge Capillary Waveguides," diploma thesis, Ludwig-Maximilians-Universitäat München, München, Germany, 2011.

[75] L. Schaper, L. Goldberg, T. Kleinwächter, J.-P. Schwinkendorf, and J. Osterhoff, "Longitudinal gas-density profilometry for plasma-wakefield acceleration targets," *Nucl. Instr. Meth. Phys. Res. A*, vol. 740, pp. 208–211, 2014. Proceedings of the first European Advanced Accelerator Concepts Workshop 2013.

[76] P. Messner, "Target Design and Diagnostics for Laser Wakefield Acceleration," Master's thesis, University of Hamburg, Hamburg, Germany, 2015.

[77] "Radiant Zemax," 2013. `http://www.zemax.com`.

[78] M. Schnepp. Private communication.

[79] T. Mehrling, J. Grebenyuk, F. S. Tsung, K. Floettmann, and J. Osterhoff, "Transverse emittance growth in staged laser-wakefield acceleration," *Phys. Rev. ST Accel. Beams*, vol. 15, p. 111303, 2012.

[80] P. Strauch, "Numerical simulations on electron bunch degradation due to co-linear ponderomotive scattering," bachelor's thesis, University of Hamburg, Hamburg, Germany, 2013.

[81] P. Neuhäußer, "Analysis of a Method for Determination of Bunch Length and Beam Arrival Time by Collinear Ponderomotive Scattering at REGAE," Master's thesis, University of Hamburg, Hamburg, Germany, 2014.

[82] R. Paschotta, "Beam Parameter Product." *Encyclopedia of Laser Physics and Technology*. Accessed online June 11, 2016. URL: `https://www.rp-photonics.com/beam_parameter_product.html`.

[83] I. N. Bronstein, K. A. Semendjajew, G. Musiol, and H. Mühlig, *Taschenbuch der Mathematik*. Thun und Frankfurt am Main, Germany: Verlag Harri Deutsch, fifth ed., 2001.

[84] K. Peters. Private communication.

[85] M. J. de Loos and S. B. van der Geer, "General Particle Tracer." `http://www.pulsar.nl/gpt`.

[86] P. Neuhäußer. Private communication.

[87] N. Delbos. Private communication.

[88] M. Diem, "Analysis of an Electron Spectrometer Extension at REGAE," bachelor's thesis, University of Hamburg, Hamburg, Germany, 2014.

[89] A. Sävert, S. P. D. Mangles, M. Schnell, E. Siminos, J. M. Cole, M. Leier, M. Reuter, M. B. Schwab, M. Möller, K. Poder, O. Jäckel, G. G. Paulus, C. Spielmann, S. Skupin, Z. Najmudin, and M. C. Kaluza, "Direct Observation of the Injection Dynamics of a Laser Wakefield Accelerator Using Few-Femtosecond Shadowgraphy," *Phys. Rev. Lett.*, vol. 115, no. 5, pp. 055002–5, 2015.

[90] C. P. Browne and W. W. Buechner, "Broad-Range Magnetic Spectrograph," *Rev. Sci. Instrum.*, vol. 27, no. 11, pp. 899–907, 1956.

[91] R. L. Burman and A. I. Yavin, "Multi-purpose magnetic particle analyzer," *Nucl. Instrum. Methods*, vol. 7, no. 2, pp. 101–112, 1960.

[92] S. I. Warshaw, "Tangent focal plane approximations in the Browne-Buechner spectrometer," *Nucl. Instrum. Methods*, vol. 72, no. 1, pp. 5–12, 1969.

[93] "Median (in statistics)." *Encyclopedia of Mathematics.* Accessed online June 05, 2016. URL: `http://www.encyclopediaofmath.org/index.php?title=Median_(in_statistics)&oldid=26624`.

[94] "Percentile." *Encyclopedia of Mathematics.* Accessed online June 05, 2016. URL: `http://www.encyclopediaofmath.org/index.php?title=Percentile&oldid=31604`.

[95] "Quartile." *Encyclopedia of Mathematics.* Accessed online June 05, 2016. URL: `http://www.encyclopediaofmath.org/index.php?title=Quartile&oldid=31439`.

[96] I. Dornmair, C. B. Schroeder, K. Floettmann, B. Marchetti, and A. R. Maier, "Plasma-driven ultrashort bunch diagnostics," *Phys. Rev. Accel. Beams*, vol. 19, no. 6, p. 062801, 2016.

[97] G. Genoud, F. Wojda, M. Burza, A. Persson, and C. G. Wahlström, "Active control of the pointing of a multi-terawatt laser," *Rev. Sci. Instrum.*, vol. 82, no. 3, pp. 033102–7, 2011.

[98] A. R. Maier, "LUX laser beamline for LWFA." Presentation at the 2nd European Advanced Accelerator Concepts Workshop, 13–19 September 2015.

[99] N. Plambeck, "Vibration Measurements and Frequency Analyses for a TW-class Laser Transport Beamline," Master's thesis, University of Hamburg, Hamburg, Germany, 2014.

[100] C. Werle. Private communication.

[101] R. Trebino, *Frequency-Resolved Optical Gating: The Measurement of Ultrashort Laser Pulses.* Boston, MA, USA: Kluwer Academic Publishers, 2002.

[102] R. Loch. Max Planck Institute for the Structure and Dynamics of Matter (MPSD). Private communication.

[103] T. Gehrke, "Earth magnetic and AC magnetic field measurements and compensation at REGAE." Internal REGAE Report 03/2012, 2012.

[104] S. Bayesteh, H. Delsim-Hashemi, and K. Floettmann, "Beam Profile Monitors at REGAE," in *Proceedings of IBIC2013*, (Oxford, UK), pp. 212–215, 2013. MOPF06.

[105] H. Delsim-Hashemi, K. Floettmann, M. Seebach, and S. Bayesteh, "Charge Monitors at the Relativistic Electron Gun for Atomic Exploration-REGAE," in *Proceedings of IBIC2013*, (Oxford, UK), pp. 868–871, 2013. WEPF24.

[106] I. G. Valais, I. S. Kandarakis, D. N. Nikolopoulos, C. M. Michail, S. L. David, G. K. Loudos, D. A. Cavouras, and G. S. Panayiotakis, "Luminescence Properties of $(\mathrm{Lu,Y})_2\mathrm{SiO}_5 : \mathrm{Ce}$ and $\mathrm{Gd}_2\mathrm{SiO}_5 : \mathrm{Ce}$ Single Crystal Scintillators Under X-Ray Excitation for Use in Medical Imaging Systems," *IEEE Trans. Nucl. Sci.*, vol. 54, no. 1, pp. 11–18, 2007.

[107] S. Bayesteh, *Transverse electron beam diagnostics at REGAE.* Ph.D. thesis, University of Hamburg, Hamburg, Germany, 2014.

[108] D. Lipka, J. Lund-Nielsen, and M. Seebach, "Resonator for charge measurement at REGAE," in *Proceedings of IBIC2013*, (Oxford, UK), pp. 872–875, 2013. WEPF25.

[109] M. Hachmann and K. Floettmann, "Measurement of ultra low transverse emittance at REGAE," *Nucl. Instr. Meth. Phys. Res. A*, pp. 1–3, 2016. Proceedings of the second European Advanced Accelerator Concepts Workshop 2015.

[110] Hamamatsu Photonics K.K, “X-ray Scintillators.” `http://www.hamamatsu.com/resources/pdf/etd/FOS_ACS_GPXS_ALS_TXPR1024E.pdf`. Accessed online June 13, 2016.

[111] K. Krausert, “Development of Measurement Methods for Transverse Beam Profiles in the Micrometer Range at the REGAE Beamline,” Master’s thesis, University of Hamburg, Hamburg, Germany, 2015.

[112] H. Delsim-Hashemi. DESY MPY. Private communication.

[113] R. K. Li and P. Musumeci, “Single-Shot MeV Transmission Electron Microscopy with Picosecond Temporal Resolution,” *Phys. Rev. Applied*, vol. 2, p. 024003, 2014.

[114] D. Xiang, F. Fu, J. Zhang, X. Huang, L. Wang, X. Wang, and W. Wan, “Accelerator-based single-shot ultrafast transmission electron microscope with picosecond temporal resolution and nanometer spatial resolution,” *Nucl. Instr. Meth. Phys. Res. A*, vol. 759, no. 0, pp. 74–82, 2014.

[115] M. Hansli, A. Angelovski, R. Jakoby, A. Penirschke, K. Flöttmann, D. Lipka, H. Schlarb, S. Vilcins, F. Grüner, and B. Zeitler, “A Beam Arrival Time Cavity for REGAE at DESY,” in *Proceedings of IPAC2014*, (Dresden, Germany), pp. 1820–1822, 2014. TUPRI104.

[116] M. Hansli, *Kavitätsbasierende Sensoren zur Strahldiagnose für geringste Intensitäten.* Ph.D. thesis, Technische Universität Darmstadt, Darmstadt, Germany, 2016.

[117] J. Bach. Edwards GmbH, Kirchheim, Germany. Private communication.

[118] R. Lai and A. J. Sievers, “Determination of a charged-particle-bunch shape from the coherent far infrared spectrum,” *Phys. Rev. E*, vol. 50, no. 5, pp. R3342–R3344, 1994.

[119] R. Lai and A. J. Sievers, “On using the coherent far IR radiation produced by a charged-particle bunch to determine its shape: I Analysis,” *Nucl. Instr. Meth. Phys. Res.*, vol. 397, no. 2-3, pp. 221–231, 1997.

[120] S. Casalbuoni, B. Schmidt, and P. Schmüser, “Far-Infrared Transition and Diffraction Radiation Part I: Production, Diffraction Effects and Optical Propagation,” TESLA-FEL Report 2005-15, DESY, Hamburg, Germany, 2005.

[121] M. Hachmann, K. Floettmann, T. Gehrke, and F. Mayet, “Design and characterization of permanent magnetic solenoids for REGAE,” *Nucl. Instr. Meth. Phys. Res. A*, pp. 1–4, 2016. Proceedings of the second European Advanced Accelerator Concepts Workshop 2015.

[122] B. Schmidt. DESY FLA. Private communication.

[123] S. Wunderlich. DESY FLA. Private communication.

[124] R. W. Boyd, *Nonlinear Optics.* Burlington, MA, USA: Academic Press, third ed., 2007.

[125] F. Träger, ed., *Handbook of Lasers and Optics.* Berlin, Germany: Springer, second ed., 2012.

[126] Saint-Gobain Crystals, “CsI(Tl), CsI(Na) Cesium Iodide Scintillation Material.” `http://www.crystals.saint-gobain.com/uploadedFiles/SG-Crystals/Documents/CsI%28Tl%29%20and%20%28Na%29%20data%20sheet.pdf`. Accessed online June 13, 2016.

[127] G. Schaumann. University of Darmstadt, Darmstadt, Germany. Private communication.

[128] M. N. Christensen, J. Byskov-Nielsen, B. H. Christensen, and P. Balling, “Single-shot ablation of sapphire by ultrashort laser pulses,” *Appl. Phys. A*, vol. 101, no. 2, pp. 279–282, 2010.

[129] “OpenFOAM,” 2016. `http://www.openfoam.com`.

[130] Linde AG, “Entzündliche Gase.” `http://www.linde-gas.de/de/safety_and_quality/gas_risks/flammable_gases/index.html`. Accessed online June 13, 2016.

[131] K. Floettmann and V. V. Paramonov, “Beam dynamics in transverse deflecting rf structures,” *Phys. Rev. ST Accel. Beams*, vol. 17, no. 2, pp. 024001–11, 2014.

[132] M. Titberidze, F. Grüner, A. R. Maier, B. Zeitler, H. Schlarb, M. Felber, T. Lamb, C. Sydlo, K. Flöttmann, U. Mavrič, J. Müller, S. Epp, and E. Janas, “Present and Future Optical-to-Microwave Synchronization Systems at REGAE Facility for Electron Diffraction and Plasma Acceleration Experiments,” in *Proceedings of IPAC2015*, (Richmond, VA, USA), pp. 833–836, 2015. MOPHA026.

[133] E. Cullerton and B. Chase, “1.3 GHz Phase Averaging Reference Line.” Poster presentation at the LLRF2013. Accessed online May 18, 2016.

[134] F. Mayet, “Simulation and characterization of the RF system and global stability analysis at the REGAE linear electron accelerator,” Master’s thesis, University of Hamburg, Hamburg, Germany, 2012.

[135] V. Ziemann, “Vacuum Tracking,” tech. rep., SLAC, Standford, CA, USA, 1992. SLAC-PUB-5962.

[136] J. M. Lafferty, ed., *Foundations of Vacuum Science and Technology.* New York, NY, USA: John Wiley & Sons, Inc., 1998.

[137] M. Ady and R. Kersevan, “Molflow+,” 2014. `http://test-molflow.web.cern.ch`.

[138] S. Lederer. DESY MVS. Private communication.

[139] C. R. Prokop, P. Piot, B. E. Carlsten, and M. Church, “Beam dynamics performances and applications of a low-energy electron-beam magnetic bunch compressor,” *Nucl. Instr. Meth. Phys. Res. A*, vol. 719, no. 0, pp. 17–28, 2013.

[140] K. Floettmann, “rf-induced beam dynamics in rf guns and accelerating cavities,” *Phys. Rev. ST Accel. Beams*, vol. 18, p. 064801, 2015.

[141] L. Serafini and J. B. Rosenzweig, “Envelope analysis of intense relativistic quasilaminar beams in rf photoinjectors: A theory of emittance compensation,” *Phys. Rev. E*, vol. 55, pp. 7565–7590, 1997.

[142] K. Floettmann, “Emittance compensation in split photoinjectors,” *Phys. Rev. Accel. Beams*, vol. 20, p. 013401, 2017.

[143] M. Reiser, *Theory and Design of Charged Particle Beams.* Weinheim, Germany: Wiley-VCH Verlag GmbH & Co. KGaA, second ed., 2008.

[144] E. Goulielmakis, M. Schultze, M. Hofstetter, V. S. Yakovlev, J. Gagnon, M. Uiberacker, A. L. Aquila, E. M. Gullikson, D. T. Attwood, R. Kienberger, F. Krausz, and U. Kleineberg, “Single-cycle nonlinear optics,” *Science*, vol. 320, no. 5883, pp. 1614–1617, 2008.

[145] K. Zhao, Q. Zhang, M. Chini, Y. Wu, X. Wang, and Z. Chang, “Tailoring a 67 attosecond pulse through advantageous phase-mismatch,” *Opt. Lett.*, vol. 37, no. 18, pp. 3891–3893, 2012.

[146] D. L. Webster, “Cathode-Ray Bunching,” *J. Appl. Phys.*, vol. 10, no. 7, pp. 501–9, 1939.

[147] P. Piot, Y. E. Sun, T. J. Maxwell, J. Ruan, A. H. Lumpkin, M. M. Rihaoui, and R. Thurman-Keup, “Observation of Coherently-Enhanced Tunable Narrow-Band Terahertz Transition Radiation from a Relativistic Sub-Picosecond Electron Bunch Train,” *Appl. Phys. Lett.*, vol. 98, no. 26, 2011.

[148] S. Antipov, C. Jing, P. Schoessow, A. Kanareykin, V. Yakimenko, A. Zholents, and W. Gai, “High power terahertz radiation source based on electron beam wakefields,” *Rev. Sci. Instrum.*, vol. 84, no. 2, p. 022706, 2013.

[149] F. Lemery and P. Piot, “Ballistic bunching of photoinjected electron bunches with dielectric-lined waveguides,” *Phys. Rev. ST Accel. Beams*, vol. 17, no. 11, pp. 112804–10, 2014.

[150] A.-S. Müller, “Accelerator-Based Sources of Infrared and Terahertz Radiation,” *Rev. Accl. Sci. Tech*, vol. 03, no. 01, pp. 165–183, 2010.

Acknowledgments

At this point I want to express my gratitude to the countless people who have contributed to this work – with or without their knowledge.

First of all, I want to thank Prof. Dr. Florian Grüner, who gave me the opportunity to work on the external injection project at Regae, thus providing the framework for this Ph.D. thesis. Thank you for the faith you put into me and your support – not only concerning the topic. Also, thank you very much for the supervision and evaluation of the Ph.D. work.

It is very important to me to express my gratitude to Dr. Klaus Flöttmann, who is the mastermind behind Regae and the initiator of the linearization concept. Thank you very much for your support and advise, and the supervision of the Ph.D. project. And thank you very much for the countless stimulating discussions. It was and to this day continues to be a pleasure learning from an expert like you, and your impressively broad knowledge.

Then I would like to thank Prof. Dr. Vasili Tsakanov for evaluating the thesis. It was an honor and a nice surprise that you even could participate in my disputation.

I want to thank Dr. Andreas Maier for his support, not only concerning the Regae project and project related topics. Also, the improvements of the Angus laser system envisioned and persistently pursued by you and your team make Angus the reliable work horse not only for the Lux experiment, but also for the external injection project. The same goes for the development of the laser transport beam line and other concepts. Andi, thanks for your company at the various conferences enjoyed together, and, of course, also for the numerous invitations to dinner with reliably delicious food.

I am indebted to my dear office colleagues, Matthias Schnepp and Dr. Andreas Walker, not only for their advise and expertise shared concerning problems related to their respective fields of work, but also for enduring my constant grumbling about the project status and the stagnating progress. It was a pleasure residing with you, guys! In particular, it was also a pleasure having a reliable coffee mate like you, Andi, sharing the passion for *good* coffee.

Furthermore, I want to thank all of my fellow Ph.D. students in the Grüner-Maier-environment, making this journey most enjoyable. Among these, a big thank you goes to Irene Dornmair for her refreshingly sarcastic view on the world in general and local events in particular, and of course for sharing her knowledge on plasma- and LWFA physics, and especially for proofreading my thesis. And thanks for the uncountable muffin and/or coffee breaks. I furthermore want to thank Niels Delbos, not only for proofreading, but also for the clear view on physics, the constructive criticism, and the structured approaches, which helped to solve numerous project issues. Also, most importantly, thanks for triggering the Taekwon-Do switch, man! It is an honor to train

and suffer with you. I also want to thank Chris Werle – the unrivaled master of *Schweinsbraten* and unmatched creator of cakes. Thanks for your help on various topics like laser optics or the BA–MBA transfer. Thanks to all the Ph.D. students of the second (Theresa Brümmer, Vincent Leroux, Spencer Jolly, . . . ; Frederike Ahr) and third generation (Manuel Kirchen, Paul Winkler, Philipp Messner, Max Trunk, . . .). Thanks to all the master (Sören Jalas, . . .), bachelor (Sören Jalas, . . .), and working students (Sören Jalas, . . .) of the group, and the various alumni. In this context I have and want to thank the whole LUX team for the development and design of the laser transport beam line and other laser and vacuum related concepts, which strongly influenced the experimental setup presented in this work.
I explicitly want to thank *my* master and bachelor students. In this respect, I am especially grateful to Konstantin Krausert, Tim Gehrke, and Marcel Diem, as well as to my loyal and committed working students Kevin Peters and Nick Guse. Also thanks to my fellow REGAE-related Ph.D. students Mikheil Titberidze, Max Hachmann, and Daniel Riebesehl.

I am indebted to Fenna Reinhold and Heike Kaminski, our team assistants. You always had an open ear and kept things running. Without you, all of us would be doomed for sure. In particular, I want to thank both of you for your kind support with the organization of my disputation.

I want to thank Martin Stieben among other things for his support with the *physnet* cluster. It was an invaluable help to have an *Uboot* [39] in the *physnet* computer center. In this respect, I would also like to thank Frank Mayet for his support with Mac-related stuff.

I am very grateful to Dr. Hossein Delsim-Hashemi, the diagnostics master mind at REGAE. Thank you for your very kind support, not only in terms of the eSpec upgrade. I also want to thank Dr. Stephanie Manz and the other REGAE people in the MPSD group of Prof. Dr. R. J. Dwayne Miller.

I am grateful for the broad support provided by the various technical groups of the University of Hamburg and in particular at DESY. Despite the fact that the beam line has not been set up at this point in time, countless working hours have been put into the conception, planning, and design of the system, as well as into the mechanical construction of various sub-parts required for the upgrade. So I want to thank Lutz-Olaf Berger and Dariusz Kocoň (ELI Beamlines), and the DESY ZM-department for the mechanical designs, which due to their complexity required several iterations and countless adaptions. I want to thank Stephan Fleig and the whole University workshop. Most importantly, I want to express my gratitude to MVS, the vacuum group of the DESY machine division, in particular to Nils Plambeck and – first and foremost – to Dr. Sven Lederer.

In this context, I also want to mention the notorious DESY-M coffee round, which it was and still is a great pleasure and fun to participate in, and which helped to solve several issues in a very efficient way. Also, it enabled a glimpse into the world and complexity of *big* machines.

I would also like to acknowledge the support for this work by the members of the LAOLA-collaboration. Similarly, I would like to recognize the support and interest in the project by our colleagues working at ELI Beamlines.

I am indebted to the PIER Helmholtz Graduate School (PHGS), which gave me the opportunity to gain insight into fields beyond accelerator physics, be it by learning from Ph.D. students from different research fields who presented their findings in the PIER Ph.D. seminars, or by taking various courses as part of the PIER Graduate Week. The PHGS also provided me with a travel grant, which enabled me to make an important conference visit.

Furthermore, I would like to thank a few people who are not directly related to physics. I am very grateful to my Taekwon-Do master, Shin-Gyu Kang. It is a great honor to learn martial arts at the Kang Center in Hamburg. Taekwon-Do and the people at the Kang Center provided a balance to the daily project strains and problems. I have met a lot of nice people there and enjoyed (and still enjoy) the countless activities with all of you – be it Taekwon-Do-related or not.

Speaking of friends… thanks to Katharina Seßler and Florian Feineis. Thanks to Christina "Tei" Wollinger and Fabian Schorcht for their frequent visits. Special thanks to Dr. Bronja Berenfeld: Dr. Bo, thanks for the great time in Hamburg and the constant motivation. Also, thanks to the whole Team Krusty crew for the annual madness and distraction in Leipzig, and many things beyond that.

I am indebted to my dear cousin Ester Gnandt for proofreading and improving my formulations by more than 1500 suggestions, *such* that this thesis is much more readable. Thanks also to all the other relatives persistently showing their interest in the progress of my Ph.D. work, supporting me, and visiting me here in the north.

Zu guter Letzt möchte ich mich bei meiner Familie für die bedingungslose Unterstützung bedanken. Danke an meine Geschwister Simon, Ursula und Hedwig. Und lieben Dank an meine Mutter Birgit, sowie meinen Vater, Christoph Zeitler. Schade, dass du den Abschluss meiner Doktorarbeit nicht mehr erleben konntest, Papa.

Jetzt bist du frei…